



HAL
open science

Enhancing plasma performance with radiofrequency waves in magnetic confinement fusion devices

Rémi Dumont

► **To cite this version:**

Rémi Dumont. Enhancing plasma performance with radiofrequency waves in magnetic confinement fusion devices. Plasma Physics [physics.plasm-ph]. AMU - Aix Marseille Université, 2018. tel-01954912

HAL Id: tel-01954912

<https://cea.hal.science/tel-01954912>

Submitted on 14 Dec 2018

HAL is a multi-disciplinary open access archive for the deposit and dissemination of scientific research documents, whether they are published or not. The documents may come from teaching and research institutions in France or abroad, or from public or private research centers.

L'archive ouverte pluridisciplinaire **HAL**, est destinée au dépôt et à la diffusion de documents scientifiques de niveau recherche, publiés ou non, émanant des établissements d'enseignement et de recherche français ou étrangers, des laboratoires publics ou privés.

AIX-MARSEILLE UNIVERSITÉ

Thèse présentée pour obtenir
l'Habilitation à Diriger des Recherches

Rémi Dumont

**Enhancing plasma performance
with radiofrequency waves
in magnetic confinement fusion devices**

Soutenue le 14 septembre 2018 devant le jury composé de :

Jean-Marcel Rax	Professeur des Universités, École Polytechnique	Rapporteur
Bruno Després	Professeur des Universités, Université Paris 6	Rapporteur
Mervi Mantsinen	Professeur de Recherche, ICREA Barcelone	Rapporteur
Pascale Hennequin	Directrice de Recherche, École Polytechnique	Examinatrice
Didier Moreau	Expert de Haut Niveau, CEA	Examineur
Peter Beyer	Professeur des Universités, Université d'Aix-Marseille	Tuteur

CEA, IRFM, F-13108 Saint-Paul-lez-Durance, France.

Il sortit, avala l'air frais de la nuit, en soupira d'aise, se soulagea tout en contemplant les étoiles, se dit : "Ouais, le cosmos" et rentra dormir.

- V. Grossman, Vie et Destin

Remerciements

L'essentiel des travaux présentés dans ces pages a été mené au sein de l'Institut de Recherches sur la Fusion par Confinement magnétique (IRFM), au CEA Cadarache. Parmi les chefs d'Institut et de Service qui s'y sont succédés, je souhaite remercier particulièrement J. Jacquinot, M. Chatelier et A. Bécoulet, ainsi que B. Saoutic, X. Litaudon et F. Imbeaux. J'ai également eu le plaisir de travailler dans d'autres laboratoires, parmi lesquels PPPL (Princeton, USA) et JET (Culham, UK). L'environnement stimulant que j'ai trouvé dans tous ces lieux a été déterminant pour la conduite de mes recherches.

Ce manuscrit risque de trahir un certain penchant pour la théorie et la simulation numérique. Toutefois, en physique des plasmas, le contact permanent entre scientifiques du CEA, du CNRS, de l'Université et de divers laboratoires en Europe ou ailleurs fait que la frontière entre théoricien, numéricien et expérimentateur s'estompe parfois. Ainsi, prendre une part active à l'opération des machines de fusion Tore Supra, WEST et JET a été pour moi source de plaisir et de fierté. L'ensemble de ces interactions a déterminé d'une manière ou d'une autre la réflexion et les résultats présentés dans ce document.

En l'absence de certains collègues, il est probable que ce manuscrit et la présentation publique qui en a été faite auraient été bien différents. A ce titre, je souhaite d'abord remercier L.-G. Eriksson et D. N. Smithe pour m'avoir guidé et inspiré. J'aimerais également souligner l'influence de C. K. Phillips, N. J. Fisch, X. Garbet, Ph. Ghendrih, G. Giruzzi, G. T. Hoang, J. Hosea, G. Huijsmans, E. F. Jaeger, Ph. Lamalle, J.-M. Rax, B. Saoutic, S. Sharapov et D. Van Eester. Enfin, ce travail a grandement bénéficié de l'apport des étudiants que j'ai encadrés, parmi lesquels je mentionnerai ici J.-B. Girardo et D. Zarzoso.

Contents

Preamble	1
1 Introduction	3
1.1 Plasma waves	3
1.1.1 Maxwell's equations	4
1.1.2 Properties of a magnetized plasma	6
1.1.3 Energy transfers	8
1.2 External heating of magnetic fusion plasmas	11
1.2.1 Radiofrequency waves	11
1.2.2 Energetic particles	12
1.2.3 Improving plasma performance with RF waves	13
1.3 Organization of this manuscript	14
2 Hamiltonian theory of electromagnetic perturbations	17
2.1 Kinetic description of particles	17
2.1.1 Quasi-local trajectories	17
2.1.2 Adiabatic invariants	18
2.1.3 Anisotropic Maxwellians	19
2.2 Hamiltonian perturbations	20
2.2.1 Linear response	20
2.2.2 Orbit integrals	21
2.2.3 Quasi-local limit	23
2.3 Hamiltonian contributions	28
2.3.1 All-orders expression	28
2.3.2 WKB harmonics	29
3 Wave electromagnetic field	31
3.1 Variational principle	31
3.1.1 Maxwell's equations	31
3.1.2 Maxwellian functional	33
3.1.3 Plasma functional	35
3.1.4 Energy conservation	39
3.2 Dielectric response	40
3.2.1 General expression	40
3.2.2 Anisotropic Maxwellians	41

3.2.3	Resonant functional: WKB harmonics	42
4	Quasilinear plasma response	45
4.1	Hamiltonian quasilinear theory	45
4.1.1	Fokker-Planck equation	45
4.1.2	Quasilinear diffusion coefficient	47
4.1.3	Energy conservation	48
4.2	Derivation of a quasi-local model	50
4.2.1	Quasilinear diffusion coefficient	50
4.2.2	Coulomb collisions	52
4.2.3	A quasi-local Fokker-Planck solver	54
4.2.4	Derived quasilinear quantities	56
5	On phase-space engineering using RF waves	59
5.1	LH-EC synergy	60
5.2	Heavy impurity control	60
5.3	MHD control	63
5.4	Energetic Geodesic Acoustic Modes	65
5.5	Poloidal flow drive	67
5.6	Alpha-channeling	69
6	Conclusions	71
A	Geometry	73
A.1	Toroidal coordinates	73
A.2	Magnetic equilibrium	74
A.3	Local magnetic frames	76
A.4	Cylindrical geometry	79
B	Plasma functional: numerical implementation	82
B.1	Adiabatic functional	82
B.2	Resonant functional	82
C	Collocation algorithm	89
C.1	General formulation	89
C.2	Dielectric response evaluation	91
D	ICRF heating in a tokamak: a minimal model	92
D.1	Power density	93
D.2	Quasilinear diffusion coefficient	93
D.3	Low energy, isotropic distribution	95
D.4	High-energy tail	96
E	Selected publications	109

Preamble

A successful magnetic fusion reactor must fulfill a certain number of prerequisites in terms of physics and technology [1,2]. In its most simplified form, the main physics challenge can be summarized in the form of the Lawson criterion which expresses the balance between fusion power production and energy losses, i.e.

$$nT\tau_E \gtrsim 3 \cdot 10^{21} \text{keV} \cdot \text{s} \cdot \text{m}^{-3}, \quad (1)$$

with n the plasma density, T the fuel ion temperature and τ_E the energy confinement time. The cross-section of Deuterium-Tritium reactions has a maximum value, imposing an optimal temperature which can only be attained by using external heating systems to provide energy to the plasma. Stability and equilibrium constraints inherent to magnetically confined plasmas dictate that the plasma pressure nT must not exceed a rather low fraction of the magnetic energy $B^2/2\mu_0$ with B the confining magnetic field [3]. Having already defined an optimal temperature, this places an upper limit on achievable densities n . In this somewhat simplistic analysis, the remaining parameter is therefore τ_E , the energy confinement time. Neoclassical theory, which describes collisional transport in toroidal geometry, can be employed to predict τ_E [4]. However, it is well known that this estimate is much larger, and thus optimistic in terms of performance, than the typically measured values. Two main factors degrading the energy confinement with respect to neoclassical predictions have been identified:

- MHD instabilities inherent to the equilibrium properties (kink and tearing modes...), destabilized by the presence of energetic particles (toroidal Alfvén eigenmodes...), or even created by these particles (fishbones...),
- turbulence resulting from micro-scale instabilities.

The physics phenomena underlying these processes are complex, and their effects are not additive. Magnetic fusion plasmas are self-organized system which exhibit a high level of coupling between the processes at play: neoclassical transport, turbulence and MHD instabilities. Some control can still be exerted on the plasma behavior, and ultimately on the fusion performance, by using external systems. Neutral Beam Injection (NBI) allows high density and temperature to be sustained by external matter and energy injection. Electromagnetic field in the form of Radiofrequency (RF) waves allow electrical work to flow from a generator to the plasma particles. Historically, they have been employed for plasma non-inductive heating and current drive. In more recent applications, they are also used to influence neoclassical transport, MHD activity, and also turbulence, with various

levels of sophistication. In this manuscript, we focus on a mathematical model for the RF wave propagation, damping, and resulting plasma response. This model and its numerical implementation are required to simulate RF waves when they are employed in phase-space engineering applications. Several of these advanced concepts are described.

Chapter 1

Introduction

1.1 Plasma waves

The physical description of an electromagnetic wave propagating in a given medium necessitates a self-consistent handling of the particles comprising the medium (and their mutual interactions) on the one hand, and of the electromagnetic field on the other hand. In the case of a plasma, the generic problem is summarized in Fig. 1.1.

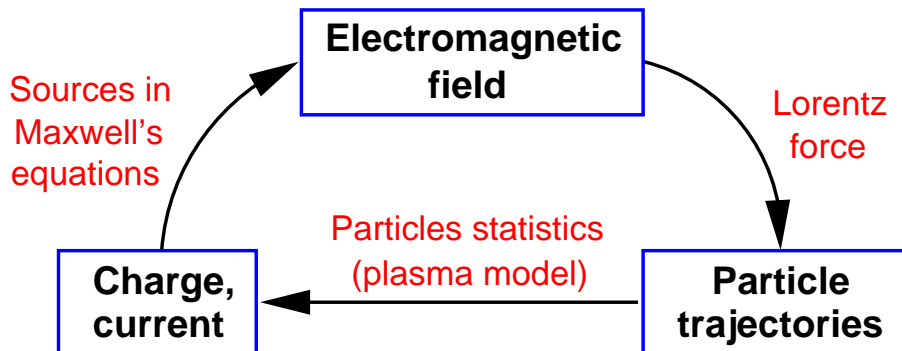


Figure 1.1: Self-consistent description of the electromagnetic field in a plasma.

The electromagnetic field, given by the Maxwell's equations, influences the particle trajectories. Since the handling of all individual particles is largely beyond the computational capabilities of available computers in the present, but also in any foreseeable future, a plasma model is needed to derive statistical quantities, such as the charge and current density. In turn, these quantities enter as sources in the Maxwell's equations, and influence the field. Depending on the problem under study, various approximations are introduced to close this loop.

In the case of radiofrequency (RF) wave, there exists a clear timescale separation in the problem. The wave period (τ) is always much smaller than the collisional time (τ_{coll}) which itself is comparable to the typical time it takes for the secular evolution of the distribution function to take place (τ_{QL}), so that $\tau \ll \tau_{coll} \sim \tau_{QL}$. Even relatively low frequency

heating waves, at $f \sim 10\text{MHz}$, are such that $\tau = 0.1\mu\text{s} \ll \tau_{coll}, \tau_{QL}$. Practically, this means that the problem of the wave field evaluation on the one hand and of the plasma response evaluation on the other hand are handled independently: the former is obtained by solving the Maxwell's equations assuming the distribution functions are known, whereas the latter is obtained from the Fokker-Planck equation, evaluated assuming the wave electromagnetic field is given. This simplification is illustrated in Fig. 1.2.

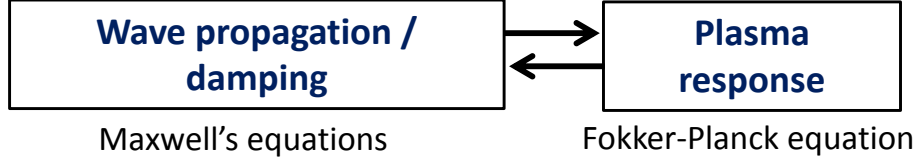


Figure 1.2: Simplified description of the coupled wavefield and plasma response evolution.

1.1.1 Maxwell's equations

The macroscopic electromagnetic field in the plasma is described by the Maxwell's equations, which we can choose to write in the form:

$$\nabla \cdot \mathbf{D} = \rho_{free} + \rho_{ext}, \quad (1.1)$$

$$\nabla \cdot \mathbf{B} = 0, \quad (1.2)$$

$$\nabla \times \mathbf{E} = -\frac{\partial \mathbf{B}}{\partial t}, \quad (1.3)$$

$$\nabla \times \mathbf{H} = \mathbf{j}_{free} + \mathbf{j}_{ext} + \frac{\partial \mathbf{D}}{\partial t}. \quad (1.4)$$

In these relations, \mathbf{E} is the electric field, \mathbf{D} is the electric displacement, \mathbf{H} is the magnetic intensity, \mathbf{B} is the magnetic induction (which we shall refer to as the magnetic field). \mathbf{j}_{free} is the current carried by the free charges flowing in the medium, and ρ_{free} is the corresponding charge density. \mathbf{j}_{ext} and ρ_{ext} are the current and charge densities from external sources, such as antennas. It is important to notice that in this form, the polarization and magnetization currents are included in \mathbf{D} and \mathbf{H} . Formally, it is possible to solve these equations as long as we are able to describe the medium response to a given electromagnetic excitation. In other words, we need to establish the constitutive relations of the medium:

$$\mathbf{D} \stackrel{?}{=} \mathbf{D}[\mathbf{E}, \mathbf{B}], \quad (1.5)$$

and

$$\mathbf{H} \stackrel{?}{=} \mathbf{H}[\mathbf{E}, \mathbf{B}]. \quad (1.6)$$

In classical electromagnetism [5], it is usual to introduce a polarization vector \mathbf{P} , and also a magnetization vector \mathbf{M} to write

$$\mathbf{D} \equiv \epsilon_0 \mathbf{E} + \mathbf{P}, \quad (1.7)$$

and

$$\mathbf{H} \equiv \mathbf{B}/\mu_0 - \mathbf{M}, \quad (1.8)$$

with $\epsilon_0 = 1/36\pi \times 10^{-9}\text{F/m}$ the vacuum dielectric permittivity and $\mu_0 = 4\pi \times 10^{-7}\text{H/m}$ the vacuum magnetic permeability. We can then manipulate Eq. 1.4 to obtain the perhaps more familiar form

$$\nabla \times \mathbf{B} = \mu_0(\mathbf{j}_{free} + \mathbf{j}_{mag} + \mathbf{j}_{pol} + \mathbf{j}_{ext}) + \frac{1}{c^2} \frac{\partial \mathbf{E}}{\partial t}, \quad (1.9)$$

with $\partial_t \mathbf{P} \equiv \mathbf{j}_{pol}$, and $\nabla \times \mathbf{M} \equiv \mathbf{j}_{mag}$. \mathbf{j}_{pol} and \mathbf{j}_{mag} are respectively the polarization and magnetization currents.

So far, we have followed the exact same method employed, e.g., in solid state physics. However, in plasma physics, it is impractical to separate the polarization, the magnetization and the free charges currents. Indeed, all charges are free (at least in a fully ionized plasma), yet all do contribute to the polarization of the medium. Therefore, we choose to rewrite Eq. 1.9 in the microscopic form

$$\nabla \times \mathbf{B} = \mu_0(\mathbf{j} + \mathbf{j}_{ext}) + \frac{1}{c^2} \frac{\partial \mathbf{E}}{\partial t}, \quad (1.10)$$

where \mathbf{j} is the total current flowing in the plasma in response to the wave perturbation. It is now straightforward to deduce the wave equation from Eqs. 1.3 and 1.10

$$\nabla \times \nabla \times \mathbf{E} + \frac{1}{c^2} \frac{\partial^2 \mathbf{E}}{\partial t^2} = -\mu_0 \frac{\partial(\mathbf{j} + \mathbf{j}_{ext})}{\partial t}. \quad (1.11)$$

Despite its apparent simplicity, this relation is extremely complicated, firstly because of its non-linear nature (in all generality, \mathbf{j} is a non-linear function of \mathbf{E}) and secondly because of the plasma properties. In all this work, we will always assume that the relation between \mathbf{j} and \mathbf{E} is linear in essence, restricting ourselves to waves of moderate amplitude, which can therefore be treated as perturbations. This will allow us to retain the self-consistent nature of the problem within acceptable computational requirements.

In order to assess the level of realism of this hypothesis, we consider the problem of heating a plasma with RF waves. In a magnetic fusion reactor such as ITER, the maximum electric field in the plasma associated to waves in the ion cyclotron range of frequencies is estimated to be of the order $|E| \sim 30\text{kV/m}$ (see, e.g., Ref. [6]). The propagating wave in this case belongs to the compressional branch, for which the refraction index is approximately given by [7]

$$\epsilon \approx \epsilon_0 \frac{c^2}{v_a^2}, \quad (1.12)$$

with v_a the Alfvén velocity. If we consider a deuterium plasma with a density $n_e \sim 10^{20}\text{m}^{-3}$ confined by a magnetic field $B \sim 5\text{T}$, we obtain $\epsilon \sim 1.3 \times 10^{-8}\text{F/m}$. The corresponding electromagnetic energy density is thus given by

$$w = \epsilon \frac{|E|^2}{2} \sim 6\text{J/m}^3. \quad (1.13)$$

The thermal energy contained in the plasma if we assume a uniform temperature $T_e = T_i \sim 5\text{keV}$ is given by

$$w_{th} \equiv 2n_e T_i \sim 160\text{J/m}^3. \quad (1.14)$$

We see that $w \ll w_{th}$, so that the linear hypothesis is legitimate. Of course, the electric field can be locally stronger in some situations but a more subtle analysis shows that a linear assumption is usually quite adequate to describe plasma waves excited by auxiliary systems [8].

1.1.2 Properties of a magnetized plasma

In an isotropic dielectric medium, the fact that \mathbf{j} is a linear function of \mathbf{E} can be written as

$$\mathbf{j}(\mathbf{r}, t) = \sigma(\mathbf{r}, t)\mathbf{E}(\mathbf{r}, t). \quad (1.15)$$

σ is the linear conductivity. Eq. 1.15 is local, both spatially (i.e., the response at location \mathbf{r} only depends on the excitation at location \mathbf{r}) and temporally (i.e., the response at instant t depends only on the excitation at instant t). However, several properties of the plasma make the description more complicated than in this ideal dielectric medium.

Anisotropy: In many situations, plasmas are immersed in strong magnetic fields (magnetic fusion plasmas, space plasmas...). In this case, the response will obviously differ depending on the direction of the excitation. The relation between \mathbf{j} and \mathbf{E} thus becomes tensorial in essence, as in a crystal for instance. Hence, we write

$$\mathbf{j}(\mathbf{r}, t) = \boldsymbol{\sigma} \cdot \mathbf{E}(\mathbf{r}, t), \quad (1.16)$$

where $\boldsymbol{\sigma}$ is now a tensor.

Time dispersion: The plasma comprises electrons and ions, which evidently have different weights. Depending on the wave frequency, due to their inertia, the heavy ions may respond to the excitation with a delay compared to the lighter electrons. In this case, the response of the plasma at instant t is determined by the excitation at all previous instants t' . Taking into account the causality principle, we obtain a relation which is non-local in time:

$$\mathbf{j}(\mathbf{r}, t) = \int_{-\infty}^t dt' \boldsymbol{\sigma}(\mathbf{r}, t, t') \cdot \mathbf{E}(\mathbf{r}, t'). \quad (1.17)$$

Due to the non-local character of the relation between \mathbf{j} and \mathbf{E} , it is usual to refer to $\boldsymbol{\sigma}(\mathbf{r}, t, t')$ as the conductivity kernel.

Space dispersion: In a plasma, the finite temperature of the species induces a thermal agitation, and the particles have erratic displacements superimposed to their integrable motion. This means that the particles at position \mathbf{r} are influenced by the electromagnetic field in the domain they explore due to this non-deterministic part of their motion. Space dispersion is therefore a consequence of thermal effects. We can thus expect a cold plasma to be non-dispersive in space (but not in time).

In general, the relation between \mathbf{j} and \mathbf{E} must therefore be written in a spatially non-local form:

$$\mathbf{j}(\mathbf{r}, t) = \int d^3\mathbf{r}' \boldsymbol{\sigma}(\mathbf{r}, \mathbf{r}', t) \cdot \mathbf{E}(\mathbf{r}', t). \quad (1.18)$$

Gathering these three essential properties, it is clear that the functional $\mathbf{j}(\mathbf{E})$ must be written in the form

$$\mathbf{j}(\mathbf{r}, t) = \int_{-\infty}^t dt' \int d^3\mathbf{r}' \boldsymbol{\sigma}(\mathbf{r}, \mathbf{r}', t, t') \cdot \mathbf{E}(\mathbf{r}', t'). \quad (1.19)$$

If the plasma is stationary, the conductivity can only depend on the time elapsed between the excitation (t') and the response (t). In other words, the conductivity kernel must verify $\boldsymbol{\sigma}(\mathbf{r}, \mathbf{r}', t, t') = \boldsymbol{\sigma}(\mathbf{r}, \mathbf{r}', t - t')$. Furthermore, if the plasma is homogeneous, the conductivity can only depend on the difference between the excitation location (\mathbf{r}') and the response location (\mathbf{r}), which simply reflects the fact that the medium is invariant by translation. We obtain $\boldsymbol{\sigma}(\mathbf{r}, \mathbf{r}', t, t') = \boldsymbol{\sigma}(\mathbf{r} - \mathbf{r}', t, t')$.

When both conditions are fulfilled, Eq. 1.19 then becomes

$$\mathbf{j}(\mathbf{r}, t) = \int_{-\infty}^t dt' \int d^3\mathbf{r}' \boldsymbol{\sigma}(\mathbf{r} - \mathbf{r}', t - t') \cdot \mathbf{E}(\mathbf{r}', t'). \quad (1.20)$$

It is useful to perform a Fourier analysis of the oscillating quantities and write the electric field and the current density as superpositions of plane waves. It is readily seen that in Fourier space, Eq. 1.20 takes a local character:

$$\mathbf{j}_{\mathbf{k}, \omega} = \boldsymbol{\sigma}_{\mathbf{k}, \omega} \cdot \mathbf{E}_{\mathbf{k}, \omega}, \quad (1.21)$$

where $\mathbf{j}_{\mathbf{k}, \omega}$, $\mathbf{E}_{\mathbf{k}, \omega}$ and $\boldsymbol{\sigma}_{\mathbf{k}, \omega}$ are respectively the Fourier transforms of the current, electric field and conductivity kernel.

The homogeneous/stationary plasma assumption is quite convenient, as it opens the way to the very useful notions of dispersion relation, dielectric tensor. . . However, an analysis of its range of validity shows that the homogeneous plasma assumption is often not justified. Another major drawback of the plane wave decomposition is that a plane wave in a uniform medium contains infinite energy by construction, and is thus not adapted to the description of energy exchanges [8, 9]. The solution to this is to refine the plane wave decomposition by using a WKB form for all oscillating quantities [10]. The electric field is then written as

$$\mathbf{E}(r, t) = \frac{1}{2} [\mathbf{E}_0(r, t) e^{i\phi} + \mathbf{E}_0^*(r, t) e^{-i\phi}]. \quad (1.22)$$

Assuming that the wave properties vary slowly both spatially and temporally with respect to the wavelength and wave-period respectively, the eikonal function can be approximated as¹

$$\phi(t) = \mathbf{k} \cdot \mathbf{r} - \omega t. \quad (1.23)$$

The WKB form allows one to describe the plasma as quasi-local, i.e. local from the wave point of view, while retaining the possibility of describing a slowly varying medium.

¹Owing to the validity conditions of the WKB approximation, it must be noted that this derivation is not adapted to describe abrupt space or time changes in the medium properties, such as cut-offs or resonances.

1.1.3 Energy transfers

The description of energy transfers taking place between the medium and the wave is obviously contained in the Maxwell's equations. Dotting Eq. 1.3 with \mathbf{H} , Eq. 1.4 with \mathbf{E} and using the vector relation $\nabla \cdot (\mathbf{E} \times \mathbf{H}) = \mathbf{H} \cdot \nabla \times \mathbf{E} - \mathbf{E} \cdot \nabla \times \mathbf{H}$, the Poynting theorem can be expressed as a conservation relation:

$$\nabla \cdot \mathbf{S} + \mathbf{E} \cdot \frac{\partial \mathbf{D}}{\partial t} + \mathbf{H} \cdot \frac{\partial \mathbf{B}}{\partial t} = -(\mathbf{j}_{free} + \mathbf{j}_{ext}) \cdot \mathbf{E}, \quad (1.24)$$

with the Poynting vector defined as

$$\mathbf{S} \equiv \mathbf{E} \times \mathbf{H}. \quad (1.25)$$

This form has the advantage of clearly showing the energy flow of the electromagnetic wave (\mathbf{S}), the power required to establish the electric field in the medium ($\mathbf{E} \cdot \partial_t \mathbf{D}$) and the power required to establish the magnetic field in the medium ($\mathbf{H} \cdot \partial_t \mathbf{B}$). On the right hand side is the dissipated power, caused by the Joule effect.

Another possibility is to use Eqs. 1.3 and 1.9 to write the energy conservation in the form

$$\frac{\partial W}{\partial t} + \nabla \cdot \mathbf{S} + (\mathbf{j}_{pol} + \mathbf{j}_{mag}) \cdot \mathbf{E} = -(\mathbf{j}_{free} + \mathbf{j}_{ext}) \cdot \mathbf{E}, \quad (1.26)$$

with the vacuum energy density

$$W \equiv \frac{\epsilon_0}{2} |\mathbf{E}|^2 + \frac{1}{2\mu_0} |\mathbf{B}|^2, \quad (1.27)$$

and the Poynting vector defined as

$$\mathbf{S} \equiv \frac{1}{\mu_0} \mathbf{E} \times \mathbf{B}. \quad (1.28)$$

The two relations (1.24) and (1.26) are written with the intention of keeping the reversible processes on the left hand side, whereas the irreversible energy exchange (dissipation) is on the right hand side. In a solid, for instance, the two first terms of Eq. 1.26 can be identified respectively as the electromagnetic energy variation and the power flowing in the electromagnetic wave. The third and fourth term represent the work exerted by the polarization and magnetization current, caused by the displacement of atoms or nuclei around their equilibrium positions in response to the applied electromagnetic field. This energy exchange is reversible: when the excitation is switched off, the power is transferred back from the medium to the wave. On the right hand side appears the power dissipated by the Joule effect. This energy transfer is irreversible and contributes to the heating of the medium. Indeed, in a solid, it is generally safe to assume that the mean free path is much smaller than the wavelength². This means that the equilibrium between the electromagnetic field and the medium is practically instantaneous. In a plasma, as discussed previously, the situation is more complicated: there is no clear separation between the free

²If we assume that the distance between two atoms is 1nm, and that this constitutes the average mean free path of a current carrier, we see that the wave frequency needed to have a wavelength comparable to this mean free path is $f \gtrsim 10^{17}$ Hz, which is in the X-rays range of frequencies.

carrier current, the polarization and magnetization currents. In other words, $\mathbf{j} \cdot \mathbf{E}$ contains reversible and irreversible contributions which can not be separated in a straightforward way. Another crucial point is that the mean free path is usually much longer than the wavelength: there is no equilibrium between the electromagnetic field and the medium on a single wave period. Therefore, we will need to work with quantities averaged over a number of wave periods to describe the exchanges of energy between the plasma and the wave: an analysis on the timescale of the wave period does not yield much useful information.

We rewrite the Poynting theorem (Eq. 1.26) in the form

$$\frac{\partial W}{\partial t} + \nabla \cdot \mathbf{S} + \mathbf{j} \cdot \mathbf{E} = -\mathbf{j}_{ext} \cdot \mathbf{E}. \quad (1.29)$$

We define the time average of a given quantity A as

$$\langle A \rangle \equiv \frac{1}{\tau} \int_0^\tau dt A(t), \quad (1.30)$$

with $\tau\omega \gg 2\pi$, where $\omega/2\pi$ is the wave frequency. If we consider the product of two quantities \mathbf{A} and \mathbf{B} written in the WKB form (1.22), it is readily shown that the time-average operation yields

$$\langle \mathbf{A} \cdot \mathbf{B} \rangle = \frac{1}{2} \Re(\mathbf{A}_0 \cdot \mathbf{B}_0^*). \quad (1.31)$$

The time-average of the first term of (1.29) leads to

$$\left\langle \frac{\partial}{\partial t} \left[\frac{|\mathbf{B}|^2}{2\mu_0} + \frac{\epsilon_0 |\mathbf{E}|^2}{2} \right] \right\rangle = \frac{1}{2\mu_0} \frac{\partial}{\partial t} |\mathbf{B}_0|^2 + \frac{\epsilon_0}{2} \frac{\partial}{\partial t} |\mathbf{E}_0|^2. \quad (1.32)$$

For the second term, we obtain

$$\left\langle \nabla \cdot \left(\frac{\mathbf{E} \times \mathbf{B}}{\mu_0} \right) \right\rangle = \frac{1}{2\mu_0} \nabla \cdot \Re(\mathbf{E}_0 \times \mathbf{B}_0^*). \quad (1.33)$$

Obviously, the complexity of our problem lies in the third term on the left hand side of Eq. 1.29, because of the dispersive nature of the plasma. Assuming that the plasma is stationary and locally uniform, the current can be written as

$$\mathbf{j}(\mathbf{r}, t) = \frac{1}{2} \left[e^{i(\mathbf{k} \cdot \mathbf{r} - \omega t)} \int_{-\infty}^t dt' \int d^3 \mathbf{r}' \boldsymbol{\sigma}(\mathbf{r} - \mathbf{r}', t - t') \cdot \mathbf{E}_0(\mathbf{r}', t') e^{i(\mathbf{k}(\mathbf{r}' - \mathbf{r}) - \omega(t' - t))} + \text{c.c.} \right], \quad (1.34)$$

where c.c. means “complex conjugate”. We can use the fact that the envelope of the electromagnetic field varies slowly to perform the Taylor expansion:

$$\mathbf{E}_0(\mathbf{r}', t') \approx \mathbf{E}_0(\mathbf{r}, t) + (\mathbf{r}' - \mathbf{r}) \cdot \frac{\partial \mathbf{E}_0}{\partial \mathbf{r}'} \Big|_{\mathbf{r}'=\mathbf{r}} + (t' - t) \cdot \frac{\partial \mathbf{E}_0}{\partial t'} \Big|_{t'=t}. \quad (1.35)$$

In the obtained expression, the Fourier transform of $\boldsymbol{\sigma}$ and its derivatives with respect to \mathbf{k} and ω can be readily identified. This gives

$$\mathbf{j}(\mathbf{r}, t) = \frac{1}{2} \left\{ e^{i(\mathbf{k} \cdot \mathbf{r} - \omega t)} \left[\boldsymbol{\sigma}_{\mathbf{k}, \omega} \cdot \mathbf{E}_0(\mathbf{r}, t) - i \frac{\partial \boldsymbol{\sigma}_{\mathbf{k}, \omega}}{\partial \mathbf{k}} \cdot \frac{\partial \mathbf{E}_0}{\partial \mathbf{r}} + i \frac{\partial \boldsymbol{\sigma}_{\mathbf{k}, \omega}}{\partial \omega} \cdot \frac{\partial \mathbf{E}_0}{\partial t} \right] + \text{c.c.} \right\}. \quad (1.36)$$

Dotting the latter expression with \mathbf{E} and averaging over time yields

$$\langle \mathbf{j} \cdot \mathbf{E} \rangle = \frac{1}{4} \left\{ \mathbf{E}_0^* \cdot \left[\boldsymbol{\sigma}_{\mathbf{k},\omega} \cdot \mathbf{E}_0 - i \frac{\partial \boldsymbol{\sigma}_{\mathbf{k},\omega}}{\partial \mathbf{k}} \cdot \frac{\partial \mathbf{E}_0}{\partial \mathbf{r}} + i \frac{\partial \boldsymbol{\sigma}_{\mathbf{k},\omega}}{\partial \omega} \cdot \frac{\partial \mathbf{E}_0}{\partial t} \right] + \text{c.c.} \right\}. \quad (1.37)$$

We introduce the dielectric tensor [11]

$$\boldsymbol{\epsilon} = \epsilon_0 \left(\mathbf{1} + \frac{i}{\omega \epsilon_0} \boldsymbol{\sigma}_{\mathbf{k},\omega} \right), \quad (1.38)$$

which may be decomposed as

$$\boldsymbol{\epsilon} = \boldsymbol{\epsilon}^h + i \boldsymbol{\epsilon}^a, \quad (1.39)$$

where the Hermitian part $\boldsymbol{\epsilon}^h$ is defined as

$$\boldsymbol{\epsilon}^h \equiv \frac{\boldsymbol{\epsilon} + \boldsymbol{\epsilon}^\dagger}{2}, \quad (1.40)$$

and the anti-Hermitian part as

$$\boldsymbol{\epsilon}^a \equiv \frac{\boldsymbol{\epsilon} - \boldsymbol{\epsilon}^\dagger}{2i}, \quad (1.41)$$

where the \dagger symbol designates the adjoint, i.e. $(\boldsymbol{\epsilon}^\dagger)_{ij} = (\boldsymbol{\epsilon})_{ji}^*$.

Using this decomposition, one obtains

$$\langle \mathbf{j} \cdot \mathbf{E} \rangle = \frac{\omega}{2} \mathbf{E}_0^* \cdot \boldsymbol{\epsilon}^a \cdot \mathbf{E}_0 - \frac{\omega}{2} \nabla \cdot \left(\mathbf{E}_0^* \cdot \frac{\partial \boldsymbol{\epsilon}^h}{\partial \mathbf{k}} \cdot \mathbf{E}_0 \right) + \frac{1}{2} \frac{\partial}{\partial t} \left(\mathbf{E}_0^* \cdot \frac{\partial}{\partial \omega} (\omega \boldsymbol{\epsilon}^h) \cdot \mathbf{E}_0 - \epsilon_0 |\mathbf{E}_0|^2 \right). \quad (1.42)$$

Finally, the time-average of the right-hand side of Eq. 1.29 corresponds to the power dissipated on the wave-exciting device. In the context of an antenna aimed at heating a plasma, it makes sense to define the power coupled by the antenna to the ionized medium as

$$P_{ant} \equiv -\mathbf{j}_{ext} \cdot \mathbf{E}. \quad (1.43)$$

Eventually, the energy conservation can be written as

$$\frac{\partial W}{\partial t} + \nabla \cdot (\mathbf{S} + \mathbf{T}) = P_{ant} - P_{abs}, \quad (1.44)$$

where W represents the electromagnetic energy density:

$$W \equiv \frac{1}{2} \left[\frac{|\mathbf{B}_0|^2}{\mu_0} + \mathbf{E}_0^* \cdot \frac{\partial}{\partial \omega} (\omega \boldsymbol{\epsilon}^h) \cdot \mathbf{E}_0 \right]. \quad (1.45)$$

\mathbf{S} , the Poynting vector, describes the power transported by the wave field:

$$\mathbf{S} \equiv \frac{1}{\mu_0} \Re(\mathbf{E}_0^* \times \mathbf{B}_0). \quad (1.46)$$

\mathbf{T} is the kinetic flux:

$$\mathbf{T} \equiv -\frac{\omega}{2} \mathbf{E}_0^* \cdot \frac{\partial \boldsymbol{\epsilon}^h}{\partial \mathbf{k}} \cdot \mathbf{E}_0. \quad (1.47)$$

It corresponds to the electromagnetic power transport caused by the coherent motion of the particles. It is clear from the latter expression that in the case of a cold plasma, where the absence of space dispersion implies $\partial\epsilon/\partial\mathbf{k} = 0$, this quantity is zero.

Finally, the dissipated power can be written as

$$P_{abs} \equiv \omega \mathbf{E}_0^* \cdot \boldsymbol{\epsilon}^a \cdot \mathbf{E}_0, \quad (1.48)$$

and directly involves the anti-Hermitian part of the dielectric tensor. It should be kept in mind that $\nabla \cdot \mathbf{T}$ and P_{abs} have different natures: the first one corresponds to power which is reversibly exchanged between the electromagnetic wave and the plasma and therefore does not contribute to its heating. The latter, on the other hand, corresponds to power irreversibly transferred to the plasma. In general, the separation of these two terms is quite difficult to achieve unambiguously [12–14].

1.2 External heating of magnetic fusion plasmas

Here, “heating” must be understood in a broad (and historical) sense. Auxiliary systems are mostly used for plasma heating by transferring electrical work to the plasma in the form of heat, but they also generally have the capability to drive non-inductive current, plasma rotation, generate energetic populations. . .

1.2.1 Radiofrequency waves

Radiofrequency waves are electromagnetic perturbations induced by external antennas. If wave damping is weak, eigenmodes tend to develop and the electromagnetic field has a global structure typically occupying the whole plasma volume, which is usually a troublesome situation in real experiments. On the other hand, if the wavelength is short compared to the plasma size and the damping mechanisms are sufficiently efficient, then in a typical “WKB” representation, the wave propagates away from the antenna in the plasma until a resonant damping mechanism takes place and allows energy to flow from the RF generator to the plasma particles. In modern experiments, waves in three distinct domains of frequencies are used:

Electron Cyclotron Waves: At frequency in the 100GHz range, their propagation is quasi-optical and they are damped by the electrons at the electron cyclotron resonance or its harmonics. They can be used to heat the plasma (ECRH) or drive non-inductive current with a somewhat modest current drive efficiency (ECCD). Also usable in this domain of frequencies are the Electron Bernstein Waves (EBW) which are employed to heat overdense plasma in stellarators or spherical torii.

Lower Hybrid Waves: Injected by couplers, their frequencies is of the order of a few GHz. They are Landau-damped by electrons, and have the capability to create energetic electron populations. With an asymmetric toroidal spectrum, it is possible to drive non-inductive current with a high efficiency. In some situations, they can be damped by energetic ions, including alphas (usually considered a parasitic phenomenon). Another difficulty is the fact that they cannot easily propagate or drive current in dense plasmas, making their relevance to future reactors uncertain.

Ion Cyclotron Waves: In the range of 10-100MHz, the fast magnetosonic wave is excited by metallic straps and propagates until it is damped mostly by ions at the ion cyclotron resonance frequency or its harmonics, typically generating energetic ion populations. They can also be used in alternative schemes to heat the electrons by Landau damping/Transit Time Magnetic Pumping or linear mode conversion to Ion Bernstein Waves (IBW). The physics of these waves is rather rich, and their effect in terms of fluid moment generation, flow drive... is even richer and not fully explored nor understood despite their early role in magnetic fusion research.

1.2.2 Energetic particles

Energetic³ electrons or ions are loosely defined as particles of a given species s with velocities largely in excess to the thermal velocity $v_{th,s}$ for this species characterized by its temperature T_s and the mass m_s of its elements, i.e.

$$v \gg v_{th,s} \equiv \sqrt{\frac{2T_s}{m_s}}. \quad (1.49)$$

Since the cross-section of fusion reactions is maximal at fairly large energies, the possibility to sustain out-of-equilibrium populations among which fusion reactions occur and transferring the resulting energy to a thermal plasma or even to a converted wave has received significant interest. However, it has been rigorously shown that valid concepts of fusion plasma confinement by magnetic fields must first and foremost involve majority species in thermal equilibrium [15]. As a consequence, research on reactors purely based on energetic particles is not a very active field, nowadays. Nevertheless, fast particle populations are usually present in tokamaks, stellarators or other types of confining devices. They can consist of electrons or ions, depending on the plasma conditions, and on the auxiliary systems employed for plasma heating:

- Fast electrons are essentially the result of Lower Hybrid (LH) waves, which create a superthermal tail in parallel velocities by Landau damping. Electron Cyclotron waves can also create energetic electrons albeit to a lesser extent than LH waves, except when the LH-EC synergy is at play. Runaway electrons obviously qualify as energetic particles but this topic is beyond the scope of the present manuscript (see, e.g. Ref. [16] and citations therein).
- An intrinsic source of fast ions in a reactor is the alpha particles created by the D-T fusion reactions



where α refers to a ${}^4\text{He}$ ion born with an energy around 3.5MeV.

A second, extrinsic source of energetic ions is Neutral Beam Injection (NBI) systems, which inject neutral particles with energies $E \sim 100 - 1000\text{keV}$ in the plasma. These neutrals are ionized and result in a population of fast ions with kinetic properties fixed by the injector geometry, beam energy and target plasma parameters.

³also called “fast” in many occurrences in this manuscript.

A third source is the result of radiofrequency (RF) waves in the Ion Cyclotron Range of Frequency (ICRF). These waves are excited by external antennas and propagate in the plasma until they are absorbed by cyclotron damping. Depending on the RF system features and the target plasma parameters, it is possible to drive ions up to energies in the range of several MeV.

Whereas these fast particle sources appear to be well separate, their simultaneous use does not result in a mere addition of effects. For instance, ICRF waves can drive NBI ions to energies exceeding their injection energy. As a result, the wave propagation and damping properties can be affected. Another coupled effect is the LH wave damping by alphas, thereby diverting power originally targeted at driving non-inductive current. These examples constitute cases of direct coupling, but the picture is actually much more complicated since fast particles also influence the discharge dynamic properties by affecting the transport of various fluid moments, as well as MHD and/or turbulent activity. And of course, these energetic particles eventually slow down on the bulk species, and contribute to the thermal plasma heating.

1.2.3 Improving plasma performance with RF waves

For a DT plasma in the range of 10 – 20keV, the Lawson criterion is often expressed as [1]

$$n_i T_i \tau_E \gtrsim 3 \cdot 10^{21} \text{keV} \cdot \text{s} \cdot \text{m}^{-3}, \quad (1.51)$$

with n_i the ion density, T_i the ion temperature (both assumed homogeneous) and τ_E the energy confinement time. It can be formulated in a slightly different fashion by assuming parabolic temperature and density profiles:

$$n_{i0} T_{i0} \tau_E \gtrsim 5 \cdot 10^{21} \text{keV} \cdot \text{s} \cdot \text{m}^{-3}, \quad (1.52)$$

where the subscript 0 refers to the central value. Introducing β_{th} as the ratio of plasma thermal pressure to magnetic pressure

$$\beta_{th} \equiv \frac{n_e T_e + n_i T_i}{\frac{B^2}{2\mu_0}}, \quad (1.53)$$

with B the confining magnetic field and assuming $T_e = T_i$, the triple product Eq. 1.52 may then be rewritten as

$$B_0^2 \beta_{th}(0) \tau_E \gtrsim 4 \text{T}^2 \cdot \text{s}. \quad (1.54)$$

From a plasma operation standpoint, improving the fusion yield is thus done by increasing β_{th} (or counteracting its degradation caused by undesirable phenomena such as MHD activity or impurity contamination) and/or τ_E .

Successful plasma heating results in an increase of β_{th} . This is caused by power damping by the absorbing species, or collisional relaxation of energetic particles on the bulk species. In modern applications, the corresponding simulations are performed using integrated modeling codes [17]. Here, we are mostly interested in methods in which energetic

electrons or ions are employed as mediators to increase β_{th} and τ_E . The only notable exception is direct flow drive by RF waves, which does not directly involve fast particles.

The various possibilities have been summarized in the diagram shown in Fig. 1.3. Some aspects have been left out of this scheme, the most notable one being that in many situations, RF waves are primarily used for plasma heating by direct power damping on thermal or nearly thermal species (Electron Cyclotron Resonance Heating, Fast Wave Electron Heating...). Therefore, one may note that the frontier between “increase τ_E ” and “increase β_{th} ” is somewhat blurry. This is especially true for EC and LH waves, which combine the effects of bulk plasma heating and improving confinement. In order not to excessively overload the diagram, this has been summarized as a dashed arrow.

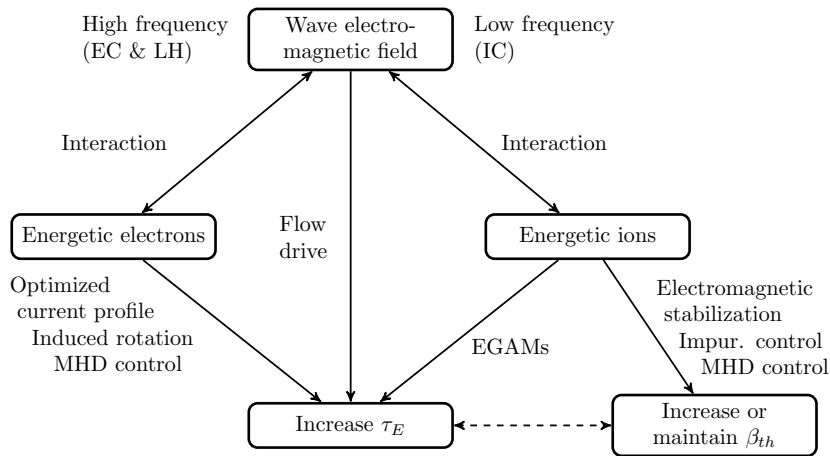


Figure 1.3: Various methods to improve the fusion yield by using radiofrequency waves.

1.3 Organization of this manuscript

This manuscript is organized as follows: this part, chapter 1, briefly reviews the basic elements required in our physics description, namely RF waves, energetic particles and how RF waves can be used to improve plasma performance. In chapter 2, we present a Hamiltonian framework in which self-consistency between the wave electromagnetic field and the plasma response is achieved. It is a continuation of a long-lasting effort applicable to various domains [18–22]. This theory consists of describing the unperturbed system in terms of an Hamiltonian and associate conjugate action-angle variables, and the response of the system to an electromagnetic perturbation as a perturbation to this Hamiltonian. Embedding this perturbed Hamiltonian in a variational principle allows the electromagnetic field to be computed for a given excitation. The secular response of the system can be obtained when the electromagnetic field is assumed to be known, and used to solve the Fokker-Planck equation in order to deduce an updated distribution function. An advantage of this approach is that explicit expressions for the various Hamiltonian contributions with a well-controlled level of approximation can be obtained and used in the two parts of the computation (wave and quasilinear), which is then naturally self-consistent.

In chapters 3 and 4, these general expressions are employed to respectively demonstrate how the electromagnetic field can be obtained from the Maxwell's equations expressed in a variational form, and also to obtain a perturbed distribution function accounting for the secular effect of these fields. Chapter 3 presents the foundations of a full-wave electromagnetic code named *EVE*, which has been initially developed as an ICRF code [23–25], but has been successfully used for MHD waves in the Alfvén range of frequencies as well. It can also be extended with a rather limited effort (at least formally) to higher frequencies, and could be used to describe LH and EC waves in the presence of energetic electrons. Chapter 4 aims at showing how the Hamiltonian expressions can be considerably simplified to result in a minimal quasilinear model. The associated code, named *AQL*, is also presented. It has been extensively used as a complement to *EVE* to simulate actual experiments in Tore Supra [26], WEST [27], JET [28], or ITER [6]. An upside of the Hamiltonian formalism is that it can be employed to derive models (and associated codes) with higher levels of sophistication. For instance, a limitation of *AQL* is that it does not retain finite orbit width effects, which can play an important role in Tore Supra or JET. This limitation can be overcome by employing less drastic simplifications of the Hamiltonian contributions appearing in the quasilinear diffusion coefficient. Such effort is not described in these pages.

Chapter 5 contains several examples of how radiofrequency waves can be used to improve the discharge properties. In these pages, we mostly focus on the use of RF waves interacting with energetic ions or electrons, or directly on the microscopic structures responsible for plasma turbulence, to achieve so-called phase-space engineering. A lot has been already done in this area, but a whole range of possibilities remains to be explored, both theoretically and experimentally. Hopefully, these techniques will progressively shift from the physicist realm to become part of the various actuators available for the operation of an efficient fusion reactor.

Since this manuscript is also aimed at students and newcomers in this field, we have included in appendices A, C, B and D technical details with a range of application extending beyond the subject at hand.

Finally, a set of publications from the author of the present manuscript have been listed and grouped topically in appendix E. Six of them have been included *in extenso*.

Chapter 2

Hamiltonian theory of electromagnetic perturbations

In this chapter, we review the building blocks which will be used to obtain the electromagnetic wavefield for a given excitation and plasma parameters on the one hand (chapter 3) and the secular response to a given wavefield on the other hand (chapter 4). Note that the geometric and plasma equilibrium aspects appear in appendix A.

2.1 Kinetic description of particles

2.1.1 Quasi-local trajectories

In this work, the unperturbed particle trajectories are described in the drift approximation. The ordering is given by the small parameter $\epsilon_d \equiv |\nabla\rho_i|$ with ρ_i a “typical” ion Larmor radius. In the absence of unperturbed electric field, the particle guiding-center velocity is given by

$$\dot{\mathbf{r}}_{gc} = \mathbf{v}_{gc} = v_{\parallel} \mathbf{e}_{\parallel} + \mathbf{v}_{dr}, \quad (2.1)$$

with \mathbf{v}_{dr} is drift velocity containing the usual curvature and gradient drifts:

$$\mathbf{v}_{dr} = \frac{v_{\parallel}^2}{\Omega_{cs}} \mathbf{e}_{\parallel} \times (\mathbf{e}_{\parallel} \cdot \nabla \mathbf{e}_{\parallel}) + \frac{v_{\perp}^2}{2\Omega_{cs}^2} \mathbf{e}_{\parallel} \times \nabla \Omega_{cs}. \quad (2.2)$$

To first order in ϵ_d , the particle position is given by

$$\mathbf{r} = \mathbf{r}_{gc} + \mathbf{r}_c, \quad (2.3)$$

with

$$\mathbf{r}_c \equiv \frac{v_{\perp}}{\Omega_{cs}} [\sin(\phi_c) \mathbf{e}_{\perp 1} + \cos(\phi_c) \mathbf{e}_{\perp 2}]. \quad (2.4)$$

In the absence of static electric field, the particle velocity is decomposed as

$$\mathbf{v} = \mathbf{v}_{gc} + \mathbf{v}_{\perp}, \quad (2.5)$$

with

$$\mathbf{v}_{\perp} = v_{\perp} [\cos(\phi_c) \mathbf{e}_{\perp 1} - \sin(\phi_c) \mathbf{e}_{\perp 2}]. \quad (2.6)$$

It should be noted that the latter expression is obtained by neglecting the slow variation of the local magnetic basis along the magnetic field line. The gyro-phase is given by [29]

$$\dot{\phi}_c = \Omega_{cs} + \frac{v_{\parallel}}{2} \mathbf{e}_{\parallel} \cdot (\nabla \times \mathbf{e}_{\parallel} + 2\nabla \mathbf{e}_{\perp 1} \cdot \mathbf{e}_{\perp 2}). \quad (2.7)$$

Note that the drift velocity, as well as the second term on the right-hand side of the previous expression, are corrections of order ε_d . According to Defs. A.38, we can also write the perpendicular velocity vector as

$$\mathbf{v}_{\perp} = v_{\perp} (e^{i\phi_c} \mathbf{e}_{-} + e^{-i\phi_c} \mathbf{e}_{+}), \quad (2.8)$$

and the Larmor radius vector as

$$\mathbf{r}_c = -i\rho_c (e^{i\phi_c} \mathbf{e}_{-} - e^{-i\phi_c} \mathbf{e}_{+}). \quad (2.9)$$

Of particular importance is the relation

$$\mathbf{r}_c \cdot \nabla = \rho_c (e^{i(\phi_c - \pi/2)} \nabla_{+} + e^{-i(\phi_c - \pi/2)} \nabla_{-}), \quad (2.10)$$

with

$$\nabla_{\pm} \equiv \nabla \cdot \mathbf{e}_{\mp} = T_{\pm}^i \partial_i, \quad (2.11)$$

where Defs. A.48 have been used.

2.1.2 Adiabatic invariants

It is convenient to characterize the particle motion in terms of adiabatic invariants. In this work, we will consider the set of invariants of the unperturbed motion $\mathbf{I} \equiv (E, \mu, P_{\phi})$ with the energy $E \equiv m_s v^2/2$, the magnetic moment $\mu \equiv m_s v_{\perp}^2/2/B_0$. P_{ϕ} is the canonical toroidal momentum given by [30]

$$P_{\phi} \equiv m_s \frac{F}{B_0} v_{\parallel} + q_s \frac{\Phi_p}{2\pi} = m_s \frac{F}{B_0} v_{\parallel} + q_s \psi, \quad (2.12)$$

with the same notations as in Eq. A.6. It should be noted that P_{ϕ} is the only invariant which depends explicitly on the radial position through the poloidal flux ψ , defined as

$$\psi \equiv \int ds J |\nabla \theta \cdot \mathbf{B}_0| \quad (2.13)$$

The first and third action variables are directly linked to the invariants by the relations

$$J_1 = -\frac{m_s}{q_s} \mu, \quad (2.14)$$

and

$$J_3 = P_{\phi}. \quad (2.15)$$

We have

$$\frac{\partial f_{s,0}}{\partial J_i} = \frac{\partial f_{s,0}}{\partial I_k} \frac{\partial I_k}{\partial J_i}, \quad (2.16)$$

where $\partial f_{s,0}/\partial I_k$ is assumed to be a known quantity. We have from Hamiltonian theory

$$\frac{\partial E}{\partial J_k} = \frac{\partial H_{s,0}}{\partial J_k} = \Omega_k. \quad (2.17)$$

Evidently

$$\frac{\partial \mu}{\partial J_k} = -\frac{q_s}{m_s} \delta_{k,1}, \quad (2.18)$$

and

$$\frac{\partial P_\phi}{\partial J_k} = \delta_{k,3}, \quad (2.19)$$

so that

$$N_i \frac{\partial f_{s,0}}{\partial J_i} = N_k \Omega_k \frac{\partial f_{s,0}}{\partial E} - N_1 \frac{q_s}{m_s} \frac{\partial f_{s,0}}{\partial \mu} + N_3 \frac{\partial f}{\partial P_\phi}. \quad (2.20)$$

2.1.3 Anisotropic Maxwellians

Plasma heating by ICRF waves results in the acceleration of resonant ions in the perpendicular direction. The modification in the parallel direction mainly results from pitch-angle scattering and remains rather moderate in standard experimental situations (cf. chapter 4). The use of an anisotropic Maxwellian distribution, i.e. a Maxwellian featuring $T_{\parallel,s} \neq T_{\perp,s}$ is therefore rather common. In all this document, when anisotropic Maxwellians are employed, we will impose $T_s \equiv T_{\parallel,s}$, with T_s the normalization temperature. In this framework, a commonly employed expression is

$$f_{s,0}(\mathbf{r}, \mathbf{p}) = \frac{n_s}{(2\pi m_s)^{3/2} T_{\perp,s} T_s^{1/2}} e^{-m_s v_\perp^2 / 2 T_{\perp,s}} e^{-m_s v_\parallel^2 / 2 T_s}. \quad (2.21)$$

However, as pointed out by Dendy et al., the previous expression is not acceptable because it does not satisfy the Vlasov equation to lowest order [31]. To fulfill this condition, it is necessary to specify the equilibrium distribution function in terms of the adiabatic invariants, so that

$$f_{s,0}(\mathbf{r}, \mathbf{p}) = A \exp\left(-\frac{\mu B_{0,res}}{T_{\perp,s}} - \frac{E - \mu B_{0,res}}{T_s}\right), \quad (2.22)$$

with A a constant. $B_{0,res}$ is the magnetic field magnitude at the location where the interaction occurs. Unlike Eq. 2.21, the latter distribution features a θ dependence when expressed in terms of local position/velocity.

Introducing the anisotropy factor η_\perp , the distribution function can be written as

$$f_{s,0}(\mathbf{r}, \mathbf{p}) = A \exp\left(-\frac{m_s v_\parallel^2}{2T_s}\right) \exp\left(-\frac{m_s v_\perp^2}{2\eta_\perp(\theta)T_s}\right), \quad (2.23)$$

with

$$\eta_\perp(\theta) \equiv \frac{T_{\perp,s}}{T_s} \left[\frac{B_{0,res}}{B_0(\theta)} + \frac{T_{\perp,s}}{T_s} \left(1 - \frac{B_{0,res}}{B_0(\theta)}\right) \right]^{-1}, \quad (2.24)$$

where $T_s \equiv T_s(s)$ and $T_{\perp,s} \equiv T_{\perp,s}(s)$ are flux functions. In this framework, $T_{\perp,s}$ should be seen as the perpendicular temperature at the point where the interaction occurs. The normalization is obtained by imposing that the heated particle density be equal to the local density $n_s(s)$, which is assumed to be uniform on a flux surface. This yields

$$f_{s,0}(\mathbf{r}, \mathbf{p}) = \frac{n_s}{(2\pi m_s T_s)^{3/2} \eta_{\perp}(\theta)} \exp\left(-\frac{m_s v_{\parallel}^2}{2T_s}\right) \exp\left(-\frac{m_s v_{\perp}^2}{2\eta_{\perp}(\theta)T_s}\right). \quad (2.25)$$

2.2 Hamiltonian perturbations

2.2.1 Linear response

We introduce the Hamiltonian of particles with charge q_s and mass m_s interacting with the total electromagnetic field:

$$H_s = \frac{(\mathbf{p} - q_s \mathbf{A}_0 - q_s \mathbf{A})^2}{2m_s} + q_s \varphi_0 + q_s \varphi, \quad (2.26)$$

where $(\mathbf{A}_0, \varphi_0)$ is the equilibrium electromagnetic potential. This Hamiltonian is linearized to first order in the wave field amplitude by writing $H_s \approx H_{s,0} + \delta H_s$ where

$$\delta H_s = q_s(\varphi - \mathbf{v}_{s,0} \cdot \mathbf{A}), \quad (2.27)$$

with $\mathbf{v}_{s,0}$ the unperturbed velocity, given by

$$\mathbf{v}_{s,0} = \frac{\partial H_{s,0}}{\partial \mathbf{p}}. \quad (2.28)$$

The distribution function is written as the sum of an equilibrium distribution function and a harmonic perturbation, $f_s = f_{s,0} + \delta f_s$. The link between the distribution function and the Hamiltonian is given by the Vlasov equation for each species

$$\frac{\partial f_s}{\partial t} + [f_s, H_s] = 0. \quad (2.29)$$

At this point, it is convenient to introduce the system of conjugate action-angle coordinates, $(J_i, \Phi_i)_{i=1..3}$, which is defined in the unperturbed system as [32]

$$\frac{dJ_k}{dt} = -\frac{\partial H_{s,0}}{\partial \Phi_k} = 0, \quad (2.30)$$

and

$$\frac{d\Phi_k}{dt} \equiv \Omega_k = \frac{\partial H_{s,0}}{\partial J_k}, \quad (2.31)$$

where $\Omega_k = \Omega_k(\mathbf{J})$ corresponds to the k^{th} natural frequency of the system. By definition, the unperturbed Hamiltonian and distribution function depend only on the action variable, so that it is possible to write

$$H_s = H_{s,0}(J_k) + \delta H_s(J_k, \Phi_k, t), \quad f_s(J_k, \Phi_k, t) = f_{s,0}(J_k) + \delta f_s(J_k, \Phi_k, t), \quad (2.32)$$

where the oscillating quantities oscillate at frequency ω , and are expressed as a Fourier series over the generalized angles, i.e.,

$$\delta H_s \equiv \sum_{\mathbf{N}} \delta h_{\mathbf{N}} e^{i(N_k \Phi_k - \omega t)}, \quad \delta f_s \equiv \sum_{\mathbf{N}} \delta f_{\mathbf{N}} e^{i(N_k \Phi_k - \omega t)}, \quad (2.33)$$

with $\mathbf{N} \equiv (N_1, N_2, N_3)$ a triplet of integers. The linearization of Eq. 2.29 is straightforward and yields the linear response of the particles immersed in the wave field as

$$\delta f_{\mathbf{N}} = -\delta h_{\mathbf{N}} \frac{N_i}{\omega - N_k \Omega_k} \frac{\partial f_{s,0}}{\partial J_i}. \quad (2.34)$$

The action-angle coordinates are deduced from the conjugate position-momentum coordinates by a canonical transformation, which implies $d^3 \mathbf{r} d^3 \mathbf{p} = d^3 \mathbf{J} d^3 \Phi$.

2.2.2 Orbit integrals

The evaluation of $\delta h_{\mathbf{N}}$ is performed by inverse Fourier transform of δH_s

$$\delta h_{N_1, N_2, N_3} = \frac{1}{(2\pi)^3} \int d\Phi_1 d\Phi_2 d\Phi_3 \delta H_s e^{-\mathbf{N} \cdot \Phi}, \quad (2.35)$$

with

$$\delta H_s \equiv \delta H_s(\mathbf{r}, \mathbf{p}) = \delta H_s(\mathbf{J}, \Phi). \quad (2.36)$$

As discussed in Section 2.1.2, the various orbits of the particle guiding-centers are characterized by the three invariants (E, μ, P_ϕ) of the unperturbed motion. In order to track the particle guiding-center location on a given orbit, they must be supplemented by the poloidal and toroidal angles at the guiding-center, θ and ϕ . Finally, the particle gyromotion is fully described by adding the gyro-phase ϕ_c . The Hamiltonian perturbation can be written as:

$$\delta H_s(\mathbf{r}, \mathbf{v}) = \delta H_s(E, \mu, P_\phi, \theta, \phi; \phi_c). \quad (2.37)$$

Given the nature of the problem under consideration, it is natural to reformulate the latter expression as a Fourier series over the gyro-angle:

$$\delta H_s(E, \mu, P_\phi, \theta, \phi; \phi_c) \equiv \sum_{p=-\infty}^{\infty} \delta H_{ps} e^{ip\phi_c}, \quad (2.38)$$

with

$$\delta H_{ps}(E, \mu, P_\phi, \theta, \phi) \equiv \frac{1}{2\pi} \int d\phi_c \delta H_s(E, \mu, P_\phi, \theta, \phi; \phi_c) e^{-ip\phi_c}. \quad (2.39)$$

Note that the previous expression implicitly assumes that the gyro-center motion is fully decoupled from the guiding-center motion. Since δH_{ps} only depends on quantities evaluated at the guiding-center, a Fourier expansion can be performed over the toroidal and poloidal angles to obtain

$$\delta H_s(E, \mu, P_\phi, \theta, \phi; \phi_c) \equiv \sum_{pmn} \delta H_{pmn} e^{i(p\phi_c + m\theta + n\phi)}, \quad (2.40)$$

where

$$\delta H_{pmn}(E, \mu, \psi) \equiv \frac{1}{(2\pi)^3} \int d\phi_c d\theta d\phi \delta H_s(E, \mu, P_\phi, \theta, \phi; \phi_c) e^{-i(p\phi_c + m\theta + n\phi)}, \quad (2.41)$$

with ψ the radial variable. This leads to

$$\delta h_{N_1, N_2, N_3} = \frac{1}{(2\pi)^3} \sum_{pmn} \int d^3\Phi \delta H_{pmn} e^{i[(p\phi_c - N_1\Phi_1) + (n\phi - N_3\Phi_3) + m\theta - N_2\Phi_2]}. \quad (2.42)$$

The gyro-phase is linked to the first generalized angle by a relation of the type

$$\phi_c = \Phi_1 + \Theta(E, \mu, P_\phi, \theta, \phi), \quad (2.43)$$

which, since θ and ϕ are the angles for the guiding-center, implies that the integral over Φ_1 is trivial, giving

$$\delta h_{N_1, N_2, N_3} = \frac{1}{(2\pi)^2} \sum_{pmn} \int d\Phi_2 d\Phi_3 \delta H_{pmn} e^{i[p\Theta(\theta, \phi) + (n\phi - N_3\Phi_3) + m\theta - N_2\Phi_2]} \delta_{N_1, p}. \quad (2.44)$$

The difficulty in this expression comes from the fact that θ and ϕ are functions of the generalized angles Φ_2 and Φ_3 . However, in a confining fusion device, which by definition exhibits quasi-periodicities, it can be shown that [33]

$$\begin{cases} \theta = \varepsilon\Phi_2 + \hat{\theta}(H, \mu, P_\phi, \Phi_2), \\ \phi = \Phi_3 + q\hat{\theta}(H, \mu, P_\phi, \Phi_2) + \hat{\phi}(H, \mu, P_\phi, \Phi_2), \end{cases} \quad (2.45)$$

where $\varepsilon = 0$ (resp. 1) for trapped (resp. passing) particles. q is the safety factor. $\hat{\theta}$ and $\hat{\phi}$ are both periodic functions of Φ_2 . The integration over Φ_3 can thus be performed in Eq. 2.44 to give

$$\delta h_{N_1, N_2, N_3} = \frac{1}{2\pi} \sum_{pmn} \int d\Phi_2 \delta H_{pmn} e^{i[p\Theta + nq\hat{\theta} + n\hat{\phi} + m\theta - N_2\Phi_2]} \delta_{p, N_1} \delta_{n, N_3}. \quad (2.46)$$

According to Eq. 2.31, $\Phi_2 = \Omega_2 t$, so that

$$\delta h_{N_1, N_2, N_3} = \sum_{pmn} \frac{1}{\tau_b} \int_0^{\tau_b} dt \delta H_{pmn} e^{i[p\Theta + nq\hat{\theta} + n\hat{\phi} + m\theta - N_2\Phi_2]} \delta_{p, N_1} \delta_{n, N_3}. \quad (2.47)$$

Substituting $p\Theta \equiv p(\phi_c - \Omega_1 t)$ and $nq\hat{\theta} + n\hat{\phi} \equiv n(\phi - \Omega_3 t)$ yields

$$\delta h_{N_1, N_2, N_3} = \sum_{pmn} \frac{1}{\tau_b} \int_0^{\tau_b} dt \delta H_{pmn}(H, \mu, \psi) e^{i[p\phi_c(t) + m\theta(t) + n\phi(t) - N_i \Omega_i t]} \delta_{p, N_1} \delta_{n, N_3}, \quad (2.48)$$

with $\tau_b = \tau_b(H, \mu, P_\phi)$ the bounce period of the considered particles. The above expression is an orbit integral clearly exhibiting the resonant selection process at play between the particles and the waves.

The previous expression may be rewritten as

$$\delta h_{p,N_2,n} = \frac{1}{\tau_b} \sum_m \int_0^{\tau_b} dt \delta H_{pmn}(t) e^{f_m(t)}, \quad (2.49)$$

with

$$f_m(t) \equiv i[\gamma_m(t) - (p\Omega_1 + N_2\Omega_2 + n\Omega_3)t], \quad (2.50)$$

having let

$$\gamma_m(t) \equiv p\phi_c(t) + m\theta(t) + n\phi(t). \quad (2.51)$$

2.2.3 Quasi-local limit

By performing a Fourier expansion over θ and ϕ , the variations of δH_s in the parallel directions have been incorporated in the phase term, and δH_{pmn} varies spatially only in the radial direction. In other words, if the guiding-center orbit coincides with a flux surface, δH_{pmn} can be taken out of the integral. In this work, we retain this radial variation, but assume that it remains moderate on a given guiding-center orbit [34]. More explicitly, we impose the condition

$$|\delta \dot{H}_{pmn}| = \left| \frac{\dot{\psi}}{\delta H_{pmn}} \frac{\partial \delta H_{pmn}}{\partial \psi} \right| \lesssim \frac{1}{\tau_b}. \quad (2.52)$$

This ensures that along the particle trajectory, the variation of δH_{pmn} is smooth compared to the variation of the particle/wave phase

$$|\dot{f}_m| = p(\Omega_{cs}(t) - \Omega_1) + m\dot{\theta} + n\dot{\phi} - N_2\Omega_2 - N_3\Omega_3 \approx p(\Omega_{cs}(t) - \langle \Omega_{cs} \rangle), \quad (2.53)$$

where $\langle \rangle$ refers to an average on the guiding-center orbit. This shows that $|\dot{f}_m| \sim p\Omega_{cs}r/R$ with r the minor radius and R the major radius of the considered flux surface. Since $\Omega_{cs} \sim \Omega_1 \gg \Omega_2 = 2\pi/\tau_b$, condition (2.52) effectively ensures that the phase varies very strongly along the particle orbit, so that the integral can be evaluated by a saddle point method [35]. We rewrite (2.49) in the complex plane as

$$\delta h_{p,N_2,n} = \frac{1}{\tau_b} \sum_m \int_{\mathcal{C}} dt \delta H_{pmn}(t) e^{f_m(t)}, \quad (2.54)$$

where \mathcal{C} is the path of steepest descent and t is now to be considered as a complex variable. We have

$$\frac{df_m}{dt} = i(p\Omega_{cs} + m\dot{\theta} + n\dot{\phi} - N_1\Omega_1 - N_2\Omega_2 - N_3\Omega_3), \quad (2.55)$$

which is zero when the following resonance condition is fulfilled:

$$\left. \frac{df_m}{dt} \right|_{t=t_0} = 0 = i(p\Omega_{cs}(t_0) + m\dot{\theta}(t_0) + n\dot{\phi}(t_0) - N_1\Omega_1 + N_2\Omega_2 + N_3\Omega_3), \quad (2.56)$$

or

$$p\Omega_{cs}(t_0) + k_{\parallel}(t_0)v_{\parallel}(t_0) = N_i\Omega_i, \quad (2.57)$$

where we have introduced $k_{\parallel}v_{\parallel}(t) \approx m\dot{\theta} + n\dot{\phi}$. On the other hand and anticipating future considerations, Eq. 3.42 shows that resonant energy exchanges occur only when the global

resonance condition $\omega = N_i \Omega_i$ is verified, showing that the points along the orbits where wave/particle interactions take place are actually given by $p\Omega_{cs} + k_{\parallel}v_{\parallel} = \omega$, which is consistent with results from a quasi-local derivation [11]. Depending on the shape of the considered orbit and on the resonance layer location, the particle may experience 0, 2 or 4 such points along its orbit.

A Taylor expansion of f_m around $t = t_0$ is performed:

$$f_m(t) \approx f_m(t_0) + \frac{(t-t_0)^2}{2!} \frac{d^2 f_m}{dt^2} \Big|_{t=t_0} + \frac{(t-t_0)^3}{3!} \frac{d^3 f_m}{dt^3} \Big|_{t=t_0}, \quad (2.58)$$

yielding

$$\delta h_{p,N_2,n} = \frac{1}{\tau_b} \sum_{m,t_0(m)} e^{if_m(t_0)} \int_{\mathcal{C}} d\tau \delta H_{pmn}(\tau + t_0) \exp\left(\frac{\tau^2}{2} \ddot{f}_m(t_0) + \frac{\tau^3}{6} \dddot{f}_m(t_0)\right), \quad (2.59)$$

with $\tau \equiv t - t_0$. The sum must be performed over all saddle points corresponding to poloidal number m .

Condition (2.52) ensures that δH_{pmn} varies smoothly in the vicinity of the resonance point, so that

$$\delta H_{pmn}(\tau + t_0) \sim \delta H_{pmn}(t_0), \quad (2.60)$$

and

$$\begin{aligned} \delta h_{p,N_2,n} &= \frac{1}{\tau_b} \sum_{m,t_0} \delta H_{pmn}(t_0) e^{if_m(t_0)} \int_{\mathcal{C}} d\tau \exp\left(\frac{\tau^2}{2} \ddot{f}_m(t_0) + \frac{\tau^3}{6} \dddot{f}_m(t_0)\right) \\ &= \frac{1}{\tau_b} \sum_{m,t_0} \delta H_{pmn}(t_0) e^{if_m(t_0)} \int_{\mathcal{C}} d\tau \exp\left[i\left(\frac{\tau^2}{2} \ddot{\gamma}_m(t_0) + \frac{\tau^3}{6} \ddot{\gamma}_m(t_0)\right)\right]. \end{aligned} \quad (2.61)$$

Far from third-order saddle points, such as $\ddot{\gamma}_m(t_0) = 0$, a good approximation to the previous expression is

$$\delta h_{p,N_2,n} \approx \frac{1}{\tau_b} \sum_{m,t_0} \delta H_{pmn}(t_0) e^{if_m(t_0)} \int_{\mathcal{C}} d\tau \exp\left(i\frac{\tau^2}{2} \ddot{\gamma}_m(t_0)\right). \quad (2.62)$$

Denoting $\tau \equiv r e^{i\varphi}$, the path of steepest descent is attained for

$$e^{i(2\varphi + \arg(\ddot{\gamma}_m) + \pi/2)} = -1, \quad (2.63)$$

or

$$\varphi = \frac{\pi}{4} - \frac{1}{2} \arg(\ddot{\gamma}_m), \quad (2.64)$$

so that

$$\begin{aligned} \delta h_{p,N_2,n} &\approx \frac{1}{\tau_b} \sum_{m,t_0} \delta H_{pmn}(t_0) e^{f_m(t_0) \pm i\pi/4} \int_{-\infty}^{\infty} dr e^{-|\ddot{\gamma}_m| r^2} \\ &= \frac{1}{\tau_b} \sum_{m,t_0} \sqrt{\frac{2\pi}{|\ddot{\gamma}_m(t_0)|}} \delta H_{pmn}(t_0) e^{f_m(t_0) \pm i\pi/4}, \end{aligned} \quad (2.65)$$

where the + (resp. -) sign must be chosen for $\ddot{\gamma}_m > 0$ (resp. $\ddot{\gamma}_m < 0$).

In order to handle tangent resonances without needing to add a separate contribution, it is possible to use the asymptotic expression proposed by Lamalle [34]:

$$\delta h_{p,N_2,n} \approx \frac{1}{\tau_b} \sum_{m,t_0} \Gamma_m(t_0) \delta H_{pmn}(t_0) e^{f_m(t_0)}, \quad (2.66)$$

with

$$\Gamma_m(t) \equiv 2\pi \left(\frac{2e^{i\sigma_m(t)\pi}}{|\ddot{\gamma}_m(t)|} \right)^{1/3} \Phi_0(g_m(t) e^{i\sigma_m(t)\pi/6}), \quad (2.67)$$

having defined

$$\Phi_0(x) \equiv \exp(2x^3/3) \text{Ai}(x^2), \quad (2.68)$$

with Ai the Airy function, $\sigma_m \equiv \text{sign}(\ddot{\gamma}_m)$ and

$$g_m(t) \equiv \frac{|\ddot{\gamma}_m(t)|}{(2|\ddot{\gamma}_m(t)|^2)^{1/3}}. \quad (2.69)$$

For the squared amplitude of the Hamiltonian contributions, we have therefore

$$|\delta h_{p,N_2,n}|^2 \approx \frac{1}{\tau_b^2} \sum_{\substack{m_1, t_1 [m_1] \\ m_2, t_2 [m_2]}} \Gamma_{m_1}(t_1) \Gamma_{m_2}^*(t_2) \delta H_{pm_1n}(t_1) \delta H_{pm_2n}(t_2)^* e^{f_{m_1}(t_1) + f_{m_2}^*(t_2)}. \quad (2.70)$$

The complexity in this expression lies in the sum over partial waves and resonant points. Depending on the problem to be solved, various approximations are needed to obtain numerically tractable expressions.

Finally, we note that in the limit $|\ddot{\gamma}_m(t)| \rightarrow 0$, the asymptotic expansion of the Airy function

$$\text{Ai}(x) \sim \exp\left(-\frac{2x^{3/2}}{3}\right) \frac{1}{2\sqrt{\pi}x^{1/4}}, \quad (2.71)$$

yields

$$\Gamma_m(t) \sim \sqrt{\frac{2\pi}{|\ddot{\gamma}_m(t)|}} e^{i\sigma_m(t)\pi/4}. \quad (2.72)$$

It is possible to use the expression for the squared Hamiltonian contributions given by Eq. 2.70 along with approximation (2.72) to obtain

$$|\delta h_{p,N_2,n}|^2 = \frac{2\pi}{\tau_b^2} \sum_{m_1, m_2} \sum_{t_1, t_2} \sqrt{\frac{1}{|\ddot{\gamma}_{m_1}(t_1)\ddot{\gamma}_{m_2}(t_2)|}} \delta H_{pm_1n}(t_1) \delta H_{pm_2n}^*(t_2) e^{f_{m_1}(t_1) + f_{m_2}^*(t_2)}, \quad (2.73)$$

where the sum must be carried out over all saddle points for partial waves m_1 and m_2 . We have

$$\ddot{\gamma}_{m_1}(t) \equiv p\dot{\Omega}_{cs}(t) + m_1\ddot{\theta}(t) + n\ddot{\phi}(t), \quad (2.74)$$

and

$$\ddot{\gamma}_{m_2}(t) \equiv p\dot{\Omega}_{cs}(t) + m_2\ddot{\theta}(t) + n\ddot{\phi}(t). \quad (2.75)$$

By definition $df_{m_1}/dt(t = t_1) = 0 = \dot{\gamma}_{m_1}(t_1) - N_i\Omega_i$ so that

$$\dot{\gamma}_{m_1}(t_1) = N_i\Omega_i. \quad (2.76)$$

Likewise, for poloidal mode m_2 :

$$\dot{\gamma}_{m_2}(t_2) = N_i\Omega_i. \quad (2.77)$$

The phase term in Eq. 2.73 is given by the expression

$$f_{m_1}(t_1) + f_{m_2}^*(t_2) = i[\gamma_{m_1}(t_1) - \gamma_{m_2}(t_2) - N_i\Omega_i(t_1 - t_2)]. \quad (2.78)$$

Following Lamalle [34], we introduce the saddle point corresponding to the resonance between the particle and the wave with poloidal mode $m_0 \equiv (m_1 + m_2)/2$, which verifies

$$\dot{\gamma}_{m_0}(t_0) = N_i\Omega_i. \quad (2.79)$$

Evidently

$$\dot{\gamma}_{m_1}(t_1) = \dot{\gamma}_{m_2}(t_2) = \dot{\gamma}_{m_0}(t_0). \quad (2.80)$$

The linear, quadratic and cubic time variation in γ_{m_1} is retained, yielding

$$\gamma_{m_1}(t) \approx \gamma_{m_1}(t_0) + \dot{\gamma}_{m_1}(t_0)(t - t_0) + \ddot{\gamma}_{m_1}(t_0)\frac{(t - t_0)^2}{2} + \dddot{\gamma}_{m_1}(t_0)\frac{(t - t_0)^3}{6}. \quad (2.81)$$

Accordingly

$$\dot{\gamma}_{m_1}(t) \approx \dot{\gamma}_{m_1}(t_0) + \ddot{\gamma}_{m_1}(t_0)(t - t_0) + \dddot{\gamma}_{m_1}(t_0)\frac{(t - t_0)^2}{2}. \quad (2.82)$$

On the other hand, from Eq. 2.51

$$\dot{\gamma}_{m_1}(t) = \dot{\gamma}_{m_0}(t) + \frac{m_1 - m_2}{2}\dot{\theta}(t). \quad (2.83)$$

Combining the previous two expressions and using Eq. 2.80, we obtain

$$\frac{\ddot{\gamma}_{m_1}(t_0)}{2}(t_1 - t_0)^2 + \ddot{\gamma}_{m_1}(t_0)(t_1 - t_0) + \frac{m_1 - m_2}{2}\dot{\theta}(t_0) = 0, \quad (2.84)$$

which admits the solutions

$$t_1 - t_0 = \frac{-\ddot{\gamma}_{m_1}(t_0) \pm \sqrt{\ddot{\gamma}_{m_1}^2(t_0) - (m_1 - m_2)\ddot{\gamma}_{m_1}(t_0)\dot{\theta}(t_0)}}{\ddot{\gamma}_{m_1}(t_0)}, \quad (2.85)$$

and

$$t_2 - t_0 = \frac{-\ddot{\gamma}_{m_2}(t_0) \pm \sqrt{\ddot{\gamma}_{m_2}^2(t_0) + (m_1 - m_2)\ddot{\gamma}_{m_2}(t_0)\dot{\theta}(t_0)}}{\ddot{\gamma}_{m_2}(t_0)}. \quad (2.86)$$

Far away from third order saddle points, we deduce from the previous relations

$$t_1 - t_0 \approx -\frac{m_1 - m_2}{2}\frac{\dot{\theta}(t_0)}{\ddot{\gamma}_{m_1}(t_0)}, \quad (2.87)$$

and

$$t_2 - t_0 \approx \frac{m_1 - m_2}{2} \frac{\dot{\theta}(t_0)}{\ddot{\gamma}_{m_2}(t_0)}. \quad (2.88)$$

We obtain

$$\begin{aligned} \gamma_{m_1}(t_1) - \gamma_{m_2}(t_2) &= (m_1 - m_2)\theta(t_0) + (t_1 - t_2)N_i\Omega_i \\ &+ \frac{m_1 - m_2}{2}(t_1 + t_2 - 2t_0)\dot{\theta}(t_0) \\ &+ \ddot{\gamma}_{m_1}(t_0)\frac{(t_1 - t_0)^2}{2} - \ddot{\gamma}_{m_2}(t_0)\frac{(t_2 - t_0)^2}{2}. \end{aligned} \quad (2.89)$$

Coming back to the phase term (Eq. 2.78), we can write

$$\begin{aligned} f_{m_1}(t_1) + f_{m_2}^*(t_2) &= i(m_1 - m_2)\theta(t_0) \\ &+ i\frac{m_1 - m_2}{2}\dot{\theta}(t_0)(t_1 + t_2 - 2t_0) \\ &+ i\left[\ddot{\gamma}_{m_1}(t_0)\frac{(t_1 - t_0)^2}{2} - \ddot{\gamma}_{m_2}(t_0)\frac{(t_2 - t_0)^2}{2}\right]. \end{aligned} \quad (2.90)$$

Far from third order points, Eqs. 2.87 and 2.88 can be used to obtain the approximate expression

$$f_{m_1}(t_1) + f_{m_2}^*(t_2) \approx i(m_1 - m_2)\theta(t_0) - i\left(\frac{m_1 - m_2}{2}\right)^3 \frac{2\dot{\theta}^2(t_0)\ddot{\theta}(t_0)}{\ddot{\gamma}_{m_1}(t_0)\ddot{\gamma}_{m_2}(t_0)} \equiv i\Phi_{12}(t_0). \quad (2.91)$$

Eq. 2.73 yields

$$|\delta h_{p,N_2,n}|^2 \approx \frac{2\pi}{\tau_b^2} \sum_{m_1, m_2} \sum_{t_0} \frac{\delta H_{pm_1n}(t_1)\delta H_{pm_2n}^*(t_2)}{\sqrt{|\ddot{\gamma}_{m_1}(t_1)\ddot{\gamma}_{m_2}(t_2)|}} e^{i\Phi_{12}(t_0)}, \quad (2.92)$$

where the sum is carried out over the ‘‘average’’ saddle points $t_0^{m_1, m_2}$ and t_1 (resp. t_2) is given by Eq. 2.87 (resp. 2.88). If, furthermore, the angular acceleration of the particle is neglected upon crossing the resonance, i.e. $\dot{\theta}(t_0) = 0$, we obtain the simpler expression

$$|\delta h_{p,N_2,n}|^2 \approx \frac{2\pi}{\tau_b^2} \sum_{m_1, m_2} \sum_{t_0} \frac{\delta H_{pm_1n}(t_0)\delta H_{pm_2n}^*(t_0)}{|\ddot{\gamma}_{m_0}(t_0)|} e^{i(m_1 - m_2)\theta(t_0)}, \quad (2.93)$$

where, again, it is important to note that resonant time t_0 corresponds to $m_0 = (m_1 + m_2)/2$, underlining the symmetric nature of this expression with respect to poloidal numbers m_1 and m_2 . It should be pointed out that this symmetry is also been obtained when the summation over bounce harmonics is carefully handled, as shown by P. U. Lamalle in Ref. [34].

2.3 Hamiltonian contributions

2.3.1 All-orders expression

At this point, it is still necessary to express δH_{pmn} as a function of the electromagnetic potential. This is done by performing a Taylor expansion of the particle Hamiltonian around the guiding-center location:

$$\delta H_s(\mathbf{r}) = \delta H_s(\mathbf{r}_{gc} + \mathbf{r}_c) = \sum_{l=0}^{\infty} \frac{(\mathbf{r}_c \cdot \nabla)^l}{l!} \delta H_s(\mathbf{r})|_{\mathbf{r}_{gc}}. \quad (2.94)$$

Eq. 2.10 and the binomial theorem are employed to perform the following expansion

$$(\mathbf{r}_c \cdot \nabla)^l = \rho_c^l \sum_{k=0}^l \binom{l}{k} e^{i(2k-l)(\phi_c - \pi/2)} \nabla_+^k \nabla_-^{l-k}, \quad (2.95)$$

which after reordering the sums to express the obtained expression for δH_s in terms of the cyclotron phase harmonics yields the compact formula

$$\delta H_s(\mathbf{r}) = \sum_{p=-\infty}^{\infty} e^{ip(\phi_c - \pi/2)} \sum_{k=0}^{\infty} \rho_c^{2k+|p|} \frac{\nabla_+^{k+} \nabla_-^{k-}}{k_+! k_-!} \delta H_s(\mathbf{r})|_{\mathbf{r}_{gc}}, \quad (2.96)$$

with

$$\begin{cases} k_+ = k + p, & k_- = k & \text{if } p > 0, \\ k_+ = k, & k_- = k - p & \text{otherwise,} \end{cases} \quad (2.97)$$

which may also be written as [34]

$$k_+ \equiv k + \max(0, p), \quad k_- \equiv k + \max(0, -p). \quad (2.98)$$

Using Eq. 2.8, we can write the Hamiltonian (Eq. 2.27) at the particle guiding-center as

$$\delta H_s(\mathbf{r}_{gc}) = q_s \left[(\varphi - v_{\parallel} A_{\parallel}) - v_{\perp} (e^{i\phi_c} A_+ + e^{-i\phi_c} A_-) \right] \equiv \delta H_0 + \delta H_{+1} e^{i\phi_c} + \delta H_{-1} e^{-i\phi_c}, \quad (2.99)$$

with

$$\begin{cases} \delta H_0 & \equiv q_s (\varphi - v_{\parallel} A_{\parallel}), \\ \delta H_{+1} & \equiv -q_s v_{\perp} A_+ = -q_s v_{\perp} R_+ (A_{\alpha} + i A_{\beta}), \\ \delta H_{-1} & \equiv -q_s v_{\perp} A_- = -q_s v_{\perp} R_- (A_{\alpha} - i A_{\beta}), \end{cases} \quad (2.100)$$

where we have defined $A_{\pm} \equiv \mathbf{A} \cdot \mathbf{e}_{\mp}$ and used Eqs. A.55 and A.57.

We finally obtain for the expanded Hamiltonian

$$\delta H_s(\mathbf{r}) = \sum_{p=-\infty}^{\infty} e^{ip(\phi_c - \pi/2)} \sum_{L=-1}^1 e^{iL\pi/2} \sum_{\kappa=0}^{\infty} \rho_c^{2\kappa+|p-L|} \frac{\nabla_+^{\kappa+} \nabla_-^{\kappa-}}{k_+! k_-!} \delta H_L, \quad (2.101)$$

with

$$k_+ = \kappa + \max(0, p - L), \quad k_- = \kappa + \max(0, -p + L), \quad (2.102)$$

yielding for the contribution to the ICRF harmonic resonance p :

$$\delta H_{ps}(\mathbf{r}) = \sum_{L=-1}^1 e^{i(L-p)\pi/2} \sum_{\kappa=0}^{\infty} \rho_c^{2\kappa+|p-L|} \frac{\nabla_+^{k_+}}{k_+!} \frac{\nabla_-^{k_-}}{k_-!} \delta H_L. \quad (2.103)$$

It should be noted that in all cases, $k_+ + k_- = 2\kappa + |p - L|$, which is the exponent of ρ_c in Eq. 2.101, thus directly providing the small parameter to be considered in FLR expansions. At this point, however, the expression above includes all harmonics of the ICRF wave/particle interaction to arbitrary order in Larmor radius. In appendix B, the second order FLR expressions effectively implemented in the EVE code are deduced.

2.3.2 WKB harmonics

An algorithm has been implemented in order to include higher harmonics of the wave-particle interaction without having to handle derivatives of order larger than two, which can be problematic in a finite element code. Another advantage is that the resulting expressions are significantly simpler. On the other hand, it is necessary to assume that the perpendicular wave vector, \mathbf{k}_\perp , is known at any location and for any relevant value of k_\parallel (in such algorithms, it is usually assumed to be given by the fast wave wavenumber, i.e. $\mathbf{k}_\perp \sim \mathbf{k}_{\perp,FW}$). This means that the Hamiltonian perturbation (2.94) is assumed to be given by

$$\delta H_s(\mathbf{r}) = \delta H_s(\mathbf{r}_{gc}) \exp(i\mathbf{k}_\perp \cdot \mathbf{r}_c). \quad (2.104)$$

From Eq. 2.4 and writing the perpendicular wave vector as

$$\mathbf{k}_\perp = k_\perp [\cos(\beta)\mathbf{e}_{\perp 1} + \sin(\beta)\mathbf{e}_{\perp 2}], \quad (2.105)$$

with β the angle characterizing the direction of \mathbf{k}_\perp (see Ref. [49] for a discussion of this particular point), we obtain

$$\delta H_s(\mathbf{r}) = \delta H_s(\mathbf{r}_{gc}) \exp[ik_\perp \rho_c \sin(\phi_c + \beta)], \quad (2.106)$$

and

$$\delta H_s(\mathbf{r}) = \delta H_s(\mathbf{r}_{gc}) \sum_{p=-\infty}^{\infty} J_p(k_\perp \rho_c) e^{ip(\phi_c + \beta)}. \quad (2.107)$$

Therefore, using Eq. 2.99, we have

$$\delta H_s(\mathbf{r}) = \sum_{L=-1}^1 \delta H_L \sum_{p=-\infty}^{\infty} J_p(k_\perp \rho_c) e^{i(p+L)\phi_c} e^{ip\beta}, \quad (2.108)$$

or equivalently

$$\delta H_{ps}(\mathbf{r}) = \sum_{L=-1}^1 \delta H_L J_{p-L}(k_\perp \rho_c) e^{i(p-L)\beta}, \quad (2.109)$$

where J_p is the Bessel function of the first kind.

Chapter 3

Wave electromagnetic field

In this chapter, we establish the variational principle by which the wavefield can be computed. By employing the ingredients presented in chapter 2, we deduce the appropriate expressions, i.e. the antenna, Maxwellian and plasma functionals [19]. They have been implemented in a numerical code named *EVE*, which is described in detail in Ref. [23]. We stress here that special attention is being paid to the fact that *EVE* must be useful for heating experiment modeling, i.e. have acceptable calculation time and be directly comparable to other wave codes [36].

3.1 Variational principle

3.1.1 Maxwell's equations

Full-wave calculations consist of directly solving the Maxwell's equations in the whole geometric volume. They may be written in the form

$$\nabla \cdot \mathbf{E} = \frac{\rho_{maxw}}{\epsilon_0}, \quad (3.1)$$

$$\nabla \cdot \mathbf{B} = 0, \quad (3.2)$$

$$\nabla \times \mathbf{E} = -\frac{\partial \mathbf{B}}{\partial t}, \quad (3.3)$$

and

$$\nabla \times \mathbf{B} = \mu_0 \mathbf{j}_{maxw} + \frac{1}{c^2} \frac{\partial \mathbf{E}}{\partial t}. \quad (3.4)$$

In this driven problem, we assume that the system consists of an antenna and a plasma, contained in a perfectly conducting vacuum vessel. This is a closed system, so that we have conservation relations for the current

$$\mathbf{j}_{ant} + \mathbf{j}_{part} + \mathbf{j}_d = \mathbf{j}_{maxw}, \quad (3.5)$$

and for the charge density

$$\rho_{ant} + \rho_{part} + \rho_d = \rho_{maxw}, \quad (3.6)$$

where \mathbf{j}_{ant} (resp. ρ_{ant}) is the current (resp. charge) density in the antenna structure. \mathbf{j}_{part} (resp. ρ_{part}) is the current (resp. charge) density carried by the plasma particles. \mathbf{j}_d corresponds to an artificial dissipative current, which is useful in particular situations (such as runs in vacuum).

Rather than the field itself, the electromagnetic potential will be used. The electric and magnetic fields are linked to the vector potential \mathbf{A} and scalar potential φ through

$$\mathbf{E} = -\frac{\partial \mathbf{A}}{\partial t} - \nabla \varphi, \quad (3.7)$$

and

$$\mathbf{B} = \nabla \times \mathbf{A}. \quad (3.8)$$

From Maxwell's equations and assuming a monochromatic wave of frequency ω , we may write

$$\mathbf{j}_{maxw} = \frac{1}{\mu_0} \nabla \times (\nabla \times \mathbf{A}) + i\omega \epsilon_0 (i\omega \mathbf{A} - \nabla \varphi) + \mathbf{j}_d, \quad (3.9)$$

and

$$\rho_{maxw} = \epsilon_0 \nabla \cdot (i\omega \mathbf{A} - \nabla \varphi) + \rho_d. \quad (3.10)$$

Following Gambier and Samain [19], we introduce the gauge-invariant antenna functional

$$\mathcal{L}_{ant}(\mathbf{A}^*, \varphi^*) \equiv \int d^3 \mathbf{r} \left\{ \mathbf{j}_{ant} \cdot \mathbf{A}^* - \rho_{ant} \varphi^* \right\}, \quad (3.11)$$

the plasma functional

$$\mathcal{L}_{part}(\mathbf{A}, \varphi, \mathbf{A}^*, \varphi^*) \equiv \int d^3 \mathbf{r} \left\{ \mathbf{j}_{part} \cdot \mathbf{A}^* - \rho_{part} \varphi^* \right\}, \quad (3.12)$$

and the Maxwellian functional

$$\mathcal{L}_{maxw}(\mathbf{A}, \varphi, \mathbf{A}^*, \varphi^*) \equiv - \int d^3 \mathbf{r} \left\{ \mathbf{j}_{maxw} \cdot \mathbf{A}^* - \rho_{maxw} \varphi^* \right\}. \quad (3.13)$$

The variational statement corresponding to the conservation relations (3.5) and (3.6) consists of extremalizing the quantity

$$\mathcal{L}_{ant}(\mathbf{A}^*, \varphi^*) + \mathcal{L}_{part}(\mathbf{A}, \varphi, \mathbf{A}^*, \varphi^*) + \mathcal{L}_{maxw}(\mathbf{A}, \varphi, \mathbf{A}^*, \varphi^*), \quad (3.14)$$

with respect to all variations of the potentials \mathbf{A}^* , φ^* when \mathbf{A} and φ are kept constant. In other words, the solution (\mathbf{A}, φ) is given by

$$\frac{\delta \mathcal{L}_{ant}(\mathbf{A}^*, \varphi^*) + \delta \mathcal{L}_{part}(\mathbf{A}, \varphi, \mathbf{A}^*, \varphi^*) + \delta \mathcal{L}_{maxw}(\mathbf{A}, \varphi, \mathbf{A}^*, \varphi^*)}{\delta(\mathbf{A}^*, \varphi^*)} = 0, \quad (3.15)$$

We expand the potentials on a basis of given functions (a_i, ϕ_i) with coefficients (α_i) , i.e.

$$(\mathbf{A}, \varphi) = \sum_i \alpha_i (\mathbf{a}_i, \phi_i). \quad (3.16)$$

From Eqs. 3.9 and 3.10, it is clear that the Maxwellian functional (3.13) is bilinear in (\mathbf{A}, φ) and $(\mathbf{A}^*, \varphi^*)$. On the other hand, in the linear wave problem under consideration in this work, the plasma functional is also bilinear in (\mathbf{A}, φ) and $(\mathbf{A}^*, \varphi^*)$. In other words, we may write

$$\mathcal{L}_{part} + \mathcal{L}_{maxw} = \sum_{ij} (L_{part,ij} + L_{maxw,ij}) \alpha_i \alpha_j^*, \quad (3.17)$$

with

$$L_{part,ij} \equiv \mathcal{L}_{part}(\mathbf{a}_i, \varphi_i, \mathbf{a}_j^*, \varphi_j^*), \quad (3.18)$$

and

$$L_{maxw,ij} \equiv \mathcal{L}_{maxw}(\mathbf{a}_i, \varphi_i, \mathbf{a}_j^*, \varphi_j^*). \quad (3.19)$$

If we assume that the antenna current is independent of the field developing in the plasma, the antenna functional does not depend on (\mathbf{A}, φ) , and

$$\mathcal{L}_{ant} = \sum_j L_{ant,j} \alpha_j^*, \quad (3.20)$$

with

$$L_{ant,j} \equiv \mathcal{L}_{ant}(\mathbf{a}_j^*, \varphi_j^*). \quad (3.21)$$

Using Eqs. 3.17 and 3.20, the variational statement (3.15) may be rewritten as

$$\frac{\delta \{ [L_{ant,j} + (L_{part,ij} + L_{maxw,ij}) \alpha_i] \alpha_j^* \}}{\delta \alpha_j^*} = 0, \quad (3.22)$$

or yet, for every possible value of j ,

$$(L_{part,ij} + L_{maxw,ij}) \alpha_i + L_{ant,j} = 0. \quad (3.23)$$

The solution of this linear system yields the electromagnetic potential and thus the electromagnetic field.

3.1.2 Maxwellian functional

The Maxwellian functional is given by

$$\mathcal{L}_{maxw} = - \int d^3 \mathbf{r} \{ \mathbf{j}_{maxw} \cdot \mathbf{A}^* - \rho_{maxw} \varphi^* \}. \quad (3.24)$$

The current \mathbf{j}_{maxw} and charge ρ_{maxw} density are given in terms of the potential in Eqs. 3.9 and 3.10. Using the vector relation

$$\mathbf{A}^* \cdot [\nabla \times (\nabla \times \mathbf{A})] = (\nabla \times \mathbf{A}^*) \cdot (\nabla \times \mathbf{A}) - \nabla \cdot (\mathbf{A}^* \times (\nabla \times \mathbf{A})) \quad (3.25)$$

yields

$$\begin{aligned} \mathcal{L}_{maxw} = & - \int d^3 \mathbf{r} \left\{ \frac{1}{\mu_0} (\nabla \times \mathbf{A}) \cdot (\nabla \times \mathbf{A}^*) - \epsilon_0 (i\omega \mathbf{A} - \nabla \varphi) \cdot (-i\omega \mathbf{A}^* - \nabla \varphi^*) \right\} \\ & + \int d^2 \mathbf{S} \cdot \left\{ \epsilon_0 (i\omega \mathbf{A} - \nabla \varphi) \varphi^* + \frac{1}{\mu_0} \mathbf{A}^* \times (\nabla \times \mathbf{A}) \right\} - \mathcal{L}_{dsp}, \end{aligned} \quad (3.26)$$

with the dissipation functional

$$\mathcal{L}_{dsp} \equiv \int d^3\mathbf{r} \{ \mathbf{j}_d \cdot \mathbf{A}^* - \rho_d \varphi^* \}. \quad (3.27)$$

The rationale for the latter is that in some applications, it is useful to introduce an artificial resistive damping in the medium. This is needed, for instance, to run the code in the absence of plasma when no mechanism is available to dissipate the wave power. The (assumed isotropic) supplemental dissipation is obtained by writing $\mathbf{j}_d \equiv \epsilon_0 \omega_d \mathbf{E}$, which imposes for the charge density $\rho_d = -i\epsilon_0 \omega_d \nabla \cdot \mathbf{E} / \omega$. Usually, values of ω_d / ω as low as $10^{-3} - 10^{-2}$ are sufficient to obtain a satisfactory convergence of the code in vacuum. The functional is readily rewritten in the form

$$\mathcal{L}_{dsp}(\psi) = i\epsilon_0 \int_{\psi' < \psi} d\mathbf{r}' \frac{\omega_d}{\omega} (i\omega \mathbf{A} - \nabla \varphi) \cdot (-i\omega \mathbf{A}^* - \nabla \varphi^*) + \mathcal{S}_{dsp}, \quad (3.28)$$

with

$$\mathcal{S}_{dsp} = i\epsilon_0 \int_{\psi} d^2\mathbf{S} \cdot \frac{\omega_d}{\omega} (i\omega \mathbf{A} - \nabla \varphi) \varphi^*. \quad (3.29)$$

We note that rather than adding a new functional, the dissipative term may be readily included in the Maxwellian functional by substituting the $1/c^2$ factor appearing in the second term of Eq. 3.26 with $(1 + i\omega_d/\omega)/c^2$. Eq. 3.26 can thus be rewritten as

$$\begin{aligned} \mathcal{L}_{maxw} = & - \int d^3\mathbf{r} \left\{ \frac{1}{\mu_0} (\nabla \times \mathbf{A}) \cdot (\nabla \times \mathbf{A}^*) - \epsilon_0 \left(1 + i \frac{\omega_d}{\omega} \right) (i\omega \mathbf{A} - \nabla \varphi) \cdot (-i\omega \mathbf{A}^* - \nabla \varphi^*) \right\} \\ & + \int d^2\mathbf{S} \cdot \left\{ \epsilon_0 \left(1 + i \frac{\omega_d}{\omega} \right) (i\omega \mathbf{A} - \nabla \varphi) \varphi^* + \frac{1}{\mu_0} \mathbf{A}^* \times (\nabla \times \mathbf{A}) \right\}. \end{aligned} \quad (3.30)$$

The way the surface term is treated depends on the type of boundary conditions employed. If we assume that the calculation volume is bounded by a perfect conductor, we have $\varphi = 0$ on the surface. Also, the continuity conditions for \mathbf{A} at the vacuum/vessel interface impose that the tangential components must vanish. Denoting $\hat{\mathbf{n}}$ the unit vector normal to the magnetic surface and pointing outwards, we may write

$$\begin{aligned} d^2\mathbf{S} \cdot \mathbf{A}^* \times (\nabla \times \mathbf{A}) &= d^2S \hat{\mathbf{n}} \cdot [\mathbf{A}^* \times (\nabla \times \mathbf{A})] \\ &= d^2S (\hat{\mathbf{n}} \times \mathbf{A}^*) \cdot (\nabla \times \mathbf{A}), \end{aligned} \quad (3.31)$$

which vanishes on the surface since $\hat{\mathbf{n}} \times \mathbf{A}^*$ only involves the tangential components of \mathbf{A} . Therefore, when the integral is carried out over the whole vacuum vessel volume, we may write

$$\mathcal{L}_{maxw} = - \int d^3\mathbf{r} \left\{ \frac{1}{\mu_0} (\nabla \times \mathbf{A}) \cdot (\nabla \times \mathbf{A}^*) - \epsilon_0 \left(1 + i \frac{\omega_d}{\omega} \right) (i\omega \mathbf{A} - \nabla \varphi) \cdot (-i\omega \mathbf{A}^* - \nabla \varphi^*) \right\}. \quad (3.32)$$

For convenience, we introduce the Maxwellian functional integrated from the magnetic axis up to magnetic surface ψ , denoted $\mathcal{L}_{maxw}(\psi)$:

$$\begin{aligned} \mathcal{L}_{maxw}(\psi) = & - \int_{\psi' < \psi} d^3 \mathbf{r}' \left\{ \frac{1}{\mu_0} (\nabla \times \mathbf{A}) \cdot (\nabla \times \mathbf{A}^*) \right. \\ & \left. - \epsilon_0 \left(1 + i \frac{\omega_d}{\omega} \right) (i\omega \mathbf{A} - \nabla \varphi) \cdot (-i\omega \mathbf{A}^* - \nabla \varphi^*) \right\} + \mathcal{S}_{maxw}(\psi), \end{aligned} \quad (3.33)$$

with

$$\mathcal{S}_{maxw}(\psi) \equiv \int_{\psi} d^2 \mathbf{S} \cdot \left\{ \frac{1}{\mu_0} \mathbf{A}^* \times (\nabla \times \mathbf{A}) + \epsilon_0 \left(1 + i \frac{\omega_d}{\omega} \right) (i\omega \mathbf{A} - \nabla \varphi) \varphi^* \right\}. \quad (3.34)$$

The surface term may be rewritten as

$$\mathcal{S}_{maxw}(\psi) \equiv \int_{\psi} d^2 \mathbf{S} \cdot \left\{ \frac{1}{\mu_0} \mathbf{A}^* \times \mathbf{B} + \epsilon_0 \left(1 + i \frac{\omega_d}{\omega} \right) \varphi^* \mathbf{E} \right\}. \quad (3.35)$$

Evidently

$$\mathcal{L}_{maxw}(\psi = \psi_c) = \mathcal{L}_{maxw}, \quad (3.36)$$

where ψ_c refers to the flux surface coinciding with the vacuum vessel.

3.1.3 Plasma functional

General expression

The plasma functional is given by

$$\mathcal{L}_{part} \equiv \sum_s \mathcal{L}_{part,s} = \sum_s \int d^3 \mathbf{r} \{ \mathbf{j}_{part,s} \cdot \mathbf{A}^* - \rho_{part,s} \varphi^* \}. \quad (3.37)$$

The sum is to be carried out over all plasma species, denoted by index s .

To first order, the change in charge density caused by the wave is given by the kinetic expression

$$\rho_{part,s} = q_s \int d^3 \mathbf{p} \delta f_s(\mathbf{r}, \mathbf{p}, t). \quad (3.38)$$

Likewise, for the current density perturbation

$$\mathbf{j}_{part,s} = q_s \int d^3 \mathbf{p} \{ \delta \mathbf{v}_s(\mathbf{r}, \mathbf{p}, t) f_{s,0}(\mathbf{r}, \mathbf{p}) + \mathbf{v}_{s,0}(\mathbf{r}, \mathbf{p}) \delta f_s(\mathbf{r}, \mathbf{p}, t) \}, \quad (3.39)$$

with the velocity perturbation induced by the wave field

$$\delta \mathbf{v}_s = \frac{\partial H_s}{\partial \mathbf{p}} = - \frac{q_s}{m_s} \mathbf{A}. \quad (3.40)$$

This yields for the plasma functional

$$\mathcal{L}_{part,s} = -\epsilon_0 \int d^3 \mathbf{r} \omega_{ps}^2 |\mathbf{A}|^2 - \int d^3 \mathbf{p} d^3 \mathbf{r} \delta f_s \delta H_s^*, \quad (3.41)$$

with $\omega_{ps}^2 \equiv n_s q_s^2 / m_s / \epsilon_0$. n_s is the unperturbed density.

Using the expansion over generalized angles (2.33), Eq. 3.41 can be rewritten as

$$\mathcal{L}_{part,s} = -\epsilon_0 \int d^3 \mathbf{r} \omega_{ps}^2 |\mathbf{A}|^2 + (2\pi)^3 \sum_{\mathbf{N}} \int d^3 \mathbf{J} \frac{N_i}{\omega - N_k \Omega_k} \frac{\partial f_{s,0}}{\partial J_i} |\delta h_{\mathbf{N}}|^2, \quad (3.42)$$

where the integral over the generalized angles has been carried out, resulting in the cancellation of all terms containing $\delta h_{\mathbf{N}} \delta h_{\mathbf{N}'}^*$ with $\mathbf{N} \neq \mathbf{N}'$. The second term on the right-hand side of this expression shows that the condition for an energy exchange to take place between the wave and the particles is two-fold. It requires that i) the global resonance condition $\omega - \mathbf{N} \cdot \boldsymbol{\Omega} = 0$ be verified, ii) $\delta h_{\mathbf{N}}$ be not zero. In order to make the latter condition explicit and to obtain a practical expression for \mathcal{L}_{part} , the elementary contributions $\delta h_{\mathbf{N}}$ have to be evaluated.

Using Eq. 2.20 in Eq. 3.42, the particle functional may be decomposed as

$$\mathcal{L}_{part,s} \equiv \mathcal{L}_{part,s}^{(adiab)} + \mathcal{L}_{part,s}^{(res)}, \quad (3.43)$$

with the non-resonant (or adiabatic) particle functional defined as

$$\mathcal{L}_{part,s}^{(adiab)} = -\epsilon_0 \int d^3 \mathbf{r} \omega_{ps}^2 |\mathbf{A}|^2 - (2\pi)^3 \sum_{\mathbf{N}} \int d^3 \mathbf{J} \frac{\partial f_{s,0}}{\partial E} |\delta h_{\mathbf{N}}|^2, \quad (3.44)$$

and the resonant functional

$$\mathcal{L}_{part,s}^{(res)} = (2\pi)^3 \sum_{\mathbf{N}} \int d^3 \mathbf{J} \frac{\omega}{\omega - \mathbf{N} \cdot \boldsymbol{\Omega}} \mathcal{D} f_{s,0} |\delta h_{N_1, N_2, N_3}|^2, \quad (3.45)$$

having introduced the differential operator \mathcal{D} acting on the unperturbed distribution function

$$\mathcal{D} f_{s,0} \equiv \frac{\partial f_{s,0}}{\partial E} - \frac{N_1}{\omega} \frac{q_s}{m_s} \frac{\partial f_{s,0}}{\partial \mu} + \frac{N_3}{\omega} \frac{\partial f_{s,0}}{\partial P_\phi}. \quad (3.46)$$

This expression is similar to the numerator appearing in Eq. 11 of Edery et al. [22].

Adiabatic functional

Since the equilibrium distribution function is independent of the generalized angle, the Parseval identity for the Hamiltonian:

$$\sum_{\mathbf{N}} |\delta h_{\mathbf{N}}|^2 = \frac{1}{(2\pi)^3} \int d^3 \Phi |\delta H_s|^2, \quad (3.47)$$

can be employed in Eq. 3.44 to write

$$(2\pi)^3 \sum_{\mathbf{N}} \int d^3 \mathbf{J} \frac{\partial f_{s,0}}{\partial E} |\delta h_{\mathbf{N}}|^2 = \int d^3 \mathbf{J} d^3 \Phi \frac{\partial f_{s,0}}{\partial E} |\delta H_s|^2. \quad (3.48)$$

In the latter expression, only $|\delta H_s|^2$ has a dependence on the generalized angle Φ_1 . We introduce the decomposition of δH_s in harmonics of the cyclotron phase

$$\delta H_s \equiv \sum_p \delta H_{ps} e^{ip\phi_c}, \quad (3.49)$$

Using this relation with Eq. 2.43, we obtain

$$\begin{aligned} \int d\Phi_1 |\delta H_s|^2 &= 2\pi \sum_p \delta H_{ps} \delta H_{ps}^* \\ &= 2\pi q_s^2 \left[(\varphi - v_{\parallel} A_{\parallel}) (\varphi^* - v_{\parallel} A_{\parallel}^*) + \frac{v_{\perp}^2}{2} (A_{\perp 1} A_{\perp 1}^* + A_{\perp 2} A_{\perp 2}^*) \right], \end{aligned} \quad (3.50)$$

where Eqs. 2.100 have been employed.

We can use this to rewrite Eq. 3.44 as

$$\begin{aligned} \mathcal{L}_{part,s}^{(adiab)} &= -\epsilon_0 \int d^3 \mathbf{r} \omega_{ps}^2 \mathbf{A} \cdot \mathbf{A}^* \\ &\quad - q_s^2 \int d^3 \mathbf{p} d^3 \mathbf{r} \frac{\partial f_{s,0}}{\partial E} \left[(\varphi - v_{\parallel} A_{\parallel}) (\varphi^* - v_{\parallel} A_{\parallel}^*) + \frac{v_{\perp}^2}{2} (A_{\perp 1} A_{\perp 1}^* + A_{\perp 2} A_{\perp 2}^*) \right], \end{aligned} \quad (3.51)$$

where \mathbf{p} and \mathbf{r} refer to the guiding-center variables. After a few algebraic manipulations with the velocity integrals, we eventually obtain

$$\begin{aligned} \mathcal{L}_{part,s}^{(adiab)} &= \epsilon_0 \frac{m_s}{T_s} \int d^3 \mathbf{r} \omega_{ps}^2 \chi_0(\mathbf{r}) \varphi \varphi^* + \epsilon_0 \int d^3 \mathbf{r} \omega_{ps}^2 \chi_1(\mathbf{r}) (A_{\perp 1} A_{\perp 1}^* + A_{\perp 2} A_{\perp 2}^*) \\ &\quad + \epsilon_0 \int d^3 \mathbf{r} \omega_{ps}^2 \chi_2(\mathbf{r}) A_{\parallel} A_{\parallel}^* - \epsilon_0 \sqrt{\frac{T_s}{2m_s}} \int d^3 \mathbf{r} \omega_{ps}^2 \chi_3(\mathbf{r}) (A_{\parallel} \varphi^* - A_{\parallel}^* \varphi). \end{aligned} \quad (3.52)$$

where we have introduced

$$\chi_0(\mathbf{r}) \equiv - \int d^3 \mathbf{p} \frac{T_s}{n_s} \frac{\partial f_{s,0}}{\partial E}, \quad (3.53)$$

$$\chi_1(\mathbf{r}) \equiv -1 - \int d^3 \mathbf{p} \frac{m_s v_{\perp}^2}{2} \frac{1}{n_s} \frac{\partial f_{s,0}}{\partial E}, \quad (3.54)$$

$$\chi_2(\mathbf{r}) \equiv -1 - 2 \int d^3 \mathbf{p} \frac{m_s v_{\parallel}^2}{2} \frac{1}{n_s} \frac{\partial f_{s,0}}{\partial E}, \quad (3.55)$$

and

$$\chi_3(\mathbf{r}) \equiv - \int d^3 \mathbf{p} \sqrt{\frac{T_s}{2m_s}} m_s v_{\parallel} \frac{1}{n_s} \frac{\partial f_{s,0}}{\partial E}, \quad (3.56)$$

Resonant functional: continuous limit

The resonant functional appearing in Eq. 3.43 is given by

$$\mathcal{L}_{part,s}^{(res)} = (2\pi)^3 \sum_{\mathbf{N}} \int d^3 \mathbf{J} \frac{\omega}{\omega - \mathbf{N} \cdot \boldsymbol{\Omega}} \mathcal{D} f_{s,0} |\delta h_{N_1, N_2, N_3}|^2. \quad (3.57)$$

Using the quasi-local form Eq. 2.93 in the previous expression, we obtain

$$\begin{aligned} \mathcal{L}_{part,s}^{(res)} &= (2\pi)^3 \sum_{p, N_2, n} \int d^3 \mathbf{J} \frac{\omega}{\omega - N_i \Omega_i} \mathcal{D} f_{s,0} \\ &\quad \times \frac{2\pi}{\tau_b^2} \sum_{m_1, m_2} \sum_{t_0} \frac{\delta H_{pm_1 n}(t_0) \delta H_{pm_2 n}^*(t_0)}{|\dot{\gamma}_{m_0}(t_0)|} e^{i(m_1 - m_2)\theta(t_0)}, \end{aligned} \quad (3.58)$$

which can be recast in the form

$$\begin{aligned} \mathcal{L}_{part,s}^{(res)} = (2\pi)^3 \sum_{p,n} \int d^3\mathbf{J} \frac{1}{\tau_b} \sum_{m_1,m_2} \sum_{N_2} \sum_{t_0} \frac{2\pi}{\tau_b} \frac{1}{|\dot{\gamma}_{m_0}(t_0)|} \frac{\omega}{\omega - N_i \Omega_i} \mathcal{D}f_{s,0} \\ \times \delta H_{pm_1n}(t_0) \delta H_{pm_2n}^*(t_0) e^{i(m_1-m_2)\theta(t_0)}. \end{aligned} \quad (3.59)$$

From Eq. 2.79, the time it takes for a particle to cross the resonance corresponding to N_2 to the resonance corresponding to $N_2 + 1$ is given by

$$\delta t = \frac{\Omega_2}{|\dot{\gamma}_{m_0}(t_0)|} = \frac{2\pi}{\tau_b} \frac{1}{|\dot{\gamma}_{m_0}(t_0)|}, \quad (3.60)$$

which means that the sum over N_2 and t_0 may be transformed into a time integral. $N_2 \Omega_2$ must be replaced by $\dot{\gamma}_{m_0} - p\Omega_1 - n\Omega_3$, and

$$\mathcal{L}_{part,s}^{(res)} = (2\pi)^3 \sum_{p,n} \int d^3\mathbf{J} \frac{1}{\tau_b} \int_0^{\tau_b} dt \sum_{m_1,m_2} \frac{\omega}{\omega - \dot{\gamma}_{m_0}(t)} \mathcal{D}f_{s,0} \delta H_{pm_1n}(t) \delta H_{pm_2n}^*(t) e^{i(m_1-m_2)\theta(t)}. \quad (3.61)$$

The previous expression is independent of Φ_1 and Φ_3 . Furthermore, $d\Phi_2 = \Omega_2 dt = 2\pi dt/\tau_b$ so that we can perform the transform

$$(2\pi)^2 \int d^3\mathbf{J} \frac{2\pi}{\tau_b} \int_0^{\tau_b} dt = \int d^3\mathbf{J} d^3\Phi = \int d^3\mathbf{r} d^3\mathbf{p}, \quad (3.62)$$

and

$$\mathcal{L}_{part,s}^{(res)} = \sum_{p,m_1,m_2,n} \int d^3\mathbf{p} d^3\mathbf{r} \frac{\omega}{\omega - p\Omega_{cs} - k_{\parallel,0}v_{\parallel}} \mathcal{D}f_{s,0} e^{i(m_1-m_2)\theta} \delta H_{pm_1n} \delta H_{pm_2n}^*, \quad (3.63)$$

where Def. 2.51 has been used and the parallel wavevector corresponding to poloidal mode m_0 , $k_{\parallel,0} \equiv m_0 \nabla_{\parallel} \theta + n \nabla_{\parallel} \phi$ has been introduced.

Eq. 3.63 can be further manipulated in the context of a second-order FLR expansion. This is detailed in appendix B. The important point for what follows is that it embeds the dielectric response in the form

$$\mathcal{I}_{kk}^{(q)} \equiv \frac{q_s^2}{\epsilon_0} \int d^3\mathbf{p} u_{\perp}^q v_{\perp}^{\alpha_{\perp}} v_{\parallel}^{\alpha_{\parallel}} \frac{\omega}{\omega - p\Omega_{cs} - k_{\parallel,0}v_{\parallel}} \mathcal{D}f_{s,0}. \quad (3.64)$$

Another possibility is to handle the wave-particle interaction in the framework of a WKB treatment (see section 2.3.2). In this case, the dielectric kernel is given by

$$\mathcal{I}_{kk}^{L\bar{L}} \equiv \frac{q_s^2}{\epsilon_0} \int d^3\mathbf{p} v_{\perp}^{\alpha_{\perp}} v_{\parallel}^{\alpha_{\parallel}} \frac{\omega}{\omega - p\Omega_{cs} - k_{\parallel}v_{\parallel}} \mathcal{D}f_{s,0} J_{p-L} \left(\frac{k_{\perp}v_{\perp}}{\Omega_{cs}} \right) J_{p-\bar{L}} \left(\frac{k_{\perp}v_{\perp}}{\Omega_{cs}} \right). \quad (3.65)$$

3.1.4 Energy conservation

An essential feature of the variational formulation employed in this work is that it embeds energy conservation. Straightforward algebra allows to recast (3.33) as

$$-i\frac{\omega}{2}\mathcal{L}_{maxw}(\psi) = -i\omega W_{field}(\psi) + \mathcal{S}_{Poynting}(\psi) + \dot{W}_{dsp}(\psi) - \frac{1}{2} \int d^2\mathbf{S} \cdot \mathbf{j}_{maxw}\varphi^*, \quad (3.66)$$

with

$$W_{field}(\psi) \equiv \int_{\psi' < \psi} d^3\mathbf{r}' \left(\frac{\epsilon_0 |\mathbf{E}|^2}{2} - \frac{|\mathbf{B}|^2}{2\mu_0} \right), \quad (3.67)$$

$$\mathcal{S}_{Poynting}(\psi) \equiv \frac{1}{2\mu_0} \int_{\psi} d^2\mathbf{S} \cdot (\mathbf{E}^* \times \mathbf{B}), \quad (3.68)$$

and

$$\dot{W}_{dsp}(\psi) \equiv \omega_d \int_{\psi' < \psi} d^3\mathbf{r}' \frac{\epsilon_0 |\mathbf{E}|^2}{2}. \quad (3.69)$$

From Maxwell's equations, the last term appearing in Eq. 3.66 may be transformed to obtain the more compact form

$$-i\frac{\omega}{2}\mathcal{L}_{maxw}(\psi) = -i\omega W_{field}(\psi) + \mathcal{S}_{Poynting}(\psi) + \dot{W}_{dsp}(\psi) - \frac{1}{2} \int d^2\mathbf{S} \cdot (\mathbf{j}_{part} + \mathbf{j}_{ant})\varphi^*. \quad (3.70)$$

A similar treatment may be applied to the antenna functional (3.11) to obtain

$$-i\frac{\omega}{2}\mathcal{L}_{ant}(\psi) = \dot{W}_{ant}(\psi) + \frac{1}{2} \int d^2\mathbf{S} \cdot \mathbf{j}_{ant}\varphi^*, \quad (3.71)$$

with

$$\dot{W}_{ant}(\psi) \equiv \frac{1}{2} \int_{\psi' < \psi} d^3\mathbf{r}' \mathbf{j}_{ant} \cdot \mathbf{E}^*, \quad (3.72)$$

the time derivative of the work needed from an external generator to maintain the field in the cavity. The time-averaged power exchanged between the wave and the particles in the volume delimited by magnetic surface ψ is given by the real part of

$$\dot{W}_{part}(\psi) = \frac{1}{2} \int_{\psi' \leq \psi} d^3\mathbf{r}' \mathbf{E}^* \cdot \mathbf{j}_{part}, \quad (3.73)$$

and it is readily seen that

$$-i\frac{\omega}{2}\mathcal{L}_{part}(\psi) = \dot{W}_{part}(\psi) + \frac{1}{2} \int d^2\mathbf{S} \cdot \mathbf{j}_{part}\varphi^*. \quad (3.74)$$

Summing Eqs. 3.70, 3.71 and 3.74 yields the conservation law valid on every flux surface

$$\begin{aligned} -i\omega W_{field}(\psi) + \mathcal{S}_{Poynting}(\psi) + \dot{W}_{dsp}(\psi) + \dot{W}_{ant}(\psi) + \dot{W}_{part}(\psi) = \\ -i\frac{\omega}{2\mu_0} \{ \mathcal{L}_{part}(\psi) + \mathcal{L}_{ant}(\psi) + \mathcal{L}_{maxw}(\psi) \} = 0. \end{aligned} \quad (3.75)$$

\dot{W}_{part} includes an irreversible part and a reversible part, which may be written as the divergence of the so-called kinetic flux, yielding a surface integral (see section 1.1.3

for a discussion of this point). It must be pointed out that this separation is a tricky issue [12, 37] which has been treated in an elegant way by D. Smithe by introducing a symmetrical version of the dielectric tensor [14]. Here, we write

$$\dot{W}_{part}(\psi) \equiv \mathcal{P}_{abs} + \mathcal{S}_{kin}, \quad (3.76)$$

to obtain the local conservation law

$$-i\omega W_{field}(\psi) + \mathcal{S}_{Poynting}(\psi) + \dot{W}_{dsp}(\psi) + \dot{W}_{ant}(\psi) + \mathcal{P}_{abs}(\psi) + \mathcal{S}_{kin}(\psi) = 0. \quad (3.77)$$

It may be shown that \mathcal{P}_{abs} is directly given by

$$\mathcal{P}_{abs} = -i\frac{\omega}{2\mu_0}\mathcal{L}_{part}, \quad (3.78)$$

so that the kinetic flux is given by

$$\mathcal{S}_{kin} = \frac{1}{2} \int d^2\mathbf{S} \cdot \mathbf{j}_{part}\varphi^*. \quad (3.79)$$

The latter relation is, however, of little practical interest since \mathbf{j}_{part} is actually never explicitly written as a function of the electromagnetic field (unlike in dielectric tensor-based approaches).

When the whole vacuum vessel is considered, the global energy conservation is deduced

$$-i\omega W_{field} + \dot{W}_{dsp} + \dot{W}_{ant} + \dot{W}_{part} = 0. \quad (3.80)$$

The real part directly shows that the total coupled power is dissipated either through damping by particles (\dot{W}_{part}) or artificial dissipation (\dot{W}_{dsp}).

3.2 Dielectric response

3.2.1 General expression

Both Eqs. 3.52 and 3.63 have the advantage of being able to accommodate any kind of distribution function provided the dielectric response, i.e. Eqs. 3.53, 3.54 and 3.64, are evaluated correctly. In this document, in order to retain compatibility with Fokker-Planck solvers, we always assume that the local distribution function is normalized according to

$$\int d^3\mathbf{p} f_{s0}(p_{\parallel}, p_{\perp}) = n_{s0}. \quad (3.81)$$

Eq. 3.64 can then be rewritten as

$$\mathcal{I}_{kk}^{(q)} \equiv \left(\frac{\omega_{ps}}{c}\right)^2 \frac{m_s c^2}{T_s} v_{th}^{\alpha_{\parallel} + \alpha_{\perp}} x_{0,s} \mathcal{W}_{\alpha_{\parallel}, q + \alpha_{\perp}}, \quad (3.82)$$

with

$$\mathcal{W}_{i,j} \equiv \frac{1}{\sqrt{\pi}} \int_{-\infty}^{\infty} du_{\parallel} \frac{u_{\parallel}^i}{u_{\parallel} - x_{p,s}} 2 \int_0^{\infty} du_{\perp} u_{\perp}^{j+1} \mathcal{K}(u_{\parallel}, u_{\perp}), \quad (3.83)$$

with $u_{\parallel,\perp} \equiv v_{\parallel,\perp}/v_{th}$. Also, we have defined

$$x_{p,s} \equiv \frac{\omega - p\Omega_{cs}}{k_{\parallel}v_{th}}, \quad (3.84)$$

and

$$\mathcal{K}(u_{\parallel}, u_{\perp}) \equiv -T_s\pi^{3/2}m_s^3v_{th}^3\frac{1}{n_s}\mathcal{D}f_{s,0}. \quad (3.85)$$

It is also interesting to rewrite the adiabatic response functions χ_0 , χ_1 , χ_2 and χ_3 (Eqs. 3.53-3.56) in the more convenient form

$$\chi_0 = \frac{2}{\sqrt{\pi}} \int du_{\parallel} du_{\perp} u_{\perp} \mathcal{K}_{adiab}(u_{\parallel}, u_{\perp}), \quad (3.86)$$

$$\chi_1 = -1 + \frac{2}{\sqrt{\pi}} \int du_{\parallel} du_{\perp} u_{\perp}^3 \mathcal{K}_{adiab}(u_{\parallel}, u_{\perp}), \quad (3.87)$$

$$\chi_2 = -1 + \frac{4}{\sqrt{\pi}} \int du_{\parallel} du_{\perp} u_{\perp} u_{\parallel}^2 \mathcal{K}_{adiab}(u_{\parallel}, u_{\perp}), \quad (3.88)$$

and

$$\chi_3 = \frac{2}{\sqrt{\pi}} \int du_{\parallel} du_{\perp} u_{\perp} u_{\parallel} \mathcal{K}_{adiab}(u_{\parallel}, u_{\perp}), \quad (3.89)$$

with

$$\mathcal{K}_{adiab}(u_{\parallel}, u_{\perp}) \equiv -T_s\pi^{3/2}m_s^3v_{th}^3\frac{1}{n_s}\frac{\partial f_{s,0}}{\partial E}. \quad (3.90)$$

Whereas the numerical evaluation of Eqs. 3.86-3.89 does not pose any particular difficulties, the calculation of Eq. 3.83 is more complicated. The employed algorithm for arbitrary distributions is presented in appendix C.

3.2.2 Anisotropic Maxwellians

In this section, we use the anisotropic Maxwellian distribution function, Eq. 2.25 to write

$$f_{s,0}(\mathbf{r}, \mathbf{p}) = \frac{n_s}{(2\pi m_s T_s)^{3/2} \eta_{\perp}} \exp\left(-\frac{m_s v_{\parallel}^2}{2T_s}\right) \exp\left(-\frac{m_s v_{\perp}^2}{2\eta_{\perp} T_s}\right). \quad (3.91)$$

In this case, it is readily shown that

$$\mathcal{K}_{adiab}(u_{\parallel}, u_{\perp}) = \frac{1}{\eta_{\perp}} e^{-u_{\parallel}^2} e^{-u_{\perp}^2/\eta_{\perp}}, \quad (3.92)$$

where the same notations as previously have been used. Eqs. 3.86-3.89 simplify as

$$\chi_0 = 1, \quad (3.93)$$

$$\chi_1 = -1 + \eta_{\perp}, \quad (3.94)$$

and

$$\chi_2 = \chi_3 = 0. \quad (3.95)$$

From Eq. 3.46, we have the relation

$$\mathcal{D}f_{s,0} = -\frac{1}{T_s} \mathcal{A}_{ps} f_{s,0}, \quad (3.96)$$

with

$$\mathcal{A}_{ps} \equiv 1 - \frac{p\Omega_{cs,res}}{\omega} \left(1 - \frac{1}{\eta_{\perp}}\right). \quad (3.97)$$

The dielectric kernel (Eq. 3.83) takes the simple form

$$\mathcal{W}_{i,j} = \mathcal{A}_{ps} I_{\parallel,i} I_{\perp,j}. \quad (3.98)$$

The perpendicular integrals are directly related to the Euler Gamma function:

$$I_{\perp,j} \equiv \frac{2}{\eta_{\perp}} \int_0^{\infty} du_{\perp} u_{\perp}^{j+1} e^{-u_{\perp}^2/\eta_{\perp}} = \eta_{\perp}^{j/2} \Gamma\left(\frac{j}{2} + 1\right). \quad (3.99)$$

In the FLR version version of the code, only the first five integrals are actually needed. The parallel integrals are given by

$$I_{\parallel,n} \equiv \frac{1}{\pi^{1/2}} \int_{-\infty}^{\infty} du_{\parallel} \frac{u_{\parallel}^n}{u_{\parallel} - x_{p,s}} e^{-u_{\parallel}^2}, \quad (3.100)$$

which may be directly related to the plasma dispersion function Z , so that we may write for the first three functions (which are the only ones needed in this FLR version of the code):

$$\begin{cases} I_{\parallel,0} = Z(x_{p,s}), \\ I_{\parallel,1} = 1 + x_{p,s}Z(x_{p,s}), \\ I_{\parallel,2} = x_{p,s}[1 + x_{p,s}Z(x_{p,s})]. \end{cases} \quad (3.101)$$

3.2.3 Resonant functional: WKB harmonics

Eq. 3.65 yields

$$\begin{aligned} \mathcal{I}_{kk}^{L\bar{L}} = & -\frac{2\mathcal{A}_{ps}n_s}{T_{\parallel,s}} \left[\frac{\omega}{k_{\parallel}v_{th,\parallel}} \int_{-\infty}^{\infty} du_{\parallel} \frac{u_{\parallel}^{\alpha_{\parallel}}}{u_{\parallel} - x_{p,s}} e^{-u_{\parallel}^2} \right] \\ & \times \int_0^{\infty} du_{\perp} u_{\perp}^{\alpha_{\perp}+1} J_{p-L} \left(\frac{\sqrt{2}k_{\perp}v_{th,s\perp}}{\Omega_{cs}} u_{\perp} \right) J_{p-\bar{L}} \left(\frac{\sqrt{2}k_{\perp}v_{th,s\perp}}{\Omega_{cs}} u_{\perp} \right) e^{-u_{\perp}^2}. \end{aligned} \quad (3.102)$$

The bracketed quantity is almost the parallel integral already seen previously (see Eq. 3.100). We define

$$I_{\perp,n}^{L\bar{L}} \equiv 2 \int_0^{\infty} du_{\perp} u_{\perp}^{n+1} J_{p-L} \left(\frac{\sqrt{2}k_{\perp}v_{th,s\perp}}{\Omega_{cs}} u_{\perp} \right) J_{p-\bar{L}} \left(\frac{\sqrt{2}k_{\perp}v_{th,s\perp}}{\Omega_{cs}} u_{\perp} \right) e^{-u_{\perp}^2}, \quad (3.103)$$

so that

$$\mathcal{I}_{kk}^{L\bar{L}} = \frac{n_s}{T_{\parallel,s}} \mathcal{A}_{ps} I_{\parallel,\alpha_{\parallel}} I_{\perp,\alpha_{\perp}}^{L\bar{L}}. \quad (3.104)$$

An analytical evaluation of the perpendicular integrals $I_{\perp,n}^{L\bar{L}}$ (Eq. 3.103) is made possible by the general relation [38]

$$\int_0^\infty e^{-\rho^2 x^2} J_p(\alpha x) J_p(\beta x) x dx = \frac{1}{2\rho^2} \exp\left(-\frac{\alpha^2 + \beta^2}{4\rho^2}\right) I_p\left(\frac{\alpha\beta}{2\rho^2}\right), \quad (3.105)$$

valid for $\Re(p) > 1$, $|\arg(\rho)| < \pi/4$, $\alpha > 0$, $\beta > 0$. I_p is the modified Bessel function of the first kind. Owing to the numerous zero elements in $(\mathcal{H}_{lk}^{0,0})$, it turns out that only a few of these integrals are necessary. Introducing

$$\lambda \equiv \frac{k_\perp^2 v_{th,s\perp}^2}{\Omega_{cs}^2}, \quad (3.106)$$

and

$$\mu \equiv \sqrt{2\lambda}, \quad (3.107)$$

they have the explicit expressions

$$I_{\perp,0}^{0,0} = e^{-\lambda} I_p(\lambda), \quad (3.108)$$

$$I_{\perp,1}^{1,0} = I_{\perp,1}^{0,1} = \frac{e^{-\lambda}}{\mu} [p I_p(\lambda) + \lambda (I_p'(\lambda) - I_p(\lambda))], \quad (3.109)$$

$$I_{\perp,1}^{-1,0} = I_{\perp,1}^{0,-1} = \frac{e^{-\lambda}}{\mu} [p I_p(\lambda) - \lambda (I_p'(\lambda) - I_p(\lambda))], \quad (3.110)$$

$$I_{\perp,2}^{1,1} = e^{-\lambda} [I_{p-1}(\lambda) + \lambda (I_{p-1}'(\lambda) - I_{p-1}(\lambda))], \quad (3.111)$$

$$I_{\perp,2}^{-1,-1} = e^{-\lambda} [I_{p+1}(\lambda) + \lambda (I_{p+1}'(\lambda) - I_{p+1}(\lambda))], \quad (3.112)$$

and

$$I_{\perp,2}^{1,-1} = I_{\perp,2}^{-1,1} = e^{-\lambda} \lambda [I_p'(\lambda) - I_p(\lambda)]. \quad (3.113)$$

Chapter 4

Quasilinear plasma response

Arguably the most powerful aspect of the Hamiltonian framework presented in chapter 2 is the fact that it can be used to articulate a variational statement by which the electromagnetic field can be obtained as was done in chapter 3, but also to obtain a global Fokker-Planck equation. The advantage is that the two sides of the calculation are naturally consistent between each other. This Fokker-Planck equation naturally includes potentially important effects such as finite orbit width effects [39, 40] or Hamiltonian chaos aspects [21, 41]. However, even codes working in terms of motion invariants (or combinations thereof) usually do not solve the global problem. An example of an advanced Fokker-Planck numerical solver is the orbit following Monte Carlo (OFMC) code SPOT [42]. We refer the interested reader to publications related to the ongoing effort of coupling SPOT with EVE, the wave code based on the Hamiltonian formalism discussed in chapter 3 [43].

In this chapter, we present how the Fokker-Planck equation is derived in the framework of the Hamiltonian description of chapter 2. The fact that energy conservation is automatically ensured is underlined. The goal here is to build a physics model able to capture the main features of the secular plasma response with minimal effort. Rather than assuming *a priori* that the interaction between the ions and the wave takes place at the finite locations defined by the local ion cyclotron resonance $\omega - p\Omega_{cs} - k_{\parallel}v_{\parallel} = 0$, as is often done, we derive the relevant local expressions for the quasilinear diffusion part from the global ones. This is achieved by performing quasi-local approximations of the various global quantities, following the procedure detailed in chapter 2. Note that this asymptotic limit allows one to recover the classical results obtained when the quasi-local approach is employed from the start [8, 11, 44] but the Hamiltonian approach lends itself to more refined studies (see, e.g., Refs. [21, 34, 45]).

4.1 Hamiltonian quasilinear theory

4.1.1 Fokker-Planck equation

In the framework of the Hamiltonian theory employed throughout this manuscript, the Fokker-Planck equation is deduced from the Vlasov equation (Eq. 2.29), written here in

terms of action-angle variables

$$\frac{\partial f_s}{\partial t} - \frac{\partial H_s}{\partial \Phi_i} \frac{\partial f_s}{\partial J_i} + \frac{\partial H_s}{\partial J_i} \frac{\partial f_s}{\partial \Phi_i} = 0. \quad (4.1)$$

We use the same expansion as in chapter 2 (Eq. 2.33), namely

$$H_s = H_{s,0}(J_k, t) + \sum_{N_1, N_2, N_3} \delta h_{N_1, N_2, N_3}(J_k) e^{i(N_i \Phi_i - \omega t)} + \text{c.c.}, \quad (4.2)$$

and

$$f_s = f_{s,0}(J_k, t) + \sum_{N_1, N_2, N_3} \delta f_{N_1, N_2, N_3}(J_k) e^{i(N_i \Phi_i - \omega t)} + \text{c.c.}, \quad (4.3)$$

where c.c. designates the complex conjugate of the previous term. Note that the equilibrium quantities $H_{s,0}$ and $f_{s,0}$ depend on time in a secular fashion. δH_s and δf_s , on the other hand, feature an oscillatory time-dependence at the wave frequency ω .

The advantage of the angle-action formalism is that the quasilinear mode selection, which is performed by a space-time averaging operation over a finite volume-time period, cleanly reduces to an angle-time averaging operation, i.e.

$$\langle \dots \rangle \equiv \frac{1}{(2\pi)^3} \int d\Phi_1 d\Phi_2 d\Phi_3 \frac{\omega}{2\pi} \int_0^{2\pi/\omega} dt \dots \quad (4.4)$$

The secular modification of f_s is then directly extracted by writing

$$f_{s,0}(t) = \langle f_s \rangle. \quad (4.5)$$

Averaging the Fokker-Planck equation and keeping the first order contributions of H_s and f_s yields

$$\frac{\partial f_{s,0}}{\partial t} - i \sum_{\mathbf{N}} N_i \frac{\partial}{\partial J_i} [\delta h_{\mathbf{N}} \delta f_{\mathbf{N}}^* - \delta h_{\mathbf{N}}^* \delta f_{\mathbf{N}}] = \left(\frac{\partial f_{s,0}}{\partial t} \right)_{\text{coll.}}, \quad (4.6)$$

where a collisional term has been added on the right-hand side to reflect the fact that the slow time variation of the equilibrium distribution is necessarily influenced by collisions.

Using the expression for the linear response to the wave (Eq. 2.34), we can rewrite the previous equation in the compact form

$$\frac{\partial f_{s,0}}{\partial t} = \frac{\partial}{\partial J_i} D_{ij}^{(QL)} \frac{\partial f_{s,0}}{\partial J_j} + \left(\frac{\partial f_{s,0}}{\partial t} \right)_{\text{coll.}}, \quad (4.7)$$

with the quasilinear diffusion operator

$$\bar{D}_{ij}^{(QL)} = \pi \sum_{N_1, N_2, N_3} N_i N_j |\delta h_{N_1, N_2, N_3}|^2 \delta(\omega - N_k \Omega_k). \quad (4.8)$$

At this stage, the Fokker-Planck equation (4.7) is global. This is clear from the quasilinear diffusion operator (Eq. 4.8), which features a global resonance: only those particles with an unperturbed motion in strict resonance with the wave can exchange energy. It must however be realized that the sum over (N_1, N_2, N_3) represents an infinite number of usually densely packed such resonances.

4.1.2 Quasilinear diffusion coefficient

It is more convenient to express the diffusion coefficient in terms of the invariants of the motion. Following section 2.1.2, a rather natural choice is $\mathbf{I} \equiv (E, \Lambda, P_\phi)$. Λ is preferred over μ for algebraic reasons, and is defined as $\Lambda \equiv \mu B_0(0)/E$ with $B_0(0)$ the magnetic field at a given reference location (typically the magnetic axis).

The wave term in the Fokker-Planck equation then takes the form

$$\langle \mathcal{D}_w(f_s) \rangle = \frac{1}{g^{1/2}} \frac{\partial}{\partial I_i} g^{1/2} D_{ij}^{(QL)} \frac{\partial f_{s,0}}{\partial I_j}, \quad (4.9)$$

and

$$D_{ij}^{(QL)} = \frac{\partial I_i}{\partial J_k} \frac{I_j}{\partial J_l} \bar{D}_{kl}^{(QL)}. \quad (4.10)$$

The Jacobian of this transformation is given by

$$g^{1/2} = \frac{E}{\omega_b} \frac{1}{\omega_{cs}(0)}. \quad (4.11)$$

With the help of Eqs. 2.17, 2.18, 2.19 and 4.11, we obtain for the energy-energy element of the diffusion tensor

$$D_{EE}^{(QL)} = \pi \sum_{N_1, N_2, N_3} N_i \Omega_i N_j \Omega_j |\delta h_{N_1, N_2, N_3}|^2 \delta(\omega - N_k \Omega_k), \quad (4.12)$$

or

$$D_{EE}^{(QL)} = \pi \omega^2 \sum_{N_1, N_2, N_3} |\delta h_{N_1, N_2, N_3}|^2 \delta(\omega - N_k \Omega_k). \quad (4.13)$$

As shown in section 2.2.2, the wave-particle interaction dictates that only the Hamiltonian contributions with $N_1 = p$ and $N_3 = n$ survive, so that we may write, limiting ourselves to the interaction at harmonics p and toroidal wavenumber n (for the sake of concision, the indices p and n are omitted from now on)

$$\begin{aligned} D_{EE}^{(QL)} &= \pi \omega^2 \sum_{N_2} |\delta h_{p, N_2, n}|^2 \delta(\omega - N_k \Omega_k) \\ &= \frac{\pi}{\omega_b} \omega^2 \sum_{N_2} |\delta h_{p, N_2, n}|^2 \delta\left(N_2 - \frac{\omega - p\Omega_1 - n\Omega_3}{\Omega_2}\right), \end{aligned} \quad (4.14)$$

$$D_{E\Lambda}^{(QL)} = D_{\Lambda E}^{(QL)} = \frac{\pi}{\omega_b} \omega \left(\frac{p\Omega_{cs}(0) - \Lambda\omega}{E} \right) \sum_{N_2} |\delta h_{p, N_2, n}|^2 \delta\left(N_2 - \frac{\omega - p\Omega_1 - n\Omega_3}{\Omega_2}\right), \quad (4.15)$$

$$D_{\Lambda\Lambda}^{(QL)} = \frac{\pi}{\omega_b} \left(\frac{p\Omega_{cs}(0) - \Lambda\omega}{E} \right)^2 \sum_{N_2} |\delta h_{p, N_2, n}|^2 \delta\left(N_2 - \frac{\omega - p\Omega_1 - n\Omega_3}{\Omega_2}\right), \quad (4.16)$$

$$D_{EP_\phi}^{(QL)} = D_{P_\phi E}^{(QL)} = \frac{\pi}{\omega_b} n\omega \sum_{N_2} |\delta h_{p, N_2, n}|^2 \delta\left(N_2 - \frac{\omega - p\Omega_1 - n\Omega_3}{\Omega_2}\right), \quad (4.17)$$

$$D_{\Lambda P_\phi}^{(QL)} = D_{P_\phi \Lambda}^{(QL)} = \frac{\pi}{\omega_b} n \left(\frac{p\Omega_{cs}(0) - \Lambda\omega}{E} \right) \sum_{N_2} |\delta h_{p,N_2,n}|^2 \delta \left(N_2 - \frac{\omega - p\Omega_1 - n\Omega_3}{\Omega_2} \right), \quad (4.18)$$

and

$$D_{P_\phi P_\phi}^{(QL)} = \frac{\pi}{\omega_b} n^2 \sum_{N_2} |\delta h_{p,N_2,n}|^2 \delta \left(N_2 - \frac{\omega - p\Omega_1 - n\Omega_3}{\Omega_2} \right). \quad (4.19)$$

Evidently

$$D_{E\Lambda}^{(QL)} = D_{\Lambda E}^{(QL)} = \frac{1}{E} \left(\frac{p\Omega_{cs}(0)}{\omega} - \Lambda \right) D_{EE}^{(QL)}, \quad (4.20)$$

$$D_{\Lambda\Lambda}^{(QL)} = \frac{1}{E^2} \left(\frac{p\Omega_{cs}(0)}{\omega} - \Lambda \right)^2 D_{EE}^{(QL)}, \quad (4.21)$$

$$D_{EP_\phi}^{(QL)} = D_{P_\phi E}^{(QL)} = \frac{\pi}{\omega_b} \frac{n}{\omega} D_{EE}^{(QL)}, \quad (4.22)$$

$$D_{\Lambda P_\phi}^{(QL)} = D_{P_\phi \Lambda}^{(QL)} = \frac{n}{\omega} \left(\frac{p\Omega_{cs}(0)}{\omega} - \Lambda \right) D_{EE}^{(QL)}, \quad (4.23)$$

and

$$D_{P_\phi P_\phi}^{(QL)} = \frac{\pi}{\omega_b} \frac{n^2}{\omega^2} D_{EE}^{(QL)}, \quad (4.24)$$

so that only the expression for $D_{EE}^{(QL)}$ is actually needed.

4.1.3 Energy conservation

As discussed in section 3.1.4, energy conservation is a direct consequence of the variational formulation [19]. We recall here the local Poynting theorem (3.77), which may be rewritten in the form

$$-i\omega W_{field}(\psi) + \mathcal{S}_{Poynting}(\psi) + \dot{W}_{dsp}(\psi) + \mathcal{P}_{abs}(\psi) + \mathcal{S}_{kin}(\psi) = -\dot{W}_{ant}(\psi). \quad (4.25)$$

As already discussed in chapter 3, a delicate task is to obtain the power irreversibly transferred from the wave to the particles, which requires the evaluation of the kinetic flux [12, 14, 37, 46]. In the present approach, however, this step is unnecessary since the dissipated power is directly available from the particle functional \mathcal{L}_{part} . To demonstrate this point, it is necessary to evaluate the secular variation of the kinetic energy of the particles in interaction with the wave in the framework of the quasilinear theory, which is given by

$$W = \frac{m_s}{2} \int d^3\mathbf{r} d^3\mathbf{p} v^2 f_{s,0}(\mathbf{r}, \mathbf{p}, t), \quad (4.26)$$

so that the energy increase caused by the power transferred from the wave to the particles through non-collisional damping may be written as

$$\mathcal{P}_{abs} = \frac{dW}{dt} = \frac{m_s}{2} \int d^3\mathbf{r} d^3\mathbf{p} v^2 \frac{\partial}{\partial J_j} D_{ij}^{(QL)} \frac{\partial f_{s,0}}{\partial J_i}. \quad (4.27)$$

Using $d^3\mathbf{r}d^3\mathbf{p} = (2\pi)^3 d^3\mathbf{J}$ in the integral and integrating by parts yields

$$\mathcal{P}_{abs} = -\pi \frac{m_s}{2} (2\pi)^3 \int d^3\mathbf{J} \left(N_j \frac{\partial v^2}{\partial J_j} \right) N_i \frac{\partial f_{s,0}}{\partial J_i} \delta(\omega - N_k \Omega_k) |\delta h_{\mathbf{N}}|^2. \quad (4.28)$$

The quantity in parentheses may be rewritten as

$$N_j \frac{\partial v^2}{\partial J_j} = \frac{2}{m_s} N_j \frac{\partial E}{\partial J_j} = \frac{2}{m_s} N_j \Omega_j, \quad (4.29)$$

so that, using the global resonance condition imposed by the delta function

$$\mathcal{P}_{abs} = -\omega \pi (2\pi)^3 \int d^3\mathbf{J} N_i \frac{\partial f_{s,0}}{\partial J_i} \delta(\omega - N_k \Omega_k) |\delta h_{\mathbf{N}}|^2, \quad (4.30)$$

which is strictly identical to the imaginary part of the plasma functional (3.42), thereby demonstrating

$$\mathcal{P}_{abs} = \frac{\omega}{2} \Im(\mathcal{L}_{part}). \quad (4.31)$$

We also deduce from Eq. 3.74 that the kinetic flux is given by

$$\mathcal{S}_{kin}(\psi) = -\frac{1}{2} \Re \left\{ \int_{\psi} d^2\mathbf{S} \cdot \mathbf{j}_{part} \varphi^* \right\}. \quad (4.32)$$

Fig. 4.1 shows the power balance corresponding to the ^3He case in ITER discussed in Ref. [23]. After the field is reconstructed, the power coupled by the antenna is given by Eq. 3.71, the Poynting flux is available from Eq. 3.68, and the power absorbed on species, \mathcal{P}_{abs} , is directly deduced from the plasma functional (Eq 4.31). The kinetic flux is then deduced from the energy balance, Eq. 4.25.

It is often convenient to separate the power absorbed by the various plasma species. Using the decomposition of Eq. 3.37 in terms of a sum over species, we may write

$$\mathcal{P}_{abs}(\psi) \equiv \sum_s \mathcal{P}_{abs,s}(\psi), \quad (4.33)$$

with

$$\mathcal{P}_{abs,s}(\psi) = \frac{\omega}{2} \Im(\mathcal{L}_{part,s}(\psi)), \quad (4.34)$$

which is directly available from the wave calculation and corresponds to the power absorbed by species s inside magnetic surface ψ . An important quantity for experiment modeling is the power density absorbed by species s on magnetic surface ρ . It is obtained by writing

$$p_s(\psi) = \frac{1}{\mathcal{V}(\rho)} \left. \frac{d\Im(\mathcal{L}_{part,s})}{d\rho} \right|_{\psi}, \quad (4.35)$$

with the volume element defined as

$$\mathcal{V}(\rho) = 2\pi \oint d\theta J(\rho, \theta). \quad (4.36)$$

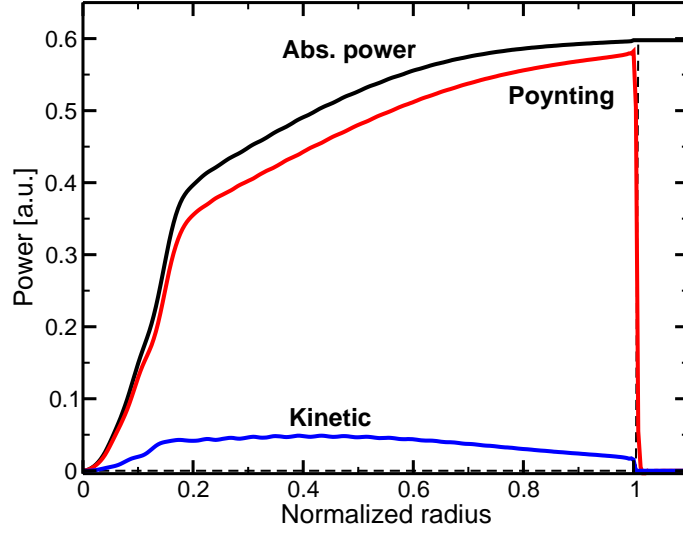


Figure 4.1: Power balance corresponding to a ${}^3\text{He}(\text{DT})$ scenario in ITER [23]. Shown are the Poynting flux, the (cumulative) absorbed power, and the kinetic flux deduced from the energy balance. The cumulative power coupled by the antenna is also shown as a dashed line and matches the absorbed power on the vacuum vessel.

4.2 Derivation of a quasi-local model

4.2.1 Quasilinear diffusion coefficient

We now turn to the calculation of $D_{EE}^{(QL)}$. Using the quasi-local expression for the Hamiltonian contributions, Eq. 2.66, we have

$$\delta h_{p,N_2,n} \approx \frac{1}{\tau_b} \sum_{m,t_0[m]} \Gamma_m(t_0) \delta H_{pmn}(t_0) e^{i[\gamma_m(t_0) - (p\Omega_1 + N_2\Omega_2 + n\Omega_3)]}. \quad (4.37)$$

We recall that t_0 is given by

$$\dot{\gamma}_{m_0}(t_0) = p\Omega_{cs}(t_0) + m_0\dot{\theta}(t_0) + n\dot{\phi}(t_0) = N_i\Omega_i, \quad (4.38)$$

which by virtue of the Dirac function which selects a given value of N_2 yields the usual quasi-local resonance

$$\omega = p\Omega_{cs}(t_0) + k_{\parallel}(t_0)v_{\parallel}(t_0). \quad (4.39)$$

Using the procedure detailed in chapter 3, we obtain

$$D_{EE}^{(QL)} = \frac{\pi}{\omega_b} \omega^2 \left\{ \frac{1}{\tau_b^2} \sum_{m_1, m_2} \sum_{t_0} |\Gamma_{m_0}(t_0)|^2 \delta H_{pm_1n}(t_0) \delta H_{pm_2n}^*(t_0) e^{i(m_1 - m_2)\theta(t_0)} \right\}, \quad (4.40)$$

with $m_0 = (m_1 + m_2)/2$.

We note that if the function γ_{m_0} depends only weakly on the poloidal wavenumber (which is typical of cyclotron interaction or Cerenkov interaction at sufficiently high toroidal numbers), we have

$$\begin{aligned} D_{EE}^{(QL)} &\approx \frac{\pi}{\omega_b} \omega^2 \left\{ \frac{1}{\tau_b^2} \sum_{m_1, m_2} \sum_{t_0} |\Gamma_{m_0}(t_0)|^2 \delta H_{pm_1 n}(t_0) \delta H_{pm_2 n}^*(t_0) e^{i(m_1 - m_2)\theta(t_0)} \right\} \\ &= \frac{\pi}{\omega_b} \omega^2 \left\{ \frac{1}{\tau_b^2} \sum_{t_0} |\Gamma_{m_0}(t_0)|^2 \sum_{m_1, m_2} \delta H_{pm_1 n}(t_0) \delta H_{pm_2 n}^*(t_0) e^{i(m_1 - m_2)\theta(t_0)} \right\} \quad (4.41) \\ &= \frac{\omega^2}{2\tau_b} \sum_{t_0} |\Gamma_{m_0}(t_0) \delta H_{pn}(t_0)|^2. \end{aligned}$$

The quantity $|\Gamma_{m_0}(t_0)| \equiv \tau_{res}$ represents the time spent by the particle in resonance with the wave, allowing to rewrite the previous expression in a relatively transparent fashion as

$$D_{EE}^{(QL)} \approx \frac{\omega^2}{2} \sum_{t_0} \left(\frac{\tau_{res}^2(t_0)}{\tau_b} \right) |\delta H_{pn}(t_0)|^2. \quad (4.42)$$

From the local resonance condition, the resonance time is approximately given by

$$\tau_{res} \equiv \frac{1}{|pv_{\parallel} \nabla_{\parallel} \Omega_{cs}|^{1/2}}, \quad (4.43)$$

whereas the bounce time is

$$\tau_b = \oint \frac{dl}{v_{\parallel}}, \quad (4.44)$$

with dl the elemental arc-length along the field line.

We can go one step further in simplifying the problem if we assume, as Stix did in his seminal paper [47], that the particle parallel motion is uniform along its unperturbed orbit (in a quasi-local sense). If we assume that τ_{res}^2/τ_b only varies slowly along the particle orbit as the particle crosses the local resonance, then we have simply

$$D_{EE}^{(QL)} \approx D_0 \sum_{t_0} |\delta H_{pn}(t_0)|^2, \quad (4.45)$$

where all quantities in the Hamiltonian are evaluated at the local resonance and the constant D_0 is determined by imposing that the total absorbed power be equal to the coupled RF power.

In the framework of this quasi-local model, we may use a uniform approximation to the Hamiltonian contributions H_{pn} by employing a Kennel-Engelmann-type expression [48]. In fact, this is already available to us from our previous derivation of a WKB Hamiltonian (see section 2.3.2), using \mathbf{k}_{\perp} from the fast wave dispersion relation and assuming that the propagation angle β is zero (actually a subtle assumption [49]). This yields

$$\begin{aligned} \delta H_{pn} &= -q_s \frac{v_{\perp}}{\sqrt{2}} A_+ J_{p-1}(k_{\perp} v_{\perp} / \Omega_{cs}) - q_s \frac{v_{\perp}}{\sqrt{2}} A_- J_{p+1}(k_{\perp} v_{\perp} / \Omega_{cs}) \\ &\quad + q_s (\varphi - v_{\parallel} A_{\parallel}) J_p(k_{\perp} v_{\perp} / \Omega_{cs}). \end{aligned} \quad (4.46)$$

The last term in this equation corresponds to the interaction between the parallel electric field and the particles. Since we are interested in ion heating and we only consider the fast wave, the main contribution to the electric field is the perpendicular potential vector \mathbf{A}_\perp , so that may we may write

$$|\delta H_{pn}|^2 \approx q_s^2 \frac{v_\perp^2}{2\omega^2} |E_+ J_{p-1}(k_\perp v_\perp / \Omega_{cs}) + E_- J_{p+1}(k_\perp v_\perp / \Omega_{cs})|^2, \quad (4.47)$$

which is a well-known expression (see, e.g. [11, 30]).

Since we have adopted a quasi-local form for the Fokker-Planck equation, it is convenient to express the diffusion tensor in terms of the local velocity (v_\parallel, v_\perp) . We have

$$\Lambda \equiv \frac{m_i v_\perp^2}{2E} \frac{B_0(0)}{B_0} = \frac{u_\perp^2}{u^2} \frac{B_0(0)}{B_0}, \quad (4.48)$$

and

$$E \equiv \frac{m_i}{2} (v_\parallel^2 + v_\perp^2) = \frac{m_i v_{th,i}^2}{2} u^2, \quad (4.49)$$

from which we deduce

$$D_{v_\perp v_\perp}^{(QL)} = \frac{1}{m_i v_\perp^2} \left(p \frac{\Omega_{cs}}{\omega} \right)^2 D_{EE}^{(QL)}, \quad (4.50)$$

and

$$D_{v_\parallel v_\parallel}^{(QL)} = \frac{1}{m_i v_\parallel^2} \left(1 - p \frac{\Omega_{cs}}{\omega} \right)^2 D_{EE}^{(QL)}. \quad (4.51)$$

At the cyclotron resonance, we have $\omega \sim p\Omega_{cs}$, so that

$$|D_{v_\perp v_\perp}^{(QL)}| \gg |D_{v_\perp v_\parallel}^{(QL)}|, |D_{v_\parallel v_\perp}^{(QL)}| \gg |D_{v_\parallel v_\parallel}^{(QL)}|, \quad (4.52)$$

which is the justification for the subsequent neglecting of all terms but the perpendicular one in the quasilinear diffusion tensor. From expressions 4.45, 4.47 and 4.50, we see that the wave contribution to the distribution function evolution takes the simple form

$$\left(\frac{\partial f_i}{\partial t} \right)_{\text{wave}} \equiv \hat{Q} f_i = \frac{1}{u_\perp} \frac{\partial}{\partial u_\perp} u_\perp D_w \frac{\partial f_i}{\partial u_\perp}, \quad (4.53)$$

with

$$D_w = D_0 \sum_{t_0} |E_+ J_{p-1}(k_\perp v_\perp / \Omega_{cs}) + E_- J_{p+1}(k_\perp v_\perp / \Omega_{cs})|^2. \quad (4.54)$$

4.2.2 Coulomb collisions

The classical derivation of the Coulomb collision operator is by essence local in the velocity space [50–52]. If we denote “i” the heated species, the collisional part of the Fokker-Planck equation at a given space location can be written as

$$\frac{\partial f_i}{\partial t} = \sum_s \hat{C}(f_i, f_s), \quad (4.55)$$

where the sum is carried out over all plasma species. A complex problem is the correct handling of the $\hat{C}(f_i, f_i)$ term (self-collisions) [52, 53]. We choose here to disregard this issue by employing a linearized operator where self-collisions are supposed negligible, and assuming that the background species are all Maxwellians. The resulting operator can be written as the divergence of a quasilinear flux, i.e. $\hat{C}(f_i, f_s) \equiv -\nabla_{\mathbf{v}} \cdot \mathbf{S}_c$ with $\mathbf{S}_c = -\mathbf{D} \cdot \nabla_{\mathbf{v}} f_s + \mathbf{F}_c f_s$.

At this stage, it is convenient to introduce a reference frequency characterizing the collisions between test ions belonging to the heated species and the background constituted by one of the bulk ion species (usually the majority ion, denoted here ‘‘M’’)

$$\nu_i \equiv \nu_{i/M} \equiv \frac{\Gamma^{i/M}}{v_{th,i}^3}, \quad (4.56)$$

where $v_{th,i}$ is a thermal velocity characterizing the heated species (for instance, the thermal velocity before heating). Introducing the normalized time $\tau \equiv \nu_i t$, the normalized velocity $u \equiv v/v_{th,i}$ and pitch angle cosine $\lambda \equiv v_{\parallel}/v$, we then obtain the collision term in the compact form [8]

$$\frac{\partial f_i}{\partial \tau} = \frac{1}{u^2} \frac{\partial}{\partial u} \left[u^2 \left(D_{uu} \frac{\partial f_i}{\partial u} - F_u f_i \right) \right] + \frac{1}{u^2} \left[\frac{\partial}{\partial \lambda} (1 - \lambda^2) \frac{\Theta_c}{2u} \frac{\partial f_i}{\partial \lambda} \right], \quad (4.57)$$

with

$$D_{uu} = \frac{1}{2u} \sum_{\beta} \frac{\nu_{i/\beta}}{\nu_i} \Psi(u_{\beta}), \quad (4.58)$$

$$F_u = - \sum_{\beta} \frac{\nu_{i/\beta}}{\nu_i} \frac{T_i}{T_{\beta}} \Psi(u_{\beta}), \quad (4.59)$$

and

$$\frac{\Theta_c}{2u} = \sum_{\beta} \frac{\nu_{i/\beta}}{\nu_i} \frac{\Theta(u_{\beta})}{2u}, \quad (4.60)$$

where β designates the bulk species, i.e. all plasma species except the heated one. We introduce $u_{\beta} \equiv v/v_{th,\beta}$. Also

$$\Gamma^{a/b} \equiv \frac{n_b Z_a^2 Z_b^2 e^4 \log(\Lambda^{a/b})}{4\pi \epsilon_0^2 m_a^2}, \quad (4.61)$$

with $\log(\Lambda^{a/b})$ the Coulomb logarithm. Besides

$$\Psi(x) \equiv \frac{\text{erf}(x) - x \text{erf}'(x)}{x^2}, \quad (4.62)$$

and

$$\Theta(x) \equiv \frac{1}{x^2} \left[\left(x^2 - \frac{1}{2} \right) \text{erf}(x) + \frac{x}{2} \text{erf}'(x) \right]. \quad (4.63)$$

Note that we have

$$\frac{\nu_{i/\beta}}{\nu_i} = \frac{n_{\beta}}{n_M} \frac{Z_{\beta}^2 \log(\Lambda^{i/\beta})}{Z_M^2 \log(\Lambda^{i/M})} \approx \frac{n_{\beta}}{n_M} \frac{Z_{\beta}^2}{Z_M^2}, \quad (4.64)$$

and also

$$u_\beta = u \frac{v_{th,i}}{v_{th,\beta}}. \quad (4.65)$$

4.2.3 A quasi-local Fokker-Planck solver

At this point, it would be useful to take advantage of the model described previously in order to predict the plasma response to a given wave-field. The idea is to be as numerically efficient as possible, retaining only the following physics ingredients to simulate ICRF plasma heating:

- Building of the superthermal ion tail by RF-induced diffusion, balanced by collisions. For a given initial equilibrium distribution function $f_i(t_{\text{initial}})$, we impose that in the absence of RF source, f_i will tend towards a given f_{eq} at large t . This is needed to describe a distribution function which has been pre-heated by, e.g. neutral beam injection. Designing a comprehensive model for NBI heating is beyond the scope of our study.
- Heating of the various thermal plasma species by collisional relaxation of the ICRF-heated ions. This is essential because transport properties, which eventually determine the plasma performance, are dependent on this heat source term.
- Fast ions lost due to prompt losses, i.e. orbit widths comparable or exceeding the device size.

A generic form for a local Fokker-Planck equation fulfilling these requirements is

$$\partial_\tau f_i = \sum_\beta \hat{C}(f_i, f_\beta) - \sum_\beta \hat{C}(f_{eq}, f_\beta) + \hat{Q}f_i - \hat{L}f_i + \mathcal{S}_{\text{fuelling}}, \quad (4.66)$$

where $\hat{Q}f_i$ represents the wave quasilinear term, $\hat{L}f_i$ a fast ion loss term and $\mathcal{S}_{\text{fuelling}}$ is a particle source adjusted to compensate for losses caused either by the loss term, or by the choice of an insufficiently extended velocity grid.

In the presence of the quasi-local Coulomb operator, Eq. 4.57, a common procedure is to expand the distribution function in terms of Legendre polynomials

$$f_i(u, \lambda) \equiv \sum_n f_n(u) P_n(\lambda), \quad (4.67)$$

or conversely

$$f_n(u) \equiv \frac{2n+1}{2} \int_{-1}^1 d\lambda f_i(u, \lambda) P_n(\lambda). \quad (4.68)$$

The rationale is that the pitch-angle scattering term appearing in Eq. 4.57 takes a diagonal form, i.e.

$$\frac{\partial}{\partial \lambda} (1 - \lambda^2) \frac{\Theta_c}{2u} \frac{\partial f_i}{\partial \lambda} = - \sum_n n(n+1) \frac{\Theta_c}{2u} f_n(u) P_n(\lambda). \quad (4.69)$$

We assume a generic form for the loss term, i.e.

$$\hat{L}f_i = \frac{\Lambda_{fil}(u, \lambda)}{\tau_{fil}} f_i, \quad (4.70)$$

with τ_{fil} the typical fast ion loss time, and $\Lambda_{fil}(u, \lambda)$ a function of velocity and pitch-angle which cancels in regions where ions are confined, and approaches 1 in regions of velocity space where particles are lost¹.

We impose that the total heated ion density is conserved, and that any lost ion must be reintroduced as a thermal ion. This is done by setting

$$\mathcal{S}_{\text{fuelling}} = \frac{n_i}{\pi^{3/2} v_{th,i}} e^{-u^2} \mathcal{S}_0, \quad (4.72)$$

with \mathcal{S}_0 a constant. Since the employed forms of the collision and quasilinear diffusion operators conserve density, we immediately obtain

$$\mathcal{S}_0 = \frac{2\pi}{n_i \tau_{fil}} \int dud\lambda u^2 \Lambda_{fil}(u, \lambda) f_i(u, \lambda). \quad (4.73)$$

The corresponding term in the Fokker-Planck equation is straightforward to implement.

If we project Eq. 4.66 using expansion 4.67 onto basis polynomial P_m , we obtain

$$\begin{aligned} \sum_n \delta_{nm} \partial_\tau f_n &= \sum_n \delta_{nm} \left[D_{uu} \partial_u^2 f_n + \left(\frac{1}{u^2} \partial_u (u^2 D_{uu}) - F_u \right) \partial_u f_n \right. \\ &\quad \left. + \left(-\frac{1}{u^2} \partial_u (u^2 F_u) - n(n+1) \frac{\Theta_c}{2u^3} \right) f_n \right] \\ &+ \sum_n (2m+1) \left[D_{00}^{mn} \partial_u^2 f_n + \left(\frac{1}{u^2} \partial_u (u^2 D_{00}^{mn}) - \frac{1}{u} D_{01}^{mn} + \frac{1}{u} D_{10}^{mn} \right) \partial_u f_n \right. \\ &\quad \left. - \left(\frac{1}{u^2} \partial_u (u D_{01}^{mn}) + \frac{1}{u^2} D_{11}^{mn} \right) f_n \right] \\ &- \sum_n (2m+1) \frac{\Lambda_{mn}}{\tau_{fil}} f_n + u^2 \mathcal{S}_{\text{fuelling}} \delta_{m0} \\ &+ \delta_{m0} \left[\frac{2}{u} \partial_u (u^2 D_{uu}) + \frac{1}{u^2} \partial_u (u^2 F_u) - 2(2u^2 - 1) D_{uu} - 2u F_u \right] f_{eq}(u). \end{aligned} \quad (4.74)$$

In the latter expression, f_{eq} is assumed to be an isotropic Maxwellian. Using more complicated equilibrium distribution function shapes does not pose any conceptual difficulty, but makes the source term somewhat more complex.

¹As an example of a most natural form for Λ_{fil} , one can employ the isotropic expression

$$\Lambda_{fil}(u) \equiv \frac{1}{1 + e^{-(E - E_{fil})/\Delta E}}, \quad (4.71)$$

with ΔE an adjustable parameter. This ensures that all ions with energy exceeding E_{fil} are virtually lost. Of course, more sophisticated expressions can be employed as well.

We have introduced the following moments

$$D_{00}^{mn}(u) \equiv \frac{1}{2} \int_{-1}^1 d\lambda (1 - \lambda^2) D_w(u, \lambda) P_m(\lambda) P_n(\lambda), \quad (4.75)$$

$$D_{01}^{mn}(u) \equiv \frac{1}{2} \int_{-1}^1 d\lambda (1 - \lambda^2) \lambda D_w(u, \lambda) P'_m(\lambda) P_n(\lambda), \quad (4.76)$$

$$D_{10}^{mn}(u) \equiv \frac{1}{2} \int_{-1}^1 d\lambda (1 - \lambda^2) \lambda D_w(u, \lambda) P_m(\lambda) P'_n(\lambda), \quad (4.77)$$

$$D_{11}^{mn}(u) \equiv \frac{1}{2} \int_{-1}^1 d\lambda (1 - \lambda^2) \lambda^2 D_w(u, \lambda) P'_m(\lambda) P'_n(\lambda), \quad (4.78)$$

and

$$\Lambda_{mn}(u) \equiv \frac{1}{2} \int_{-1}^1 d\lambda \Lambda_{fil}(u, \lambda) P_m(\lambda) P_n(\lambda). \quad (4.79)$$

All these expressions lend themselves to implementation in an efficient numerical code, which was named AQL. An early version of AQL is described and extensively employed in Ref. [6].

4.2.4 Derived quasilinear quantities

From the distribution function and various operators, it is possible to derive various quasilinear quantities of physical interest.

The heated ion density is defined as

$$n_i \equiv \int d^3\mathbf{v} f_i(\mathbf{v}), \quad (4.80)$$

and can be expressed in terms of the first Legendre moment of f_i (Eq. 4.67) as

$$n_i = 4\pi \int_0^\infty du u^2 f_0. \quad (4.81)$$

The perpendicular and parallel energy content can be directly obtained by writing

$$W_{\perp, \parallel} \equiv \int d^3\mathbf{v} \frac{mv_{\perp, \parallel}^2}{2} f_i(\mathbf{v}), \quad (4.82)$$

yielding

$$W_{\parallel} = T_i \int d^3\mathbf{v} u_{\parallel}^2 f_i = \frac{4\pi}{3} T_i \int_0^\infty du u^4 \left(f_0 + \frac{2}{5} f_2 \right), \quad (4.83)$$

and

$$W_{\perp} = T_i \int d^3\mathbf{v} u_{\perp}^2 f_i = \frac{4\pi}{3} T_i \int_0^\infty du u^4 \left(2f_0 - \frac{2}{5} f_2 \right), \quad (4.84)$$

where f_0 and f_2 are the coefficients in the Legendre expansion of the distribution function (Eq. 4.67). It is readily seen that in the isotropic case, $W_{\perp} = 2W_{\parallel}$, as it must.

A crucial quantity, needed to perform the distribution function calculation is the absorbed power $p_{abs,qlin}$, which is deduced from Eq. 4.53 as

$$p_{abs,qlin} \equiv \int d^3\mathbf{v} \frac{mv^2}{2} \hat{Q}f_i, \quad (4.85)$$

and may be rewritten as

$$\begin{aligned} p_{abs,qlin} &= 4\pi\nu_i T_i v_{th,i}^3 \int du d\lambda u^2 (1 - \lambda^2) D_w(u, \lambda) \left(u \frac{\partial f_i}{\partial u} - \lambda \frac{\partial f_i}{\partial \lambda} \right) \\ &= 8\pi T_i v_{th,i}^3 \int du u^2 \sum_n \left[u D_{00}^{0n} \frac{\partial f_n}{\partial u} - D_{01}^{0n} f_n \right], \end{aligned} \quad (4.86)$$

where the moments of both the distribution function and quasilinear diffusion coefficients (Eqs. 4.75 and 4.76) are used. One should systematically compare the results obtained from the two expressions above to ensure that the Legendre expansion retains a sufficient number of harmonics.

Another important quantity is the power transferred to the background plasma by collisions, which is given by

$$p_{coll} \equiv \int d^3\mathbf{v} \frac{mv^2}{2} \hat{C}f_i, \quad (4.87)$$

and may be written in terms of f_0 only

$$p_{coll} = 8\pi\nu_i T_i v_{th,i}^3 \int_0^\infty du [\partial_u (u^3 D_{uu}) + u^3 F_u] f_0, \quad (4.88)$$

where an integration by parts has been carried out in order to avoid involving the derivative of f_i in the calculations.

This expression may be used in the course of the calculation because of its simplicity and numerical efficiency. If one is interested in the power transferred from the heated ion to a given (Maxwellian) background species β , then straightforward algebraic manipulations of Eq. 4.88 using Eqs. 4.58 and 4.59 yield

$$p_{coll}^{i \rightarrow \beta} = 8\pi\nu_i \left(\frac{\nu_i/\beta}{\nu_i} \right) v_{th,i}^3 \int_0^\infty du u \left[\Psi_d(u_\beta) - u^2 \frac{T_i}{T_\beta} \Psi(u_\beta) \right] f_0, \quad (4.89)$$

with

$$\Psi_d(x) \equiv x \operatorname{erf}'(x). \quad (4.90)$$

Finally, the power lost because of fast ion losses is given by

$$p_{fil} \equiv \int d^3\mathbf{v} \frac{mv^2}{2} \hat{L}f_i. \quad (4.91)$$

Substituting Eq. 4.70 and using expansion Eq. 4.67 yields the following expression

$$p_{fil} = 4\pi\nu_i T_i v_{th,i}^3 \int du u^4 \frac{\Lambda_n}{\tau_{fil}} f_n, \quad (4.92)$$

with the Legendre moment of the loss function

$$\Lambda_n \equiv \frac{1}{2} \int_{-1}^1 d\lambda \Lambda_{fil}(u, \lambda) P_n(\lambda) = \Lambda_{0n}(u), \quad (4.93)$$

where Λ_{0n} refers to Eq. 4.79.

Chapter 5

On phase-space engineering using RF waves

After these technical chapters, we wish to discuss here the concept of engineering phase-space using radiofrequency waves. As recounted by Fisch [54], the original rationale for the use of RF waves was plasma heating, i.e. managing to irreversibly transfer a given amount of energy from an external generator to the plasma. In this case, the fine details of the wave-particle interactions occurring in the velocity space are of limited practical importance.

Since then, much progress has been done in this area. The general idea is that RF (and NBI systems, to some extent) offer a flexibility which can be exploited to influence an otherwise tightly coupled system. If experiments in present devices already feature a large amount of non-linear coupling phenomena between the various quantities characterizing the plasma, burning plasmas will be even more difficult to modify. On the other hand, using external power comes with a cost in terms of reactor efficiency, and thus obviously degrades the overall performance. Nevertheless, since the “natural” plasma state - or the state the plasma would reach in the absence of any external control (assuming such a state even exists in the first place) - can be sub-optimal in terms of fusion performance because of MHD instabilities, of turbulence or any other intrinsic process, it may be globally advantageous to spend some power to control it. This is already done in various devices, and will probably be done in future machines, if only to control the burn phase and possibly improve its efficiency.

It must be realized, however, that phase-space engineering is only possible to some extent. For instance, it is tempting to take this logic to the extreme, and confine the power production in an “optimal” location of phase space and recirculate part of this power to maintain the conditions necessary for the power production on the one hand, and extract another part of this power for net production on the other hand. This appealing idea actually made its appearance since the inception of fusion research, and motivated the design of many reactor concepts. However, Rider [15] has shown that although generating the fusion power by creating wildly out-of-equilibrium fuel populations could work in principle, the cost of reusing part of this power (recirculating) against collisions to maintain the out-of-equilibrium state was prohibitive.

Nevertheless, even in the confines of relatively conservative fusion reactor concepts, a lot of progress remains to be done and many possibilities still need to be explored. The advantage is that these ideas combine the progress towards the goal of energy-production by fusion with an indisputable physics interest. We describe here a few examples of such control involving radiofrequency waves with varying degrees of maturity.

5.1 LH-EC synergy

The presence of a toroidal current is a prerequisite for plasma equilibrium in a tokamak. Fisch and co-workers [55] have proposed that this current could be driven by RF waves, which has been a breakthrough since it made the steady-state operation of tokamaks a possibility. In this area, Tore Supra has had a pioneering role [26, 56] (see reprint in appendix E). RF current drive consists of influencing the electron population in an asymmetric fashion with respect to the parallel velocity in order to drive non-inductive current in tokamaks by 1) pushing preferentially the electron in one parallel direction with respect to the plasma current, 2) creating an asymmetric resistivity. The fact that a careful design of the wave spectrum is required to locally modify the kinetic properties of the electron distribution function in velocity space appears clearly when one employs the adjoint method [57, 58]. Dumont and Giruzzi [59] (see reprint in chapter E) have extended the adjoint technique to describe the so-called LH-EC synergy. Its principle is to exploit the enhanced parallel quasilinear diffusion on a pre-existing plateau created by LH waves to increase the originally modest EC current drive efficiency, a process which can be qualified as phase-space engineering. As a confirmation of the validity of this concept, the LH-EC synergy was simultaneously observed in steady-state discharges performed in the Tore Supra tokamak, and manifested itself by a 4-fold improvement of the “normal” EC efficiency in the presence of LH power [60]. Fig. 5.1(a) shows a calculation of the normalized EC current drive efficiency in the absence and in the presence of LH waves, illustrating the large efficiency enhancement which can be anticipated by having EC waves damp in the region of the LH quasilinear plateau [59, 61]. Fig. 5.1(b) shows the current deduced from measurements, compared to the predicted linear EC current [60].

The uncertainties related to the possibility of using LH waves in next-step fusion devices make the relevance of the LH-EC synergy for fusion reactors questionable. Nevertheless, the general concept of modeling a portion of the phase space with one type of wave or with externally injected energetic particles in order to influence the propagation/damping of another wave retains its attractiveness. A prime example is the third harmonic damping of ICRF waves in JET, which is only possible if a significant population of fast deuterons is already present in the plasma [62].

5.2 Heavy impurity control

One of the most important changes in fusion research in the last decade is that several devices have had their carbon walls replaced by metallic plasma facing component-based walls¹. One of the incentives for this modification is that tritium retention in carbon-

¹It should be noted that metallic walls were quite common in the early days of fusion research.

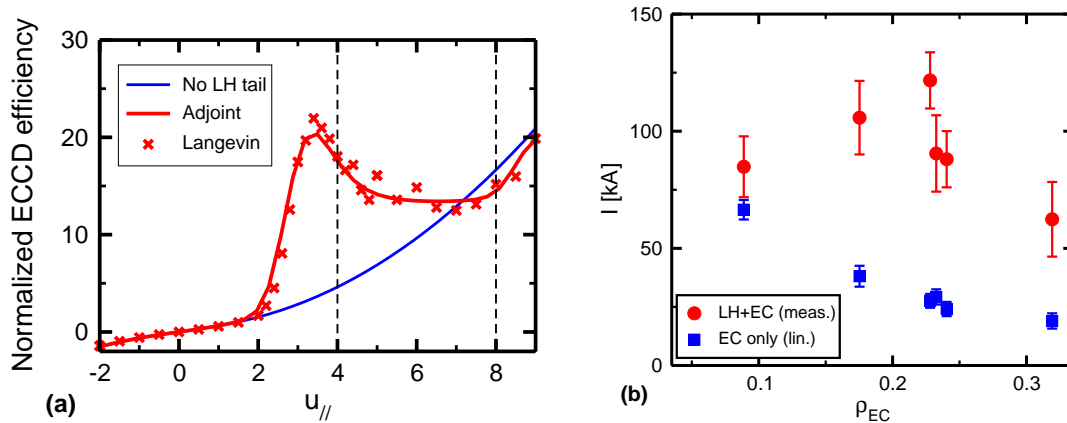


Figure 5.1: (a) Normalized ECCD efficiency computed by solving the adjoint equations (solid), and by numerical integration of the Langevin equations (crosses). Also shown is the Fisch-Boozer efficiency (thin line). (b) Measured additional current driven by EC waves in the presence of LH waves (dots) and computed linear EC current (squares) vs ρ_{EC} , location of maximum EC power deposition. Adapted from Ref. [61].

based elements is too large to be acceptable in a fusion reactor. In ASDEX Upgrade, a Tungsten (W) wall has been installed, whereas JET has been testing an ITER-relevant combination of tungsten/beryllium components. The consequences of these change have been quite profound. In terms of plasma operation, W has been observed to penetrate up to the plasma core in many situations. As a result, its density can sometimes peak near the magnetic axis until it radiates most of the discharge power [63].

In ASDEX Upgrade, central Electron Cyclotron Heating/Current Drive has been found to have a favorable impact on the W concentration [64]. This has been attributed to an enhanced level of anomalous particle diffusion combined with a density pump-out, which prevents density peaking and associated W accumulation. In JET, there is no EC system and the ICRF system must be used for impurity control. It has been found that at low levels of power, the IC system was responsible for enhanced impurity levels in the plasma, probably because of an increased W source². At higher power levels, however, locating the IC resonance in the vicinity of the magnetic axis has been found to slow down the impurity accumulation, or even prevent it from occurring. There is currently a lot of activity in this area but the most widespread interpretation is that the change in neoclassical transport caused by the fast ions is the dominant mechanism. This causes the inward particle pinch to either cancel or even revert [65–67]. It is likely that depending on the device and plasma parameters, a combination of changes in neoclassical and turbulent transport is responsible for the global dynamics of the heavy impurities in the discharge [68].

Concentrating on neoclassical transport, if we assume that the tungsten is in the Pfirsch-Schlüter regime of collisionality, and is located at a given location on a flux surface,

²Although to this day, this source has not been unambiguously identified.

one obtains for the neoclassical flux [65]

$$\langle \mathbf{\Gamma}_Z^{neo} \cdot \nabla r \rangle = \frac{e^2 n_i T_i}{\epsilon^2 m_i \Omega_i^2 \tau_{iZ} Z} \left[\frac{d \log p_i}{dr} - \left(\frac{3}{2} - 0.33 f_c \right) \frac{d \log T_i}{dr} \right], \quad (5.1)$$

with n_i , T_i , p_i the bulk ion density, temperature and pressure, respectively. Ω_i is the bulk ion cyclotron frequency. ϵ is the inverse aspect ratio of the considered flux surface. τ_{iZ} is the ion-impurity collision time, and f_c is the fraction of circulating ions.

Clearly, if

$$\eta_i \equiv \frac{d \log(T_i)}{d \log(n_i)} \gtrsim \frac{6}{1 + 2f_t}, \quad (5.2)$$

with f_t the fraction of trapped ions, the impurity flux is directed outward, i.e. impurities are chased away from the plasma core. Therefore, it is tempting to find methods to increase the temperature gradient at constant density. This is the idea behind the enhanced screening of minority ICRF ions: although there are by definition few such ions, the temperature resulting from the RF heating is such that temperature screening efficiency can become comparable to the temperature screening caused by the bulk ions [68].

In order to illustrate this effect, we consider here standard minority hydrogen heating in deuterium in JET [69]. Writing $\eta \equiv n_H/n_e$, retaining only the species-specific dependence in the neoclassical flux, and assuming for the sake of concision an homogeneous distribution of the heavy impurity, we obtain

$$\langle \mathbf{\Gamma}_Z^{neo} \cdot \nabla r \rangle \propto n_e \left[\frac{R}{L_n} \left(\frac{1-\eta}{v_{th,D}} + \frac{\eta}{v_{th,H}} \right) - \frac{1}{2} \left(\frac{1-\eta}{v_{th,D}} \frac{R}{L_{T,D}} + \frac{\eta}{v_{th,H}} \frac{R}{L_{T,H}} \right) \right], \quad (5.3)$$

with L_x the gradient length for quantity x . The latter expression has been obtained assuming the density profiles are proportional, and that the temperature is isotropic. This assumption is of course disputable since ICRF is known to induce strongly anisotropic distributions, but it is useful to produce semi-analytical estimates. We note that in the presence of fast hydrogen ions, the first term in the bracket is slightly reduced, which decreases the inward particle pinch. The most important effect is in the second term, since $R/L_{T,H}$ can be much larger than $R/L_{T,D}$.

In Fig. 5.2 is shown the contribution of deuterium and hydrogen ions in the temperature screening term of the neoclassical flux. Γ_T is defined as

$$\Gamma_T \equiv -\frac{n_i}{2v_{th,i}} \frac{R}{L_{T,i}}, \quad (5.4)$$

with i either deuterium or hydrogen. Γ_0 is the same term in the absence of hydrogen ions.

As n_H/n_e increases, the temperature screening caused by hydrogen ions increases much faster than the deuterium screening decreases. Minority screening can become comparable to the bulk ion screening, effectively doubling the net screening. This means that among other parameters, the minority concentration can play an important role in fine-tuning the scenario. It should be noted that these simulations are aimed at gaining some insight into the associated physics. Extensive modeling requires accounting for temperature anisotropy, neoclassical and anomalous transport for all species. MHD is known to play an important role in the impurity dynamics as well, but it is left out of this model [70]. To this day, a complete and clear physical picture and solid operational recipes still have to be established.

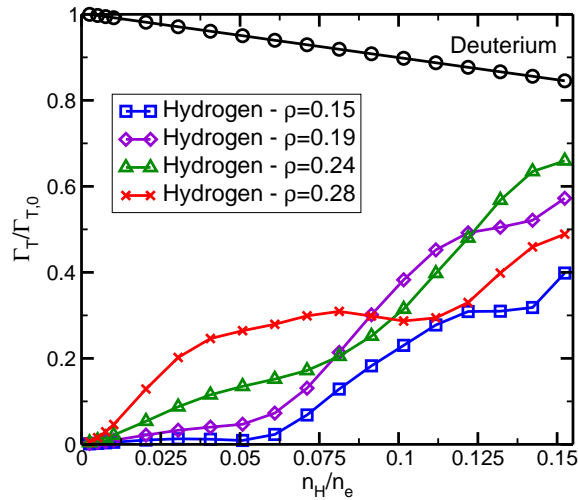


Figure 5.2: Ratio of the screening factors Γ of deuterium (black) and hydrogen ions at various normalized radii. Extract from Ref. [69].

5.3 MHD control

Controlling MHD events by external means has been an early priority in fusion research. As an illustration, the fact that energetic ions had a stabilizing effect on various MHD instabilities, among which the sawtooth, has been established many years ago [71–73]. By applying NBI or RF power, it is possible to increase the sawtooth period, which appears at first to be an appealing idea, since a very hot core is formed. The issue, however, is that the massive sawtooth crash which follows can have deleterious outcomes, such as the destabilization of Neoclassical Tearing Modes (NTM)³, much more detrimental to the global confinement than the sawteeth themselves [74]. In addition to this, it has been recognized that sawteeth may be sometimes desirable to evacuate heavy impurities from the plasma center, by degrading (to some extent) the core particle confinement. Therefore, flexible tools capable of modulating the sawtooth activity are desirable. Such tools include external power sources to tailor the fast ion population [75].

Initially, the process responsible for sawtooth destabilization has been attributed to shear variations in the vicinity of the $q = 1$ surface. This has triggered the development of advanced schemes consisting of driving localized current by means of EC waves [76, 77] or IC waves, using the rather subtle Ion Cyclotron Current Drive (ICCD) effect [78]. This necessitates the use of asymmetric antenna phasings, which are more prone to operational issues than the more classical dipole phasing. More recently, however, it has been established that energetic ions themselves could have either a stabilizing or a destabilizing effect, depending on the features of the corresponding distribution function [79, 80]. This has relaxed some of the constraints on the asymmetric antenna phasing, and allowed more classical RF conditions to be used to successfully control sawteeth [81, 82].

³We note that the process by which sawtooth crashes trigger NTM is, to this day, not completely explained.

Fig. 5.3 shows two JET discharges with similar conditions, in which the confining magnetic field and/or toroidal current are ramped in order to displace the IC resonance position with respect to the sawtooth inversion radius. A clear destabilization of the

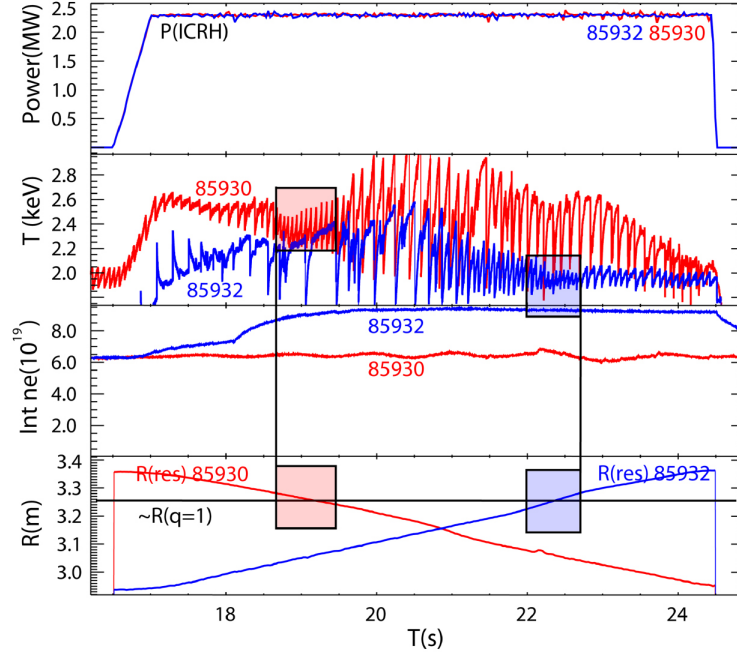


Figure 5.3: Two JET pulses employing dipole-phased ICRH in the absence of NBI power. Pulse 85930 (red) ramped down the toroidal magnetic field and toroidal current respectively from 2.7T to 2.33T and from 2.4MA to 2.1A. Pulse 85932 ramped in the exact opposite direction. The plot shows identical ICRH power, an ECE channel measuring the central temperature midway through the pulses (about 21s), the line integrated density and the resonance positions relative to an approximate position of the measured inversion radius. Small sawteeth and corresponding resonance positions are indicated in shaded boxes. Extract from Ref. [81].

sawteeth is observed when the resonance is in the vicinity of the $q = 1$ surface. The ICCD contribution has been estimated to be very low in these conditions (dipole phasing), which means that the predominant effect is the fast ion contribution to the MHD potential energy. So far, this scheme has not been completely validated for H-mode plasmas in JET. Nevertheless, the fact that the resonance location lies on the low field side of the plasma, the use of dipole phasing, and the larger than expected window of destabilization leads to a certain confidence that this scheme can be successfully applied to ITER.

This short presentation of sawtooth control using energetic ions is one example among a large variety of possible means to control various instabilities. Another notable example is the destabilization of various Alfvén Eigenmodes (AEs) by energetic ions, either alphas or originating from neutral beams [83,84]. ICRH ions are capable of this as well [85–88]. It should be mentioned here that energetic ions can also excite Energetic Particle Modes, i.e.

modes which are non-existent in the absence of fast ions, whereas AEs or other eigenmodes are always present in the discharge, albeit potentially stable [89].

5.4 Energetic Geodesic Acoustic Modes

Whereas the direct impact of turbulence on energetic particles (EPs) has been found to be limited [90], the influence of these particles on turbulence, on the other hand, has received relatively little attention so far. The possibility of controlling, to some extent, the creation and features of the fast ion populations opens the possibility of a potential action on an intrinsically self-regulated system involving turbulence, mean flows, zonal flows [91] and also higher frequency phenomena such as Geodesic Acoustic Modes (GAMs) [92]. Although the latter have an efficiency presumably smaller than stationary or low frequency flow shear generation mechanisms [93], they have been shown to play a central role in the L-H transition, which is believed to involve the same actors in the plasma edge [94].

The reason why GAMs are only observed in the plasma edge, however, is because they are subject to strong Landau damping and therefore cannot impact core turbulence in a stationary fashion. The possibility of overcoming this limitation by exciting similar modes with fast particles therefore represents an appealing prospect. In this case, the mode is usually referred to as an EGAM, and has been predicted theoretically [95,96] and unambiguously observed in experiments [97,98]. Recently, detailed numerical studies of the EGAMs properties [99] and their influence on turbulence [100] have been conducted in the framework of gyrokinetic simulations. Another advantage of EGAMs is that unlike GAMs which are non-linearly generated by the turbulence itself, the energetic particle sources can be tuned to some extent, and thus opens the possibility of a turbulence control in the plasma core.

Fig. 5.4(left) shows how the energetic ion source has been implemented in the gyrokinetic code GYSELA [100] to mimic, in the simplest way, the pumping of particles at a given parallel velocity v_0 to push them towards either larger or smaller velocities. With this simple source, EGAMs are successfully excited when this source is switched on, as shown in Fig. 5.4(right).

The appearance of EGAMs in the turbulence simulations has had unexpected consequences. After a first phase during which the turbulence level is spectacularly reduced and the subsequent transport is reduced as well, EGAMs have been observed to synchronize with the ITG turbulent structures, resulting in transport modulations at the EGAM frequency, and an overall increase of the heat transport [100]. This is shown in Fig. 5.5, in which $\chi_{E \times B}$ is shown versus time and minor radius. Three phases, denoted A, B and C are visible: (A) the EP source is applied to an established steady-state turbulence regime, (B) a transport barrier develops and (C) EGAMs and turbulence coexist and interact with each other in a non-trivial fashion.

This outcome has triggered further efforts: since regular GAMs have been shown to efficiently suppress turbulence, the link between GAM and EGAM has been studied in details [102]. The non-linear process responsible for the coupling between EGAM and ITG modes is currently under investigation. Further gyrokinetic simulations with more advanced sources, and including extensive parameter scans, are currently underway to

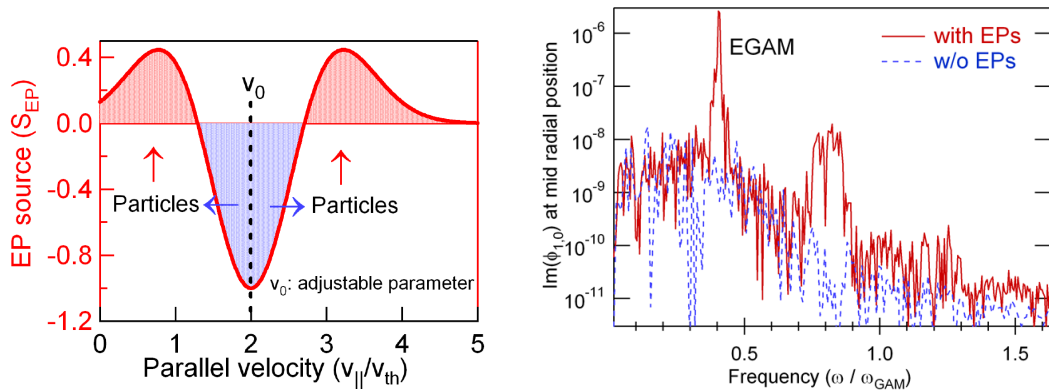


Figure 5.4: (Left) A schematic representation of the source of energetic particle versus normalized parallel velocity. (Right) Amplitude of the (1,0) component of the electric potential in the presence (red line) and in the absence of fast particles (blue, dotted line). Extract from Refs. [100,101].

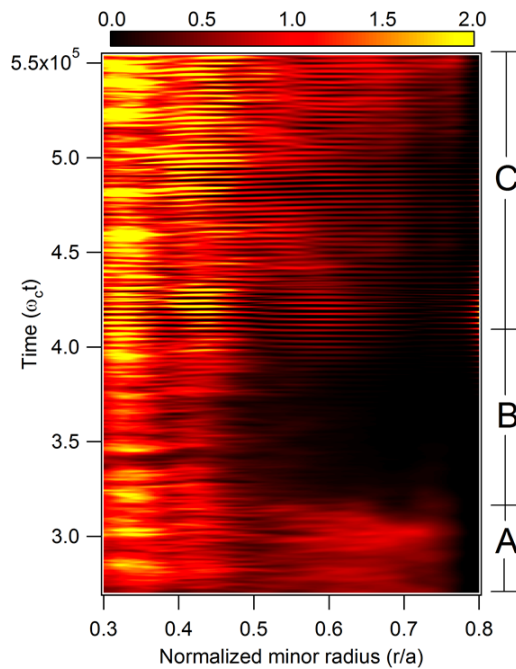


Figure 5.5: 2D representation of the $\mathbf{E} \times \mathbf{B}$ heat diffusivity versus normalized radius and time, showing the three phases discussed in the text. Extract from Ref. [100]

assess the generality of the obtained result.

5.5 Poloidal flow drive

The idea of directly impacting turbulence by using RF waves has been contemplated from the early 1990's [103]. Poloidal flow drive using RF waves stems from the fact that Ion Bernstein Waves (IBWs) excited by an external antenna have been observed to be capable of inducing profile modifications consistent with the triggering of Internal Transport Barriers (ITBs) [104,105]. In TFTR, using an IBW antenna, RF-induced flows have been unambiguously observed [106,107].

However, the direct excitation of IBW has proven very difficult, and its application on a reactor-class device is not envisaged at this stage. Another possible method to obtain IBWs and another suitable converted wave, the Ion Cyclotron Wave (ICW) [108,109], is to use a standard ICRF system, i.e. exciting the fast magnetosonic wave, and a plasma composition and RF parameters tuned so that efficient mode-conversion is achieved. Fig. 5.6(a) shows a full wave calculation of a DH(^3He) mode-conversion scenario in the Alcator C-mod tokamak. The Ion Cyclotron Wave lies above and below mid-plane, on the low field side of the conversion layer. This wave has the capability to drive a poloidal flow by exerting a poloidal force on the plasma species (Fig. 5.6(b)), shown here as a surface-averaged quantity [110].

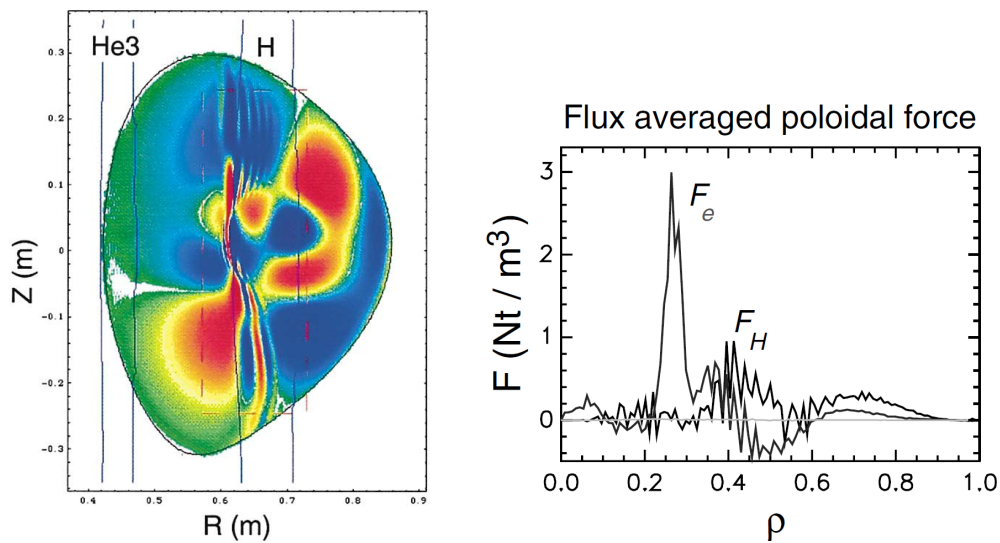


Figure 5.6: (Left) Real part of the perpendicular wave electric field computed by AORSA for a DH(^3He) mode-conversion ICRF scenario in Alcator C-Mod. (Right) Flux surface-averaged poloidal force on electrons and hydrogen ions with 1 MW of RF power absorbed. Extract from Ref. [110].

This promising concept has triggered an intense interest, both theoretically [46,111–113], and numerically [110,114]. The physical description of the processes at hand in-

volves a challenging mathematical analysis [46]. The basic idea is that the momentum conservation equation can be written as

$$m\partial_t\boldsymbol{\Gamma} + \nabla \cdot \boldsymbol{\Pi}_{\text{CGL}} - \mathbf{J} \times \mathbf{B} = \mathbf{F}, \quad (5.5)$$

with

$$\boldsymbol{\Gamma} \equiv \int d^3\mathbf{v} \mathbf{v} f. \quad (5.6)$$

$\boldsymbol{\Pi}_{\text{CGL}}$ is the secular part of the stress tensor, \mathbf{J} is the fluid current density and \mathbf{B} the equilibrium magnetic field. A careful analysis shows that \mathbf{F} , the secular force on the right hand side, may be rewritten in the form

$$\mathbf{F} = \mathbf{F}_{\text{reactive}}^{(0)} + \mathbf{F}_{\text{resistive}}^{(0)} + \mathbf{F}^{(1)}, \quad (5.7)$$

and contains “non-CGL” parts of the stress tensor. It turns out that $\mathbf{F}_{\text{reactive}}^{(0)}$, which can locally have a large amplitude, is an extension of the ponderomotive force deduced from cold plasma theory. It also flux surface-averages to zero, although a full consensus on this point has yet to be reached [113], and is therefore unable to induce any flow. $\mathbf{F}_{\text{resistive}}^{(0)}$, on the other hand, has a convenient expression when the electric field is expressed in the Fourier space

$$\mathbf{F}_{\text{resistive}}^{(0)} = \sum_{\mathbf{k}, \mathbf{k}'} \frac{\mathbf{k} + \mathbf{k}'}{4\omega} e^{i(\mathbf{k}' - \mathbf{k}) \cdot \mathbf{r}} (\mathbf{k} + \mathbf{k}') \mathbf{E}_{\mathbf{k}}^* \cdot \mathbf{W}^{(a)} \cdot \mathbf{E}_{\mathbf{k}'}, \quad (5.8)$$

where $\mathbf{E}_{\mathbf{k}}$ is the Fourier component corresponding to wavenumber \mathbf{k} and $\mathbf{W}^{(a)}$ is the anti-hermitian part of the generalized dielectric kernel introduced by D. Smithe [14]. It appears that $\mathbf{F}_{\text{resistive}}^{(0)} \sim \mathbf{k}\dot{W}/\omega$ where \dot{W} is the dissipated wave power, so that this term clearly corresponds to the wave momentum input. The last term in Eq. 5.7, not explicitly given here, does not correspond to any momentum input but can nevertheless drive bipolar poloidal sheared flows by redistributing the plasma momentum. Note that for the parameters chosen in the simulations presented in Ref. [115], it was found to be small compared to the direct momentum input term.

Recently, successful experiments have been performed in Alcator C-mod [116,117]. Interesting observations have also been made in JET [118]. As is often the case, however, the transposition to H-mode plasmas is far from straightforward, one element being that the RF power is usually small compared to the NBI power used to ensure the L-H transition. The number of experiments which have spent a substantial part of their program on this topic is somewhat limited, and certainly did not include scans in all possible parameters. Furthermore, central core heating to chase heavy impurities has become the priority for the RF systems installed in ongoing metallic-environment tokamaks, so that the time/power left for more prospective studies is rather limited. Nevertheless, the prospect of enhancing confinement by driving poloidal flows should motivate a continuous effort on both the experimental and theoretical sides. As for the latter, either a fluid, a gyrokinetic or a 6D turbulence code is the adapted tool to describe the (potential) impact of a RF driven flow on turbulence. It has been pointed out that some fluid models could be unable to treat this problem correctly [114]. Regardless of the kinetic or fluid treatment, the RF code must provide the corresponding non-linear force, a challenging task in itself. A practical

procedure to input the corresponding momentum source in turbulence codes still needs to be devised.

5.6 Alpha-channeling

Alpha-channeling essentially involves all the concepts discussed in these pages: waves, energetic particles, and also instabilities. Although the experimental evidence required to validate this idea is still only partial, and its practical implementation in a reactor has not been realized yet, it is elegant and the underlying physics is fascinating. The basic idea is rather simple: since the alphas have a birth energy of around 3.5MeV, well in excess of the critical velocity in magnetic fusion plasmas, they tend to slow down through collisions on the plasma electrons. On the other hand, fusion reactions require hot ions which are obtained by external heating, or in a burning plasma by energy equipartition with the electrons. These two processes have a cost in terms of efficiency, and devising a method to directly channel the free energy contained in the alpha particle population to the fuel ions, and thus increase fusion reactivity, is quite appealing. A total energy balance study has concluded that there was a clear benefit in terms of reactor economics [119]. From a practical point of view, this operation is done by employing waves to induce a diffusion of the alpha particles in energy space, corresponding to a diffusion in the radial direction [120]. Since they are born at high energies, the resulting distribution is characterized by a lower total energy, and the energy difference is employed for wave amplification. One has to find electromagnetic waves able to induce this velocity-space diffusion and be absorbed by the fuel ions.

Since the wave-particle resonance condition places stringent conditions on the type of wave which could accomplish such a task, it has been shown that the simultaneous use of two waves could significantly relax these conditions: one wave, with $\omega \sim \Omega_{c\alpha}$, breaks the adiabatic invariance of the alpha-particle motion and is thus able to extract its perpendicular energy, whereas the other one, with $\omega \ll \Omega_{c\alpha}$, transports it radially up to the plasma edge, decreasing its parallel energy in the process. Fisch has originally proposed to use a combination of a mode-converted IBW and a Toroidal Alfvén eigenmode [121,122]. The former decreases the alpha energy, whereas the latter displace the particles towards the edge at approximately constant energy. Therefore, the connection between high energy/plasma core - low energy/plasma edge is still ensured, and the constraints on the waves parameters are not as stringent as in the single wave case. Note that other modes, such as EGAMs could also be possible candidates to modify the particle energy with no little radial displacement, but this possibility remains at this stage entirely speculative. Nevertheless, this is an interesting prospect in the light of recent observations of EGAMs coexisting with Alfvén instabilities in ASDEX Upgrade [123].

In past and ongoing fusion experiments, it has not been possible to fully qualify the concept of alpha-channeling, most likely because the alpha population were/are too limited. In TFTR, however, important prerequisites have been successfully checked [54]. The first one is the “ k_{\parallel} flip” of the IBW. The second one is the wave-induced diffusion of energetic ions. Classical, quasilinear, estimates of the required power to channel the alpha energy before collisional relaxation could take place gave an estimate of 100MW of IBW

power, which represents a huge amount of circulating power even in a reactor. However, it was observed in the experiment that the induced diffusion was much larger than expected [124]. The proposed explanation was that the IBW was in fact exciting an internal eigenmode. Recently, Compressional Alfvén Eigenmodes have been identified as potential candidates for this enhanced transport in NSTX [125]. In any case, this observation has the practical consequence that the required power to channel the alpha energy could be much lower than initially predicted, thereby reinforcing the attractiveness of this concept. Hopefully, ITER will provide valuable information on the idea as a whole.

Chapter 6

Conclusions

Putting the history of magnetic fusion research into perspective is an interesting exercise in many respects. On the one hand, some devices have specialized in sustaining steady-state plasmas for long durations (Tore Supra, LHD. . .). On the other hand, two machines have demonstrated high DT fusion performance (TFTR and JET). Finally, by concentrating on scenario development and/or precise physics points, other devices have allowed progress to take place along these two paths. To some extent and in a simplified picture, ITER can be envisaged as a confluence between these two routes: high fusion performance and long duration discharges. To the plasma physicist, one of the main differences between ITER and its predecessors is the fact that it will shelter a burning plasma, i.e. a plasma which requires little external power input to maintain fusion reactions.

Whereas a burning plasma is a necessary condition for an efficient reactor, the drawback is that it is also by nature a highly coupled system, which makes it difficult to control. And even assuming that it is possible to devise a reactor which is able to self-sustain without any control, it may not be optimal in terms of fusion performance. In other words, for the same plasma (or say, quantity of fusion fuel), it would be possible to extract more fusion power if, for instance, heat transport was reduced compared to its “design” value, or if the radiated power level was lower. In this respect, the role of RF waves is progressively shifting from being a mere channel through which electrical power is irreversibly transferred from an external generator to the plasma core, to a sophisticated control method aimed at influencing its properties. This can be done either directly, or creating/maintaining/modifying energetic particle populations which, in turn, impact the discharge properties.

In this manuscript, we have focused on a detailed description of how a common mathematical framework can be used to self-consistently describe both the electromagnetic wave propagation and the secular modifications of the distribution functions. This was done by showing that under the action of a given electromagnetic field, an expression for the linear Hamiltonian response could be deduced with a well-controlled degree of approximation (chapter 2). In chapter 3, this response has been embedded in a variational principle, which allows the electromagnetic field to be computed for a set of given plasma conditions. In order to obtain the plasma response to the wave propagation and damping, a typical simplification consists of considering the wavefield as a given, i.e. resulting from the linear response, and solve a quasilinear equation. The Hamiltonian framework directly provides

this time- and space-averaged Fokker-Planck equation, as illustrated in chapter 4.

In these technical parts, we have chosen to specialize on ICRF waves, assuming that a second order expansion in Larmor radius was valid. The resulting expressions have been implemented in a numerically efficient full wave code, named EVE. In the same vein, various simplifications have been used in chapter 4 and lead to the “classical” quasi-local expressions for the quasilinear diffusion coefficient obtained by different methods. It should be realized, however, that the same mathematical framework can be applied to different problems as well. For instance, higher frequency waves can be described by adapting the level of approximation of the Hamiltonian response. Extending the EVE code to LH waves could be done with reasonable effort. It was not shown in these pages, but EVE has also been successfully used to describe waves in the Alfvén range of frequencies.

Finally a selected set of topical problems for fusion in general, all involving RF waves, has been briefly presented in chapter 5. They all aim, to various extent, at modifying the phase-space characteristics in order to improve the overall current drive efficiency (LH-EC synergy), influence particle transport (heavy impurity control), stabilize or destabilize MHD instabilities and thus impact the global discharge properties (MHD control), destabilize chosen classes of kinetic instabilities in an attempt to control turbulence (EGAMs), drive sheared plasma rotation (poloidal flow drive) or channel the immense amount of free energy contained in the fusion alpha particles to fuel ions (alpha-channeling).

We have opted for a rather detailed presentation of a mathematical framework, along with the subsequent derivation of expressions usable in simulations codes. However, in the domain of RF heating of fusion plasmas, there is a continuous need for direct comparisons to experiments either to interpret observations (which range from such “basic” measurements as the diamagnetic energy increase resulting from RF heating to sophisticated ones such as fast ion losses measurements or phase-contrast imagery) or to bridge gaps in the available diagnostics, including during an experimental session. Along the same idea, among the attached publications, we chose to retain theoretically-oriented as well as experimentally-oriented ones: a continuous interaction between theory, simulation and experiments is a necessary condition for the success of fusion research.

Appendix A

Geometry

A great deal of the prescriptions for the geometry and magnetic field configuration in these pages is inspired from the MHD codes HELENA, CASTOR and MISHKA [126]. It has been kept as general as possible to be able to handle any toroidal 2D equilibrium. It is also designed with the perspective of being extended from 2D to 3D geometry in a relatively straightforward fashion.

A.1 Toroidal coordinates

The reference coordinates system is the lab basis $(\hat{X}, \hat{Y}, \hat{Z})$ (see Fig. A.1).

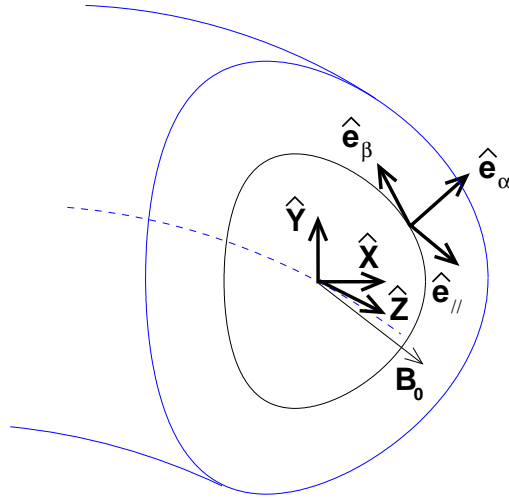


Figure A.1: Lab $(\hat{X}, \hat{Y}, \hat{Z})$ and Stix $(\mathbf{e}_\alpha, \mathbf{e}_\beta, \mathbf{e}_\parallel)$ bases in toroidal geometry.

Owing to the symmetries of the system, a more natural system of coordinates in quasi-periodic fusion devices is (s, θ, ϕ) with s the radial coordinate (proportional to the square root of the poloidal flux: $s \propto \psi^{1/2}$), the poloidal angle θ and the toroidal angle ϕ .

For a given vector $\mathbf{X} \equiv x\hat{X} + y\hat{Y} + z\hat{Z}$, defining $D \equiv \partial_s x \partial_\theta y - \partial_\theta x \partial_s y$, the three

contravariant basis vectors are given by

$$\begin{cases} \mathbf{e}^s \equiv \nabla s = (\partial_\theta y \hat{X} - \partial_\theta x \hat{Y})/D, \\ \mathbf{e}^\theta \equiv \nabla \theta = (-\partial_s y \hat{X} + \partial_s x \hat{Y})/D, \\ \mathbf{e}^\phi \equiv \nabla \phi = \hat{Z}/R, \end{cases} \quad (\text{A.1})$$

where $R \equiv R_0 + X$, with R_0 the distance between the torus main symmetry axis and the origin of the reference coordinate system. The associated metric elements are given by

$$\begin{cases} g^{11} = |\nabla s|^2 = [(\partial_\theta x)^2 + (\partial_\theta y)^2]/D^2, \\ g^{12} = g^{21} = \nabla s \cdot \nabla \theta = -[\partial_s x \partial_\theta x + \partial_s y \partial_\theta y]/D^2, \\ g^{22} = |\nabla \theta|^2 = [(\partial_s x)^2 + (\partial_s y)^2]/D^2, \\ g^{13} = g^{23} = g^{31} = g^{32} = 0, \\ g^{33} = 1/R^2. \end{cases} \quad (\text{A.2})$$

The reciprocal Jacobian is given by

$$\frac{1}{J} = \mathbf{e}^s \cdot (\mathbf{e}^\theta \times \mathbf{e}^\phi) = \frac{1}{RD}. \quad (\text{A.3})$$

The associated covariant basis is given by

$$\begin{cases} \mathbf{e}_s \equiv J \nabla \theta \times \nabla \phi = \partial_s x \hat{X} + \partial_s y \hat{Y}, \\ \mathbf{e}_\theta \equiv J \nabla \phi \times \nabla s = \partial_\theta x \hat{X} + \partial_\theta y \hat{Y}, \\ \mathbf{e}_\phi = R \hat{Z}. \end{cases} \quad (\text{A.4})$$

The covariant metric elements can thus be deduced

$$\begin{cases} g_{11} = (J/R)^2 |\nabla \theta|^2 = (\partial_s x)^2 + (\partial_s y)^2, \\ g_{12} = g_{21} = -(J/R)^2 \nabla s \cdot \nabla \theta = \partial_s x \partial_\theta x + \partial_s y \partial_\theta y, \\ g_{22} = (J/R)^2 |\nabla s|^2 = (\partial_\theta x)^2 + (\partial_\theta y)^2, \\ g_{13} = g_{23} = g_{31} = g_{32} = 0, \\ g_{33} = R^2. \end{cases} \quad (\text{A.5})$$

A.2 Magnetic equilibrium

In the system of coordinates described in the previous section, the axisymmetric confining magnetic field can be conveniently written as

$$\mathbf{B}_0 = \nabla \phi \times \nabla \psi + F \nabla \phi, \quad (\text{A.6})$$

where $F \equiv F(\psi)$ is the toroidal flux function. On the other hand, the poloidal flux ψ is related to the radial coordinate by the relation $\nabla \psi \equiv f(s) \nabla s$, with f the poloidal flux function. fJ is the Jacobian of the (ψ, θ, ϕ) coordinates system. The coordinates of the magnetic field are given by

$$B_0^1 \equiv \mathbf{B}_0 \cdot \mathbf{e}^s = 0, \quad B_{01} \equiv \mathbf{B}_0 \cdot \mathbf{e}_s = g_{12} \frac{f}{J}, \quad (\text{A.7})$$

$$B_0^2 \equiv \mathbf{B}_0 \cdot \mathbf{e}^\theta = \frac{f}{J}, \quad B_{02} \equiv \mathbf{B}_0 \cdot \mathbf{e}_\theta = g_{22} \frac{f}{J}, \quad (\text{A.8})$$

and

$$B_0^3 \equiv \mathbf{B}_0 \cdot \mathbf{e}^\phi = \frac{F}{R^2}, \quad B_{03} \equiv \mathbf{B}_0 \cdot \mathbf{e}_\phi = F. \quad (\text{A.9})$$

The total magnetic field magnitude is

$$B_0 = \left(g_{22} \frac{f^2}{J^2} + \frac{F^2}{R^2} \right)^{1/2}. \quad (\text{A.10})$$

The toroidal field is directed along \hat{Z} and its magnitude is given by

$$B_t = \frac{F}{R}, \quad (\text{A.11})$$

and the poloidal field magnitude is given by

$$B_p = g_{22}^{1/2} \frac{f}{J}. \quad (\text{A.12})$$

The relation between the safety factor q and the poloidal flux function f is obtained by writing

$$dl_p = \frac{B_p}{B_t} dl_t, \quad (\text{A.13})$$

with l_p (resp. l_t) the poloidal (resp. toroidal) projection of the considered field line. On the other hand, $dl_t = Rq d\theta$ yields

$$q = \frac{1}{2\pi} \oint dl_p \frac{B_t}{RB_p} = \frac{F}{2\pi f} \oint dl_p \frac{J}{R^2 g_{22}^{-1/2}}. \quad (\text{A.14})$$

The poloidal arc-length is given by

$$dl_p = \sqrt{(\partial_\theta x)^2 + (\partial_\theta y)^2} d\theta = g_{22}^{1/2} d\theta, \quad (\text{A.15})$$

which gives

$$q = \frac{F}{2\pi f} \int_0^{2\pi} d\theta \frac{J}{R^2}. \quad (\text{A.16})$$

Of course, if q is directly available, rather than f , the latter expression can be inverted to deduce f .

The toroidal flux inside magnetic surface ψ is obtained by integrating the magnetic field over the whole poloidal section limited by $s = s(\psi)$, i.e.

$$\Phi_t \equiv \int d^2\mathbf{S} \cdot \mathbf{B}_0, \quad (\text{A.17})$$

with

$$d^2\mathbf{S} \equiv \int ds d\theta J \nabla \phi, \quad (\text{A.18})$$

so that

$$\Phi_t = \int ds d\theta \frac{JF}{R^2}. \quad (\text{A.19})$$

Note that if the equilibrium is provided in Straight Field Line coordinates, i.e.

$$q(\psi) = \frac{JF}{fR^2}, \quad (\text{A.20})$$

Eq. A.19 yields

$$\Phi_t = 2\pi \int d\psi q(\psi), \quad (\text{A.21})$$

where the fact that both f and q are flux functions has been taken into account.

Along the same lines, the poloidal flux is given

$$\Phi_p \equiv \int d\phi ds J \nabla \theta \cdot \mathbf{B}_0, \quad (\text{A.22})$$

which, in the case of an axisymmetric equilibrium, allows one to recover

$$\Phi_p \equiv \int 2\pi ds f(s) = 2\pi\psi(s). \quad (\text{A.23})$$

A.3 Local magnetic frames

In kinetic problems, it is convenient to resort to orthogonal reference systems having the third direction along the confining magnetic field. Given the freedom of choices of the two other ones, we will use the normal to the flux surface. The three vectors defining the Stix frame [11] are defined as (see Fig. A.1)

$$\begin{cases} \mathbf{e}_\alpha \equiv \nabla s / |\nabla s|, \\ \mathbf{e}_\beta \equiv \mathbf{e}_\parallel \times \mathbf{e}_\alpha, \\ \mathbf{e}_\parallel \equiv \mathbf{B}_0 / B_0. \end{cases} \quad (\text{A.24})$$

EVE solves for the variables $(u_1, u_2, u_3, u_4) \equiv (sA_\alpha, sA_\beta, A_\parallel, \varphi/c)$. The first two components are multiplied by s in order to obtain a well-behaved solution at the origin and facilitate the implementation of the boundary conditions.

To transform the potential vector \mathbf{A} coordinates between the lab frame and the Stix frame, the following matrices are introduced:

1. $(\mathbf{e}_\alpha, \mathbf{e}_\beta, \mathbf{e}_\parallel) \rightarrow (\mathbf{e}_s, \mathbf{e}_\theta, \mathbf{e}_\phi)$: $U_{i\sigma} \equiv \mathbf{e}_i \cdot \mathbf{e}_\sigma$ with

$$\begin{pmatrix} A_s \\ A_\theta \\ A_\phi \end{pmatrix} = U_{i\sigma} \begin{pmatrix} A_\alpha \\ A_\beta \\ A_\sigma \end{pmatrix} = \bar{U}_{i\sigma} \begin{pmatrix} u_1 \\ u_2 \\ u_3 \end{pmatrix}, \quad (\text{A.25})$$

with elements

$$U_{11} = \frac{1}{|\nabla s|}, \quad U_{12} = \frac{Fg_{12}}{JB_0|\nabla s|}, \quad U_{13} = \frac{fg_{12}}{JB_0}, \quad (\text{A.26})$$

$$U_{21} = 0, \quad U_{22} = \frac{Fg_{22}}{JB_0|\nabla s|}, \quad U_{23} = \frac{fg_{22}}{JB_0}, \quad (\text{A.27})$$

$$U_{31} = 0, \quad U_{32} = -\frac{f}{B_0}|\nabla s|, \quad U_{33} = \frac{F}{B_0}. \quad (\text{A.28})$$

Also

$$\begin{cases} \bar{U}_{i\sigma} = U_{i\sigma}/s & \text{for } (i, \sigma) = (1 \dots 3, 1 \dots 2), \\ \bar{U}_{i\sigma} = U_{i\sigma} & \text{otherwise.} \end{cases} \quad (\text{A.29})$$

2. $(\mathbf{e}_\alpha, \mathbf{e}_\beta, \mathbf{e}_\parallel) \rightarrow (\mathbf{e}^s, \mathbf{e}^\theta, \mathbf{e}^\phi)$: $U_\sigma^i \equiv \mathbf{e}^i \cdot \mathbf{e}_\sigma$ with

$$\begin{pmatrix} A^s \\ A^\theta \\ A^\phi \end{pmatrix} = U_\sigma^i \begin{pmatrix} A_\alpha \\ A_\beta \\ A_\parallel \end{pmatrix} = \bar{U}_\sigma^i \begin{pmatrix} u_1 \\ u_2 \\ u_3 \end{pmatrix}, \quad (\text{A.30})$$

with elements

$$JU_1^1 = J|\nabla s|, \quad JU_2^1 = 0, \quad JU_3^1 = 0, \quad (\text{A.31})$$

$$JU_1^2 = J\frac{g^{21}}{|\nabla s|}, \quad JU_2^2 = \frac{F}{B_0|\nabla s|}, \quad JU_3^2 = \frac{f}{B_0}, \quad (\text{A.32})$$

$$JU_1^3 = 0, \quad JU_2^3 = -\frac{fg_{22}}{JB_0|\nabla s|}, \quad JU_3^3 = J\frac{F}{R^2B_0}, \quad (\text{A.33})$$

and

$$\begin{cases} \bar{U}_\sigma^i = U_\sigma^i/s & \text{for } (i, \sigma) = (1 \dots 3, 1 \dots 2), \\ \bar{U}_\sigma^i = U_\sigma^i & \text{otherwise.} \end{cases} \quad (\text{A.34})$$

The Stix frame has the advantage of making the formulation and implementation of the boundary conditions relatively simple. On the other hand, it is ill-defined as $s \rightarrow 0$ and can entail poor numerical convergence. Jaeger et al. [127] have therefore introduced an alternative basis $(\mathbf{e}_{\perp 1}, \mathbf{e}_{\perp 2}, \mathbf{e}_\parallel)$ to describe the unperturbed particle motion with

$$\mathbf{e}_{\perp 1} \equiv \frac{\hat{X} - (\hat{X} \cdot \mathbf{e}_\parallel)\mathbf{e}_\parallel}{|\hat{X} - (\hat{X} \cdot \mathbf{e}_\parallel)\mathbf{e}_\parallel|}, \quad (\text{A.35})$$

$$\mathbf{e}_{\perp 2} \equiv \mathbf{e}_\parallel \times \mathbf{e}_{\perp 1}, \quad (\text{A.36})$$

and

$$\mathbf{e}_\parallel \equiv \mathbf{B}_0/B_0. \quad (\text{A.37})$$

In order to express the field in rotating components, it is also useful to introduce the complex basis vectors

$$\mathbf{e}_\pm \equiv \frac{\mathbf{e}_{\perp 1} \mp i\mathbf{e}_{\perp 2}}{2}. \quad (\text{A.38})$$

These unit vectors do not suffer any singularity at the origin and reduce to the lab reference frame when the poloidal magnetic field is zero [127].

The associated transformation matrices are given by

1. $(\mathbf{e}_{\perp 1}, \mathbf{e}_{\perp 2}, \mathbf{e}_{\parallel}) \rightarrow (\mathbf{e}_s, \mathbf{e}_\theta, \mathbf{e}_\phi)$: $T_{i\sigma} \equiv \mathbf{e}_i \cdot \mathbf{e}_\sigma$ with

$$\begin{pmatrix} A_s \\ A_\theta \\ A_\phi \end{pmatrix} = T_{i\sigma} \begin{pmatrix} A_{\perp 1} \\ A_{\perp 2} \\ A_{\parallel} \end{pmatrix}, \quad (\text{A.39})$$

2. $(\mathbf{e}_{\perp 1}, \mathbf{e}_{\perp 2}, \mathbf{e}_{\parallel}) \rightarrow (\mathbf{e}^s, \mathbf{e}^\theta, \mathbf{e}^\phi)$: $T_\sigma^i \equiv \mathbf{e}^i \cdot \mathbf{e}_\sigma$ with

$$\begin{pmatrix} A^s \\ A^\theta \\ A^\phi \end{pmatrix} = T_\sigma^i \begin{pmatrix} A_{\perp 1} \\ A_{\perp 2} \\ A_{\parallel} \end{pmatrix}, \quad (\text{A.40})$$

with, for the first column

$$JT_1^1 = \frac{R\partial_\theta y}{\sqrt{1-b_x^2}}, \quad JT_1^2 = \frac{-1}{\sqrt{1-b_x^2}} \left(R\partial_s y + b_x \frac{f}{B_0} \right), \quad JT_1^3 = -\frac{b_x}{\sqrt{1-b_x^2}} \frac{JF}{R^2 B_0}. \quad (\text{A.41})$$

The covariant elements on the first columns are obtained by writing

$$JT_{i1} = \sum_k g_{ik} JT_1^k. \quad (\text{A.42})$$

$$T_{12} = \frac{F}{RB_0} \frac{\partial_s y}{\sqrt{1-b_x^2}}, \quad T_{22} = \frac{F}{RB_0} \frac{\partial_\theta y}{\sqrt{1-b_x^2}}, \quad T_{32} = -\frac{fR}{B_0 J} \frac{\partial_\theta y}{\sqrt{1-b_x^2}}. \quad (\text{A.43})$$

The corresponding contravariant column is given by

$$JT_2^i = J \sum_k g^{ik} T_{k2}. \quad (\text{A.44})$$

Finally, for the third column

$$JT_3^1 = 0, \quad JT_3^2 = \frac{f}{B_0}, \quad JT_3^3 = \frac{JF}{B_0 R^2}, \quad (\text{A.45})$$

and

$$JT_{i3} = \sum_k g_{ik} JT_3^k. \quad (\text{A.46})$$

In these expressions, we have used $b_x \equiv \mathbf{B}_0 \cdot \hat{X}/B_0$, giving

$$b_x = \frac{f}{JB_0} \partial_\theta x. \quad (\text{A.47})$$

Other useful elements related to rotating components are

$$T_\pm^i \equiv \mathbf{e}^i \cdot \mathbf{e}_\mp = \frac{T_1^i \pm iT_2^i}{2}. \quad (\text{A.48})$$

It is worth noting that

$$(T_\pm^i)^* \equiv \mathbf{e}^i \cdot (\mathbf{e}_\mp)^* = (T_\mp^i). \quad (\text{A.49})$$

A last useful matrix is needed to perform the transformation $(\mathbf{e}_\alpha, \mathbf{e}_\beta) \rightarrow (\mathbf{e}_{\perp 1}, \mathbf{e}_{\perp 2})$:

$$\begin{pmatrix} A_{\perp 1} \\ A_{\perp 2} \end{pmatrix} = R_{i\sigma} \begin{pmatrix} A_\alpha \\ A_\beta \end{pmatrix} = \bar{R}_{i\sigma} \begin{pmatrix} u_1 \\ u_2 \end{pmatrix}, \quad (\text{A.50})$$

with elements

$$R_{11} = \frac{R}{J|\nabla s|} \frac{1}{\sqrt{1-b_x^2}} \partial_\theta y, \quad R_{12} = \frac{R}{J|\nabla s|} \frac{b_z}{\sqrt{1-b_x^2}} \partial_\theta x, \quad (\text{A.51})$$

$$R_{21} = -\frac{R}{J|\nabla s|} \frac{b_z}{\sqrt{1-b_x^2}} \partial_\theta x, \quad R_{22} = \frac{R}{J|\nabla s|} \frac{1}{\sqrt{1-b_x^2}} \partial_\theta y, \quad (\text{A.52})$$

with

$$b_z \equiv \frac{\mathbf{B}_0 \cdot \hat{Z}}{B_0} = \frac{F}{B_0 R}. \quad (\text{A.53})$$

Also

$$\bar{R}_{i\sigma} = R_{i\sigma}/s \text{ for } (i, \sigma) = (1 \dots 2, 1 \dots 2). \quad (\text{A.54})$$

Finally, we define

$$R_+ \equiv \mathbf{e}_\alpha \cdot \mathbf{e}_- = \frac{R_{1\alpha} + iR_{2\alpha}}{2}, \quad R_- \equiv \mathbf{e}_\alpha \cdot \mathbf{e}_+ = \frac{R_{1\alpha} - iR_{2\alpha}}{2}, \quad (\text{A.55})$$

and

$$\bar{R}_+ \equiv R_+/s, \quad \bar{R}_- \equiv R_-/s. \quad (\text{A.56})$$

It is readily deduced that

$$\mathbf{e}_\beta \cdot \mathbf{e}_- = iR_+, \quad \mathbf{e}_\beta \cdot \mathbf{e}_+ = -iR_-. \quad (\text{A.57})$$

Also, one may note that

$$(\bar{R}_\pm)^* = \bar{R}_\mp. \quad (\text{A.58})$$

A.4 Cylindrical geometry

In many instances, it is useful to operate the code in cylindrical geometry. This is often done by setting a large value to R_0/a_0 but in this case, all other quantities (toroidal wavenumber...) have to be rescaled accordingly. Also, this induces small terms in the geometric elements which can lead to numerical problems in the course of the calculation. This is why the possibility of using a true cylindrical geometry has been introduced. In this case, the equilibrium is given by

$$\begin{cases} x = R_0 + a_0 s \cos(\theta), \\ y = a_0 s \sin(\theta), \\ z = R_0 \phi \end{cases} \quad (\text{A.59})$$

The Jacobian is given by

$$J = R_0 D, \quad (\text{A.60})$$

with

$$D = a_0^2 s. \quad (\text{A.61})$$

For the contravariant basis vectors, we obtain

$$\mathbf{e}^s = \nabla s = \frac{1}{a_0} (\cos(\theta) \hat{X} + \sin(\theta) \hat{Y}), \quad (\text{A.62})$$

$$\mathbf{e}^\theta = \nabla \theta = \frac{1}{a_0 s} (-\sin(\theta) \hat{X} + \cos(\theta) \hat{Y}), \quad (\text{A.63})$$

$$\mathbf{e}^\phi = \nabla \phi = \frac{1}{R_0} \hat{Z}. \quad (\text{A.64})$$

The only non-zero terms of the contravariant metric tensor are given by

$$g^{11} = \frac{1}{a_0^2}, \quad g^{22} = \frac{1}{a_0^2 s^2}, \quad g^{33} = \frac{1}{R_0^2}. \quad (\text{A.65})$$

The covariant basis vectors are

$$\mathbf{e}_s = a_0 (\cos(\theta) \hat{X} + \sin(\theta) \hat{Y}), \quad (\text{A.66})$$

$$\mathbf{e}_\theta = a_0 s (-\sin(\theta) \hat{X} + \cos(\theta) \hat{Y}), \quad (\text{A.67})$$

$$\mathbf{e}_\phi = R_0 \hat{Z}, \quad (\text{A.68})$$

with corresponding non-zero terms in the metric tensor

$$g_{11} = a_0^2, \quad g_{22} = a_0^2 s^2, \quad g_{33} = R_0^2. \quad (\text{A.69})$$

The expressions (A.7), (A.8) and (A.9) are still valid. In the specific case of the cylindrical geometry under consideration, they can be simplified as

$$B_0^1 \equiv \mathbf{B}_0 \cdot \mathbf{e}^s = 0, \quad B_{01} \equiv \mathbf{B}_0 \cdot \mathbf{e}_s = 0, \quad (\text{A.70})$$

$$B_0^2 \equiv \mathbf{B}_0 \cdot \mathbf{e}^\theta = \frac{f}{R_0 a_0^2 s}, \quad B_{02} \equiv \mathbf{B}_0 \cdot \mathbf{e}_\theta = \frac{s f}{R_0}, \quad (\text{A.71})$$

and

$$B_0^3 \equiv \mathbf{B}_0 \cdot \mathbf{e}^\phi = \frac{F}{R_0}, \quad B_{03} \equiv \mathbf{B}_0 \cdot \mathbf{e}_\phi = F. \quad (\text{A.72})$$

The total magnetic field magnitude is

$$B_0 = \frac{1}{R_0} \left(F^2 + \frac{f^2}{a_0^2} \right)^{1/2}. \quad (\text{A.73})$$

The toroidal field is directed along \hat{Z} and its magnitude is given by

$$B_t = \frac{F}{R_0}, \quad (\text{A.74})$$

and the poloidal field magnitude is given by

$$B_p = \frac{f}{R_0 a_0}. \quad (\text{A.75})$$

Eq. A.16 yields

$$q = \frac{a_0^2 F_s}{R_0 f}, \quad (\text{A.76})$$

showing that we have $q = rB_t/(RB_p)$, which is consistent with the expression usually employed in a cylinder.

Appendix B

Plasma functional: numerical implementation

B.1 Adiabatic functional

The adiabatic plasma functional, Eq. 3.52, is relatively straightforward to implement. For a distribution even with respect to v_{\parallel} , it can be written in terms of the state vector elements as

$$\mathcal{L}_{part,s}^{(adiab)} = \epsilon_0 \int ds d\theta d\phi J \omega_{ps}^2 \left\{ \frac{m_s c^2}{T_s} \chi_0(\mathbf{r}) u_4 u_4^* + \chi_1(\mathbf{r}) (\bar{R}_{11}^2 + \bar{R}_{12}^2) (u_1 u_1^* + u_2 u_2^*) \right\}, \quad (\text{B.1})$$

with \bar{R}_{11} and \bar{R}_{12} given by expressions A.51. We have also used $R_{22} = R_{11}$ and $R_{21} = -R_{22}$. This directly yields the following master elements:

$$\Theta_{p,11,m\bar{m}}^{(00)} = \Theta_{p,22,m\bar{m}}^{(00)} = \omega_{ps}^2 \left(J \chi_1 (\bar{R}_{11}^2 + \bar{R}_{12}^2) \right)_{\bar{m}-m}, \quad (\text{B.2})$$

and

$$\Theta_{p,44,m\bar{m}}^{(00)} = \omega_{ps}^2 \frac{m_s c^2}{T_s} \left(J \chi_0 \right)_{\bar{m}-m}, \quad (\text{B.3})$$

all other being zero. χ_0 and χ_1 are given by Eqs. 3.53 and 3.54, respectively.

B.2 Resonant functional

Second order FLR expression

From (2.100), it appears that δH_L may be expressed as an inner product (see Defs. A.56):

$$\delta H_L = q_s \bar{\mathcal{H}}_{Lk} u_k, \quad (\text{B.4})$$

with

$$\bar{\mathcal{H}}_{Lk} \equiv \begin{pmatrix} -v_{\perp} (\delta_{L,-1} \bar{R}_{-} + \delta_{L,1} \bar{R}_{+}) \\ i v_{\perp} (\delta_{L,-1} \bar{R}_{-} - \delta_{L,1} \bar{R}_{+}) \\ -v_{\parallel} \delta_{L,0} \\ c \delta_{L,0} \end{pmatrix}, \quad (\text{B.5})$$

or equivalently

$$\bar{\mathcal{H}}_{Lk} = v_{\perp}^{(\delta_{k,1}+\delta_{k,2})} v_{\parallel}^{\delta_{k,3}} c^{\delta_{k,4}} \begin{pmatrix} -(\delta_{L,-1}\bar{R}_{-} + \delta_{L,1}\bar{R}_{+}) \\ i(\delta_{L,-1}\bar{R}_{-} - \delta_{L,1}\bar{R}_{+}) \\ -\delta_{L,0} \\ \delta_{L,0} \end{pmatrix}. \quad (\text{B.6})$$

We may write

$$\frac{\nabla_{+}^{k_{+}} \nabla_{-}^{k_{-}}}{k_{+}! k_{-}!} \delta H_L = q_s \sum_{k'_{+}=0}^{k_{+}} \sum_{k'_{-}=0}^{k_{-}} \left\{ \frac{\nabla_{+}^{k_{+}-k'_{+}}}{(k_{+}-k'_{+})!} \frac{\nabla_{-}^{k_{-}-k'_{-}}}{(k_{-}-k'_{-})!} \bar{\mathcal{H}}_{Lk} \right\} \frac{\nabla_{+}^{k'_{+}} \nabla_{-}^{k'_{-}}}{k'_{+}! k'_{-}!} u_k. \quad (\text{B.7})$$

Letting

$$\mathcal{H}_{Lk}^{d_{+},d_{-}} \equiv \begin{pmatrix} -(\delta_{L,-1} \nabla_{+}^{d_{+}} \nabla_{-}^{d_{-}} \bar{R}_{-} / (d_{+}! d_{-}!) + \delta_{L,1} \nabla_{+}^{d_{+}} \nabla_{-}^{d_{-}} \bar{R}_{+} / (d_{+}! d_{-}!)) \\ i(\delta_{L,-1} \nabla_{+}^{d_{+}} \nabla_{-}^{d_{-}} \bar{R}_{-} / (d_{+}! d_{-}!) - \delta_{L,1} \nabla_{+}^{d_{+}} \nabla_{-}^{d_{-}} \bar{R}_{+} / (d_{+}! d_{-}!)) \\ -\delta_{L,0} \delta_{d_{+},0} \delta_{d_{-},0} \\ \delta_{L,0} \delta_{d_{+},0} \delta_{d_{-},0} \end{pmatrix}, \quad (\text{B.8})$$

we obtain

$$\frac{\nabla_{+}^{k_{+}} \nabla_{-}^{k_{-}}}{k_{+}! k_{-}!} \delta H_L = q_s \sum_{k'_{+}=0}^{k_{+}} \sum_{k'_{-}=0}^{k_{-}} \mathcal{H}_{Lk}^{k_{+}-k'_{+},k_{-}-k'_{-}} \left\{ \frac{\nabla_{+}^{k'_{+}} \nabla_{-}^{k'_{-}}}{k'_{+}! k'_{-}!} u_k \right\} v_{\perp}^{\delta_{k,1}+\delta_{k,2}} v_{\parallel}^{\delta_{k,3}} c^{\delta_{k,4}}, \quad (\text{B.9})$$

and

$$\delta H_{ps}(\mathbf{r}) = q_s \sum_{L=-1}^1 e^{i(L-p)\pi/2} \sum_{\kappa=0}^{\infty} \rho_c^{2\kappa+|p-L|} v_{\perp}^{\delta_{k,1}+\delta_{k,2}} v_{\parallel}^{\delta_{k,3}} c^{\delta_{k,4}} \dots \sum_{k'_{+}=0}^{k_{+}} \sum_{k'_{-}=0}^{k_{-}} \mathcal{H}_{Lk}^{k_{+}-k'_{+},k_{-}-k'_{-}} \left\{ \frac{\nabla_{+}^{k'_{+}} \nabla_{-}^{k'_{-}}}{k'_{+}! k'_{-}!} u_k \right\}, \quad (\text{B.10})$$

which can also be conveniently rewritten as

$$\delta H_{ps}(\mathbf{r}) = q_s \sum_{q=p-1}^{p+1} e^{-iq\pi/2} \sum_{\kappa=0}^{\infty} \rho_c^{2\kappa+|q|} v_{\perp}^{\delta_{k,1}+\delta_{k,2}} v_{\parallel}^{\delta_{k,3}} c^{\delta_{k,4}} \dots \sum_{k'_{+}=0}^{k_{+}} \sum_{k'_{-}=0}^{k_{-}} \mathcal{H}_{p-q,k}^{k_{+}-k'_{+},k_{-}-k'_{-}} \left\{ \frac{\nabla_{+}^{k'_{+}} \nabla_{-}^{k'_{-}}}{k'_{+}! k'_{-}!} u_k \right\}, \quad (\text{B.11})$$

with

$$k_{+} = \kappa + \max(0, q), \quad k_{-} = \kappa + \max(0, -q). \quad (\text{B.12})$$

At this stage, it is possible to numerically implement the all-order functional. Nevertheless, we choose here to retain Finite Larmor Radius (FLR) effects up to second order in the resonant plasma functional (3.63). To do so, it is necessary to obtain the Hamiltonian

contribution to first order in $k_{\perp}\rho_c$. It is clear from Eq. B.11 that this implies retaining only the $\kappa = 0$ term in the Larmor radius sum, and limiting ourselves to $|q| \leq 1$, which has the effect of selecting the ICRF harmonics $p = -2 \dots 2$, as expected from previous works [37]. This also has the advantage of restricting k_+ and k_- to being zero or one. In this case, the pragmatic approach is to directly expand Eq. B.11 as

$$\delta H_{ps}(\mathbf{r}) = q_s v_{\perp}^{\delta_{k,1} + \delta_{k,2}} v_{\parallel}^{\delta_{k,3}} c^{\delta_{k,4}} \left\{ \left(\mathcal{H}_{p,k}^{0,0} + i\rho_c [\mathcal{H}_{p+1,k}^{0,1} - \mathcal{H}_{p-1,k}^{1,0}] \right) u_k \dots \right. \\ \left. + i\rho_c [\mathcal{H}_{p+1,k}^{0,0} \nabla_{-} u_k - \mathcal{H}_{p-1,k}^{0,0} \nabla_{+} u_k] \right\}, \quad (\text{B.13})$$

or equivalently

$$\delta H_{ps}(\mathbf{r}) = q_s v_{\perp}^{\delta_{k,1} + \delta_{k,2}} v_{\parallel}^{\delta_{k,3}} c^{\delta_{k,4}} \left\{ \left(\mathcal{H}_{p,k}^{0,0} + i\rho_c [\mathcal{H}_{p+1,k}^{0,1} - \mathcal{H}_{p-1,k}^{1,0}] \right) u_k \dots \right. \\ \left. + i\rho_c \sum_{c=1}^3 [\mathcal{H}_{p+1,k}^{0,0} T_{-}^c - \mathcal{H}_{p-1,k}^{0,0} T_{+}^c] \partial_c u_k \right\}. \quad (\text{B.14})$$

At this stage, it is interesting to introduce a normalization temperature T_s and associated thermal velocity v_{th} (regardless of the potential non-Maxwellian nature of the considered distribution function). This allows the velocity integrals to be formally isolated from the Fourier integrals. We also introduce the thermal Larmor radius $\rho_{th} \equiv v_{th}/\Omega_{cs}$ and rewrite the latter expression as

$$\delta H_{ps}(\mathbf{r}) = q_s v_{\perp}^{\delta_{k,1} + \delta_{k,2}} v_{\parallel}^{\delta_{k,3}} c^{\delta_{k,4}} \left[\Gamma_{p,k}^{(0),0} u_k \dots \right. \\ \left. + u_{\perp} \left(\Gamma_{p,k}^{(0),1} u_k + \Gamma_{p,k}^{(\theta),1} \partial_{\theta} u_k + \Gamma_{p,k}^{(\phi),1} \partial_{\phi} u_k + \Gamma_{p,1}^{(s),1} \partial_s u_k \right) \right], \quad (\text{B.15})$$

where $u_{\perp} \equiv v_{\perp}/v_{th}$.

The auxiliary functions are defined as

$$\Gamma_{p,k}^{(0),0} \equiv \mathcal{H}_{p,k}^{0,0}, \quad (\text{B.16})$$

$$\Gamma_{p,k}^{(0),1} \equiv i\rho_{th} [\mathcal{H}_{p+1,k}^{0,1} - \mathcal{H}_{p-1,k}^{1,0}], \quad (\text{B.17})$$

$$\Gamma_{p,k}^{(s),1} \equiv i\rho_{th} [\mathcal{H}_{p+1,k}^{0,0} T_{-}^1 - \mathcal{H}_{p-1,k}^{0,0} T_{+}^1], \quad (\text{B.18})$$

$$\Gamma_{p,k}^{(\theta),1} \equiv i\rho_{th} [\mathcal{H}_{p+1,k}^{0,0} T_{-}^2 - \mathcal{H}_{p-1,k}^{0,0} T_{+}^2], \quad (\text{B.19})$$

and

$$\Gamma_{p,k}^{(\phi),1} \equiv i\rho_{th} [\mathcal{H}_{p+1,k}^{0,0} T_{-}^3 - \mathcal{H}_{p-1,k}^{0,0} T_{+}^3]. \quad (\text{B.20})$$

Introducing the spectral decomposition for u_k , the previous expression may also be written as

$$\begin{aligned} \delta H_{ps}(\mathbf{r}) = & q_s v_{\perp}^{\delta_{k,1}+\delta_{k,2}} v_{\parallel}^{\delta_{k,3}} c^{\delta_{k,4}} \dots \\ & \sum_{mn} \left\{ \left[\Gamma_{p,k}^{(0),0} + u_{\perp} \left(\Gamma_{p,k}^{(0),1} + im \Gamma_{p,k}^{(\theta),1} + in \Gamma_{p,k}^{(\phi),1} \right) \right] u_{kmn} \right. \\ & \left. + u_{\perp} \Gamma_{p,k}^{(s),1} \partial_s u_{kmn} \right\} e^{i(m\theta+n\phi)}, \end{aligned} \quad (\text{B.21})$$

from which we deduce

$$\begin{aligned} \delta H_{pm_1n} = & q_s v_{\perp}^{\delta_{k,1}+\delta_{k,2}} v_{\parallel}^{\delta_{k,3}} c^{\delta_{k,4}} \sum_m \left\{ \left[\left(\Gamma_{p,k}^{(0),0} \right)_{m_1-m} + u_{\perp} \left(\Gamma_{p,k}^{(0),1} \right)_{m_1-m} \dots \right. \right. \\ & \left. \left. + im u_{\perp} \left(\Gamma_{p,k}^{(\theta),1} \right)_{m_1-m} + in u_{\perp} \left(\Gamma_{p,k}^{(\phi),1} \right)_{m_1-m} \right] u_{kmn} \dots \right. \\ & \left. + \left(\Gamma_{p,k}^{(s),1} \right)_{m_1-m} \partial_s u_{kmn} \right\}, \end{aligned} \quad (\text{B.22})$$

where $(\)_M$ means that the M -th Fourier harmonic in poloidal angle has to be considered.

It is worth noting that, from Def. B.8,

$$(\mathcal{H}_{Lk}^{d_+,d_-})^* = \mathcal{H}_{-Lk}^{d_-,d_+}. \quad (\text{B.23})$$

Along with Eq. (A.49), this property ensures

$$\left(\Gamma_{p,k}^{(0,s,\theta,\phi),q} \right)^* = \Gamma_{-p,k}^{(0,s,\theta,\phi),q}, \quad (\text{B.24})$$

which may be beneficial in terms of computation time.

We have also

$$\begin{aligned} \delta H_{pm_2n} = & q_s v_{\perp}^{\delta_{k,1}+\delta_{k,2}} v_{\parallel}^{\delta_{k,3}} c^{\delta_{k,4}} \sum_m \left\{ \left[\left(\Gamma_{p,k}^{(0),0} \right)_{\bar{m}-m_2}^* + u_{\perp} \left(\Gamma_{p,k}^{(0),1} \right)_{\bar{m}-m_2}^* \dots \right. \right. \\ & \left. \left. - i \bar{m} u_{\perp} \left(\Gamma_{p,k}^{(\theta),1} \right)_{\bar{m}-m_2}^* - in u_{\perp} \left(\Gamma_{p,k}^{(\phi),1} \right)_{\bar{m}-m_2}^* \right] u_{k\bar{m}n}^* \dots \right. \\ & \left. + \left(\Gamma_{p,k}^{(s),1} \right)_{\bar{m}-m_2}^* \partial_s u_{k\bar{m}n}^* \right\}, \end{aligned} \quad (\text{B.25})$$

where $(f)_M^*$ means here the M -th Fourier harmonic of the complex conjugate.

The complete second-order version of resonant particle functional is finally obtained

by inserting Eqs. B.22 and B.25 into Eq. 3.63 and organizing the various terms as

$$\begin{aligned}
\mathcal{L}_{part,s}^{(res)} = & \sum_{p,m_1,m_2,n} \sum_{m,\bar{m}} \int dsc^{\delta_{k,4}+\delta_{\bar{k},4}} \dots \\
& \left\{ \left[\left(J\mathcal{I}_{k\bar{k}}^{(0)} \right)_{m_2-m_1} \left(\Gamma_{p,k}^{(0),0} \right)_{m_1-m} \left(\Gamma_{p,\bar{k}}^{(0),0} \right)_{\bar{m}-m_2}^* \right. \right. \\
& + \left(J\mathcal{I}_{k\bar{k}}^{(1)} \right)_{m_2-m_1} \left(\Gamma_{p,k}^{(0),1} + in\Gamma_{p,k}^{(\phi),1} \right)_{m_1-m} \left(\Gamma_{p,\bar{k}}^{(0),0} \right)_{\bar{m}-m_2}^* \\
& + \left(J\mathcal{I}_{k\bar{k}}^{(1)} \right)_{m_2-m_1} \left(\Gamma_{p,k}^{(0),0} \right)_{m_1-m} \left(\Gamma_{p,\bar{k}}^{(0),1} + in\Gamma_{p,\bar{k}}^{(\phi),1} \right)_{\bar{m}-m_2}^* \\
& + \left(J\mathcal{I}_{k\bar{k}}^{(2)} \right)_{m_2-m_1} \left(\Gamma_{p,k}^{(0),1} + in\Gamma_{p,k}^{(\phi),1} \right)_{m_1-m} \left(\Gamma_{p,\bar{k}}^{(0),1} + in\Gamma_{p,\bar{k}}^{(\phi),1} \right)_{\bar{m}-m_2}^* \\
& + im \left(J\mathcal{I}_{k\bar{k}}^{(1)} \right)_{m_2-m_1} \left(\Gamma_{p,k}^{(\theta),1} \right)_{m_1-m} \left(\Gamma_{p,\bar{k}}^{(0),0} \right)_{\bar{m}-m_2}^* \\
& + im \left(J\mathcal{I}_{k\bar{k}}^{(2)} \right)_{m_2-m_1} \left(\Gamma_{p,k}^{(\theta),1} \right)_{m_1-m} \left(\Gamma_{p,\bar{k}}^{(0),1} + in\Gamma_{p,\bar{k}}^{(\phi),1} \right)_{\bar{m}-m_2}^* \\
& - im \left(J\mathcal{I}_{k\bar{k}}^{(1)} \right)_{m_2-m_1} \left(\Gamma_{p,k}^{(0),0} \right)_{m_1-m} \left(\Gamma_{p,\bar{k}}^{(\theta),1} \right)_{\bar{m}-m_2}^* \\
& - im \left(J\mathcal{I}_{k\bar{k}}^{(2)} \right)_{m_2-m_1} \left(\Gamma_{p,k}^{(0),1} + in\Gamma_{p,k}^{(\phi),1} \right)_{m_1-m} \left(\Gamma_{p,\bar{k}}^{(\theta),0} \right)_{\bar{m}-m_2}^* \\
& + m\bar{m} \left(J\mathcal{I}_{k\bar{k}}^{(2)} \right)_{m_2-m_1} \left(\Gamma_{p,k}^{(\theta),1} \right)_{m_1-m} \left(\Gamma_{p,\bar{k}}^{(\theta),1} \right)_{\bar{m}-m_2}^* \left. \right] u_{kmn} u_{k\bar{m}\bar{n}}^* \\
& + \left[\left(J\mathcal{I}_{k\bar{k}}^{(1)} \right)_{m_2-m_1} \left(\Gamma_{p,k}^{(0),1} \right)_{m_1-m} \left(\Gamma_{p,\bar{k}}^{(s),1} \right)_{\bar{m}-m_2}^* \right. \\
& + \left(J\mathcal{I}_{k\bar{k}}^{(2)} \right)_{m_2-m_1} \left(\Gamma_{p,k}^{(0),1} + in\Gamma_{p,k}^{(\phi),1} \right)_{m_1-m} \left(\Gamma_{p,\bar{k}}^{(s),1} \right)_{\bar{m}-m_2}^* \\
& + im \left(J\mathcal{I}_{k\bar{k}}^{(2)} \right)_{m_2-m_1} \left(\Gamma_{p,k}^{(\theta),1} \right)_{m_1-m} \left(\Gamma_{p,\bar{k}}^{(s),1} \right)_{\bar{m}-m_2}^* \left. \right] u_{kmn} \partial_s u_{k\bar{m}\bar{n}}^* \\
& + \left[\left(J\mathcal{I}_{k\bar{k}}^{(1)} \right)_{m_2-m_1} \left(\Gamma_{p,k}^{(s),1} \right)_{m_1-m} \left(\Gamma_{p,\bar{k}}^{(0),0} \right)_{\bar{m}-m_2}^* \right. \\
& + \left(J\mathcal{I}_{k\bar{k}}^{(2)} \right)_{m_2-m_1} \left(\Gamma_{p,k}^{(s),1} \right)_{m_1-m} \left(\Gamma_{p,\bar{k}}^{(0),1} + in\Gamma_{p,\bar{k}}^{(\phi),1} \right)_{\bar{m}-m_2}^* \\
& - im \left(J\mathcal{I}_{k\bar{k}}^{(2)} \right)_{m_2-m_1} \left(\Gamma_{p,k}^{(s),1} \right)_{m_1-m} \left(\Gamma_{p,\bar{k}}^{(\theta),1} \right)_{\bar{m}-m_2}^* \left. \right] \partial_s u_{kmn} u_{k\bar{m}\bar{n}}^* \\
& + \left[\left(J\mathcal{I}_{k\bar{k}}^{(2)} \right)_{m_2-m_1} \left(\Gamma_{p,k}^{(s),1} \right)_{m_1-m} \left(\Gamma_{p,\bar{k}}^{(s),1} \right)_{\bar{m}-m_2}^* \right] \partial_s u_{kmn} \partial_s u_{k\bar{m}\bar{n}}^* \left. \right\}. \tag{B.26}
\end{aligned}$$

We have the dielectric kernel

$$\mathcal{I}_{k\bar{k}}^{(q)} \equiv \frac{q_s^2}{\epsilon_0} \int d^3\mathbf{p} u_{\perp}^q v_{\perp}^{\alpha_{\perp}} v_{\parallel}^{\alpha_{\parallel}} \frac{\omega}{\omega - p\Omega_{cs} - k_{\parallel,0}v_{\parallel}} \mathcal{D}f_{s,0}, \tag{B.27}$$

where

$$\alpha_{\perp} \equiv \delta_{k,1} + \delta_{\bar{k},1} + \delta_{k,2} + \delta_{\bar{k},2}, \tag{B.28}$$

$$\alpha_{\parallel} \equiv \delta_{k,3} + \delta_{\bar{k},3}. \tag{B.29}$$

Fast algorithm

The numerical evaluation of the above expression is costly, essentially because of the fact that $k_{\parallel,0}$ depends on m_1 and m_2 :

$$k_{\parallel,0}v_{\parallel} = \frac{m_1 + m_2}{2}\dot{\theta} + n\dot{\phi}. \quad (\text{B.30})$$

This means that the products have to be performed between all Fourier harmonics, which is very demanding in terms of computing resources. If, on the other hand, we substitute $m_1 + m_2$ with $m + \bar{m}$ in $k_{\parallel,0}$, i.e. write

$$k_{\parallel,0}v_{\parallel} \approx \frac{m + \bar{m}}{2}\dot{\theta} + n\dot{\phi}, \quad (\text{B.31})$$

these products may be performed in real space, so that the sum over m_1 and m_2 may be suppressed. The plasma functional then takes a more civilized form:

$$\begin{aligned} \mathcal{L}_{part,s}^{(res)} = & \sum_{p,n} \sum_{m,\bar{m}} \int ds c^{\delta_{k,4} + \delta_{\bar{k},4}} \dots \\ & \left[\left\{ J\mathcal{I}_{k\bar{k}}^{(0)} \Gamma_{p,k}^{(0),0} \Gamma_{p,\bar{k}}^{(0),0*} \right. \right. \\ & + J\mathcal{I}_{k\bar{k}}^{(1)} \left(\Gamma_{p,k}^{(0),1} + in\Gamma_{p,k}^{(\phi),1} \right) \Gamma_{p,\bar{k}}^{(0),0*} \\ & + J\mathcal{I}_{k\bar{k}}^{(1)} \Gamma_{p,k}^{(0),0} \left(\Gamma_{p,\bar{k}}^{(0),1} + in\Gamma_{p,\bar{k}}^{(\phi),1} \right)^* \\ & + J\mathcal{I}_{k\bar{k}}^{(2)} \left(\Gamma_{p,k}^{(0),1} + in\Gamma_{p,k}^{(\phi),1} \right) \left(\Gamma_{p,\bar{k}}^{(0),1} + in\Gamma_{p,\bar{k}}^{(\phi),1} \right)^* \left. \right\}_{\bar{m}-m} \\ & + im \left\{ J\mathcal{I}_{k\bar{k}}^{(1)} \Gamma_{p,k}^{(\theta),1} \Gamma_{p,\bar{k}}^{(0),0*} + J\mathcal{I}_{k\bar{k}}^{(2)} \Gamma_{p,k}^{(\theta),1} \left(\Gamma_{p,\bar{k}}^{(0),1} + in\Gamma_{p,\bar{k}}^{(\phi),1} \right)^* \right\}_{\bar{m}-m} \\ & - im \left\{ J\mathcal{I}_{k\bar{k}}^{(1)} \Gamma_{p,k}^{(0),0} \Gamma_{p,\bar{k}}^{(\theta),1*} + J\mathcal{I}_{k\bar{k}}^{(2)} \left(\Gamma_{p,k}^{(0),1} + in\Gamma_{p,k}^{(\phi),1} \right) \Gamma_{p,\bar{k}}^{(\theta),0*} \right\}_{\bar{m}-m} \\ & + m\bar{m} \left\{ J\mathcal{I}_{k\bar{k}}^{(2)} \Gamma_{p,k}^{(\theta),1} \Gamma_{p,\bar{k}}^{(\theta),1*} \right\}_{\bar{m}-m} \left. \right] u_{kmn} u_{k\bar{m}n}^* \\ & + \left[\left\{ J\mathcal{I}_{k\bar{k}}^{(1)} \Gamma_{p,k}^{(0),1} \Gamma_{p,\bar{k}}^{(s),1*} + J\mathcal{I}_{k\bar{k}}^{(2)} \left(\Gamma_{p,k}^{(0),1} + in\Gamma_{p,k}^{(\phi),1} \right) \Gamma_{p,\bar{k}}^{(s),1*} \right\}_{\bar{m}-m} \right. \\ & + im \left\{ J\mathcal{I}_{k\bar{k}}^{(2)} \Gamma_{p,k}^{(\theta),1} \Gamma_{p,\bar{k}}^{(s),1*} \right\}_{\bar{m}-m} \left. \right] u_{kmn} \partial_s u_{k\bar{m}n}^* \\ & + \left[\left\{ J\mathcal{I}_{k\bar{k}}^{(1)} \Gamma_{p,k}^{(s),1} \Gamma_{p,\bar{k}}^{(0),0} + J\mathcal{I}_{k\bar{k}}^{(2)} \Gamma_{p,k}^{(s),1} \left(\Gamma_{p,\bar{k}}^{(0),1} + in\Gamma_{p,\bar{k}}^{(\phi),1} \right)^* \right\}_{\bar{m}-m} \right. \\ & - im \left\{ J\mathcal{I}_{k\bar{k}}^{(2)} \Gamma_{p,k}^{(s),1} \Gamma_{p,\bar{k}}^{(\theta),1} \right\}_{\bar{m}-m} \left. \right] \partial_s u_{kmn} u_{k\bar{m}n}^* \\ & + \left[\left\{ J\mathcal{I}_{k\bar{k}}^{(2)} \Gamma_{p,k}^{(s),1} \Gamma_{p,\bar{k}}^{(s),1*} \right\}_{\bar{m}-m} \right] \partial_s u_{kmn} \partial_s u_{k\bar{m}n}^* \left. \right\}. \end{aligned} \quad (\text{B.32})$$

These expressions are convenient because they can be readily inserted in a symbolic manipulation software to automatize the building of the code computing the master elements, and the various quantities which have to be Fourier-transformed appear clearly

between braces. Finally, they lend themselves well to an extension to non-Maxwellian distribution functions.

WKB harmonics

Using Eq. B.4, Eq. 2.109 may be recast in the form

$$\delta H_{ps}(\mathbf{r}) = q_s \sum_{L=-1}^1 \bar{\mathcal{H}}_{Lk} J_{p-L}(k_{\perp} \rho_c) e^{i(p-L)\beta} u_k, \quad (\text{B.33})$$

so that

$$\delta H_{ps}(\mathbf{r}) = q_s v_{\perp}^{\delta_{k,1} + \delta_{k,2}} v_{\parallel}^{\delta_{k,3}} c^{\delta_{k,4}} \sum_{L=-1}^1 \mathcal{H}_{Lk}^{0,0} J_{p-L}(k_{\perp} \rho_c) e^{i(p-L)\beta} u_k, \quad (\text{B.34})$$

and

$$\delta H_{ps}^*(\mathbf{r}) = q_s v_{\perp}^{\delta_{\bar{k},1} + \delta_{\bar{k},2}} v_{\parallel}^{\delta_{\bar{k},3}} c^{\delta_{\bar{k},4}} \sum_{\bar{L}=-1}^1 \left(\mathcal{H}_{\bar{L}\bar{k}}^{0,0} \right)^* J_{p-\bar{L}}(k_{\perp} \rho_c) e^{-i(p-\bar{L})\beta} u_{\bar{k}}^*. \quad (\text{B.35})$$

Using Eqs. B.34 and B.35 introduces a serious difficulty: performing the Fourier transforms of these two quantities and integrating over velocity afterwards would be much too time-consuming. Therefore, the plasma functional is built by performing the products in real space. The price to pay for this operation, as explained previously, is that k_{\parallel} may not depend on m_1 and m_2 . On the other hand, the replacement of $m_1 + m_2$ by $m + \bar{m}$ can be used to remain in real space and it is expected that this substitution should not result in large errors in the calculation (which should nevertheless be checked against the full calculation for harmonics $|p| \leq 2$ whenever applicable).

$$\begin{aligned} \mathcal{L}_{part,s}^{(res)} &= \frac{q_s^2}{\epsilon_0 c^2} \sum_{p,m_1,m_2,n} \int d^3 \mathbf{p} d^3 \mathbf{r} \frac{\omega}{\omega - p \Omega_{cs} - k_{\parallel} v_{\parallel}} \mathcal{D} f_{s,0} v_{\perp}^{\delta_{k,1} + \delta_{k,2} + \delta_{\bar{k},1} + \delta_{\bar{k},2}} v_{\parallel}^{\delta_{k,3} + \delta_{\bar{k},3}} \\ &\quad c^{\delta_{k,4} + \delta_{\bar{k},4}} \sum_{L,\bar{L}=-1}^1 \mathcal{H}_{Lk}^{0,0} \left(\mathcal{H}_{\bar{L}\bar{k}}^{0,0} \right)^* J_{p-L}(k_{\perp} \rho_c) J_{p-\bar{L}}(k_{\perp} \rho_c) e^{i(\bar{L}-L)\beta} u_k u_{\bar{k}}^* e^{i(m_1 - m_2)\theta}, \end{aligned} \quad (\text{B.36})$$

or equivalently

$$\mathcal{L}_{part,s}^{(res)} = \sum_{p,m,\bar{m},n} \int ds d\theta J \sum_{L,\bar{L}=-1}^1 \mathcal{H}_{Lk}^{0,0} \left(\mathcal{H}_{\bar{L}\bar{k}}^{0,0} \right)^* \mathcal{I}_{kk}^{L\bar{L}} e^{i(\bar{L}-L)\beta} e^{i(m-\bar{m})\theta} u_{kmn} u_{\bar{k}\bar{m}n}^*, \quad (\text{B.37})$$

with

$$\mathcal{I}_{kk}^{L\bar{L}} \equiv \int d^3 \mathbf{p} v_{\perp}^{\alpha_{\perp}} v_{\parallel}^{\alpha_{\parallel}} \frac{\omega}{\omega - p \Omega_{cs} - k_{\parallel} v_{\parallel}} \mathcal{D} f_{s,0} J_{p-L} \left(\frac{k_{\perp} v_{\perp}}{\Omega_{cs}} \right) J_{p-\bar{L}} \left(\frac{k_{\perp} v_{\perp}}{\Omega_{cs}} \right), \quad (\text{B.38})$$

having defined

$$\alpha_{\perp} \equiv \delta_{k,1} + \delta_{\bar{k},1} + \delta_{k,2} + \delta_{\bar{k},2}, \quad (\text{B.39})$$

$$\alpha_{\parallel} \equiv \delta_{k,3} + \delta_{\bar{k},3}. \quad (\text{B.40})$$

Appendix C

Collocation algorithm

In this appendix, we detail the algorithm which has been implemented to numerically evaluate the dielectric kernel (Eq. 3.83), which we rewrite in a slightly different form

$$\mathcal{W}_{i,j}(\xi) \equiv \frac{2}{\sqrt{\pi}} \int_{-\infty}^{\infty} du_{\parallel} \frac{u_{\parallel}^i}{u_{\parallel} - \xi} \int_0^{\infty} du_{\perp} u_{\perp}^{j+1} \mathcal{K}(u_{\parallel}, u_{\perp}). \quad (\text{C.1})$$

C.1 General formulation

This algorithm is based on a collocation method, where the same grid is employed for the integration variable u_{\parallel} and the pole. In RF codes, the frequency is real¹. Here, we extend it to arbitrary complex frequencies, which has a cost in terms of computational requirements, but is needed to, e.g. studies instabilities such as EGAMs [99].

This algorithm is adapted to the evaluation of expressions of the generic form

$$K \equiv \int_{-\infty}^{\infty} dv \frac{g(v)}{v - \omega e^{i\varphi}}, \quad (\text{C.2})$$

where the complex generalized "frequency" Ω is decomposed as a module ω and an argument φ , i.e. $\Omega \equiv \omega \exp(i\varphi)$. We introduce a velocity mesh $v_j \equiv j\Delta v$ with $j = -N \dots N$ an integer and $\Delta v \equiv v_{max}/N$ with v_{max} large enough to capture the whole distribution function features. The idea is that we use the same mesh for v and ω , i.e. $\omega_k \equiv k\Delta v$ with $k = 0 \dots N$. Eq. C.2 can be evaluated at the mesh points k as

$$K_k = \int_{-\infty}^{\infty} dv \frac{g(v)}{v - \omega_k e^{i\varphi}}. \quad (\text{C.3})$$

g is approximated as

$$g(v) \equiv \sum_j g_j h_j(v), \quad (\text{C.4})$$

¹Unless external collision effects are added but in this case, the distribution function is usually considered Maxwellian, so that the dielectric response involves the plasma dispersion function of complex argument.

with the tent-like finite elements defined as

$$h_j(v) = \begin{cases} 1 - |v - v_j|/\Delta v & \text{if } |v - v_j| \leq \Delta v, \\ 0 & \text{otherwise,} \end{cases} \quad (\text{C.5})$$

and $g_j \equiv g(v_j)$, the integrand value at collocation points.

Eq. C.3 may now be rewritten as

$$K_k = \sum_{j=-N}^N g_j \kappa_{j,k}, \quad (\text{C.6})$$

with the kernel

$$\kappa_{j,k} \equiv \int_{-1}^1 dx \frac{1 - |x|}{x + j - ke^{i\varphi}}. \quad (\text{C.7})$$

The difficulty related to the handling of $\Im(\Omega) \neq 0$ is apparent: when $\varphi = 0$, we have that $\kappa_{j,k}$ only depends on $j - k$, which is very beneficial in terms of numerical evaluation. Here, on the other hand, κ will have to be evaluated for all j and k taken independently. The computational burden remains however within very reasonable limits.

The kernel can be computed analytically. Assuming $\varphi > 0$, $j - ke^{i\varphi} \neq \pm 1$ and $j - ke^{i\varphi} \neq 0$, we obtain

$$\kappa_{j,k} = \log\left(\frac{j - ke^{i\varphi} + 1}{j - ke^{i\varphi} - 1}\right) - (j - ke^{i\varphi}) \log\left(\frac{(j - ke^{i\varphi})^2}{(j - ke^{i\varphi})^2 - 1}\right). \quad (\text{C.8})$$

The exceptions can be handled separately and we obtain

$$\kappa_{j,k} = \begin{cases} \pm 2 \log(2) & \text{if } j - ke^{i\varphi} = \pm 1, \\ i\pi & \text{if } j - ke^{i\varphi} = 0. \end{cases} \quad (\text{C.9})$$

The numerical evaluation of Expressions C.8 and C.9 is straightforward, since the integral is performed without having to cross the branch cut. To satisfy causality, the case $\Im(\Omega) \leq 0$ needs to be handled by performing an analytical continuation of the obtained result for $\varphi < 0$. We finally obtain for Eq. C.3

$$K_k = \begin{cases} \sum_{j=-N}^N g_j \kappa_{j,k} & \text{if } \varphi \geq 0, \\ \sum_{j=-N}^N g_j \kappa_{j,k} + 2i\pi g(\omega_k \exp(i\varphi)) & \text{if } \varphi < 0. \end{cases} \quad (\text{C.10})$$

The advantage here is that the numerical evaluation of these expressions can be performed efficiently.

C.2 Dielectric response evaluation

We now come back to the evaluation of Eq. C.1. In view of the previous section, it is useful to rewrite it as

$$\mathcal{W}_{i,j}(\xi) \equiv \int_{-\infty}^{\infty} du_{\parallel} \frac{1}{u_{\parallel} - \xi} g_{i,j}(u_{\parallel}), \quad (\text{C.11})$$

with

$$g_{i,j}(u_{\parallel}) \equiv \frac{2}{\sqrt{\pi}} u_{\parallel}^i \int_0^{\infty} du_{\perp} u_{\perp}^{j+1} \kappa(u_{\parallel}, u_{\perp}). \quad (\text{C.12})$$

Evaluating the previous expression is straightforward. We note that the collocation method presented before will, by definition, yield $W_{i,j}(\xi_k)$ with ξ_k the collocation point. Since there is no possibility of knowing at which ξ this function will be needed to obtain the dielectric response, it has been found that spline evaluations of $W_{i,j}(\xi)$ deduced from the $W_{i,j}(\xi_k)$ was a numerically efficient and robust method.

We note, however, that a small difficulty remains in situations where $W_{i,j}$ is needed at velocities exceeding the maximum velocity chosen for the collocation evaluation. In this case, it is best to avoid extending the velocity collocation grid too much, since it results in a lack of accuracy/speed. Following Brambilla [128], we opt instead for an asymptotic expansion of the resonant denominator, i.e.

$$\frac{1}{u_{\parallel} - \xi} \approx -\frac{1}{\xi} \sum_{n=0}^{\infty} \left(\frac{u_{\parallel}}{\xi} \right)^n, \quad (\text{C.13})$$

which yields the following polynomial expression for variable $1/\xi$:

$$\mathcal{W}_{i,j} = \frac{1}{\xi} \sum_n \mathcal{A}_{i,j}^n \left(\frac{1}{\xi} \right)^n, \quad (\text{C.14})$$

with the coefficients

$$\mathcal{A}_{i,j}^n \equiv -\frac{2}{\sqrt{\pi}} \int_{-\infty}^{\infty} du_{\parallel} u_{\parallel}^{n+i} \int_0^{\infty} du_{\perp} u_{\perp}^{j+1} \kappa(u_{\parallel}, u_{\perp}). \quad (\text{C.15})$$

Numerical evaluation of the latter expression does not pose any particular difficulty. By choosing a boundary ξ_{max} such that the features of the distribution function are retained, this method was found to work well retaining only a few terms (typically 5) in the expansion Eq. C.14.

Appendix D

ICRF heating in a tokamak: a minimal model

The aim of this appendix is the derivation of a simple model for ICRF heating. The rationale is that during experiments, or in real-time contexts, running expensive numerical tools is not a sensible option. Therefore, it is always interesting to attempt to extract the most important physics features from the comprehensive models, and transpose them into fast and reliable numerical tools. Of course, it is also necessary to compare the outcome of such simplified models to more advanced ones, to check them as well as adjust any potentially tunable parameter. The followed procedure stems from the results presented in chapter 4, and essentially from three papers [47, 129, 130].

Our starting point is the quasi-local Fokker-Planck equation Eq. 4.66 discussed in details in chapter 4. Here, we only keep the collision and wave quasilinear terms, and assume that the ion distribution before heating is in thermal equilibrium with the other species, i.e.

$$\partial_\tau f_i = \hat{C}f_i + \hat{Q}f_i. \quad (\text{D.1})$$

The time is normalized to a characteristic collision frequency denoted ν_i (see Eq. 4.56). The local collision operator is given by (see Eq. 4.57)

$$\hat{C}f_i = \frac{1}{u^2} \frac{\partial}{\partial u} \left[u^2 \left(D_{uu} \frac{\partial f_i}{\partial u} - F_u f_i \right) \right] + \frac{1}{u^2} \left[\frac{\partial}{\partial \lambda} (1 - \lambda^2) \frac{\Theta_c}{2u} \frac{\partial f_i}{\partial \lambda} \right], \quad (\text{D.2})$$

The wave term is written as

$$\hat{Q}f_i = \frac{1}{u_\perp} \frac{\partial}{\partial u_\perp} u_\perp D_w \frac{\partial f_i}{\partial u_\perp}, \quad (\text{D.3})$$

with D_w the quasilinear diffusion coefficient.

We will follow here a step-by-step procedure aimed at directly implementing the proposed model in real-time control systems or interpretative/predictive reduced codes.

D.1 Power density

We assume that the total RF power P_{RF} , frequency f and the dominant toroidal number n are known quantities¹. We consider the local resonance condition

$$\omega = p\omega_{ci} + \frac{n}{R}v_{\parallel}, \quad (\text{D.4})$$

where poloidal upshift effects are disregarded, i.e. $k_{\parallel} \approx n/R$. p is the cyclotron harmonic, presumed known. If we assume that the interaction involves ions with a parallel velocity ranging between 0 and $v_{th,\parallel}$, we deduce by differentiating Eq. D.4 that the interaction takes place in a spatial domain whose radial extension ΔR (see Fig. D.1) is approximately given by

$$\Delta R \approx \frac{n}{\omega}v_{th,\parallel} \approx \frac{n}{\omega} \sqrt{\frac{2T_i}{m_i}}, \quad (\text{D.5})$$

where it was assumed that the parallel temperature remains close to the bulk temperature T_i .

Determining ΔZ is more complicated: it is fixed by the plasma and antenna geometry, ICRF scenario, plasma parameters (see Fig. D.1)... In fact, for a given set of parameters, it should be deduced from multi-dimensional simulations, as it clearly can have a large influence on the final result. Here, we introduce the corresponding tunable parameter f_z , so that

$$\Delta Z = 2a_0\epsilon_1 f_z, \quad (\text{D.6})$$

with a_0 the minor radius and ϵ_1 the elongation. f_z represents the fraction of the vertical chord along which the absorption is significant.

By doing this, we have defined the toroidal interaction volume

$$V_{int} = 2\pi R \Delta R \Delta Z, \quad (\text{D.7})$$

which will be used to obtain a rough estimate of the power density as

$$p_{abs} \equiv \frac{P_{RF} - P_{loss}}{V_{int}}, \quad (\text{D.8})$$

with P_{loss} the lost power.

D.2 Quasilinear diffusion coefficient

We use the local quasilinear diffusion coefficient, Eq. 4.54, rewritten here as

$$D_w = D_p \left| J_{p-1}(k_{\perp}v_{\perp}/\omega_{ci}) + \frac{E_-}{E_+} J_{p+1}(k_{\perp}v_{\perp}/\omega_{ci}) \right|^2. \quad (\text{D.9})$$

Notice that unlike in chapter 4, the dominant $|E_+|^2$ factor has been absorbed in the constant D_p . The unknowns in the previous expression are k_{\perp} , E_-/E_+ and D_p . Since we

¹ n is usually either a unique ‘‘standard’’ value for a given tokamak/antenna/phasing, or a set of appropriately weighted values.

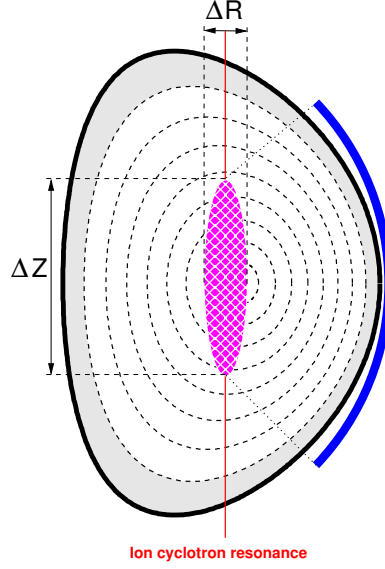


Figure D.1: Illustration of the approximate interaction (purple domain) zone between ICRF waves and plasma.

only consider heating resulting from the fast magnetosonic wave damping, one can use the local dispersion relation [11] to deduce k_{\perp} . If we opt for a cold plasma model (a reasonable assumption for the fast wave propagation), we have

$$k_{\perp}^2 \approx -\frac{\omega^2}{c^2} \frac{(n_{\parallel}^2 - R)(n_{\parallel}^2 - L)}{n_{\parallel}^2 - S}, \quad (\text{D.10})$$

and also

$$\frac{E_{-}}{E_{+}} \approx \left| \frac{n_{\parallel}^2 - L}{n_{\parallel}^2 - R} \right|, \quad (\text{D.11})$$

with $n_{\parallel} \equiv k_{\parallel} c / \omega$. R , L , S and D are the Stix dielectric tensor elements [11].

The determination of D_p is more complicated. The general form for the absorbed power is

$$p_{abs,qlin} = \int d^3\mathbf{v} \frac{mv^2}{2} \hat{Q} f_i, \quad (\text{D.12})$$

which, using Eq. D.3, may be rewritten as

$$p_{abs,qlin} = -4\pi T_i v_{th}^3 \int du_{\parallel} du_{\perp} u_{\perp}^2 D_w \frac{\partial f_i}{\partial u_{\perp}}. \quad (\text{D.13})$$

This expression involves the solution to the Fokker-Planck equation which, at this stage, remains unknown. Assuming the “initial” distribution function² is a Maxwellian

²In other words, the distribution function prior to ICRF heating.

characterized by density n_i and temperature T_i , we obtain the following expression for the linear power density

$$p_{abs,lin} = 8n_i T_i D_p \int_0^\infty du_\perp u_\perp^3 \left| J_{p-1} \left(\frac{k_\perp v_{th,i}}{\omega_{ci}} u_\perp \right) + \frac{E_-}{E_+} J_{p+1} \left(\frac{k_\perp v_{th,i}}{\omega_{ci}} u_\perp \right) \right|^2 e^{-u_\perp^2}. \quad (\text{D.14})$$

It is possible to simplify the previous expression by assuming that $|E_-/E_+| \ll 1$. For low to moderate energy ions fulfilling $k_\perp v_{th,i}/\omega_{ci} \ll 1$, we can then use the small argument expansion of the Bessel functions to obtain

$$p_{abs,lin}^{p=1} \approx 4n_i T_i D_p, \quad (\text{D.15})$$

for fundamental (minority) heating and

$$p_{abs,lin}^{p=2} \approx 2n_i T_i \left(\frac{k_\perp v_{th}}{\Omega_{ci}} \right)^2 D_p, \quad (\text{D.16})$$

for second harmonic heating.

However, we rather suggest to directly make use of Eq. D.14, whose numerical quadrature is quite easily performed on any personal computer. Eq. D.14 can be used to deduce D_p when the power density is known (e.g. given by Eq. D.8) as

$$D_p = \frac{p_{abs,lin}}{8n_i T_i \int_0^\infty du_\perp u_\perp^3 \left| J_{p-1} \left(\frac{k_\perp v_{th,i}}{\omega_{ci}} u_\perp \right) + \frac{E_-}{E_+} J_{p+1} \left(\frac{k_\perp v_{th,i}}{\omega_{ci}} u_\perp \right) \right|^2 e^{-u_\perp^2}}. \quad (\text{D.17})$$

D.3 Low energy, isotropic distribution

We consider firstly the distribution function averaged over the pitch-angle. Introducing $\lambda \equiv v_\parallel/v$, we write

$$\langle f_i \rangle(r, v) \equiv \frac{1}{2} \int_{-1}^1 d\lambda f_i(r, v, \lambda). \quad (\text{D.18})$$

Likewise, the quasilinear diffusion coefficient in velocity is averaged according to

$$\langle D_w \rangle \equiv \frac{1}{2} \int_{-1}^1 d\lambda (1 - \lambda^2) D_w. \quad (\text{D.19})$$

In the collision operator appearing in Eq. D.2, only the energy diffusion and friction survive the pitch-angle averaging procedure, so that

$$\langle \hat{C} f_i \rangle = \frac{1}{u^2} \frac{\partial}{\partial u} \left[u^2 \left(D_{uu} \frac{\partial}{\partial u} \langle f_i \rangle - F_u \langle f_i \rangle \right) \right]. \quad (\text{D.20})$$

For the wave term, we use the relation

$$\frac{\partial}{\partial u_\perp} \equiv \frac{\sqrt{1 - \lambda^2}}{u} \left[\frac{\partial}{\partial u} u - \frac{\partial}{\partial \lambda} \lambda \right], \quad (\text{D.21})$$

to approximate the pitch-angle averaged quasilinear operator in Eq. 4.53 as

$$\langle \hat{Q} f_i \rangle = \frac{1}{u^2} \frac{\partial}{\partial u} u^2 \langle D_w \rangle \frac{\partial \langle f_i \rangle}{\partial u}. \quad (\text{D.22})$$

The quasilinear quantities can be obtained directly from the expressions already provided in chapter 4, i.e. Eqs. 4.83 or 4.84 for the energy content, and 4.86 and 4.89 for the dissipated power. Of course, in all these expressions, only the f_0 terms must be kept and the only moment of D_{ql} needed is Eq. 4.75, i.e.

$$D_{00}^{00}(u) \equiv \frac{1}{2} \int_{-1}^1 d\lambda (1 - \lambda^2) D_w(u, \lambda) = \langle D_w \rangle. \quad (\text{D.23})$$

The steady-state distribution is thus determined by

$$D_{uu} \frac{d \langle f_i \rangle}{du} - F_u \langle f_i \rangle + \langle D_w \rangle \frac{d \langle f_i \rangle}{du} = 0, \quad (\text{D.24})$$

yielding

$$\langle f_i \rangle(u, r) = A_0(r) \exp \left(\int_0^u du \frac{F_u}{D_{uu} + \langle D_w \rangle} \right), \quad (\text{D.25})$$

where A_0 is a constant determined by the local density.

Whereas the isotropy hypothesis would seem to indicate that this result is only valid at very low energies, Anderson et al. [130] assert that it can still be reliably used in the evaluation of velocity-space moments of the distribution function.

D.4 High-energy tail

At velocities much larger than the critical velocity, electron drag dominates the collision relaxation, so that pitch-angle scattering becomes very inefficient. According to Stix, this occurs when

$$v_{\perp}^3 > v_{\gamma}^3/4, \quad (\text{D.26})$$

with

$$\frac{m_i v_{\gamma}^2}{2} \approx 14.810 T_e \left[\frac{2A_i^{1/2}}{n_e} \sum_{\beta} n_{\beta} Z_{\beta}^2 \right]^{2/3}, \quad (\text{D.27})$$

where the β summation is carried out over the background ions.

In this case, it makes more sense to reformulate the Fokker-Planck equation in terms of $(u_{\parallel}, u_{\perp})$, and introduce the parallel energy-integrated distribution

$$F_{\perp}(u_{\perp}) \equiv \langle f_i \rangle_{\perp} \equiv \int_{-\infty}^{\infty} du_{\parallel} f_i(u_{\parallel}, u_{\perp}). \quad (\text{D.28})$$

Following Stix [47], we assume

$$|u_{\parallel}| \ll u_{\perp}, \quad u_{\perp} \sim u, \quad \text{and} \quad u_{\perp} \frac{\partial}{\partial u_{\perp}} \sim u_{\parallel} \frac{\partial}{\partial u_{\parallel}}. \quad (\text{D.29})$$

By doing this, one obtains the following approximate expression for the collision operator³

$$\langle \hat{C}f_i \rangle_{\perp} \equiv \hat{C}F_{\perp} \approx -\frac{1}{u_{\perp}} \frac{\partial}{\partial u_{\perp}} (u_{\perp} \alpha F_{\perp}) + \frac{1}{2u_{\perp}} \frac{\partial^2}{\partial u_{\perp}^2} (u_{\perp} \beta F_{\perp}) + \frac{1}{4u_{\perp}} \frac{\partial}{\partial u_{\perp}} (\gamma F_{\perp}), \quad (\text{D.30})$$

where for convenience, we have used the familiar Stix expressions for the functions appearing in the collision operators, which are related to our D_{uu} , F_u and Θ_c by the relations

$$\begin{cases} \alpha = F_u + \frac{1}{u^2} \frac{\partial}{\partial u} u^2 D_{uu}, \\ \beta = 2D_{uu}, \\ \gamma = \frac{2\Theta_c}{u}. \end{cases} \quad (\text{D.31})$$

The wave term is more straightforward to handle:

$$\langle D_w f_i \rangle_{\perp} = \frac{1}{u_{\perp}} \frac{\partial}{\partial u_{\perp}} u_{\perp} D_w \frac{\partial F_{\perp}}{\partial u_{\perp}}. \quad (\text{D.32})$$

Combining Eqs. D.30 and D.32, one can deduce the steady-state solution as

$$F_{\perp}(u_{\perp}) = B_0 \exp \left(- \int_0^{u_{\perp}} du_{\perp} \frac{-4\alpha u_{\perp} + 2\partial_{u_{\perp}}(u_{\perp}\beta) + \gamma}{2u_{\perp}\beta + 4u_{\perp}D_w(u_{\perp})} \right). \quad (\text{D.33})$$

Although further analytical progress is possible by using approximate expressions [47, 129, 130] for the quantities appearing in this expression, Eq. D.33 can be numerically computed at quite a modest cost.

Eq. 4.82 directly yields for the perpendicular energy content

$$W_{\perp} = 2\pi v_{th,i}^3 \int du_{\perp} u_{\perp} \frac{mv_{\perp}^2}{2} F_{\perp}(u_{\perp}). \quad (\text{D.34})$$

Of course, information on the distribution function in the parallel direction needs to be obtained as well. This is done by following Anderson et al. [129], i.e. introducing the reduced parallel temperature as

$$T_{\parallel}(u_{\perp}) \equiv \frac{\int_{-\infty}^{\infty} du_{\parallel} \frac{mv_{\parallel}^2}{2} f_i(u_{\parallel}, u_{\perp})}{\int_{-\infty}^{\infty} du_{\parallel} f_i(u_{\parallel}, u_{\perp})}. \quad (\text{D.35})$$

The advantage is that for both fundamental and second harmonic heating, T_{\parallel} has the same asymptotic limit which can be written as

$$T_{\parallel}(u_{\perp}) \approx \frac{m_i v_{\gamma}^3}{4v_{\perp}}, \quad (\text{D.36})$$

³The reader should beware that Eq. 35 in Ref. [47] has a missing $\partial/\partial v_{\perp}$ on the sixth line. Ref. [129] has a corrected expression.

with v_γ given by Eq. D.27.

Once T_\parallel has been determined from Eq. D.36, it is possible to deduce from Eq. D.35 the parallel energy content as

$$W_\parallel = 2\pi v_{th,i}^3 \int_0^\infty du_\perp u_\perp T_\parallel(u_\perp) F_\perp(u_\perp). \quad (\text{D.37})$$

The absorbed power, Eq. 4.85 is then given by

$$p_{abs,qlin} = -4\pi\nu_i v_{th,i}^3 T_i \int_0^\infty du_\perp u_\perp^2 D_w \frac{\partial F_\perp}{\partial u_\perp}, \quad (\text{D.38})$$

whereas the power dissipated in collisions has the expression

$$p_{coll} = 4\pi\nu_i v_{th,i}^3 T_i \int_0^\infty du_\perp u_\perp \left[\left(\alpha u_\perp - \frac{\gamma}{4} \right) + \frac{\beta}{2} \right] F_\perp. \quad (\text{D.39})$$

The partition of this power between the various background species is obtained by using Eqs. D.31, and isolating the various terms in the sums appearing in Eq. 4.58 and Eq. 4.59.

Bibliography

- [1] J. Wesson. *Tokamaks*. Clarendon Press, Oxford, 1997.
- [2] J.-M. Rax. *Physique des tokamaks*. Physique. Éd. de l'École Polytechnique, Palaiseau, 2011. ISBN 978-2-7302-1580-0.
- [3] J. P. Freidberg. *Ideal magnetohydrodynamics*. Modern Perspectives in Energy Series. Plenum Publishing Company Limited, 1987.
- [4] P. Helander and D. J. Sigmar. *Collisional Transport in Magnetized Plasmas*. Cambridge Monographs on Plasma Physics. Cambridge University Press, 2005.
- [5] J. D. Jackson. *Classical Electrodynamics*. Wiley, New York, NY, USA, 1975. 2nd edition.
- [6] R. J. Dumont and D. Zarzoso. Heating and current drive by ion cyclotron waves in the activated phase of ITER. *Nuclear Fusion* **53**(1):013002, 2013.
- [7] R. Dumont. Waves in plasmas, 2016. Master's lecture.
- [8] M. Brambilla. *Kinetic Theory of Plasma Waves*. Clarendon Press, Oxford, 1998.
- [9] J. Rax. *Physique des plasmas: Cours et applications*. Physique. Dunod, 2005. ISBN 9782100527878.
- [10] K. Budden. *Radio Waves in the Ionosphere*. Cambridge Press, Cambridge, 1961.
- [11] T. H. Stix. *Waves in plasmas*. Springer-Verlag, New York, 1992.
- [12] B. D. McVey, R. S. Sund, and J. E. Scharer. Local power conservation for linear wave propagation in an inhomogeneous plasma. *Physical Review Letters* **55**:507, 1985.
- [13] M. Brambilla and M. Ottaviani. Mode conversion near ion-ion hybrid and IC harmonic resonances in Tokamaks. *Plasma Physics Controlled Fusion* **27**(1):1, 1985.
- [14] D. N. Smithe. Local full-wave energy and quasilinear analysis in nonuniform plasmas. *Plasma Physics and Controlled Fusion* **31**(7):1105, 1989.
- [15] T. H. Rider. *Fundamental limitations on plasma fusion systems non in thermodynamical equilibrium*. Ph.D. thesis, Massachusetts Institute of Technology., Dept. of Electrical Engineering and Computer Science, 1995.

- [16] E. Nilsson, et al. Kinetic modelling of runaway electron avalanches in tokamak plasmas. *Plasma Physics and Controlled Fusion* **57**(9):095006, 2015.
- [17] J.-F. Artaud, et al. The CRONOS suite of codes for integrated tokamak modelling. *Nuclear Fusion* **50**(4):043001, 2010.
- [18] A. Samain. Dynamic stabilization of a confined plasma. *Nuclear Fusion* **10**(3):325, 1970.
- [19] D. J. Gambier and A. Samain. Variational theory of ion cyclotron resonance heating in tokamak plasmas. *Nuclear Fusion* **25**(3):283, 1985.
- [20] X. Garbet, et al. Variational calculation of electromagnetic instabilities in tokamaks. *Journal of Computational Physics* **87**(2):249, 1990.
- [21] A. Bécoulet, D. J. Gambier, and A. Samain. Hamiltonian theory of the ion cyclotron minority heating dynamics in tokamak plasmas. *Phys. Fluids B* **3**:137, 1991.
- [22] D. Edery, et al. Variational formalism for kinetic-MHD instabilities in tokamaks. *Plasma Physics Controlled Fusion* **34**(6):1089, 1992.
- [23] R. J. Dumont. Variational approach to radiofrequency waves in magnetic fusion devices. *Nuclear Fusion* **49**:075033, 2009.
- [24] Y. O. Kazakov, et al. On resonant ICRF absorption in three-ion component plasmas: a new promising tool for fast ion generation. *Nuclear Fusion* **55**(3):032001, 2015.
- [25] Y. O. Kazakov, et al. A new ion cyclotron range of frequency scenario for bulk ion heating in deuterium-tritium plasmas: How to utilize intrinsic impurities in our favour. *Physics of Plasmas* **22**(8):082511, 2015.
- [26] R. J. Dumont, et al. Multi-megawatt, gigajoule plasma operation in Tore Supra. *Plasma Physics and Controlled Fusion* **56**(7):075020, 2014.
- [27] C. Bourdelle, et al. WEST Physics Basis. *Nuclear Fusion* **55**(6):063017, 2015.
- [28] E. Lerche, et al. Optimizing ion-cyclotron resonance frequency heating for ITER: dedicated JET experiments. *Plasma Physics and Controlled Fusion* **54**(6):069601, 2012.
- [29] R. G. Littlejohn. Hamiltonian formulation of guiding center motion. *Phys. Fluids* **24**(9):1730, 1981.
- [30] L.-G. Eriksson and P. Helander. Monte Carlo operators for orbit-averaged Fokker-Planck equations. *Physics of Plasmas* **1**(2):308, 1994.
- [31] R. O. Dendy, et al. A model for ideal $m = 1$ internal kink stabilization by minority ion cyclotron resonant heating. *Physics of Plasmas* **2**(5):1623, 1995.
- [32] H. Goldstein, C. Poole, and J. Safko. *Classical Mechanics*. Addison Wesley, Reading, MA, USA, 2002.

- [33] A. N. Kaufman. Quasilinear diffusion of an axisymmetric toroidal plasma. *Phys. Fluids* **15**(6):1063, 1972.
- [34] P. U. Lamalle. On the radiofrequency response of a tokamak plasma. *Plasma Physics Controlled Fusion* **39**:1409, 1997.
- [35] P. Dennery and A. Krzywicki. *Mathematics for physicists*. Dover Publications, New York, NY, USA, 1996.
- [36] R. V. Budny, et al. Benchmarking ICRF full-wave solvers for ITER. *Nuclear Fusion* **52**:023023, 2012.
- [37] M. Brambilla and T. Krücken. Numerical simulation of ion cyclotron heating of hot tokamak plasmas. *Nuclear Fusion* **28**:1813, 1988.
- [38] I. S. Gradshteyn and I. M. Ryzhik. *Table of Integrals, Series and Products*. Academic Press, San Diego, CA, USA, 1994.
- [39] J. Hedin, et al. The influence of finite drift orbit width on ICRF heating in toroidal plasmas. *Nuclear Fusion* **42**(5):527, 2002.
- [40] T. Hellsten, et al. Effects of finite drift orbit width and RF-induced spatial transport on plasma heated by ICRH. *Nuclear Fusion* **44**(8):892, 2004.
- [41] A. J. Lichtenberg and M. A. Lieberman. *Regular and chaotic dynamics*. Applied mathematical sciences. Springer, New York, Berlin, Heidelberg, 1992.
- [42] V. B. M. Schneider, L.-G. Eriksson and F. Imbeaux. On alpha particle effects in tokamaks with a current hole. *Plasma Physics Controlled Fusion* **47**:2087, 2005.
- [43] R. Dumont, et al. Advanced simulation of energetic ion populations in the presence of NBI and RF sources. In *Proceedings of the 41st EPS conference on Plasma Physics, Berlin (2014)*, page P2.038. 2015.
- [44] M. Schneider, et al. A rapid fast ion FokkerPlanck solver for integrated modelling of tokamaks. *Nuclear Fusion* **55**(1):013003, 2015.
- [45] A. Bécoulet, et al. Hamiltonian analysis of fast wave current drive in tokamak plasmas. *Physics of Plasmas* **1**:2908, 1994.
- [46] J. R. Myra, et al. Nonlinear fluxes and forces from radio-frequency waves with application to driven flows in tokamaks. *Physics of Plasmas* **11**:1786, 2004.
- [47] T. H. Stix. Fast wave heating of a two-component plasma. *Nuclear Fusion* **15**:737, 1975.
- [48] C. F. Kennel and F. Engelmann. Velocity space diffusion from weak plasma turbulence in a magnetic field. *Phys. Fluids* **9**:2377, 1966.
- [49] E. Jaeger, L. Berry, and D. Batchelor. Reduced order methods for full wave ICRF calculations in tokamaks. *Nuclear Fusion* **38**(3):437, 1998.

- [50] L. D. Landau. Kinetic equation for the Coulomb effect. *Phys. Z. Sowjetunion* **10**:154, 1936.
- [51] B. A. Trubnikov. *Reviews of Plasma Physics*, volume 1, page 105. Consultant Bureau, New York, m.a. leontovitch edition, 1965.
- [52] C. F. F. Karney. Fokker-Planck and quasilinear codes. *Comp. Phys. Rep.* **4**:183, 1986.
- [53] D. Van Eester and E. Lerche. Simple 1D FokkerPlanck modelling of ion cyclotron resonance frequency heating at arbitrary cyclotron harmonics accounting for Coulomb relaxation on non-Maxwellian populations. *Plasma Physics Controlled Fusion* **53**(9):092001, 2011.
- [54] N. J. Fisch. Physics of alpha channelling and related TFTR experiments. *Nuclear Fusion* **40**(6):1095, 2000.
- [55] N. J. Fisch. Confining a tokamak plasma with rf-driven currents. *Physical Review Letters* **41**:873, 1978.
- [56] D. V. Houtte, et al. Recent fully non-inductive operation results in Tore Supra with 6min, 1GJ plasma discharges. *Nuclear Fusion* **44**:L11, 2004.
- [57] T. M. Antonsen and K. R. Chu. Radio frequency current generation by waves in toroidal geometry. *Phys. Fluids* **25**:1295, 1982.
- [58] N. J. Fisch. Theory of current drive in plasmas. *Rev. Mod. Physics* **59**:175, 1987.
- [59] R. J. Dumont and G. Giruzzi. Theory of synergy between electron cyclotron and lower hybrid waves. *Physics of Plasmas* **11**(7):3449, 2004.
- [60] G. Giruzzi, et al. Synergy of Electron-Cyclotron and Lower-Hybrid Current Drive in Steady-State Plasmas. *Physical Review Letters* **93**:255002, 2004.
- [61] R. J. Dumont and G. Giruzzi. Synergy in RF Current Drive. *AIP Conference Proceedings* **787**(1):257, 2005.
- [62] M. Schneider, et al. Modelling third harmonic ion cyclotron acceleration of deuterium beams for JET fusion product studies experiments. *Nuclear Fusion* **56**(11):112022, 2016.
- [63] T. Pütterich, et al. Observations on the W-transport in the core plasma of JET and ASDEX Upgrade. *Plasma Physics and Controlled Fusion* **55**(12):124036, 2013.
- [64] R. Neu, et al. Impurity behaviour in the ASDEX Upgrade divertor tokamak with large area tungsten walls. *Plasma Physics and Controlled Fusion* **44**(6):811, 2002.
- [65] C. Angioni, et al. Tungsten transport in JET H-mode plasmas in hybrid scenario, experimental observations and modelling. *Nuclear Fusion* **54**(8):083028, 2014.

- [66] C. Angioni and P. Helander. Neoclassical transport of heavy impurities with poloidally asymmetric density distribution in tokamaks. *Plasma Physics and Controlled Fusion* **56**(12):124001, 2014.
- [67] C. Angioni, et al. The impact of poloidal asymmetries on tungsten transport in the core of JET H-mode plasmas. *Physics of Plasmas* **22**(5):055902, 2015.
- [68] F. J. Casson, et al. Theoretical description of heavy impurity transport and its application to the modelling of tungsten in JET and ASDEX upgrade. *Plasma Physics and Controlled Fusion* **57**(1):014031, 2015.
- [69] M. Goniche, et al. Ion cyclotron resonance heating for tungsten control in various JET H-mode scenarios. *Plasma Physics Controlled Fusion* **59**(5):055001, 2017.
- [70] T. C. Hender, et al. The role of MHD in causing impurity peaking in JET Hybrid plasmas. *ArXiv e-prints* 2015.
- [71] D. J. Campbell, et al. Stabilization of Sawteeth with Additional Heating in the JET Tokamak. *Physical Review Letters* **60**:2148, 1988.
- [72] C. K. Phillips, et al. Ion cyclotron range of frequencies stabilization of sawteeth on Tokamak Fusion Test Reactor. *Physics of Fluids B* **4**(7):2155, 1992.
- [73] I. T. Chapman, et al. The physics of sawtooth stabilization. *Plasma Physics and Controlled Fusion* **49**(12B):B385, 2007.
- [74] O. Sauter, et al. Control of Neoclassical Tearing Modes by Sawtooth Control. *Physical Review Letters* **88**:105001, 2002.
- [75] J. P. Graves, et al. Control of magnetohydrodynamic stability by phase space engineering of energetic ions in tokamak plasmas. *Nat. Commun.* **3**:624, 2012.
- [76] M. Lennholm, et al. Demonstration of Effective Control of Fast-Ion-Stabilized Sawteeth by Electron-Cyclotron Current Drive. *Physical Review Letters* **102**:115004, 2009.
- [77] M. Lennholm, et al. Closed Loop Sawtooth Period Control Using Variable ECCD Injection Angles on Tore Supra. *Fusion Science and Technology* **55**(1):45, 2009.
- [78] M. Lennholm, et al. Feedback control of the sawtooth period through real time control of the ion cyclotron resonance frequency. *Nuclear Fusion* **51**(7):073032, 2011.
- [79] J. P. Graves, et al. Sawtooth Evolution during JET Ion-Cyclotron-Resonance-Heated Pulses. *Physical Review Letters* **84**:1204, 2000.
- [80] J. P. Graves, et al. Sawtooth-Control Mechanism using Toroidally Propagating Ion-Cyclotron-Resonance Waves in Tokamaks. *Physical Review Letters* **102**:065005, 2009.

- [81] J. P. Graves, et al. Sawtooth control in JET with ITER relevant low field side resonance ion cyclotron resonance heating and ITER-like wall. *Plasma Physics and Controlled Fusion* **57**(1):014033, 2015.
- [82] M. Lennholm, et al. Real-time control of ELM and sawtooth frequencies: similarities and differences. *Nuclear Fusion* **56**(1):016008, 2016.
- [83] K. L. Wong, et al. Excitation of toroidal Alfvén eigenmodes in TFTR. *Physical Review Letters* **66**:1874, 1991.
- [84] W. W. Heidbrink, et al. An investigation of beam driven Alfvén instabilities in the DIII-D tokamak. *Nuclear Fusion* **31**(9):1635, 1991.
- [85] S. Ali-Arshad and D. J. Campbell. Observation of TAE activity in JET. *Plasma Physics and Controlled Fusion* **37**(7):715, 1995.
- [86] M. Saigusa, et al. Investigation of high-n TAE modes excited by minority-ion cyclotron heating in JT-60U. *Plasma Physics and Controlled Fusion* **37**(3):295, 1995.
- [87] A. Fasoli, et al. Alfvén eigenmode experiments in tokamaks and stellarators. *Plasma Physics and Controlled Fusion* **39**(12B):B287, 1997.
- [88] D. Borba, et al. Destabilization of TAE modes using ICRH in ASDEX Upgrade. *Plasma Physics and Controlled Fusion* **46**(5):809, 2004.
- [89] F. Zonca, et al. Energetic particles and multi-scale dynamics in fusion plasmas. *Plasma Physics and Controlled Fusion* **57**(1):014024, 2015.
- [90] W. Zhang, Z. Lin, and L. Chen. Transport of Energetic Particles by Microturbulence in Magnetized Plasmas. *Physical Review Letters* **101**:095001, 2008.
- [91] P. H. Diamond, et al. Zonal flows in plasmas a review. *Plasma Physics and Controlled Fusion* **47**(5):R35, 2005.
- [92] N. Winsor, J. L. Johnson, and J. M. Dawson. Geodesic Acoustic Waves in Hydro-magnetic Systems. *Physics of Fluids* **11**(11):2448, 1968.
- [93] T. S. Hahm. Rotation shear induced fluctuation decorrelation in a toroidal plasma. *Physics of Plasmas* **1**(9):2940, 1994.
- [94] G. D. Conway, et al. Mean and Oscillating Plasma Flows and Turbulence Interactions across the *L-H* Confinement Transition. *Physical Review Letters* **106**:065001, 2011.
- [95] G. Y. Fu. Energetic-Particle-Induced Geodesic Acoustic Mode. *Physical Review Letters* **101**:185002, 2008.
- [96] Z. Qiu, F. Zonca, and L. Chen. Nonlocal theory of energetic-particle-induced geodesic acoustic mode. *Plasma Physics and Controlled Fusion* **52**(9):095003, 2010.
- [97] C. J. Boswell, et al. Observation and explanation of the JET chirping mode. *Physics Letters A* **358**(2):154, 2006.

- [98] R. Nazikian, et al. Intense Geodesic Acousticlike Modes Driven by Suprathermal Ions in a Tokamak Plasma. *Physical Review Letters* **101**:185001, 2008.
- [99] D. Zarzoso, et al. Fully kinetic description of the linear excitation and nonlinear saturation of fast-ion-driven geodesic acoustic mode instability. *Physics of Plasmas* **19**(2):022102, 2012.
- [100] D. Zarzoso, et al. Impact of Energetic-Particle-Driven Geodesic Acoustic Modes on Turbulence. *Physical Review Letters* **110**:125002, 2013.
- [101] R. J. Dumont, et al. Interplay between fast ions and turbulence in magnetic fusion plasmas. *Plasma Physics and Controlled Fusion* **55**(12):124012, 2013.
- [102] J.-B. Girardo, et al. Relation between energetic and standard geodesic acoustic modes. *Physics of Plasmas* **21**(9):092507, 2014.
- [103] G. G. Craddock and P. H. Diamond. Theory of shear suppression of edge turbulence by externally driven radio-frequency waves. *Physical Review Letters* **67**:1535, 1991.
- [104] B. LeBlanc, et al. Active core profile and transport modification by application of ion Bernstein wave power in the Princeton Beta Experiment Modification. *Physics of Plasmas* **2**(3):741, 1995.
- [105] R. Cesario, et al. Reduction of the electron thermal conductivity produced by ion Bernstein waves on the Frascati Tokamak Upgrade tokamak. *Physics of Plasmas* **8**(11):4721, 2001.
- [106] B. P. LeBlanc, et al. Direct Observation of Ion-Bernstein-Wave-Induced Poloidal Flow in TFTR. *Physical Review Letters* **82**:331, 1999.
- [107] C. K. Phillips, et al. ICRF heating and profile control techniques in TFTR. *Nuclear Fusion* **40**(3Y):461, 2000.
- [108] F. W. Perkins. Heating tokamaks via the ion-cyclotron and ion-ion hybrid resonances. *Nuclear Fusion* **17**(6):1197, 1977.
- [109] E. Nelson-Melby, et al. Experimental Observations of Mode-Converted Ion Cyclotron Waves in a Tokamak Plasma by Phase Contrast Imaging. *Physical Review Letters* **90**:155004, 2003.
- [110] E. F. Jaeger, et al. Sheared Poloidal Flow Driven by Mode Conversion in Tokamak Plasmas. *Physical Review Letters* **90**:195001, 2003.
- [111] J. R. Myra and D. A. D'Ippolito. Poloidal force generation by applied radio frequency waves. *Physics of Plasmas* **7**(9):3600, 2000.
- [112] J. R. Myra, et al. Nonlinear ICRF-plasma interactions. *Nuclear Fusion* **46**(7):S455, 2006.
- [113] T. Hellsten. Momentum transport by waveparticle interaction. *Plasma Physics and Controlled Fusion* **53**(5):054007, 2011.

- [114] E. F. Jaeger, L. A. Berry, and D. B. Batchelor. Second-order radio frequency kinetic theory with applications to flow drive and heating in tokamak plasmas. *Physics of Plasmas* **7**(2):641, 2000.
- [115] E. F. Jaeger, et al. Self-consistent full-wave and Fokker-Planck calculations for ion cyclotron heating in non-Maxwellian plasmas. *Physics of Plasmas* **13**:056101, 2006.
- [116] Y. Lin, et al. Observation of Ion-Cyclotron-Frequency Mode-Conversion Flow Drive in Tokamak Plasmas. *Physical Review Letters* **101**:235002, 2008.
- [117] Y. Lin, et al. ICRF mode conversion flow drive on Alcator C-Mod. *Nuclear Fusion* **51**(6):063002, 2011.
- [118] Y. Lin, et al. Ion cyclotron range of frequency mode conversion flow drive in D(3 He) plasmas on JET. *Plasma Physics and Controlled Fusion* **54**(7):074001, 2012.
- [119] N. J. Fisch and M. C. Herrmann. Utility of extracting alpha particle energy by waves. *Nuclear Fusion* **34**(12):1541, 1994.
- [120] N. J. Fisch and J.-M. Rax. Interaction of energetic alpha particles with intense lower hybrid waves. *Physical Review Letters* **69**:612, 1992.
- [121] N. J. Fisch and M. C. Herrmann. Alpha power channelling with two waves. *Nuclear Fusion* **35**(12):1753, 1995.
- [122] M. C. Herrmann and N. J. Fisch. Cooling Energetic α Particles in a Tokamak with Waves. *Physical Review Letters* **79**:1495, 1997.
- [123] P. Lauber. Private communication, 2016.
- [124] D. S. Clark and N. J. Fisch. The possibility of high amplitude driven contained modes during ion Bernstein wave experiments in the tokamak fusion test reactor. *Physics of Plasmas* **7**(7):2923, 2000.
- [125] N. N. Gorelenkov, N. J. Fisch, and E. Fredrickson. On the anomalous fast ion energy diffusion in toroidal plasmas due to cavity modes. *Plasma Physics and Controlled Fusion* **52**(5):055014, 2010.
- [126] A. B. Mikhailovskii. Generalized MHD for numerical stability analysis of high-performance plasmas in tokamaks. *Plasma Physics Control. Fusion* **40**:1907, 1998.
- [127] E. F. Jaeger, et al. All-orders spectral calculation of radio-frequency heating in two-dimensional toroidal plasmas. *Physics of Plasmas* **8**(5):1573, 2001.
- [128] M. Brambilla and R. Bilato. Advances in numerical simulations of ion cyclotron heating of non-Maxwellian plasmas. *Nuclear Fusion* **49**(8):085004, 2009.
- [129] D. Anderson, L.-G. Eriksson, and M. Lisak. Analytical treatment of the distortion of velocity distributions in the presence of ICRH. *Nuclear Fusion* **25**(12):1751, 1985.

- [130] D. Anderson, et al. Distortion of ion velocity distributions in the presence of ICRH: A semi-analytical analysis. *Nuclear Fusion* **27**(6):911, 1987.
- [131] R. Dumont and G. Giruzzi. Hot plasma effects on the polarization of electron cyclotron waves. *Physics of Plasmas* **6**(3):660, 1999.
- [132] B. Pégourié, et al. Modelling of pellet ablation in additionally heated plasmas. *Plasma Physics and Controlled Fusion* **47**(1):17, 2005.
- [133] R. Dumont, G. Giruzzi, and E. Barbato. Combined kinetic and transport modeling of radiofrequency current drive. *Physics of Plasmas* **7**(12):4972, 2000.
- [134] E. Joffrin, et al. Integrated plasma controls for steady state scenarios. *Nuclear Fusion* **47**(12):1664, 2007.
- [135] G. Giruzzi, et al. Investigation of steady-state tokamak issues by long pulse experiments on Tore Supra. *Nuclear Fusion* **49**(10):104010, 2009.
- [136] B. Chouli, et al. Co- and counter-current rotation in Tore Supra lower hybrid current drive plasmas. *Plasma Physics and Controlled Fusion* **56**(9):095018, 2014.
- [137] F. Imbeaux, et al. Real-time control of the safety factor profile diagnosed by magneto-hydrodynamic activity on the Tore Supra tokamak. *Nuclear Fusion* **51**(7):073033, 2011.
- [138] R. J. Dumont, C. K. Phillips, and D. N. Smithe. Effects of non-Maxwellian species on ion cyclotron waves propagation and absorption in magnetically confined plasmas. *Physics of Plasmas* **12**(4):042508, 2005.
- [139] J. C. Wright, et al. Nonthermal particle and full-wave diffraction effects on heating and current drive in the ICRF and LHRF regimes. *Nuclear Fusion* **45**(11):1411, 2005.
- [140] E. F. Jaeger, et al. Global-wave solutions with self-consistent velocity distributions in ion cyclotron heated plasmas. *Nuclear Fusion* **46**(7):S397, 2006.
- [141] D. Zarzoso, et al. Analytic dispersion relation of energetic particle driven geodesic acoustic modes and simulations with NEMORB. *Nuclear Fusion* **54**(10):103006, 2014.
- [142] J. Citrin, et al. Ion temperature profile stiffness: non-linear gyrokinetic simulations and comparison with experiment. *Nuclear Fusion* **54**(2):023008, 2014.
- [143] H. Nordman, et al. Influence of the radio frequency ponderomotive force on anomalous impurity transport in tokamaks. *Physics of Plasmas* **15**(4):042316, 2008.
- [144] N. Fedorczak, et al. Tungsten transport and sources control in JET ITER-like wall H-mode plasmas. *Journal of Nuclear Materials* **463**:85, 2015.
- [145] E. Lerche, et al. Optimization of ICRH for core impurity control in JET-ILW. *Nuclear Fusion* **56**(3):036022, 2016.

- [146] J.-B. Girardo, et al. Stabilization of sawteeth with third harmonic deuterium ICRF-accelerated beam in JET plasmas. *Physics of Plasmas* **23**(1):012505, 2016.
- [147] C. Darbos, et al. The 118 GHz ECRH experiment on Tore Supra. *Fusion Engineering and Design* **5657**:605 , 2001.
- [148] X. L. Zou, et al. Electron heat transport and ECRH modulation experiments in Tore Supra tokamak. *Nuclear Fusion* **43**(11):1411, 2003.
- [149] R. Abgrall, et al. Tore Supra Team Members 1988-2008. *Fusion Science and Technology* **56**(3):1453, 2009.
- [150] A. Ekedahl, et al. Operational limits during high power long pulses with radiofrequency heating in Tore Supra. *Nuclear Fusion* **49**(9):095010, 2009.
- [151] F. Turco, et al. O-regime dynamics and modeling in Tore Supra. *Physics of Plasmas* **16**(6):062301, 2009.
- [152] Y. Corre, et al. Heat flux calculation and problem of flaking of boron carbide coatings on the Faraday screen of the ICRH antennas during Tore Supra high power, long pulse operation. *Fusion Engineering and Design* **86**(45):429 , 2011.
- [153] A. Lysoivan, et al. ICRF physics aspects of wall conditioning with conventional antennas in large-size tokamaks. *Journal of Nuclear Materials* **415**(1):S1029 , 2011. Proceedings of the 19th International Conference on Plasma-Surface Interactions in Controlled Fusion.
- [154] B. Saoutic, et al. Contribution of Tore Supra in preparation of ITER. *Nuclear Fusion* **51**(9):094014, 2011.
- [155] A. Bécoulet, et al. Science and technology research and development in support to ITER and the Broader Approach at CEA. *Nuclear Fusion* **53**(10):104023, 2013.
- [156] J. Hillairet, et al. Recent progress on lower hybrid current drive and implications for ITER. *Nuclear Fusion* **53**(7):073004, 2013.
- [157] X. Litaudon, et al. Physics and technology in the ion-cyclotron range of frequency on Tore Supra and TITAN test facility: implication for ITER. *Nuclear Fusion* **53**(8):083012, 2013.
- [158] B. Cambon, et al. Chaotic motion of charged particles in toroidal magnetic configurations. *Chaos* **24**(3):033101, 2014.
- [159] L. Delpech, et al. Advances in multi-megawatt lower hybrid technology in support of steady-state tokamak operation. *Nuclear Fusion* **54**(10):103004, 2014.
- [160] M. Goniche, et al. Advances in long pulse operation at high radio frequency power in Tore Supra. *Physics of Plasmas* **21**(6):061515, 2014.
- [161] F. Romanelli, on behalf of JET Contributors. Overview of the JET results. *Nuclear Fusion* **55**(10):104001, 2015.

Appendix E

Selected publications

We have attempted to gather selected publications in the diagramme shown in Fig. 1.3. The result is contained in Fig. E.1 describing how most of them fit in the general scheme consisting of exploiting RF waves to improve the fusion performance.

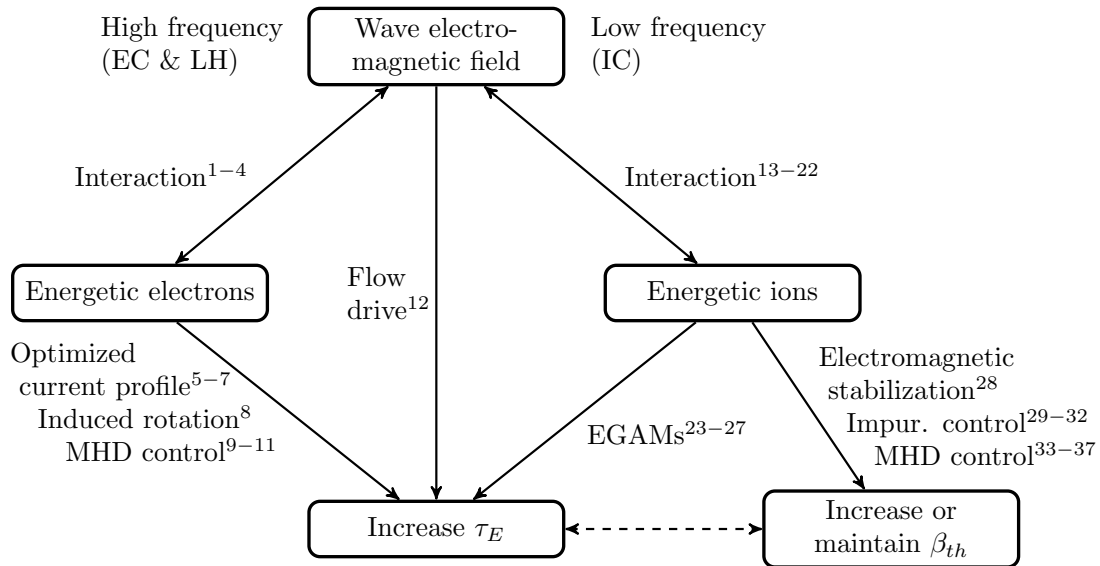


Figure E.1: Improving fusion yield by using radiofrequency waves to generate or influence energetic particle populations. The numbers in parentheses correspond to the publication list given below.

The entries marked with (†) in the following list have been included *in extenso* in the manuscript.

1. R. Dumont and G. Giruzzi. Hot plasma effects on the polarization of electron cyclotron waves. *Physics of Plasmas* **6**(3):660, 1999.
2. R. J. Dumont and G. Giruzzi. Theory of synergy between electron cyclotron and lower hybrid waves. *Physics of Plasmas* **11**(7):3449, 2004 (†).

3. G. Giruzzi, et al. Synergy of Electron-Cyclotron and Lower-Hybrid Current Drive in Steady-State Plasmas. *Physical Review Letters* **93**:255002, 2004.
4. B. Pégourié, et al. Modelling of pellet ablation in additionally heated plasmas. *Plasma Physics and Controlled Fusion* **47**(1):17, 2005.
5. R. Dumont, G. Giruzzi, and E. Barbato. Combined kinetic and transport modeling of radiofrequency current drive. *Physics of Plasmas* **7**(12):4972, 2000.
6. E. Joffrin, et al. Integrated plasma controls for steady state scenarios. *Nuclear Fusion* **47**(12):1664, 2007.
7. G. Giruzzi, et al. Investigation of steady-state tokamak issues by long pulse experiments on Tore Supra. *Nuclear Fusion* **49**(10):104010, 2009.
8. B. Chouli, et al. Co- and counter-current rotation in Tore Supra lower hybrid current drive plasmas. *Plasma Physics and Controlled Fusion* **56**(9):095018, 2014.
9. M. Lennholm, et al. Demonstration of Effective Control of Fast-Ion-Stabilized Sawteeth by Electron-Cyclotron Current Drive. *Physical Review Letters* **102**:115004, 2009.
10. M. Lennholm, et al. Closed Loop Sawtooth Period Control Using Variable ECCD Injection Angles on Tore Supra. *Fusion Science and Technology* **55**(1):45, 2009.
11. F. Imbeaux, et al. Real-time control of the safety factor profile diagnosed by magneto-hydrodynamic activity on the Tore Supra tokamak. *Nuclear Fusion* **51**(7):073033, 2011.
12. E. F. Jaeger, et al. Sheared Poloidal Flow Driven by Mode Conversion in Tokamak Plasmas. *Physical Review Letters* **90**:195001, 2003.
13. R. J. Dumont, C. K. Phillips, and D. N. Smithe. Effects of non-Maxwellian species on ion cyclotron waves propagation and absorption in magnetically confined plasmas. *Physics of Plasmas* **12**(4):042508, 2005 (†).
14. J. C. Wright, et al. Nonthermal particle and full-wave diffraction effects on heating and current drive in the ICRF and LHRF regimes. *Nuclear Fusion* **45**(11):1411, 2005.
15. E. F. Jaeger, et al. Self-consistent full-wave and Fokker-Planck calculations for ion cyclotron heating in non-Maxwellian plasmas. *Physics of Plasmas* **13**:056101, 2006.
16. E. F. Jaeger, et al. Global-wave solutions with self-consistent velocity distributions in ion cyclotron heated plasmas. *Nuclear Fusion* **46**(7):S397, 2006.
17. R. J. Dumont. Variational approach to radiofrequency waves in magnetic fusion devices. *Nuclear Fusion* **49**:075033, 2009 (†).
18. R. J. Dumont and D. Zarzoso. Heating and current drive by ion cyclotron waves in the activated phase of ITER. *Nuclear Fusion* **53**(1):013002, 2013 (†).

-
19. Y. O. Kazakov, et al. On resonant ICRF absorption in three-ion component plasmas: a new promising tool for fast ion generation. *Nuclear Fusion* **55**(3):032001, 2015.
 20. Y. O. Kazakov, et al. A new ion cyclotron range of frequency scenario for bulk ion heating in deuterium-tritium plasmas: How to utilize intrinsic impurities in our favour. *Physics of Plasmas* **22**(8):082511, 2015.
 21. M. Schneider, et al. A rapid fast ion FokkerPlanck solver for integrated modelling of tokamaks. *Nuclear Fusion* **55**(1):013003, 2015.
 22. M. Schneider, et al. Modelling third harmonic ion cyclotron acceleration of deuterium beams for JET fusion product studies experiments. *Nuclear Fusion* **56**(11):112022, 2016
 23. D. Zarzoso, et al. Fully kinetic description of the linear excitation and nonlinear saturation of fast-ion-driven geodesic acoustic mode instability. *Physics of Plasmas* **19**(2):022102, 2012.
 24. R. J. Dumont, et al. Interplay between fast ions and turbulence in magnetic fusion plasmas. *Plasma Physics and Controlled Fusion* **55**(12):124012, 2013 (†).
 25. D. Zarzoso, et al. Impact of Energetic-Particle-Driven Geodesic Acoustic Modes on Turbulence. *Physical Review Letters* **110**:125002, 2013.
 26. J.-B. Girardo, et al. Relation between energetic and standard geodesic acoustic modes. *Physics of Plasmas* **21**(9):092507, 2014.
 27. D. Zarzoso, et al. Analytic dispersion relation of energetic particle driven geodesic acoustic modes and simulations with NEMORB. *Nuclear Fusion* **54**(10):103006, 2014.
 28. J. Citrin, et al. Ion temperature profile stiffness: non-linear gyrokinetic simulations and comparison with experiment. *Nuclear Fusion* **54**(2):023008, 2014.
 29. H. Nordman, et al. Influence of the radio frequency ponderomotive force on anomalous impurity transport in tokamaks. *Physics of Plasmas* **15**(4):042316, 2008.
 30. N. Fedorczak, et al. Tungsten transport and sources control in JET ITER-like wall H-mode plasmas. *Journal of Nuclear Materials* **463**:85, 2015.
 31. E. Lerche, et al. Optimization of ICRH for core impurity control in JET-ILW. *Nuclear Fusion* **56**(3):036022, 2016
 32. M. Goniche, et al. Ion cyclotron resonance heating for tungsten control in various JET H-mode scenarios. *Plasma Physics Controlled Fusion* **59**(5):055001, 2017
 33. M. Lennholm, et al. Feedback control of the sawtooth period through real time control of the ion cyclotron resonance frequency. *Nuclear Fusion* **51**(7):073032, 2011.
 34. R. J. Dumont, et al. Multi-megawatt, gigajoule plasma operation in Tore Supra. *Plasma Physics and Controlled Fusion* **56**(7):075020, 2014 (†).

35. J. P. Graves, et al. Sawtooth control in JET with ITER relevant low field side resonance ion cyclotron resonance heating and ITER-like wall. *Plasma Physics and Controlled Fusion* **57**(1):014033, 2015.
36. J.-B. Girardo, et al. Stabilization of sawteeth with third harmonic deuterium ICRF-accelerated beam in JET plasmas. *Physics of Plasmas* **23**(1):012505, 2016.
37. M. Lennholm, et al. Real-time control of ELM and sawtooth frequencies: similarities and differences. *Nuclear Fusion* **56**(1):016008, 2016.
38. C. Darbos, et al. The 118 GHz ECRH experiment on Tore Supra. *Fusion Engineering and Design* **5657**:605 , 2001.
39. X. L. Zou, et al. Electron heat transport and ECRH modulation experiments in Tore Supra tokamak. *Nuclear Fusion* **43**(11):1411, 2003.
40. R. Abgrall, et al. Tore Supra Team Members 1988-2008. *Fusion Science and Technology* **56**(3):1453, 2009.
41. A. Ekedahl, et al. Operational limits during high power long pulses with radiofrequency heating in Tore Supra. *Nuclear Fusion* **49**(9):095010, 2009.
42. F. Turco, et al. O-regime dynamics and modeling in Tore Supra. *Physics of Plasmas* **16**(6):062301, 2009.
43. J.-F. Artaud, et al. The CRONOS suite of codes for integrated tokamak modelling. *Nuclear Fusion* **50**(4):043001, 2010.
44. Y. Corre, et al. Heat flux calculation and problem of flaking of boron carbide coatings on the Faraday screen of the ICRH antennas during Tore Supra high power, long pulse operation. *Fusion Engineering and Design* **86**(45):429 , 2011.
45. A. Lysoivan, et al. ICRF physics aspects of wall conditioning with conventional antennas in large-size tokamaks. *Journal of Nuclear Materials* **415**(1):S1029 , 2011. Proceedings of the 19th International Conference on Plasma-Surface Interactions in Controlled Fusion.
46. B. Saoutic, et al. Contribution of Tore Supra in preparation of ITER. *Nuclear Fusion* **51**(9):094014, 2011.
47. R. V. Budny, et al. Benchmarking ICRF full-wave solvers for ITER. *Nuclear Fusion* **52**:023023, 2012.
48. E. Lerche, et al. Optimizing ion-cyclotron resonance frequency heating for ITER: dedicated JET experiments. *Plasma Physics and Controlled Fusion* **54**(6):069601, 2012.
49. A. Bécoulet, et al. Science and technology research and development in support to ITER and the Broader Approach at CEA. *Nuclear Fusion* **53**(10):104023, 2013.

-
50. J. Hillairet, et al. Recent progress on lower hybrid current drive and implications for ITER. *Nuclear Fusion* **53**(7):073004, 2013.
 51. X. Litaudon, et al. Physics and technology in the ion-cyclotron range of frequency on Tore Supra and TITAN test facility: implication for ITER. *Nuclear Fusion* **53**(8):083012, 2013.
 52. B. Cambon, et al. Chaotic motion of charged particles in toroidal magnetic configurations. *Chaos* **24**(3):033101, 2014.
 53. L. Delpech, et al. Advances in multi-megawatt lower hybrid technology in support of steady-state tokamak operation. *Nuclear Fusion* **54**(10):103004, 2014.
 54. M. Goniche, et al. Advances in long pulse operation at high radio frequency power in Tore Supra. *Physics of Plasmas* **21**(6):061515, 2014.
 55. C. Bourdelle, et al. WEST Physics Basis. *Nuclear Fusion* **55**(6):063017, 2015.
 56. F. Romanelli, on behalf of JET Contributors. Overview of the JET results. *Nuclear Fusion* **55**(10):104001, 2015.

Theory of synergy between electron cyclotron and lower hybrid waves

R. J. Dumont^{a)} and G. Giruzzi

Association EURATOM-CEA sur la Fusion, CEA/DSM/DRFC CEA-Cadarache,
13108 Saint-Paul-lez-Durance, France

(Received 29 September 2003; accepted 16 March 2004; published online 7 June 2004)

A theoretical study of the improvement of the electron cyclotron current drive (ECCD) efficiency in regimes in which most of the current is driven by lower hybrid (LH) waves is presented. A perturbation technique is employed to solve the adjoint equation and derive the response function including both collisional and LH effects in the limit where the former dominate. An alternative treatment of the problem, involving a numerical solution of the Langevin equations, is proposed to gain insight into the current drive mechanism and to confirm the obtained results. The existence of a cross-effect between the two waves is demonstrated and the conditions for the synergy (i.e., significant enhancement of the ECCD efficiency in the presence of LH power) are identified. © 2004 American Institute of Physics. [DOI: 10.1063/1.1739234]

I. INTRODUCTION

Among the desirable features of a future tokamak-based fusion reactor is its steady-state operation, which implies that the toroidal current has to be totally sustained by noninductive sources.¹ Moreover, in ongoing as well as in future experiments, a sharp tailoring of the current profiles is known to have a favorable effect on the plasma confinement. These prerequisites are key elements of the advanced tokamak concept, which relies on the fact that a large fraction of the plasma current is supplied by the bootstrap current, generally triggered and supplemented by injecting neutral beams of rf waves in the plasma.²

A wide class of waves can be launched in the plasma, yet, for current drive purposes, the excitation of superthermal electrons has been the most successful method, in accordance with theoretical predictions.¹ Lower hybrid current drive (LHCD) is a well-tested and efficient method,^{3–5} based on Landau damping of the wave power. Its main drawback is that in the so-called multipass regime, the current profile remains difficult to control and calculations still lack full reliability. Note, however, that in very hot plasmas, the wave is expected to be absorbed without relying on any subtle upshift mechanism (single-pass absorption), which makes the LH wave a serious candidate to drive off-axis current in future experiments.⁴ On the other hand, electron cyclotron (EC) waves exploit the resonance with the electron gyromotion and are characterized by a narrow deposition, thus providing a means to induce a local modification of the current profile. The efficiency, however, is known to be significantly lower than for LH waves.⁶

Owing to these complementary features, combined schemes, in which LH and EC waves are used together, constitute an appealing solution for advanced tokamak discharges. In particular, both waves are expected to exert a cross-effect on superthermal electrons, often and sometimes improperly referred to as the LH-EC synergy effect. The

consequences of this cross-effect encompass the possibility to modify the LH superthermal tail, a better absorption of EC waves, and an improvement of the ECCD efficiency, which may help in controlling the current profile as predicted by numerical solutions of the Fokker–Planck equation.^{7–12} Self-consistent, dynamical calculations, including waves kinetic and heat transport effects, have stressed the advantages of such scenarios, but, owing to the nonlinear nature of these simulations, the various effects are difficult to separate.¹³ Experimentally, a cross-effect has been observed under certain conditions, but the interpretation of these measurements are difficult and have led to contradictory conclusions, due either to their transient character or to very large fast particle losses.^{14–17} More recently, a hard x-ray camera¹⁸ has been employed to analyze the emission of fast electrons in the presence of LH and EC waves during the current flat-top phase on the Tore Supra¹⁹ and the Frascati Tokamak Upgrade (FTU)²⁰ tokamaks. In both experiments, a response of the high-energy channels was observed, compatible with the existence of a cross-effect, but, due to the relatively low applied EC power, no conclusive observation could be made in terms of ECCD efficiency.

Despite these numerical and experimental results, and owing to the lack of a simple mechanism to explain the cross-effect of both waves on fast electrons, this subject is still being debated. The goal of this paper is thus to study the combined current drive process from a theoretical standpoint and to identify the conditions for the existence of a LH-EC synergy. To this aim, the adjoint method, originally proposed by Antonsen and Chu²¹ and generalized to the rf current drive problem by Fisch,¹ is extended to a situation in which two waves are simultaneously present in the plasma. Another possible method is to solve the Langevin equations, which track individual electron relaxation paths and deduce quantities of interest for the current drive problem by averaging over statistical realizations.²² These two complementary methods are employed to derive the response function, which leads to an estimate of the current drive efficiency, including

^{a)}Electronic mail: remi.dumont@cea.fr

the cross-effect and therefore the possibility of a LH-EC synergy.

This article is organized as follows. After the presentation of the kinetic aspect of the problem in Sec. II, the adjoint method is employed to compute an approximate expression of the response function for a LHCD plasma in Sec. III. Section IV is devoted to the study of the dynamics underlying the rf current drive process, through the derivation of the associated Langevin equations. The properties of the response function obtained with these two methods are examined in Sec. V. The practical consequences of the presence of LH waves on the ECCD are discussed in Sec. VI, where the synergy effect is demonstrated. Conclusions are drawn in Sec. VII.

II. KINETIC MODELING OF LH+EC CURRENT DRIVE

In the absence of a static parallel electric field and including the effects of Coulomb collisions, and LH and EC waves, the kinetic equation can be written as

$$\frac{\partial f}{\partial \tau} - \hat{C}f = \hat{D}_{LH}f + \hat{D}_{EC}f. \quad (1)$$

In this expression, $\tau \equiv \nu_e t$ is the time in terms of the collision period ν_e^{-1} , f is the electron distribution function. $\mathbf{u} \equiv \mathbf{p}/\sqrt{m_e T_e}$ is the normalized momentum, with T_e the local electron temperature. \hat{C} is the linearized collision operator. In this paper, we shall assume that for any perturbed distribution function written as $f \equiv f_m(1 + \alpha)$, the high-velocity collision operator $\hat{C}f \equiv \hat{C}(f_m \alpha)$ is linearized according to $\hat{C}(f_m \alpha) = \hat{C}(f_m, f_m \alpha) + \hat{C}(f_m \alpha, f_m) + \hat{C}(f_m \alpha, f_i)$, f_i being the ion distribution function. If $\mu \equiv u_{\parallel}/u$ refers to the cosine of the pitch angle, it can be expressed as¹

$$\hat{C}f \equiv \frac{2}{u^2} \frac{\partial}{\partial u} \left(\frac{1}{u} \frac{\partial f}{\partial u} + f \right) + \frac{Z_i + 1}{u^3} \frac{\partial}{\partial \mu} (1 - \mu^2) \frac{\partial f}{\partial \mu}, \quad (2)$$

where Z_i is the plasma ion charge. \hat{D}_{LH} (\hat{D}_{EC}) is the quasilinear operator associated with LH (EC) waves, which is related to the corresponding quasilinear diffusion tensor $\bar{\mathbf{D}}_{LH}$ ($\bar{\mathbf{D}}_{EC}$) and flux \mathbf{S}_{LH} (\mathbf{S}_{EC}) by

$$\hat{D}_{LH}f = \frac{\partial}{\partial \mathbf{u}} \cdot \bar{\mathbf{D}}_{LH} \frac{\partial f}{\partial \mathbf{u}} = - \frac{\partial}{\partial \mathbf{u}} \cdot \mathbf{S}_{LH}, \quad (3)$$

and

$$\hat{D}_{EC}f = \frac{\partial}{\partial \mathbf{u}} \cdot \bar{\mathbf{D}}_{EC} \frac{\partial f}{\partial \mathbf{u}} = - \frac{\partial}{\partial \mathbf{u}} \cdot \mathbf{S}_{EC}. \quad (4)$$

The LH wave is absorbed in the plasma by Landau damping, which implies that $\bar{\mathbf{D}}_{LH}$ is dominated by its parallel-parallel component,²³ and the corresponding quasilinear operator can thus be written under the form

$$\hat{D}_{LH} \equiv \frac{D_{LH}}{\nu_e m_e T_e} \frac{\partial}{\partial u_{\parallel}} d_{LH}(u_{\parallel}) \frac{\partial}{\partial u_{\parallel}}, \quad (5)$$

where D_{LH} is a constant determined by the wave power, so that $D_{LH,0} \equiv D_{LH}/\nu_e m_e T_e$ quantifies the wave intensity compared to collisions. $d_{LH} \equiv d_{LH}(u_{\parallel})$ represents the shape of the

diffusion coefficient. Here, we consider a regime in which the electrons undergo the effects of the wave in a region of velocity space bounded by two limits, $u_{\parallel,1}$ and $u_{\parallel,2}$, determined by the propagation properties of the wave.¹³ The following shape is assumed:

$$d_{LH}(u_{\parallel}) \equiv \begin{cases} A_l \exp[-(u_{\parallel} - u_{\parallel,l})^2 / \Delta u_{\parallel,1}^2], & u_{\parallel} < u_{\parallel,1} \\ u_{\parallel,1} / u_{\parallel}, & u_{\parallel,1} \leq u_{\parallel} \leq u_{\parallel,2} \\ A_r \exp[-(u_{\parallel} - u_{\parallel,r})^2 / \Delta u_{\parallel,2}^2], & u_{\parallel} > u_{\parallel,2}. \end{cases} \quad (6)$$

A_r , A_l , $u_{\parallel,r}$, and $u_{\parallel,l}$ are constants whose values are determined by the requirement that both d_{LH} and $\partial d_{LH} / \partial u_{\parallel}$ be continuous at $u_{\parallel} = u_{\parallel,1}$ and $u_{\parallel} = u_{\parallel,2}$.

For the problem under discussion here, a useful form of the distribution function is $f \equiv f_m(1 + \phi + \delta\phi)$, where f_m is the Maxwellian. $f_m(1 + \phi)$ is the distribution function modified by application of the LH power, solution of

$$\frac{\partial f_m \phi}{\partial \tau} - \hat{C}(f_m \phi) = \hat{D}_{LH} f_m(1 + \phi). \quad (7)$$

Upon subtracting Eq. (7) from Eq. (1), we obtain the equation for $f_m \delta\phi$, given by

$$\begin{aligned} \frac{\partial f_m \delta\phi}{\partial \tau} - \hat{C}(f_m \delta\phi) &= \hat{D}_{EC} f_m(1 + \phi + \delta\phi) \\ &\quad + \hat{D}_{LH}(f_m \delta\phi), \end{aligned} \quad (8)$$

or equivalently

$$\frac{\partial f_m \delta\phi}{\partial \tau} - \hat{C}(f_m \delta\phi) - \hat{D}_{LH}(f_m \delta\phi) = - \frac{\partial}{\partial \mathbf{u}} \cdot \mathbf{S}_{EC}. \quad (9)$$

In this expression, the right-hand term describes the electron excitation caused by the electron cyclotron waves, whereas $(\hat{C} + \hat{D}_{LH})(f_m \delta\phi)$ is representative of the relaxation under the combined effect of collisions and LH power.

The normalized current associated to f can be written as

$$j = \int d\mathbf{u} f_m(\phi + \delta\phi) \equiv j_0 + j_1, \quad (10)$$

where j_0 and j_1 are

$$j_0 \equiv \int d\mathbf{u} u_{\parallel} f_m \phi, \quad j_1 \equiv \int d\mathbf{u} u_{\parallel} f_m \delta\phi. \quad (11)$$

Note that up to this point, no approximation other than the fact that T_e and n_e , the electron temperature and density, are nonvarying on the time scale of the studied problem has been introduced. To evaluate the driven current, it is usual to resort to a Fokker-Planck code to compute the distribution function solution of Eq. (1). In this work, however, an analytical approach of the problem has been preferred. Even though it does not pretend to replace a comprehensive kinetic calculation, the linearization it is based on has the advantage of allowing a separate treatment of the two waves, which is impracticable in purely numerical calculations. This separation is the key to demonstrating unambiguously the possibility of a synergy effect.

To compute j_0 [Eq. (11)], it is necessary to solve Eq. (7). Following Eq. (3) the expression for the LH-induced quasilinear flux is

$$\mathbf{S}_{\text{LH}} = -\bar{\mathbf{D}}_{\text{LH}} \frac{\partial f_m(1 + \phi + \delta\phi)}{\partial \mathbf{u}}. \quad (12)$$

If \mathbf{S}_{LH} is not significantly modified by the presence of EC waves, or equivalently assuming that the shape of the distribution function is determined mainly by the effects of collisions and LH wave (i.e., $|\delta\phi| \ll |\phi|$), Eq. (7) can be rewritten as

$$\frac{\partial f_m \phi}{\partial \tau} - \hat{C}(f_m \phi) = -\frac{\partial}{\partial \mathbf{u}} \cdot \mathbf{S}_{\text{LH}}. \quad (13)$$

Introducing $g_0(\mathbf{u}, \mathbf{u}', \tau - \tau')$, the Green function associated with Eq. (13), solution of

$$\frac{\partial g_0}{\partial \tau} - \hat{C}g_0 = \delta(\mathbf{u} - \mathbf{u}') \delta(\tau - \tau'), \quad (14)$$

and defining the steady-state response function as

$$\chi_0(\mathbf{u}) \equiv \int_0^\infty d\tau' \int d\mathbf{u}' u'_\parallel g_0(\mathbf{u}, \mathbf{u}', \tau'), \quad (15)$$

j_0 is given by

$$j_0 = \int d\mathbf{u} \mathbf{S}_{\text{LH}} \cdot \frac{\partial \chi_0}{\partial \mathbf{u}}. \quad (16)$$

To compute j_1 , a similar treatment is applied to Eq. (8), introducing $g_1(\mathbf{u}, \mathbf{u}', \tau - \tau')$ the solution of the Green problem for Eq. (9). It solves

$$\frac{\partial g_1}{\partial \tau} - \hat{C}g_1 - \hat{D}_{\text{LHG}}g_1 = \delta(\mathbf{u} - \mathbf{u}') \delta(\tau - \tau'). \quad (17)$$

The associated steady-state response function is

$$\chi_1(\mathbf{u}) \equiv \int_0^\infty d\tau' \int d\mathbf{u}' u'_\parallel g_1(\mathbf{u}, \mathbf{u}', \tau'), \quad (18)$$

and allows one to evaluate j_1 using

$$j_1 = \int d\mathbf{u} \mathbf{S}_{\text{EC}} \cdot \frac{\partial \chi_1}{\partial \mathbf{u}}. \quad (19)$$

This method allows one to envision the CD mechanism as a two-step process:

- (1) A drive, whose features are contained in the expressions for the quasilinear fluxes \mathbf{S}_{LH} and \mathbf{S}_{EC} .
- (2) A relaxation, which is described by the response functions χ_0 and χ_1 .

The quasilinear fluxes contain the information on the distribution function, and their evaluation is a delicate task, generally involving a kinetic code. However, if one is merely interested in an estimation of the CD efficiency, as long as the interaction is well localized in velocity space, the information on the direction of these fluxes is known to be sufficient.¹ Note that this relaxes the assumption employed to derive Eq. (13) since, as a result, only the direction of \mathbf{S}_{LH} has to remain unchanged under the effect of EC waves for

the LH efficiency calculation to remain valid. However, the fact that two waves acting in perpendicular directions of velocity space are considered simultaneously makes it necessary to fully account for two-dimensional effects when computing the response function.

The problem now reduces to evaluating this response function, and in order to achieve this, two methods are available: the adjoint formalism and the Langevin equations. These will be discussed for the case of two waves in Secs. III and IV, respectively.

III. ADJOINT METHOD IN THE PRESENCE OF TWO WAVES

In this section, the adjoint formalism is extended to the case of two waves. For the sake of concision, only the significant steps of this method, extensively discussed in Ref. 1 and references therein, will be recalled.

By making use of Eq. (13) when steady state is attained, the current j_0 defined in Eq. (16) can be written as

$$j_0 = - \int d\mathbf{u} \chi_0 \hat{C}(f_m \phi). \quad (20)$$

Introducing the commutative operation for two functions $\varphi(\mathbf{u})$ and $\psi(\mathbf{u})$

$$[\varphi, \psi] \equiv \int d\mathbf{u} \varphi(\mathbf{u}) \psi(\mathbf{u}), \quad (21)$$

and defining the adjoint \hat{D}^\dagger of an operator \hat{D} as

$$[\varphi, \hat{D}^\dagger \psi] = [\hat{D} \varphi, \psi], \quad (22)$$

Eq. (20) can be rewritten as

$$j_0 = - \int d\mathbf{u} f_m \phi \hat{C}^\dagger \chi_0. \quad (23)$$

The adjoint equation is obtained by comparing Eqs. (23) and (11) and making use of the property $f_m \hat{C}^\dagger \psi = \hat{C}(f_m \psi)$. It is given as

$$\hat{C}^\dagger \chi_0 = -u_\parallel. \quad (24)$$

This equation simply describes the response of a collisional plasma and associated with Eq. (2), it leads to the well-known Fisch–Boozer (FB) response function

$$\chi_0 = \frac{1}{2(5 + Z_i)} u^4 \mu. \quad (25)$$

In order to compute j_1 , a similar treatment is applied to Eq. (9). By noting that the LH quasilinear diffusion coefficient is self-adjoint (i.e., $\hat{D}_{\text{LH}}^\dagger = \hat{D}_{\text{LH}}$), the adjoint equation takes the form

$$[\hat{C} + \hat{D}_{\text{LH}}] \chi_1 = -u_\parallel, \quad (26)$$

which describes χ_1 , the response function of a plasma in which the LH wave modifies the distribution function, modifying in turn the electron relaxation properties. Physically, it means that these electrons describe a collisional curve in velocity space, carrying elemental current $u_\parallel + \hat{D}_{\text{LH}}^\dagger \chi_1$ in-

stead of u_{\parallel} . A rigorously equivalent interpretation is that the particles carry u_{\parallel} as elemental current but describe relaxation curves influenced by the wave.

Under this form, the adjoint Eq. (26) does not appear to have an analytical solution. A further assumption is to consider that collisions dominate the relaxation process. In other words, in spite of the modification of the dynamics in the parallel direction caused by the LH wave, the relaxation curves remain mostly collisional. This approximation allows one to linearize χ_1 , letting $\chi_1 \equiv \bar{\chi} + \delta\chi$ with $|\delta\chi| \ll |\bar{\chi}|$, the small parameter being $D_{LH,0}$.

The zeroth-order expansion of Eq. (26) is

$$\hat{C}\bar{\chi} = -u_{\parallel}, \tag{27}$$

which demonstrates that $\bar{\chi}$ is exactly the FB response function χ_0 .

To first-order, we obtain

$$\hat{C}\delta\chi = -\hat{D}_{LH}\chi_0, \tag{28}$$

which, upon expanding the quasilinear operators and letting $\hat{Z} = (Z_i + 1)/2$, yields

$$\begin{aligned} u \frac{\partial \delta\chi}{\partial u} - \hat{Z} \frac{\partial}{\partial \mu} (1 - \mu^2) \frac{\partial \delta\chi}{\partial \mu} \\ = \frac{D_{LH}}{2v_e m_e T_e} u^3 \frac{\partial}{\partial u_{\parallel}} d_{LH}(u, \mu) \frac{\partial \chi_0}{\partial u_{\parallel}}. \end{aligned} \tag{29}$$

The associated Green equation is

$$u \frac{\partial G_{\chi}}{\partial u} - \hat{Z} \frac{\partial}{\partial \mu} (1 - \mu^2) \frac{\partial G_{\chi}}{\partial \mu} = \frac{\delta(u - u') \delta(\mu - \mu')}{u'^2}, \tag{30}$$

where $G_{\chi}(\mathbf{u}, \mathbf{u}')$ is the steady-state Green function of the problem.

The pitch-angle scattering term in Eq. (30) suggests the expansion²⁴

$$\delta(\mu' - \mu) = \sum_{l=0}^{\infty} \frac{(2l+1)}{2} P_l(\mu) P_l(\mu'), \tag{31}$$

(P_l) being the Legendre polynomials. Applying a variable separation yields

$$\begin{aligned} G_{\chi}(\mathbf{u}, \mathbf{u}') = \frac{H(u - u')}{u^3} \\ \times \sum_{l=0}^{\infty} \frac{(2l+1)}{2} \left(\frac{u'}{u}\right)^{\hat{Z}l(l+1)} P_l(\mu) P_l(\mu'), \end{aligned} \tag{32}$$

where H is the Heaviside function. This leads to the solution

$$\begin{aligned} \delta\chi(u, \mu) = \frac{1}{4(5 + Z_i)} \left(\frac{D_{LH}}{v_e m_e T_e}\right) u^4 \\ \times \sum_{l=0}^{\infty} \frac{(2l+1)}{2} Q_l(u) P_l(\mu), \end{aligned} \tag{33}$$

with

$$Q_l(u) \equiv \int_0^u du' \left(\frac{u'}{u}\right)^{\hat{Z}l(l+1)+4} J_l(u'), \tag{34}$$

and

$$\begin{aligned} J_l(u') \equiv \int_{-1}^1 d\mu' P_l(\mu') \left[3d_{LH}(u', \mu') \mu' (3 + \mu'^2) \right. \\ \left. + \frac{\partial d_{LH}}{\partial u'_{\parallel}} u' (3\mu'^2 + 1) \right]. \end{aligned} \tag{35}$$

IV. LANGEVIN EQUATIONS

To track the electrons trajectories on their relaxation paths, a natural and convenient method consists in solving the Langevin equations.^{1,25,26} Besides providing an insight into the dynamics underlying the relaxation process,²⁷ they allow one to compute the response function χ . Another advantage is that no specific approximation regarding the respective intensities of the collisions and of the wave has to be introduced. They can thus be used to validate the results obtained with the adjoint method (see Sec. III).

The Green function g_1 corresponding to Eq. (9) has been introduced in Sec. II. Physically, $g_1(\mathbf{u}, \mathbf{u}', \tau) d\mathbf{u}$ is the probability of finding an electron initially at the velocity-space position \mathbf{u}' at location \mathbf{u} within element $d\mathbf{u}$ after a time τ . It means that the associated steady-state response function $\chi_1(\mathbf{u})$, whose definition is given by Eq. (18), can be evaluated by computing the elemental current carried by each electron of a set whose initial location is \mathbf{u} along its relaxation trajectory, as it undergoes the effects of Coulomb collisions and LH wave power, and perform an ensemble average afterwards. Rather than directly solving Eq. (17), it is thus possible to resort to a stochastic description of this relaxation process. It can be done by casting this equation into the form

$$\frac{\partial g_1}{\partial \tau} = -\frac{\partial}{\partial \mathbf{u}} \cdot \mathbf{S}. \tag{36}$$

Introducing the friction vector \mathbf{F} and diffusion tensor $\bar{\bar{\mathbf{D}}}$ and using Einstein convention for repeated indices, the probability current components are written as

$$S_i = F_i g_1 - \frac{\partial}{\partial u_j} D_{ij} g_1. \tag{37}$$

By identification of Eqs. (2), (5), and (36), the diffusion tensor can be written as $\bar{\bar{\mathbf{D}}} \equiv \bar{\bar{\mathbf{D}}}_{\text{coll}} + \bar{\bar{\mathbf{D}}}_{LH}$, with

$$\bar{\bar{\mathbf{D}}}_{\text{coll}} = \frac{2}{u^3} \begin{pmatrix} 1 & 0 \\ 0 & (Z_i + 1)(1 - \mu^2)/2 \end{pmatrix}, \tag{38}$$

and

$$\bar{\bar{\mathbf{D}}}_{LH} = D_{LH,0} \frac{d_{LH}(u)}{u^2} \begin{pmatrix} \mu^2 & u\mu(1 - \mu^2) \\ u\mu(1 - \mu^2) & (1 - \mu^2)^2 \end{pmatrix}. \tag{39}$$

For the force term, $\mathbf{F} \equiv \mathbf{F}_{\text{coll}} + \mathbf{F}_{LH}$, with

$$\mathbf{F}_{\text{coll}} = -\frac{2}{u^3} \left[\left(1 + \frac{3}{u^2} \right) u \hat{\mathbf{e}}_u + (Z_i + 1) \mu \hat{\mathbf{e}}_{\mu} \right], \tag{40}$$

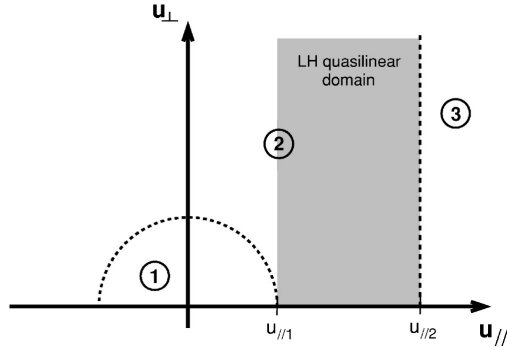


FIG. 1. Velocity-space configuration. Three domains are distinguished, each corresponding to a different situation with respect to the wave-induced dynamics. Region (1) is such as $u_0 < u_{\parallel,1}$. Region (2) encompasses $u_0 > u_{\parallel,1}$ and $u_{00} < u_{\parallel,2}$, and Region (3) corresponds to $u_{00} > u_{\parallel,2}$.

where \hat{e}_u and \hat{e}_μ are unit vectors corresponding to the u and μ directions, respectively.

To compute the drift caused by the wave, it is necessary to bear in mind that when the transformation from one coordinate system to another is not linear, as is the case when the LH quasilinear diffusion coefficient is transformed from (u_\perp, u_\parallel) to (u, μ) coordinates, the friction term needs to include a contribution from the diffusion in the first coordinate system.²² This yields

$$\mathbf{F}_{\text{LH}} = -\frac{D_{\text{LH},0}}{u^2} [(u\mu d'_{\text{LH}}(u) + (1-\mu^2)d_{\text{LH}}(u))u\hat{e}_u + (ud'_{\text{LH}}(u) - 3\mu d_{\text{LH}}(u))(1-\mu^2)\hat{e}_\mu], \quad (41)$$

with $d'_{\text{LH}} \equiv \partial d_{\text{LH}} / \partial u_\parallel$.

The Langevin equations describing the electrons trajectories can then be written as²²

$$\frac{d\mathbf{u}}{d\tau} = \mathbf{h}(\mathbf{u}, \tau) + \bar{\mathbf{g}}(\mathbf{u}, \tau) \cdot \boldsymbol{\xi}(\tau). \quad (42)$$

The components of the matrix $\bar{\mathbf{g}}$ are linked to the diffusion tensor $\bar{\mathbf{D}}$ through

$$g_{ij} = (\bar{\mathbf{D}}^{1/2})_{ij}, \quad (43)$$

where $\bar{\mathbf{D}}^{1/2}$ is obtained by diagonalizing $\bar{\mathbf{D}}$, taking the positive square root of the eigenvalues, and transforming the diagonal matrix back.

In the framework of Stratonovitch calculus, the deterministic force components are given by²²

$$h_i = F_i - (\bar{\mathbf{D}}^{1/2})_{kj} \frac{\partial}{\partial u_k} (\bar{\mathbf{D}}^{1/2})_{ij}. \quad (44)$$

The second term of the right-hand side of this equation is a correction to the noise-induced drift. Albeit straightforward, the computation of \mathbf{h} and $\bar{\mathbf{g}}$ is tedious and the resulting expressions are cumbersome. They will not be presented here.

$\boldsymbol{\xi}(\tau)$ is the Gaussian-distributed Langevin force, described by its stochastic properties

$$\langle \xi_i(\tau) \rangle = 0, \text{ and } \langle \xi_i(\tau) \xi_j(\tau') \rangle = 2 \delta_{ij} \delta(\tau - \tau'), \quad (45)$$

where $\langle \cdot \rangle$ refers to the average performed over statistical realizations.

Practically, in the simulations presented in this paper, the collision time is split in numerous time steps and each electron velocity evolves according to Eq. (42) until thermalization is attained. It should be emphasized that the integration of a stochastic equation in the case of a multiplicative noise has to be carried out with care to avoid numerical artifacts liable to distort the result. A detailed discussion of this question can be found in Ref. (27). Here, both the Euler and Heun methods have been implemented and the results have been found to be generally indistinguishable. It is recognized that two main sources of numerical error can alter the solution of stochastic equations:²⁸ firstly, the statistical error, due to the finite number of realizations, which can be evaluated from standard statistical methods, and secondly, the error induced by the time discretization. To reduce the latter, it is usual to extrapolate the result for $\Delta\tau \rightarrow 0$. For the values of $D_{\text{LH},0}$ considered in this section, this error was found to be negligible.

To illustrate the combined effects of Coulomb collisions and LH waves on the electron relaxation, randomly chosen individual relaxation paths can be studied. The velocity-space configuration of the problem appears in Fig. 1, where

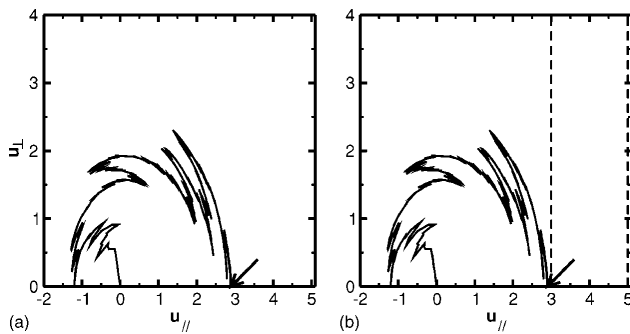


FIG. 2. Sample relaxation path. (a) Collisions only. (b) Collisions+LH wave. The initial position is denoted by an arrow. On (b), the dashed lines delimit the LH domain boundaries.

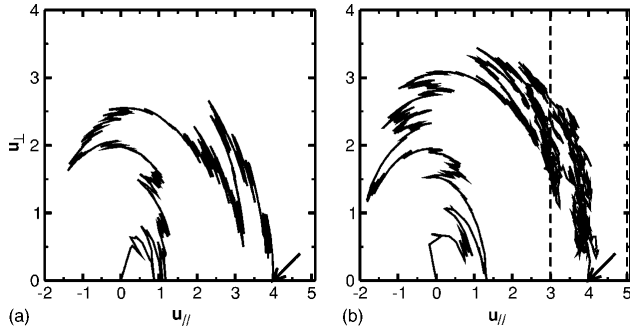


FIG. 3. Same as Fig. 2, but for initial position $(u_{\parallel 0}, u_{\perp 0}) = (4, 0)$.

three domains (labeled 1–3) are distinguished, corresponding to (1) $u_0 < u_{\parallel 1}$, (2) $u_0 > u_{\parallel 1}$ and $u_{\parallel 0} < u_{\parallel 2}$, and (3) $u_{\parallel 0} > u_{\parallel 2}$.

Such sample trajectories are shown on Figs. 2, 3, 4, and 5, which have been produced with the following parameters: $u_{\parallel 1} = 3$, $u_{\parallel 2} = 5$, $Z_i = 1$, and $D_{LH,0} = 0.1$. All these figures are divided in two: the part labeled (a), where only the collisions are included in the calculation, and (b), where the electrons undergo the combined effect of collisions and wave power.

In Fig. 2, a trajectory obtained for an electron whose initial velocity lies in region 1 is shown. In such a case and as long as the energy diffusion caused by the collisions is neglected, which is a reasonable approximation, the wave power cannot influence the electron relaxation, since the particle never reaches the wave diffusion domain. The relaxation path of an electron starting from the LH quasilinear domain (in region 2) can be seen in Fig. 3. In this case, the supplemental parallel diffusion and drift induced by the LH wave clearly lengthen the path, and will be likely to slow the relaxation process, thus enhancing the carried current. Another possibility is for the initial velocity to belong to region 2, but outside the LH domain ($u_{\parallel 0} < u_{\parallel 1}$). A sample trajectory corresponding to this case is shown in Fig. 4 and interestingly enough, although the particle has an initial parallel velocity such as $u_{\parallel 0} < u_{\parallel 1}$, it experiences the wave influence due to the pitch-angle scattering effect. This is the reason u_0 appears to be as crucial as $u_{\parallel 0}$. Finally, in Fig. 5, the relaxation of an electron having $u_{\parallel 0} > u_{\parallel 2}$ is shown (region 3). Although the wave domain is encountered, the net effect on

the relaxation length is more complicated, as the upper-velocity boundary of the LH quasilinear coefficient, at least in the model chosen here to describe the wave, induces a drift towards lower velocities (since $\partial d_{LH} / \partial u_{\parallel} |_{u_{\perp,2}} < 0$) which can accelerate the relaxation with respect to a purely collisional trajectory.

For a quantitative evaluation of the effects of LH waves on the particles thermalization, a statistical analysis has to be performed. According to Eq. (18), the response function χ_1 can be written as

$$\chi_1(\mathbf{u}_0) = \int_0^\infty d\tau' \langle u_{\parallel} \rangle(\tau'). \tag{46}$$

When the collisions are the only effect taken into account, it is possible to average the Langevin equations analytically and to deduce the response function.¹ For our purpose, however, this operation is not possible and the computation of the response function has to be performed numerically.

Here, we study $\langle u_{\parallel} \rangle$ as a function of time for various initial velocities and values of $D_{LH,0}$, the average being performed over 20 000 electrons. The result appears in Fig. 6, for initial positions $\mathbf{u}_0 = (u_{\parallel 0}, u_{\perp 0}) = (3, 0)$, $(4, 0)$, and $(5, 0)$, and normalized LH diffusion coefficients $D_{LH,0} = 0$ (collisions only), $D_{LH,0} = 0.1$, $D_{LH,0} = 0.2$, $D_{LH,0} = 0.4$. The collisional FB solution, given (for $Z_i = 1$) by $\langle u_{\parallel} \rangle(\tau) = u_{\parallel 0} (1 - 6\tau/u_0^3)$ also appears, but is perfectly superimposed with its numerical counterpart and is thus barely visible.

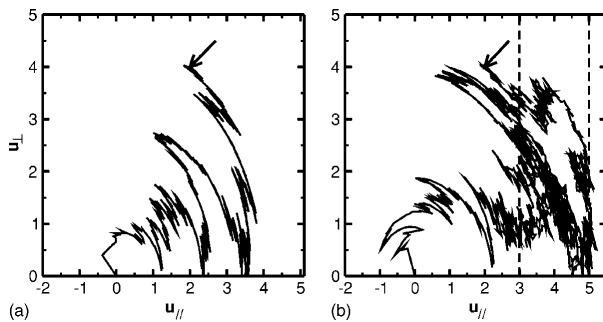


FIG. 4. Same as Fig. 2, but for initial position $(u_{\parallel 0}, u_{\perp 0}) = (2, 4)$.

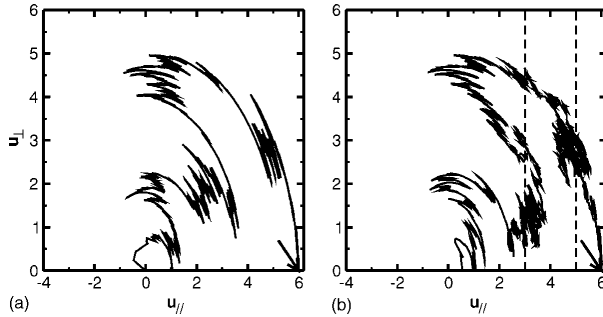


FIG. 5. Same as Fig. 2, but for initial position $(u_{\parallel 0}, u_{\perp 0}) = (5, 0)$.

It can be observed that for $(u_{\parallel 0}, u_{\perp 0}) = (3, 0)$ or $(4, 0)$, the wave clearly delays the thermalization. In the third case ($u_{\parallel 0} = 5$), the effect of the drift induced at the high-velocity boundary appears clearly, since the electrons begin by experiencing a faster decrease in parallel velocity, on average. However, the energy range of the electrons is largely spread by the wave and a significant proportion has not yet thermalized, well after the purely collisional relaxation is over. The response function is determined by the balance between these two effects and its features shall be presented in the next section.

V. RESPONSE FUNCTION OF A LHCD PLASMA

In Sec. IV, a numerical method has been presented and employed to perform a basic analysis of the velocity-space structure when the presence of LH power influences the dynamics underlying the current drive process. Although it can

be used to compute the response function, the perturbation method presented in Sec. III is more economical in terms of computational resources and is thus more adapted to a systematic study of the response function properties, which is the goal of the present section.

In what follows, the parameters for the LH quasilinear domain are $u_{\parallel 1} = 3$, $u_{\parallel 2} = 5$, $\Delta u_{\parallel 1} = 0.5$, and $\Delta u_{\parallel 2} = 1$. In Fig. 7, some level curves of the total response function $\chi_0 + \delta\chi$ are represented in $(u_{\parallel}, u_{\perp})$ space for $D_{LH,0} = 0.1$ (a) and $D_{LH,0} = 0.2$ (b). For comparison, the corresponding contours of the FB response function χ_0 appear as dashed lines.

Several observations can be made about this figure. Firstly, the overall modification of the response function is rather moderate, which is consistent with the approximation of the adjoint calculation, which requires the collisions to dominate the electron relaxation. Secondly, the response function is modified mainly in the LH quasilinear domain, but not only, and it can be seen to extend to all velocities such as $u > u_{\parallel 1}$ as well as beyond $u_{\parallel} = u_{\parallel 2}$, under the effect of pitch-angle scattering, described in Sec. IV. This behavior

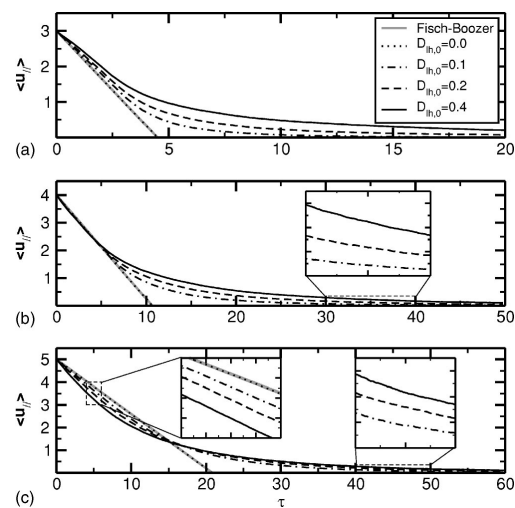


FIG. 6. $\langle u_{\parallel} \rangle$ averaged over 20 000 particles as a function of time for $u_{\perp 0} = 0$ and (a) $u_{\parallel 0} = 3$, (b) $u_{\parallel 0} = 4$, and (c) $u_{\parallel 0} = 5$. $D_{LH,0} = 0$ (dotted line), $D_{LH,0} = 0.1$ (dot-dashed line), $D_{LH,0} = 0.2$ (dashed line), $D_{LH,0} = 0.4$ (solid line). The analytical curve for collisions only (FB solution) appears as a thick gray line.

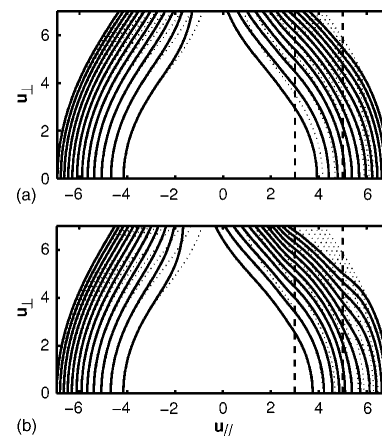


FIG. 7. Isocontours of the response function $\chi_0 + \delta\chi$ of a plasma with LH waves such as $u_{\parallel 1} = 3$, $u_{\parallel 2} = 5$, $\Delta u_{\parallel 1} = 0.5$, $\Delta u_{\parallel 2} = 1$. (a) $D_{LH,0} = 0.1$ and (b) $D_{LH,0} = 0.2$. The dashed vertical lines delimit the LH domain boundaries and the dotted contours represent the collisional response χ_0 . Contours start at $|\chi| = 25$ and are equally spaced with $|\Delta\chi| = 15$.

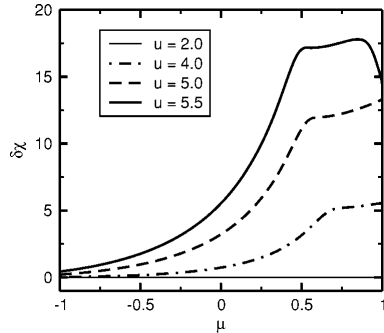


FIG. 8. $\delta\chi$ as a function of the pitch-angle $\cos \mu$ for $u=2$ (thin solid), 4 (dot-dashed), 5 (dashed), and 5.5 (thick solid). The plasma and LH wave parameters are the same as in Fig. 7(a).

is clearly visible in Fig. 8, where the response function perturbation $\delta\chi$ is shown as a function of μ for various values of u , and $D_{LH,0}=0.1$.

This figure shows the strong asymmetrical shape of $\delta\chi$. As a result, the total response function χ_1 is largely enhanced in the $u_{\parallel}>0$ region of velocity space, under the influence of the LH wave. As predicted for $u<u_{\parallel,1}$, we obtain $\delta\chi=0$, in other words χ_1 reduces to the FB response function. The pitch-angle scattering effect can cause $\delta\chi(u,\mu)$ to be non-zero even for $u_{\parallel}<u_{\parallel,1}$ and particularly for $u_{\parallel}<0$. Another observation is that $\delta\chi$ falls off rapidly for $u>u_{\parallel,2}$ and can even become negative. This effect is best viewed when $\delta\chi$ is represented as a function of u_{\parallel} , for various values of u_{\perp} , as shown in Fig. 9. For completeness, the result from the Langevin equations computation also appears for $u_{\perp}=0$, the error bars being deduced from the estimated statistical error.

One can notice that for $u\geq 6$, $\delta\chi$ is negative, which would indicate a deleterious effect of the LH wave on the EC-driven current when the latter is carried by electrons excited in this region. Although supported by the numerical solution of the Langevin equations, this conclusion must, however, be tempered by several considerations: (i) In this

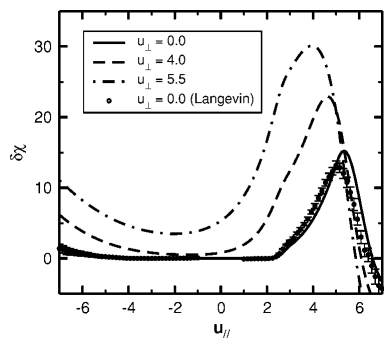


FIG. 9. $\delta\chi$ as a function of normalized parallel velocity u_{\parallel} for $u_{\perp}=0$ (solid), 4 (dashed), and 5.5 (dot-dashed). Also shown is the response function obtained by numerical solution of the Langevin equations for $u_{\perp}=0$ (circles).

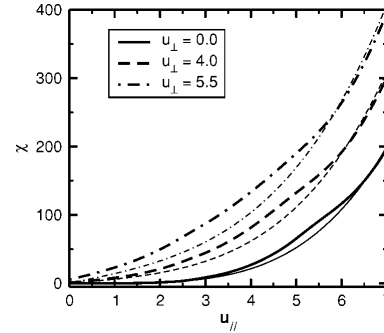


FIG. 10. Comparison of the FB response function χ_0 (thin lines) and the response function, including LH wave effects $\chi_0+\delta\chi$ (thick lines) for $D_{LH,0}=0.1$ for $u_{\perp}=0$ (solid), 4 (dashed), and 5.5 (dot-dashed).

region of velocity space, $\delta\chi$ is sensitive to the value chosen for $\Delta u_{\parallel,2}$ which is not readily available, (ii) EC wave absorption at velocities significantly above the upper bound of the LH quasilinear domain is likely to be impossible in the absence of LH wave, and (iii) The FB response function is proportional to u^4 , which makes the LH-induced modification rather weak for large values of u_{\parallel} . The latter point is supported by Fig. 10, where χ_0 and $\chi_0+\delta\chi$ are shown as a function of u_{\parallel} for the same parameters as Fig. 9.

This figure shows that beyond the upper boundary of the LH domain, the effect is indeed small. Physically, this simply means that no EC efficiency improvement takes place for $u_{\parallel}\geq u_{\parallel,2}$, aside from the fact that the very presence of a LH plateau is responsible for the EC wave absorption at this location.⁷

More important than the response function itself, as far as the rf current drive is concerned, is its velocity-space gradient, as is apparent from Eq. (19). For EC waves, the differentiation is to be performed along u_{\perp} . In Fig. 11, the quantity $\delta\chi' \equiv \partial\delta\chi/\partial u_{\perp}$ is shown versus u_{\parallel} for various values of u_{\perp} .

Whenever $u_{\parallel}<u_{\parallel,2}$, $\delta\chi'$ appears to be positive, which implies a favorable contribution of the LH wave to the EC

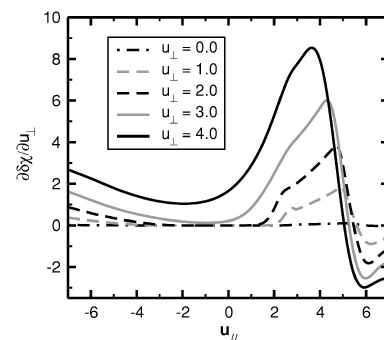


FIG. 11. $\partial\delta\chi/\partial u_{\perp}$ as a function of u_{\parallel} for $u_{\perp}=0$ (dot-dashed), 1 (dashed gray), 2 (dash), 3 (solid gray), and 4 (solid).

current. Moreover, even for moderate values of u_{\perp} , where electrons are most easily driven by EC waves, $\delta\chi'$ can be fairly large, provided an appropriate range of parallel velocities is selected, which is possible through the use of suitable launching angles.⁶ For $u_{\parallel} \gtrsim u_{\parallel,2}$, $\delta\chi'$ can have a negative value, although as stated earlier this feature should be pondered cautiously. This figure confirms that the LH wave has an overall beneficial effect on the current driven EC wave, and that a synergy between the two waves can be expected, especially when the latter are excited in the vicinity of $u_{\parallel,EC} \lesssim u_{\parallel,2}$. Note that this parameter is generally simply determined by the LH wave accessibility condition.²⁹

VI. ECCD EFFICIENCY IN THE PRESENCE OF LH WAVES

The features of the distribution function in the presence of LH waves presented in Sec. V have consequences in terms of ECCD efficiency. From Eq. (10), the total current appears as $j = j_0 + j_1$ where j_0 [Eq. (16)] is driven by the LH wave, and is implicitly assumed to be unaffected by the presence of the EC wave. In Sec. III, the response function of the plasma in the presence of LH waves was linearized according to $\chi_1 = \chi_0 + \delta\chi$, which implies that j_1 , given by Eq. (19) can be cast into the form $j_1 = j_{EC} + \delta j$, with

$$j_{EC} \equiv \int d\mathbf{u} \mathbf{S}_{EC} \cdot \frac{\partial \chi_0}{\partial \mathbf{u}}, \quad (47)$$

and

$$\delta j \equiv \int d\mathbf{u} \mathbf{S}_{EC} \cdot \frac{\partial \delta\chi}{\partial \mathbf{u}}. \quad (48)$$

j_{EC} is the EC current obtained when the cross-effect of both waves is not accounted for, and δj is a supplemental current, which qualifies for the denomination *synergy current* (or *antisynergy*, in the event that δj and j_{EC} have opposite signs). The clear distinction stems from the linearization introduced in the computation of the response function and permits a straightforward separation of the contribution of each process, which is generally the key difficulty encountered when trying to characterize a synergy effect. Note that if $D_{LH,0} \rightarrow 0$, the usual FB efficiency is recovered. For the adjoint method, this is clear from Eqs. (33) and (48), which demonstrate that $\delta j = 0$ when $D_{LH,0} = 0$. The same result is obtained from the Langevin equations. In this case, Fig. 6 indeed shows that $\delta\chi = \chi_1 - \chi_0$ is zero, so that $j_1 = j_{EC}$.

Defining j_w the amount of current generated by wave power p_w and assuming that the interaction is localized in velocity space, as is generally the case with EC waves and to a lesser extent with LH waves also, the steady-state current drive efficiency can be approximated by¹

$$\eta_w \equiv \frac{j_w}{p_w} \approx \frac{\mathbf{S}_w \cdot (\partial\chi/\partial\mathbf{u})}{\mathbf{S}_w \cdot \frac{\partial}{\partial\mathbf{u}} \left(\frac{u^2}{2} \right)}, \quad (49)$$

where χ is the response function and \mathbf{S}_w the quasilinear flux. Evaluating this expression only requires the direction of \mathbf{S}_w ,

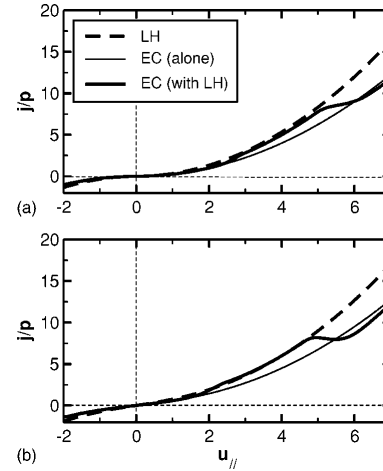


FIG. 12. Current drive efficiency as a function of u_{\parallel} for (a) $u_{\perp} = 0$ and (b) $u_{\perp} = 2$ for LH waves (dashed line) for EC waves alone (thin solid line) and for EC waves when the synergy effect with LH waves is taken into account with $D_{LH,0} = 0.1$ (thick solid line).

which unlike its magnitude, is weakly dependent on the precise shape of the distribution function and is well known¹ ($\mathbf{S}_{EC} \propto \hat{\mathbf{e}}_{\perp}$ and $\mathbf{S}_{LH} \propto \hat{\mathbf{e}}_{\parallel}$).

Here, the efficiencies of both waves are computed using Eq. (49) with the same parameters as above: $D_{LH,0} = 0.1$, $u_{\parallel,1} = 3$, $u_{\parallel,2} = 5$, $\Delta u_{\parallel,1} = 0.5$, $\Delta u_{\parallel,2} = 1$ and $Z_i = 1$. In Fig. 12, these efficiencies are shown as functions of u_{\parallel} for $u_{\perp} = 0$ and $u_{\perp} = 2$.

The 4:3 ratio between the LH and EC efficiencies is recovered, in the absence of a cross-effect.¹ If this effect is included, the corrected EC efficiency [i.e., $(j_{EC} + \delta j)/p_{EC}$] is significantly enhanced in the region of velocity space corresponding to the LH superthermal plateau. For the chosen value of $D_{LH,0}$, it becomes comparable to the LH efficiency. As discussed in Sec. III, a slight antisynergy effect is observed for u_{\parallel} above $u_{\parallel,2}$. Globally, the EC efficiency enhancement increases with u_{\perp} and can exceed the LH efficiency within a significant range of parallel velocities. Moreover, for some parameters, the countercurrent drive amount can be slightly lowered by the synergy effect, which can further enhance the current driven in an EC downshift scheme,⁶ where the wave interacts with electrons having $u_{\parallel} < 0$ as well as $u_{\parallel} > 0$.

To characterize the ECCD efficiency enhancement, following the definition, introduced in Ref. 13, the improvement factor $F_{syn} \equiv (j_{LH+EC} - j_{LH})/j_{EC}$, is studied. According to the linearization introduced in the present model, it simplifies to give

$$F_{syn} = 1 + \frac{\delta j}{j_{EC}} = 1 + \frac{\partial \delta\chi / \partial u_{\perp}}{\partial \chi_0 / \partial u_{\perp}}. \quad (50)$$

The variation of the synergy factor as a function of u_{\parallel} , when the ion charge Z_i is varied from 1 to 3, all other parameters being unchanged, is shown in Fig. 13.

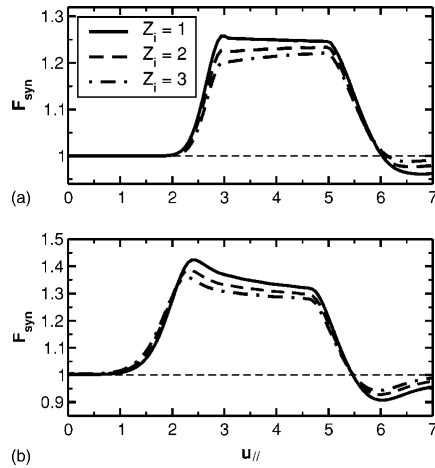


FIG. 13. Synergy factor in the presence of LH waves for $D_{\text{LH},0}=0.1$ and various values of the plasma ion charge: $Z_i=1$ (solid), $Z_i=2$ (dashed), and $Z_i=3$ (dot-dashed). (a) $u_{\perp}=0$, (b) $u_{\perp}=2$.

It is seen that the interaction with electrons whose parallel velocity lies in the vicinity of the LH quasilinear domain can be very beneficial for the EC current drive. For the chosen value of $D_{\text{LH},0}$, an improvement of the efficiency as high as 40% can be obtained. The anti-synergy effect just underlined proves to be marginal. Another observation is that even though the plasma ion charge increase is known to be detrimental to superthermal electron-based CD schemes, it only has a minor influence on the synergy mechanism itself. Finally, a particularly noticeable feature is that the improvement factor is found to be weakly dependent on the particular velocity-space location under consideration.

Hitherto, the presented simulations have all been performed for $D_{\text{LH},0}=0.1$, in order to ensure the validity of the perturbation technique employed to derive the response function from the adjoint equation. The Langevin equations formalism, introduced in Sec. IV, is more demanding from a computational point of view. Still, it has the advantage of allowing to study how the ECCD efficiency depends on $D_{\text{LH},0}$, since it is derived without any assumption regarding its value.

This study is performed by solving the Langevin equations [Eq. (42)] for 20 000 electrons at each initial velocity. For increasing values of $D_{\text{LH},0}$, the time step $\Delta\tau$ is decreased so as to remain small with respect to the variations of \mathbf{D}_{LH} [Eq. (39)] and \mathbf{F}_{LH} [Eq. (41)]. To ensure convergence, however, the computation is performed with several values of $\Delta\tau$, and the resulting averaged quantities are extrapolated to $\Delta\tau \rightarrow 0$. For large values of $D_{\text{LH},0}$, this procedure proves to be necessary to avoid the inherent bias induced by the time discretization, which adds to the purely statistical error.²⁸

The same plasma and LH wave parameters as before are chosen, with $Z_i=1$. The simulations are performed for velocity-space location $(u_{\parallel}, u_{\perp})=(4,1)$ and the quantity under study is $\delta\chi \equiv \chi_1 - \chi_0$, where χ_1 is obtained from the

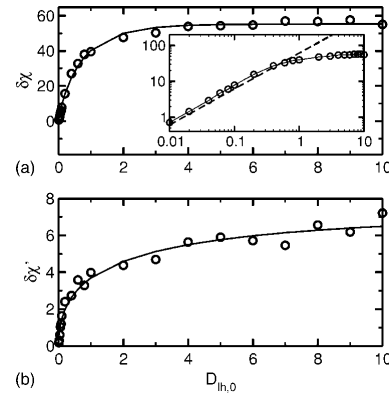


FIG. 14. (a) $\delta\chi$ and (b) $\partial\delta\chi/\partial u_{\perp}$ versus normalized LH quasilinear diffusion coefficient $D_{\text{LH},0}$ for $u_{\parallel}=4$ and $u_{\perp}=1$. The solid lines are fitting curves and on (a), the result of the adjoint method is shown as a dashed line in the inset containing $\delta\chi$ plotted on logarithm axes.

Langevin equations [Eq. (46)] and χ_0 is given by Eq. (25). As discussed in Sec. VI, the most relevant quantity, as far as the ECCD efficiency is concerned, is $\delta\chi' = \partial\delta\chi/\partial u_{\perp}$. To obtain it, simulations are performed for several values of u_{\perp} and the derivative is obtained numerically.

In Fig. 14, $\delta\chi$ and $\delta\chi'$ are plotted versus $D_{\text{LH},0}$, with associated fitting curves. For comparison, the adjoint solution for $\delta\chi$ appears also.

The adjoint solution appears to give a fair result for $D_{\text{LH},0} \lesssim 1$, in accordance with the validity range of the associated method. Its linear dependence on $D_{\text{LH},0}$ [see Eq. (33)], however, leads to an overestimate of the response function, as the numerical solution shows that $\delta\chi$ levels off when $D_{\text{LH},0}$ becomes large. To extrapolate the results as $D_{\text{LH},0}$ tends to infinity (i.e., in a perfectly saturated situation), $\delta\chi'$ is fitted using $\delta\chi' = a_0 \cdot [1 - \exp(-a_1 D_{\text{LH},0}^{a_2})]$. A least-squares fit leads to $a_0 \approx 7.3$, $a_1 \approx 0.7$, and $a_2 \approx 0.5$. This gives the extrapolated value $\lim_{D_{\text{LH},0} \rightarrow \infty} \delta\chi' \approx 7.3$, or when used in Eq. (50), $F_{\text{syn}} \approx 2.8$. This means that for the parameters considered here, the ECCD efficiency is nearly tripled when compared to its “standard” value; that is, the value obtained in the absence of LH waves.

VII. CONCLUSIONS

Owing to the complexity of a full kinetic treatment of the current drive problem in tokamaks, added to the difficulty of separating the contributions from various physical processes, the existence of a synergy between LH and EC waves has often been disputed. In this paper, a different approach has been employed to address this question from a theoretical standpoint, when the dominant source of deformation of the distribution function is LH power. Two complementary methods have been employed: a perturbation solution of the adjoint equation allows a fast derivation of the response function, including both collisional and LH effects in the limit where the former dominate. On the other

hand, solving the Langevin equations allows one to overcome this restriction and, in addition to the computation of the response function, provides an insight in the dynamics underlying the process. However, they imply a less straightforward mathematical treatment and higher computational requirements.

By application of these two formalisms, it has been shown that a synergy was indeed possible between the two waves, provided the EC parameters are chosen to drive electrons within or close to the LH quasilinear domain, which means that the two quasilinear domains have to overlap. In this case and even for moderate values of the LH quasilinear diffusion coefficient, a significant improvement of the ECCD efficiency has been obtained. Moreover, for sufficiently high values of this coefficient (i.e., when quasilinear saturation is reached), the improvement factor appears to be nearly constant. In addition, in this study, the efficiency enhancement has been found to exhibit only a mild dependence on the particular velocity space location. These trends suggest that the synergy mechanism is fairly robust and should manifest itself provided the EC waves are launched using a set of parameters compatible with the LH quasilinear domain properties.

In present experiments, the characterization of such an enhancement of the EC current drive efficiency can be a daunting task. This is mostly due to the fact that, as in numerical simulations, many phenomena are involved in the process and are difficult to separate. It is nonetheless possible to envision experimental scenarios aimed at studying the LH-EC synergy. One such scenario could be creating a fully noninductive plasma by relying on the LHCD system. After a delay equivalent to several resistive times, injecting two EC beams with opposite parallel spectra (i.e., opposite toroidal angle, to lowest order) should result in zero net EC current in the absence of a cross-effect. The measurement of an additional amount of current would then be the signature of a synergy between the two waves. Another possible scenario consists in using the LH wave to sustain a fully noninductive discharge, turn on the EC system, and let the feedback system reduce the LH power so as to maintain a zero loop voltage with constant total plasma current. From the level of EC power injected in the plasma and the resulting drop in LH power, a value for the EC efficiency in the presence of LH waves can be deduced.

ACKNOWLEDGMENTS

One of the authors (R.J.D.) wishes to express his appreciation for encouraging comments by M. Brambilla and G. Leclert.

- ¹N. J. Fisch, *Rev. Mod. Phys.* **59**, 175 (1987).
- ²T. S. Taylor, *Plasma Phys. Controlled Fusion* **39**, B47 (1997).
- ³X. Litaudon, R. Arslanbekov, and G. T. Hoang *et al.*, *Plasma Phys. Controlled Fusion* **38**, 1603 (1996).
- ⁴E. Barbato, *Plasma Phys. Controlled Fusion* **40**, A63 (1998).
- ⁵Y. Peysson and the Tore Supra Team, *Plasma Phys. Controlled Fusion* **42**, B87 (2000).
- ⁶V. Erckmann and U. Gasparino, *Plasma Phys. Controlled Fusion* **36**, 1869 (1994).
- ⁷I. Fidone, G. Giruzzi, G. Granata, and R. L. Meyer, *Phys. Fluids* **27**, 2468 (1984).
- ⁸I. Fidone, G. Giruzzi, V. Krivenski, E. Mazzucato, and L. F. Ziebell, *Nucl. Fusion* **27**, 579 (1987).
- ⁹D. Farina, M. Lontano, and R. Pozzoli, *Plasma Phys. Controlled Fusion* **30**, 879 (1988).
- ¹⁰D. Farina and R. Pozzoli, *Phys. Fluids B* **1**, 815 (1989).
- ¹¹G. Giruzzi, I. Fidone, and R. L. Meyer, *Nucl. Fusion* **29**, 1381 (1989).
- ¹²M. Shoucri, I. Shkarofsky, V. Fuchs, K. Kupfer, A. Bers, and S. Luckhardt, *Comput. Phys. Commun.* **55**, 253 (1989).
- ¹³R. Dumont, G. Giruzzi, and E. Barbato, *Phys. Plasmas* **7**, 4972 (2000).
- ¹⁴A. Ando, K. Ogura, H. Tanaka, M. Iida, S. Ide, M. Nakamura, T. Maekawa, Y. Terumichi, and S. Tanaka, *Nucl. Fusion* **26**, 107 (1986).
- ¹⁵Y. Yamamoto, K. Hoshino, H. Kawashima *et al.*, *Phys. Rev. Lett.* **58**, 2220 (1987).
- ¹⁶T. Maekawa, T. Maehara, T. Minami, Y. Kishigami, T. Kishino, K. Makino, K. Hanada, M. Nakamura, Y. Terumichi, and S. Tanaka, *Phys. Rev. Lett.* **70**, 2561 (1993).
- ¹⁷J. A. Colborn, J. P. Squire, M. Porkolab, and J. Villaseñor, *Nucl. Fusion* **38**, 783 (1998).
- ¹⁸Y. Peysson and F. Imbeaux, *Rev. Sci. Instrum.* **70**, 3987 (1999).
- ¹⁹G. Giruzzi, C. Darbos, R. Dumont *et al.*, in *Proceedings of the Eighteenth Fusion Energy Conference*, Sorrento, Italy, paper IAEA-CN-77/EXP4/02.
- ²⁰V. Pericoli-Ridolfini, E. Barbato, A. Bruschi *et al.*, in *RF Power in Plasmas*, edited by T. K. Mau and J. deGrassie (AIP, Melville, 2001), p. 225.
- ²¹T. M. Antonsen and K. R. Chu, *Phys. Plasmas* **25**, 1295 (1982).
- ²²H. Risken, *The Fokker-Planck Equation*, 2nd ed. (Springer-Verlag, Berlin, 1989).
- ²³M. Brambilla, *Kinetic Theory of Plasma Waves* (Clarendon, Oxford, 1998).
- ²⁴J. M. Rax and D. Moreau, *Nucl. Fusion* **29**, 1751 (1989).
- ²⁵M. G. Cadjan and M. F. Ivanov, *J. Plasma Phys.* **61**, 89 (1999).
- ²⁶F. Castejón and S. Eguilior, *Plasma Phys. Controlled Fusion* **45**, 159 (2003).
- ²⁷J. L. García-Palacios and F. J. Lázaro, *Phys. Rev. B* **58**, 14937 (1998).
- ²⁸A. Greiner, W. Strittmatter, and J. Honerkamp, *J. Stat. Phys.* **51**, 95 (1988).
- ²⁹P. T. Bonoli and R. C. Engle, *Phys. Fluids* **29**, 2937 (1986).

Effects of non-Maxwellian species on ion cyclotron waves propagation and absorption in magnetically confined plasmas

R. J. Dumont^{a)}
Association Euratom-CEA, CEA/DSM/DRFC, Centre de Cadarache,
13108 Saint-Paul lez Durance, France

C. K. Phillips
Princeton Plasma Physics Laboratory, Forrestal Campus, P.O. Box 451, Princeton, New Jersey 08543

D. N. Smithe
ATK Mission Research Corporation, Newington, Virginia 22122

(Received 11 November 2004; accepted 31 January 2005; published online 30 March 2005)

Magnetically confined plasmas can contain significant concentrations of nonthermal particles, arising from neutral beam injection, fusion reactions, shock heating, or wave-driven acceleration of resonant plasma species. The associated distribution functions can depart significantly from Maxwellians, which may impact the propagation and absorption of radio frequency waves. The potential effect of these particles has been investigated using a full-wave code that has been extended to handle gyrotropic, but otherwise arbitrary distribution functions. This code has been used to numerically simulate ion cyclotron resonance heating (ICRH) in magnetic fusion plasmas in which co-resonant neutral beam injection (NBI) heating may also be applied. The presence of nonthermal ion populations generated by the NBI can alter the ICRH characteristics. Two situations involving ion cyclotron range of frequency waves are presented: fast wave to ion Bernstein wave mode conversion and high harmonic fast wave electron heating. In both cases, the adequacy of an equivalent Maxwellian-based description is discussed. Results indicate that the absorption profiles are more strongly affected than the wave fields by the presence of nonthermal species. © 2005 American Institute of Physics. [DOI: 10.1063/1.1881472]

I. INTRODUCTION

Laboratory fusion plasmas, as well as many space plasmas, can comprise both thermal and nonthermal species. In collisionless space plasmas, turbulent heating or shock processes can accelerate particles, resulting in velocity-space distributions that are Lorentzian or power-law-like in nature.¹⁻³ Both neutral beam injection (NBI) and fusion reactions in laboratory fusion plasmas introduce energetic ions, which follow a slowing-down type distribution in velocity space.⁴ When radio frequency (rf) waves are applied to heat or else to drive noninductive currents in these magnetized plasmas, the wave-induced particle acceleration results in velocity-space distributions that feature energetic tails⁵ or extended quasilinear plateaus.⁶ In all of these situations, the question that arises is whether or not these nonthermal species have a noticeable impact on electromagnetic wave dynamics in the plasma.

Previous theoretical studies of the effects of nonthermal species on wave dynamics have been based on analyses of generalized dispersion relations^{1-3,7,8} or else on simplified wave field models.⁹⁻¹¹ Most of the studies that used generalized dispersion relations^{1-3,7,8} were focused on modifications to instability thresholds or to local power absorption. In the wave field studies, the wave equation was simplified by neglecting mode-conversion processes, which results in a differential form for the wave equation, and then by replacing

the wave vector in the dielectric tensor with the fast wave root of the generalized hot plasma dispersion relation.⁹⁻¹¹

More recently, all-orders full-wave solutions to the kinetic wave equation in magnetized plasmas with Maxwellian species have been obtained in one-dimensional¹²⁻¹⁴ (1D) and two-dimensional (2D) magnetized plasmas¹⁵ without the restrictions that mode conversion is negligible, or that perpendicular wavelengths are large compared to the ion gyroradius. Owing to fairly high computational requirements, these simulations have so far been limited to Maxwellian populations, which allows an analytical computation of the velocity integrals required to obtain the wave field and various energy quantities. In order to account for the presence of nonthermal populations, the dielectric response is formulated in terms of equivalent Maxwellians that reproduce the particle and energy content of the original distributions.⁷

In the studies presented in this paper, full-wave solutions for wave propagation and absorption in plasmas with non-Maxwellian components have been obtained by generalizing the 1D all-orders quasi-local code¹⁶ METS to include nonthermal species in the plasma dielectric response function. Although the specific examples considered here are relevant to heating and current drive processes in laboratory fusion plasmas, the model is sufficiently general to be applicable in other venues.

The remainder of this paper is organized as follows. In Secs. II and III, the theoretical background of this study is presented, with the absorption kernel computation discussed in the latter. After the presentation of the analytical model

^{a)}Electronic mail: remi.dumont@cea.fr

used for the nonthermal distribution function (Sec. IV), Secs. V and VI are devoted to ion cyclotron resonance heating in magnetic fusion plasmas. Specifically, a mode-conversion scheme aimed at heating electrons while a tritium beam is injected in a plasma of the Tokamak Fusion Test Reactor¹⁷ (TFTR) is studied in Sec. V. High harmonic fast wave electron heating in the presence of NBI in the National Spherical Torus Experiment¹⁸ (NSTX) is discussed in Sec. VI, in which either an isotropic or an anisotropic distribution function is used to describe the deuterium beam ions. Conclusions are drawn in Sec. VII.

II. LOCAL FULL-WAVE ANALYSIS

For time-harmonic electromagnetic fields with oscillation frequency ω , the wave equation can be written as

$$\nabla \times \nabla \times \mathbf{E} - \frac{\omega^2}{c^2} \left(\mathbf{E} + \frac{i}{\omega \epsilon_0} \mathbf{J}_p \right) = i\omega \mu_0 \mathbf{J}_s, \quad (1)$$

where \mathbf{E} and \mathbf{J}_p are the electric field and the first-order perturbed plasma current, respectively, \mathbf{J}_s is the current provided by external sources (e.g., antennas).

The relation between the plasma current and the wave electric field is given by¹⁹

$$\mathbf{J}_p(\mathbf{r}) = \int d\mathbf{r}' \bar{\boldsymbol{\sigma}}(\mathbf{r}, \mathbf{r}') \cdot \mathbf{E}(\mathbf{r}'), \quad (2)$$

where $\bar{\boldsymbol{\sigma}}$ is the conductivity kernel. In a uniform plasma, $\bar{\boldsymbol{\sigma}}$ is invariant for any translation, i.e., $\bar{\boldsymbol{\sigma}}(\mathbf{r}, \mathbf{r}') = \bar{\boldsymbol{\sigma}}(\mathbf{r} - \mathbf{r}')$, giving a purely local character to Eq. (2). In an inhomogeneous plasma, on the other hand, this relation is nonlocal, and the resulting wave equation has the integral form¹⁶

$$\nabla \times \nabla \times \mathbf{E} - \frac{\omega^2}{c^2} \int d^3\mathbf{k} \exp(i\mathbf{k} \cdot \mathbf{r}) \bar{\mathbf{K}}(\mathbf{r}, \mathbf{k}) \cdot \mathbf{E}(\mathbf{k}) = i\omega \mu_0 \mathbf{J}_s. \quad (3)$$

Here, $\bar{\mathbf{K}}$ is the dielectric kernel,¹⁶

$$\bar{\mathbf{K}}(\mathbf{r}, \mathbf{k}) = \bar{\mathbf{I}} + \frac{i}{\omega \epsilon_0} \bar{\boldsymbol{\sigma}}(\mathbf{r}, \mathbf{k}), \quad (4)$$

and can be expressed in terms of the local absorption kernel¹⁶ $\bar{\mathbf{W}}(\mathbf{r}, \mathbf{k}_1, \mathbf{k}_2)$:

$$\bar{\mathbf{K}}(\mathbf{r}, \mathbf{k}) = \bar{\mathbf{I}} + \left(1 - i \frac{\partial}{\partial \mathbf{k}_2} \cdot \frac{\partial}{\partial \mathbf{r}} \right) \bar{\mathbf{W}}(\mathbf{r}, \mathbf{k}_1, \mathbf{k}_2) \Big|_{\mathbf{k}_1 = \mathbf{k}_2 = \mathbf{k}}. \quad (5)$$

The energy balance equation accurate to first order in ρ_i/L_B , where ρ_i is the ion Larmor radius and L_B the equilibrium magnetic field scale length, is obtained by multiplication of Eq. (3) by \mathbf{E}^* on its left. After some algebraic manipulations, one gets

$$\frac{\partial W_{em}}{\partial t} - \nabla \cdot (\mathbf{P} + \mathbf{T}) = -P_{abs}, \quad (6)$$

with the Poynting flux given by

$$\mathbf{P}(\mathbf{r}) = \frac{1}{2\mu_0} \text{Re}(\mathbf{E}^* \times \mathbf{B}), \quad (7)$$

and the electromagnetic field energy by

$$W_{em} = \frac{\epsilon_0 |\mathbf{E}|^2}{2} + \frac{|\mathbf{B}|^2}{2\mu_0}. \quad (8)$$

Defining the spatial absorption

$$P_{abs}(\mathbf{r}) = \frac{\omega \epsilon_0}{2} \text{Im} \left\{ \int d^2\mathbf{k}_1 d^2\mathbf{k}_2 e^{i(\mathbf{k}_1 - \mathbf{k}_2) \cdot \mathbf{r}} \times \mathbf{E}^*(\mathbf{k}_2) \cdot \bar{\mathbf{W}}(\mathbf{r}, \mathbf{k}_1, \mathbf{k}_2) \cdot \mathbf{E}(\mathbf{k}_1) \right\} \quad (9)$$

specifies the kinetic flux as¹⁶

$$\mathbf{T}(\mathbf{r}) = -\frac{\omega \epsilon_0}{2} \text{Re} \left\{ \int d^2\mathbf{k}_1 d^2\mathbf{k}_2 e^{i(\mathbf{k}_1 - \mathbf{k}_2) \cdot \mathbf{r}} \times \frac{\partial}{\partial \mathbf{k}} \cdot [\mathbf{E}^*(\mathbf{k}_2) \cdot \bar{\mathbf{W}}(\mathbf{r}, \mathbf{k}_1, \mathbf{k}) \cdot \mathbf{E}(\mathbf{k}_1)] \Big|_{\mathbf{k} = \mathbf{k}_1} \right\}. \quad (10)$$

$\bar{\mathbf{W}}$ is thus needed to obtain the dielectric tensor $\bar{\mathbf{K}}$, hence the electromagnetic field [Eq. (3)] and the local absorption [Eq. (9)].

Numerically, the wave field is obtained by approximating Eq. (3) in the plasma by its discrete Fourier transform written as

$$\sum_j \exp(i\mathbf{k}_j \cdot \mathbf{r}_i) \left[\mathbf{k}_j \times \mathbf{k}_j \times \bar{\mathbf{I}} + \frac{\omega^2}{c^2} \bar{\mathbf{K}}(\mathbf{r}_i, \mathbf{k}_j) \right] \cdot \mathbf{E}(\mathbf{k}_j) = 0. \quad (11)$$

In the one-dimensional representation used here, $\mathbf{r}_i = x_i \hat{\mathbf{e}}_x + y_i \hat{\mathbf{e}}_y + z_i \hat{\mathbf{e}}_z$, where x_i is the i th spatial grid point, with $0 \leq i \leq N$, $y_i \equiv y(x_i)$ and $z_i \equiv z(x_i)$ define the chord along which the computation is performed. $\mathbf{k}_j \equiv k_j \hat{\mathbf{e}}_x + k_y \hat{\mathbf{e}}_y + k_z \hat{\mathbf{e}}_z$, with $k_j \equiv \pi(2j - N)/L$ where L is the length of this chord and $0 \leq j \leq N$. k_y is assumed to be constant and k_z varies in accordance with the toroidal upshift, i.e., $k_z(R) = k_{z,ant} R_{ant}/R$, R being the major radius, R_{ant} the antenna major radius, and $k_{z,ant}$ representing the launched spectrum. The numerical solution of Eq. (11) reduces to a matrix inversion, which is efficiently performed on parallel computers even when large problems are considered and when the matrix is dense, which is the case as soon as $k_\perp \rho_i$, with k_\perp the perpendicular wave number, is no longer much smaller than unity. Likewise, Eqs. (9) and (10) show that the computation of the energy quantities mostly reduces to double integrals evaluations, whose parallel computation is straightforward and involves few interprocesses communications, making the full-wave problem well suited for efficient treatment on parallel computers.

III. ABSORPTION KERNEL

If β_i is the angle between $\mathbf{k}_\perp (i=1,2)$ and $\hat{\mathbf{e}}_x$, and n denotes the n th cyclotron harmonic, then $\bar{\mathbf{W}}_s$, the local absorption kernel for species s may be written in the form

$$\begin{aligned} \bar{\bar{\mathbf{W}}}_s(\mathbf{r}, \mathbf{k}_1, \mathbf{k}_2) = & -\frac{\omega_{ps}^2}{\omega} \sum_{n=-\infty}^{\infty} \exp(in(\beta_1 - \beta_2)) \\ & \times \bar{\mathbf{C}}^{-1}(\beta_2) \cdot \bar{\bar{\Theta}}_{n,s} \cdot \bar{\mathbf{C}}(\beta_1) \end{aligned} \quad (12)$$

with $\bar{\bar{\mathbf{W}}} = \sum_s \bar{\bar{\mathbf{W}}}_s$. Among the most important features of $\bar{\bar{\mathbf{W}}}$ is the fact that it acts symmetrically on its left and on its right, unlike the usual dielectric tensor. This point is the key to the demonstration of the positive character of the spatial absorption in an all-orders description.¹⁶ $\bar{\mathbf{C}}$ is the unitary polarization matrix given by

$$\bar{\mathbf{C}}(\beta) = \frac{1}{\sqrt{2}} \begin{pmatrix} e^{i\beta} & -ie^{i\beta} & 0 \\ e^{-i\beta} & ie^{-i\beta} & 0 \\ 0 & 0 & \sqrt{2} \end{pmatrix}. \quad (13)$$

The velocity-space dependence arising from the equilibrium distribution function $f_{0,s}$ is contained in the kernel $\bar{\bar{\Theta}}_{n,s}$, which appears as

$$\bar{\bar{\Theta}}_{n,s}(\mathbf{r}, \mathbf{k}_1, \mathbf{k}_2) = i \int_0^\infty d\tau \int d^3\mathbf{v} e^{i(\omega - n\Omega_s - k_{1,\parallel}v_{\parallel})\tau} \bar{\bar{\mathbf{w}}}_{n,s}, \quad (14)$$

where

$$\bar{\bar{\mathbf{w}}}_{n,s} \equiv \frac{1}{2} \mathbf{a}_{n,s} \mathbf{b}_{n,s}, \quad (15)$$

with

$$\mathbf{a}_{n,s} \equiv [v_{\perp} J_{n+1}(\xi_{2,s}), v_{\perp} J_{n-1}(\xi_{2,s}), \sqrt{2} v_{\parallel} J_n(\xi_{2,s})] \quad (16)$$

and

$$\mathbf{b}_{n,s} \equiv [\hat{L}f_{0,s} J_{n+1}(\xi_{1,s}), \hat{L}f_{0,s} J_{n-1}(\xi_{1,s}), \sqrt{2} \hat{L}f_{0,s} J_n(\xi_{1,s})], \quad (17)$$

where $\xi_{i,s} \equiv k_{\perp,i} v_{\perp} / \Omega_s$ ($i=1,2$). Ω_s is the cyclotron frequency and the (J_n) are Bessel functions of the first kind. The differentiation operators are defined as

$$\begin{aligned} \hat{L}f_{0,s} & \equiv \left(1 - \frac{k_{\parallel} v_{\parallel}}{\omega} \right) \frac{\partial f_{0,s}}{\partial v_{\perp}} + \frac{k_{\parallel} v_{\perp}}{\omega} \frac{\partial f_{0,s}}{\partial v_{\parallel}}, \\ \hat{L}_n f_{0,s} & \equiv \frac{n\Omega_s v_{\parallel}}{\omega} \frac{\partial f_{0,s}}{\partial v_{\perp}} + \left(1 - \frac{n\Omega_s}{\omega} \right) \frac{\partial f_{0,s}}{\partial v_{\parallel}}. \end{aligned} \quad (18)$$

These expressions reduce to well-known quantities when a Maxwellian distribution function is ascribed to $f_{0,s}$.²⁰ The inclusion of the parallel gradient effect, neglected in the present work, leads to a further complication which is avoided by performing the v_{\parallel} integral first, followed by the integrations over τ and v_{\perp} as was shown by Smithe *et al.*²¹ This operation leads to a generalized plasma dispersion function, whose evaluation can still be performed analytically. Since the purpose of the extension of METS presented in this paper is the addition of the capability to handle arbitrary gyrotropic distribution functions, e.g., resulting from a Fokker–Planck calculation, the velocity integrations will be performed numerically. $\bar{\bar{\Theta}}_{n,s}$ is thus rewritten as

$$\begin{aligned} \bar{\bar{\Theta}}_{n,s}(\mathbf{r}, \mathbf{k}_1, \mathbf{k}_2) = & 2\pi \int_{-\infty}^{\infty} dv_{\parallel} \frac{1}{\omega - n\Omega_s - k_{1,\parallel}v_{\parallel}} \\ & \times \int_0^{\infty} dv_{\perp} v_{\perp} \bar{\bar{\mathbf{w}}}_{n,s}(\mathbf{r}, \mathbf{v}, \mathbf{k}_1, \mathbf{k}_2). \end{aligned} \quad (19)$$

After the v_{\perp} integral is performed numerically, the v_{\parallel} integral is evaluated using Plemelj formula as

$$\begin{aligned} \bar{\bar{\Theta}}_{n,s}(\mathbf{r}, \mathbf{k}_1, \mathbf{k}_2) = & \mathcal{P} \int_{-\infty}^{\infty} dv_{\parallel} \frac{\bar{\bar{\mathcal{W}}}_{n,s}}{\omega - n\Omega_s - k_{1,\parallel}v_{\parallel}} \\ & - i \frac{\pi}{|k_{1,\parallel}|} \bar{\bar{\mathcal{W}}}_{n,s} \Big|_{v_{\parallel}=v_{\parallel, res}}, \end{aligned} \quad (20)$$

with definition

$$\bar{\bar{\mathcal{W}}}_{n,s}(\mathbf{r}, \mathbf{k}_1, \mathbf{k}_2, v_{\parallel}) \equiv 2\pi \int_0^{\infty} dv_{\perp} v_{\perp} \bar{\bar{\mathbf{w}}}_{n,s}(\mathbf{r}, \mathbf{k}_1, \mathbf{k}_2, \mathbf{v}), \quad (21)$$

and where $v_{\parallel, res} \equiv (\omega - n\Omega_s) / k_{1,\parallel}$ corresponds to the resonant parallel velocity. \mathcal{P} refers to the Cauchy principal value, whose evaluation is one of the most time-consuming tasks of the code. By fully computing both the real and imaginary parts of $\bar{\bar{\Theta}}_{n,s}$ in this fashion, METS provides the first self-consistent full-wave treatment of wave propagation and absorption in plasmas with non-Maxwellian species.

IV. MODEL DISTRIBUTION FUNCTION

Although the 1D slab model presented here is generally applicable to any plasma in which trapping effects and parallel gradients in the equilibrium magnetic field can be ignored, for illustrative purposes, two specific cases relevant to radio frequency heating of toroidal magnetic fusion plasmas will be considered. Both of these cases include nonthermal ions present in the plasma due to neutral beam injection and the corresponding fast ion population is described by a slowing-down model in which the dominant process is assumed to be the relaxation on electrons.⁴ The slowing-down distribution function (SDDF) $f_{0,b}$ is expanded as a series of Legendre polynomials P_l ,

$$f_{0,b}(u, \mu) = \sum_{l=0}^{\infty} a_l(u) P_l(\mu), \quad (22)$$

where $\mu \equiv v_{\parallel} / v$ is the pitch-angle cosine and $u \equiv v / v_b$ is the velocity normalized to the beam injection velocity $v_b \equiv \sqrt{2E_b / m_b}$, with E_b the beam energy and m_b the beam ion mass. The coefficients a_l are given by

$$a_l(u) \equiv (2l+1) \frac{S\tau_s K_l}{v_b^3 K_0 4\pi(1+u_c^2)} A_l(u). \quad (23)$$

Here, S is the number of injected particles per second and per unit volume, τ_s the slowing-down time⁴ defined as

$$\tau_s = 2\pi^{3/2} \epsilon_0^2 \frac{m_e m_b}{Z_b^2 n_e \ln(\Lambda)} v_{th,e}^3, \quad (24)$$

with m_e the electron mass, $v_{th,e}$ the electron thermal velocity, n_e the electron density, and $\ln(\Lambda)$ the Coulomb logarithm. u_c is the critical velocity,

$$u_c^3 = \frac{3}{4} \sqrt{\frac{m_e \bar{Z}}{\pi}} \frac{v_{th,e}^3}{m_i v_b^3}, \quad (25)$$

where $\bar{Z} = \sum_i m_b n_i Z_i^2 / m_i m_e$. Z_i is the ion charge number, m_i its mass, n_i its density, and the sum has to be carried over all ion species.

The K_l coefficients are given by

$$K_l \equiv \int_{-1}^1 d\mu P_l(\mu) K(\mu), \quad (26)$$

where $K(\mu)$ is the beam angular distribution. When the charge-exchange losses are neglected, A_l can be written as

$$A_l(u) = u^{l(l+1)\beta} \left(\frac{1+u_c^3}{u^3+u_c^3} \right)^{1+l(l+1)\beta/3} H(1-u), \quad (27)$$

with $\beta = m_i Z_{eff} / (2m_b \bar{Z})$, $Z_{eff} = \sum_i n_i Z_i^2 / n_e$. H is the Heaviside function.

In the remainder of this paper, a Gaussian-shaped angular distribution will be used for the beam,

$$K(\theta) = \bar{K} \exp\left(-\frac{(\theta - \theta_0)^2}{\Delta\theta^2}\right), \quad (28)$$

where \bar{K} is a constant, θ_0 is the beam injection angle with respect to the magnetic field direction, and $\Delta\theta$ is the beam angular divergence.

In order to avoid an unphysical step at $v = v_b$, the distribution function decreases exponentially, i.e., $f_{0,b}(u > 1) = f_w(u)$ with

$$f_w(u) = \sum_{l=0}^{\infty} b_l P_l(\mu) \exp\left(-\frac{(u - u_l)^2}{\Delta u^2}\right), \quad (29)$$

with $\Delta u \ll 1$. The b_l and u_l coefficients are computed to ensure that the distribution function and its derivatives with respect to u_l and u_{\perp} are continuous. This gives

$$b_l = a_l(1) \exp\left(\frac{(1 - u_l)^2}{\Delta u^2}\right) \quad (30)$$

and

$$u_l = 1 + \frac{\Delta u^2 l(l+1)\beta u_c^3 - 3}{1 + u_c^3}. \quad (31)$$

Based on the results cited in Ref. 7, nonthermal species are often modeled in the dielectric kernel by equivalent Maxwellian (EQM) distributions featuring the same average energy and particle density as the corresponding non-Maxwellian species. To highlight the differences in wave dynamics due to nonthermal distributions, results obtained with the model slowing-down distributions will be compared to those obtained with the equivalent Maxwellian represen-

tation. Specifically, two Maxwellian distributions will be used: an isotropic EQM and a bitemperature EQM.

Defining the energy content of the SDDF as

$$\varepsilon = \frac{2}{3} \int d^3\mathbf{u} \left(\frac{u^2}{2}\right) f(\mathbf{u}), \quad (32)$$

the isotropic EQM is given by

$$f_{eq}(\mathbf{u}) = f_{eq}(u) = \frac{1}{(2\pi\varepsilon)^{3/2}} \exp\left(-\frac{u^2}{2\varepsilon}\right). \quad (33)$$

The anisotropic (bitemperature) EQM is obtained by defining

$$\varepsilon_{\parallel} = 2 \int d^3\mathbf{u} \left(\frac{u_{\parallel}^2}{2}\right) f(\mathbf{u}), \quad \varepsilon_{\perp} = \int d^3\mathbf{u} \left(\frac{u_{\perp}^2}{2}\right) f(\mathbf{u}), \quad (34)$$

so that

$$f_{eq}(\mathbf{u}) = f_{eq}(u_{\parallel}, u_{\perp}) = \frac{1}{(2\pi)^{3/2} \varepsilon_{\parallel}^{1/2} \varepsilon_{\perp}} \exp\left(-\frac{u_{\parallel}^2}{2\varepsilon_{\parallel}}\right) \exp\left(-\frac{u_{\perp}^2}{2\varepsilon_{\perp}}\right). \quad (35)$$

V. ICRF HEATING IN TFTR

The full-wave analysis presented in Sec. II is applied to a situation in which ICRF waves were used on TFTR to heat electrons, through the absorption of an ion Bernstein wave obtained by mode conversion of a fast wave excited at the antenna.²² A mixed deuterium-tritium ($D-T$) plasma was formed by injecting a 103 keV tritium neutral beam into a deuterium target plasma, resulting in a tritium concentration of 0.42 relative to the electron density. The thermal D ions, as well as the dilute thermal hydrogen and carbon impurity ions, had central temperature $T_{i0} = 31$ keV. The central electron density was $n_{e0} = 4.7 \times 10^{19} \text{ m}^{-3}$ with central electron temperature $T_{e0} = 7.8$ keV. The confinement magnetic field on the magnetic axis ($R_0 = 2.84$ m) was $B_0 = 4.7$ T. For ICRF waves with frequency $f_{RF} = 30$ MHz and parallel wave number $k_{\parallel,ant} \approx 5.2 \text{ m}^{-1}$, launched from the low field side of the torus, the unshifted fundamental deuterium (respectively tritium) cyclotron resonance is located at $R \approx 3.40$ m (respectively $R \approx 2.27$ m). In this scenario, mode conversion between the launched fast wave and short wavelength ion Bernstein wave (IBW) occurs between the D and T fundamental resonance layers, at radius $R \approx 2.78$ m. The tritium beam ions are simulated with an isotropic SDDF, whereas all other species are assumed to be Maxwellian.

In a full-wave description, the dispersion relation does not need to be computed, since no particular propagation mode is to be isolated, contrary to ray-tracing computations. However, it generally sheds considerable light on the modes potentially propagating in the plasma, and thus on the ICRF scheme itself. Practically, it is obtained from Eq. (11), writing

$$\det \left\{ \mathbf{k}_j \times \mathbf{k}_j \times \bar{\mathbf{I}} + \frac{\omega^2}{c^2} \bar{\mathbf{K}}(\mathbf{r}, \mathbf{k}_j) \right\} = 0, \quad (36)$$

and solving for (k_j) . In Fig. 1, the real part of the dispersion relation obtained with the parameters given above is shown. The branches corresponding to the incident, reflected, and

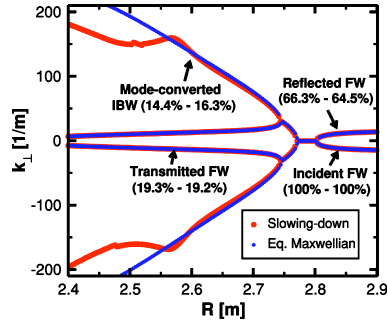


FIG. 1. (Color online). Real part of the dispersion relation for a IBW mode-conversion scheme in TFTR, obtained with a slowing-down distribution function (thick symbols), with the equivalent Maxwellian (thin symbols). The figures between parentheses give the relative fraction of power in each branch of the dispersion relation, the first one referring to the SDDF, the second one to the EQM.

transmitted fast wave, and the mode-converted Bernstein wave (which is a backward mode) are denoted. The dispersion relation typical of a mode-conversion scheme is recognized, with a back-to-back cutoff resonance featuring a conversion layer at $R \approx 2.78$ m. The fact that METS uses a set of incoming and outgoing waves as boundary conditions make it capable of predicting the respective fractions of power in each branch of the dispersion relation. With the SDDF (resp. EQM), we obtain a reflected fraction of 66.3% (resp. 64.5%), a transmitted fraction of 19.3% (resp. 19.2%), and a mode-converted fraction of 14.4% (resp. 16.3%). The power on the IBW branch is found to be entirely damped in both cases. These observations lead to conclude that the mode-conversion scenario in itself is rather weakly affected by the nature of the distribution function. The dispersion relation obtained for the SDDF differs significantly from the dispersion relation computed with the EQM on the ion Bernstein branch only for $|k_{\perp}| \gtrsim 200$ m⁻¹. In order to evaluate the potential effect of this difference on the wave field, the spectrum of the total electric field obtained from METS is shown in Fig. 2. The tail corresponding to the ion Bernstein wave is

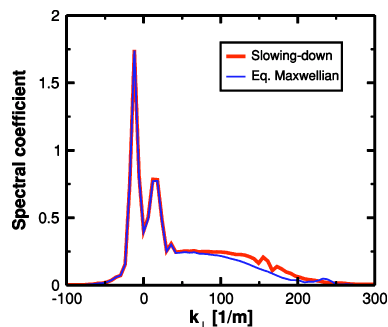


FIG. 2. (Color online). Spectrum of the electric field in TFTR, obtained with a slowing-down distribution (thick line) and with its equivalent Maxwellian (thin line).

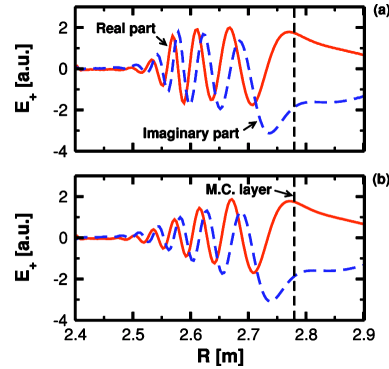


FIG. 3. (Color online). Real part (solid line) and imaginary part (dashed line) of the left-handed electric field when (a) a slowing-down distribution function or (b) the equivalent Maxwellian is used to simulate the tritium beam ions.

observed, extending to wave numbers up to $k_{\perp} \approx 200$ m⁻¹. The spectra obtained in the case of the SDDF and the EQM are fairly similar, with a globally lower tail in the former case. This is caused by the fact that with the SDDF, the power propagates further on the IBW branch before being strongly absorbed by the T ions. On the contrary, in the EQM case, the ions belonging to the fast tail of the Maxwellian distribution damp the power at smaller values of k_{\perp} , owing to the large Doppler shift of the cyclotron resonance.

In Figs. 3 and 4, the left-handed and parallel components of the electric field, respectively, defined as $E_{\perp} \equiv E_x + iE_y$ and $E_{\parallel} \equiv \mathbf{E} \cdot \mathbf{B}_0 / B_0$ are displayed as functions of major radius for both distribution functions. Also denoted is the approximate location of the mode-conversion layer. On the left-hand side of the mode-conversion layer, the electric field exhibits a wavelength $\lambda \approx 5$ cm consistent with the values of k_{\perp} on the mode-converted branch in Fig. 1. In both cases, the same general structure is observed for the SDDF and the EQM.

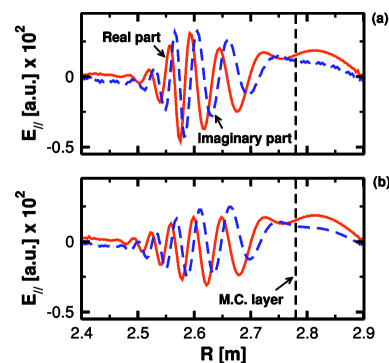


FIG. 4. (Color online). Real part (solid line) and imaginary part (dashed line) of the parallel electric field when (a) a slowing-down distribution function or (b) the equivalent Maxwellian is used to simulate the tritium beam ions.

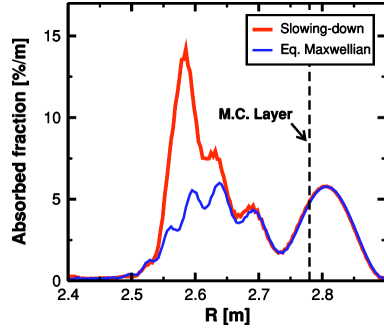


FIG. 5. (Color online). Profile of the power deposited on electrons for a slowing-down distribution function (thick line) and for its equivalent Maxwellian (thin line). Also appearing as a vertical dashed line is the approximate location of the mode-conversion layer.

From the low field side ($R=2.9$ m) to $R \approx 2.55$ m, E_{\perp} and E_{\parallel} obtained with the SDDF appear to be similar to their EQM counterparts, and differ only from this point on to the high field side. The amplitude of the oscillations in the wave structure due to the mode converted IBW decreases with distance more strongly when the SDDF is used, although the actual wavelength of the IBW obtained from the two model distributions is nearly the same.

Using Eq. (9), the power deposited on each species can be computed. In the case under study, only electrons and tritium ions are found to absorb a significant fraction of the wave power. In Fig. 5, the power deposited on electrons is shown as a function of major radius, for the two assumed tritium distribution functions. In Fig. 6, the power deposited on tritium ions is plotted as a function of major radius. The total single-pass absorption is found to be 15.6% in the case of the SDDF and 17.3% in the case of the EQM. The fraction of the total absorbed power deposited on electrons is 12.1% in the case of the SDDF and 8.1% in the case of the EQM, and the deposition profiles have a fairly similar aspect. On the other hand, the power absorbed by the T ions is 87.8%

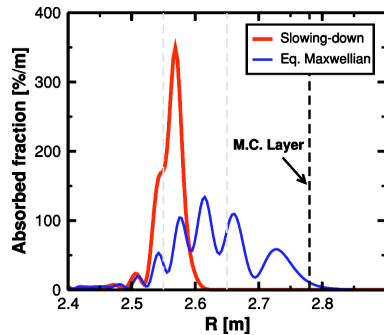


FIG. 6. (Color online). Profile of the power deposited on the tritium beam ions for a slowing-down distribution function (thick line) and for its equivalent Maxwellian (thin line). Also appearing as a vertical dashed line is the approximate location of the mode-conversion layer.

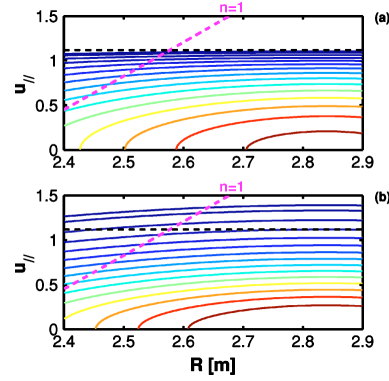


FIG. 7. (Color online). Contours of the fast ion parallel distribution function for (a) a slowing-down type or (b) a Maxwellian distribution function. The oblique dashed lines denote the velocity-space location of the Doppler-shifted fundamental tritium resonance.

with the SDDF and 91.9% in the case of the EQM. With the slowing-down distribution, however, the power deposition is much more peaked and shifted towards high field side. This discrepancy can be explained by examining differences in the parallel distribution function for the beam ions, defined as

$$F_{\parallel,b}(r, u_{\parallel}) \equiv 2\pi \int_0^{\infty} du_{\perp} u_{\perp} f_{0,b}(r, u_{\parallel}, u_{\perp}). \quad (37)$$

The contours of $n_b(r)F_{\parallel,b}(r, u_{\parallel})$, with n_b the fast ion density, obtained for the isotropic SDDF and the EQM are shown in Fig. 7 in the (R, u_{\parallel}) plane. For clarity, these contours are quadratically spaced. Also appearing in the figure is a line representing the resonant parallel velocity of the beam ions

$$u_{\parallel, res} = \left(\frac{m_b c^2}{2E_b} \right)^{1/2} \frac{1 - n\Omega_b/\omega}{n_{\parallel}}, \quad (38)$$

with $n_{\parallel} = ck_{\parallel}/\omega$ and $n=1$ in this fundamental heating case. The difference between the SDDF and the EQM is linked to the fact that above the injection energy, the SDDF density is zero, whereas in the case of the Maxwellian, a small but finite number of beam ions have a velocity large enough to satisfy the Doppler-shifted resonance condition, and thus absorb the wave. This is consistent with the fact that the tritium absorption, shown in Fig. 6, begins only at $R \approx 2.6$ m for the SDDF. To further illustrate this difference, the parallel distribution function $F_{\parallel,b}$ for the isotropic SDDF and the EQM is shown in Fig. 8 at two different positions in the plasma, $R=2.55$ m and $R=2.65$ m indicated by the dashed lines in Fig. 6. The velocity-space location of the shifted tritium resonance at each of these spatial positions is indicated by a dashed line. Since the rate of absorption is proportional to the slope of the distribution function for the resonant ions, the SDDF absorbs the wave power more strongly than the EQM near $R \approx 2.55$ m.

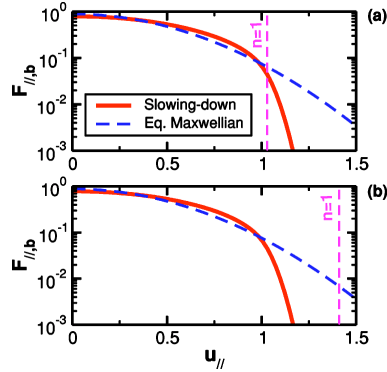


FIG. 8. (Color online). Beam ions parallel distribution function for a slowing-down type (solid line) or a Maxwellian (dashed line) distribution function at major radius (a) $R=2.55$ m and (b) $R=2.65$ m (both positions appear as grayed dashed lines in Fig. 6). The vertical dashed lines denote the velocity-space location of the Doppler-shifted fundamental tritium resonance.

VI. FAST WAVE ELECTRON HEATING IN NSTX

In the spherical torus NSTX, high harmonic fast wave (HHFW) heating can potentially be used to heat electrons and to drive noninductive toroidal current²³ through absorption of the wave by Landau damping and transit time magnetic pumping. When the wave is injected in a plasma containing neutral injection-born deuterium ions, it is reasonable to expect a modification of the propagation and absorption properties of the wave due to the influence of the fast population. The fast ions can absorb a significant amount of power, thus lowering the electron absorption.²⁴

Typical parameters of HHFW discharges in NSTX include $B_0=0.45$ T at $R_0=1$ m, $n_{e0}=2.75 \times 10^{19}$ m⁻³, and $T_{e0}=1$ keV. Perpendicular or tangential 80 keV deuterium NBI heating has been examined.²³ For these parameters, the fast D ions comprise about 15% of the plasma density. The wave frequency is $f_{FW}=30$ MHz, so that the 5th through 12th harmonics of the unshifted D cyclotron resonance are present in the plasma. The parallel wave number at the antenna is $k_{||,ant} \approx 14$ m⁻¹. In addition to the fast population, three thermal ion species are taken into account: deuterium, hydrogen, and carbon, all with central temperature $T_{i0}=1$ keV. The fast ions are simulated using a slowing-down distribution, as described in Sec. IV, either isotropic or anisotropic with $\theta_0=0^\circ$ (tangential injection) or $\theta_0=90^\circ$ (perpendicular injection).

First, the results obtained in the absence and in the presence of the beam are compared. When no beam is present, the quasineutrality is ensured by adjusting the carbon or hydrogen density, which was verified to have no impact on the result. In Fig. 9, the real parts of the left-handed and parallel wave electric field computed by METS are shown as functions of the major radius, along an equatorial chord, when no fast population is present, and when the fast ions are described either by an isotropic slowing-down distribution or by its equivalent Maxwellian. As expected for HHFW, the varia-

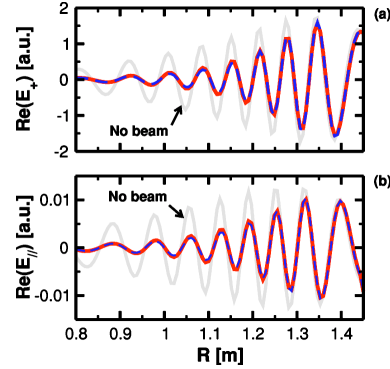


FIG. 9. (Color online). Real part of the (a) left-handed and (b) parallel wave electric field in the absence (grayed) and in the presence of a deuterium beam when the latter is represented by an isotropic SDDF (solid line) or by an isotropic EQM (dashed line, barely visible).

tions of the left-handed and of the parallel field are dominated by long wavelengths consistent with the local dispersion relation for the fast wave branch. In the presence of fast ions, a stronger attenuation of the wave field is observed, indicating an increased absorption of the wave by the plasma. The wavelength, on the other hand, is not affected. The corresponding power deposition profiles, on electrons in the absence of the beam, and on electrons and beam ions when NBI is present, are shown in Fig. 10. When no beam is injected in the plasma, the single-pass absorption is 71.6%, damped on electrons. With NBI, the single-pass absorption increases to 92.9% (respectively 95.3%) among which 28.8% (respectively 27.8%) is damped by electrons, and 71.2% (respectively 72.1%) when the latter are modeled using a SDDF (resp. an EQM). It is found that no other species absorbs a significant fraction of the wave power.

Another observation is that the EQM reproduces fairly well the fast ion absorption when the fast ion distribution is isotropic. To explain this feature, which appears to be in

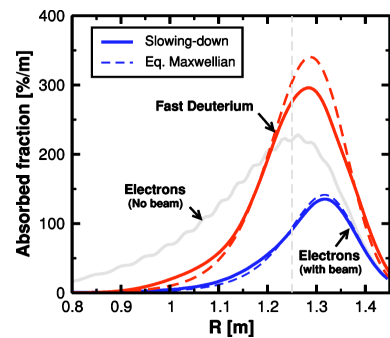


FIG. 10. (Color online). Power deposited on species as a function of major radius: electron absorption when no beam is present (grayed); fast ion and electron absorption when the former are described by an isotropic SDDF (solid line) or an isotropic EQM (dashed line).

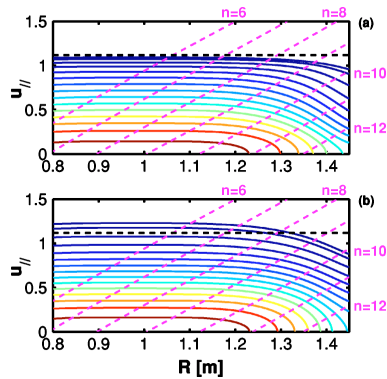


FIG. 11. (Color online). Contours of the fast ion parallel distribution function for (a) a slowing-down type or (b) a Maxwellian distribution function. The oblique dashed lines denote the velocity-space location of the Doppler-shifted deuterium resonances.

contrast to the conclusions of Sec. V, Fig. 11 shows contours of $n_b(r)F_{\parallel,b}(r, u_{\parallel})$ in the (R, u_{\parallel}) plane, for the beam ions modeled using either the SDDF or the EQM. Since, the scheme relies on the absorption of the wave at large harmonic numbers, several resonances are simultaneously present in the plasma, and appear in the figure, as well. For these parameters, the EQM is an adequate representation of the SDDF, and the simultaneous presence of multiple resonances in the plasma has the consequence that the wave is mostly absorbed by bulk ions at any location in the plasma. To further illustrate this, in Fig. 12, $F_{\parallel,b}$ is shown versus parallel velocity, at major radius $R=1.25$ m. Again, the two distribution functions differ by the fact that the SDDF drops sharply to zero for $u_{\parallel} \geq 1$, whereas the EQM has a tail extending to higher velocities. However, in this case, the presence of several resonances ($n=7-11$) allow the wave to interact with lower energy ions. Therefore, the detailed behavior of the fast velocity part of the distribution, especially for $u_{\parallel} \geq 1$, is of lesser importance than in the case presented in Sec. V.

Anisotropic velocity effects can also have a significant impact on the wave absorption profiles: parallel velocity ef-

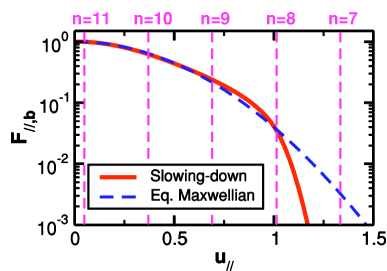


FIG. 12. (Color online). Beam ions parallel distribution function for a slowing-down type (solid line) or a Maxwellian distribution function (dashed line) at major radius $R=1.25$ m (denoted as a gray line in Fig. 10). The vertical dashed lines denote the velocity-space location of the Doppler-shifted deuterium resonances.

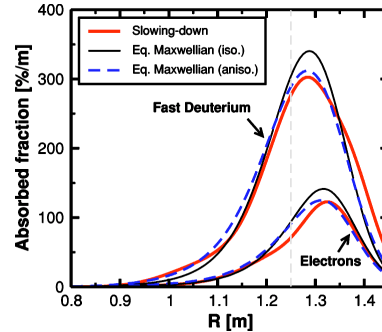


FIG. 13. (Color online). Power deposited on (a) electrons and on (b) the fast deuterium ions, when the latter are described by an anisotropic SDDF corresponding to a perpendicular injection of the beam (thick solid line), or when the isotropic (thin line) or the bi-temperature (dashed line) EQM is substituted.

fects tend to modify the absorption profile by broadening the resonance region, while perpendicular velocity effects mostly affect the wave damping at higher harmonics. To study this impact, the same parameters as before are considered, but with a slowing-down distribution function which is representative of a beam launched either tangentially or perpendicularly with respect to the magnetic field direction. In order to improve the EQM representation, a bitemperature Maxwellian is used, with $T_{\parallel} \neq T_{\perp}$ to account for the different energy content in the parallel and perpendicular directions of velocity space.

First, the beam is assumed to be injected perpendicularly to the magnetic field ($\theta_0=90^\circ$). The power deposition on fast deuterium ions and electrons is shown in Fig. 13. The absorption on the fast ions is fairly well described with the isotropic EQM, and the agreement is further improved with the bitemperature EQM. In this case, the single-pass absorptions on each species are found to agree within 3%.

If the beam is injected tangentially, on the other hand, the power deposition profile is not well reproduced using an EQM, either isotropic or bitemperature. This is shown in Fig. 14 where the fast ion absorption is shown as a function of the major radius. Considering the single-pass absorption on the D ions modeled with the SDDF as a reference ($P_D/P_{total}=51.9\%$), the isotropic EQM underestimates the ion absorption, giving $P_D/P_{total}=27.8\%$, whereas the bitemperature EQM overestimates it, with $P_D/P_{total}=70.1\%$. In Fig. 15, $F_{\parallel,b}$ for perpendicular or tangential injection, at radius $R=1.25$ m, is compared for the SDDF, the isotropic EQM, and the bitemperature EQM. When the beam is injected perpendicularly to the magnetic field, the bitemperature Maxwellian is able to reproduce the shape of the distribution. On the other hand, neither the isotropic nor the anisotropic EQM is able to retain the features of $F_{\parallel,b}$ when the beam is injected tangentially to the magnetic field and as a consequence, the absorption profiles differ significantly.

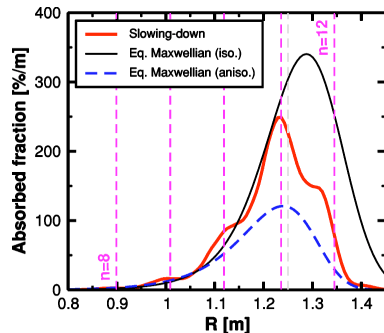


FIG. 14. (Color online). Power deposited on the fast deuterium ions, when the latter are described by an anisotropic SDDF corresponding to a perpendicular injection of the beam (thick solid line), or when the isotropic (thin line) or the bitemperature (dashed line) EQM is substituted. The vertical dashed lines denote the unshifted deuterium resonances.

VII. CONCLUSIONS

In this paper, the effects of non-Maxwellian distribution functions on the propagation and absorption of waves in the ion cyclotron range of frequencies are discussed. In order to conduct this study, METS, a full-wave, one-dimensional, all-orders code has been extended to handle arbitrary gyrotropic distribution functions, by resorting to massively parallel computers to perform numerically the velocity integrals involved in the calculation of the electromagnetic field and wave absorption.

The code has been used to investigate ICRF heating on TFTR, in a fast wave to ion Bernstein wave mode-conversion scenario, when a tritium beam was simultaneously injected in the plasma. The simulations show that the wave structure of only the finite temperature mode-converted

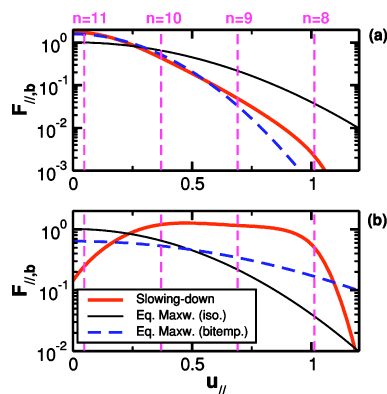


FIG. 15. (Color online). Parallel distribution function for a slowing-down type (thick line), the isotropic equivalent Maxwellian distribution function (thin line), and the bitemperature Maxwellian distribution (dashed) at major radius $R=1.25$ m (denoted as a gray line in Fig. 10) for (a) perpendicular beam injection and (b) tangential beam injection. The vertical dashed lines denote the velocity-space location of the Doppler-shifted deuterium resonances.

IBW is affected by the details of the fast ion distribution function. Although the mode-conversion scenario in itself appears to be rather weakly affected, the deposition profiles differ dramatically depending on whether the fast ion distribution function is modeled with an isotropic slowing-down distribution function, or with an equivalent Maxwellian, reproducing its particle and energy contents. This discrepancy is caused by the difference in the structure of the distribution function for $v \gtrsim \sqrt{2E_b/m_b}$: the presence of ions having $v > v_b$ in the EQM case causes a larger Doppler shift and thus a wider absorption.

HHFW electron heating on NSTX has been explored with the same code. METS predicts that in the presence of a deuterium beam, a significant fraction of the power is absorbed by the fast ions, lowering the electron absorption, which is consistent with earlier simulations²⁴ and experimental measurements.²³ In this regime, the rf wave fields are dominated by the fast wave, which is adequately described by a cold plasma model. Thus, although the attenuation of the fields is different for isotropic or anisotropic beam distributions due to a different wave absorption, the wavelength is largely unaffected by the details of the distribution function. Furthermore, owing to the fairly large number of resonances simultaneously involved in the interaction, the SDDF and EQM absorptions are similar, as long as the distribution is isotropic in velocity space. This is also the case when an anisotropic SDDF is used with the beam injected perpendicularly with respect to the magnetic field, which introduces no major structural modification of the distribution function in the parallel direction. On the other hand, if the beam is assumed to be injected tangentially to the magnetic field, it was shown that the isotropic equivalent Maxwellian description predicts too large a fast ion damping rate, and that the introduction of a bitemperature Maxwellian was not sufficient to recover a correct absorption, since it is unable to reproduce the features of the effective distribution function.

ACKNOWLEDGMENTS

Fruitful discussions with D. B. Batchelor, L. A. Berry, P. T. Bonoli, M. D. Carter, E. D'Azevedo, D. A. D'Ippolito, R. W. Harvey, E. F. Jaeger, J. R. Myra, A. L. Rosenberg, and J. C. Wright are gratefully acknowledged.

- ¹M. Gedalin, Y. Lyubarsky, M. Balikhin, and C. T. Russel, *Phys. Plasmas* **8**, 2934 (2001).
- ²M. Gedalin, M. Balikhin, R. J. Strangeway, and C. T. Russell, *J. Geophys. Res.* **107**, 1018 (2002).
- ³M. A. Hellberg and R. L. Mace, *Phys. Plasmas* **9**, 1495 (2002).
- ⁴M. Cox and D. F. H. Start, *Nucl. Fusion* **24**, 399 (1984).
- ⁵T. H. Stix, *Nucl. Fusion* **15**, 737 (1975).
- ⁶C. F. F. Karney and N. J. Fisch, *Phys. Fluids* **22**, 1817 (1979).
- ⁷R. Koch, *Phys. Lett. A* **157**, 399 (1991).
- ⁸D. Van Eester, *Plasma Phys. Controlled Fusion* **35**, 441 (1993).
- ⁹D. Van Eester, *Plasma Phys. Controlled Fusion* **36**, 1327 (1994).
- ¹⁰D. B. Batchelor, E. F. Jaeger, and P. L. Colestock, *Phys. Fluids B* **1**, 1174 (1989).
- ¹¹J. Hedin, T. Hellsten, T. Johnson, and L.-G. Eriksson, in *Proceedings of the Joint Varenna-Lausanne Workshop on the Theory of Fusion Plasmas, Varenna, Italy, 1998* (Editrice Compositori, Bologna, 1999), p. 467.
- ¹²O. Sauter and J. Vaclavik, *Nucl. Fusion* **32**, 1455 (1992).
- ¹³D. N. Smithe, C. K. Phillips, J. C. Hosea, R. P. Majeski, and J. R. Wilson, in *Proceedings of the 12th Topical Conference on Radio Frequency Power*

- in *Plasmas*, Savannah, GA, 1997, edited by P. M. Ryan and T. Intrator (American Institute of Physics, New York, 1997), p. 367.
- ¹⁴E. F. Jaeger, L. A. Berry, and D. B. Batchelor, in *Proceedings of the 13th Topical Conference on Radio Frequency Power in Plasmas, Annapolis, MD, 1999*, edited by S. Bernabei and F. Paoletti (American Institute of Physics, New York, 1999), p. 395.
- ¹⁵E. F. Jaeger, L. A. Berry, E. D'Azevedo, D. B. Batchelor, and M. D. Carter, *Phys. Plasmas* **5**, 1573 (2001).
- ¹⁶D. N. Smithe, *Plasma Phys. Controlled Fusion* **31**, 1105 (1989).
- ¹⁷D. Meade and the TFTR Group, in *Proceedings of the International Conference on Plasma Physics and Controlled Nuclear Fusion, Washington, DC, 1990* (International Atomic Energy Agency, Vienna, 1991), Vol. 1, p. 9.
- ¹⁸S. M. Kaye, M. Ono, Y.-K. M. Peng *et al.*, *Fusion Technol.* **36**, 16 (1999).
- ¹⁹I. B. Bernstein, *Phys. Fluids* **18**, 320 (1975).
- ²⁰T. H. Stix, *Waves in Plasmas* (American Institute of Physics, New York, 1997).
- ²¹D. N. Smithe, P. Colestock, T. Kammash, and R. Kashuba, *Phys. Rev. Lett.* **9**, 801 (1988).
- ²²C. K. Phillips, M. G. Bell, S. Bernabei *et al.*, *Nucl. Fusion* **40**, 461 (2000).
- ²³J. C. Hosea, R. E. Bell, M. Bitter *et al.*, in *Proceedings of the 28th European Physical Society Conference on Controlled Fusion and Plasma Physics, Madeira, Portugal, 2001*, edited by C. Silva, C. Varandas, and D. Campbell (European Physical Society, Vienna, 2001), Vol. 25A, p. 1165.
- ²⁴A. L. Rosenberg, J. E. Menard, J. R. Wilson *et al.*, *Phys. Plasmas* **11**, 2441 (2004).

Variational approach to radiofrequency waves in magnetic fusion devices

R.J. Dumont

CEA, IRFM, F-13108 Saint-Paul-lez-Durance, France

Received 16 January 2009, accepted for publication 15 May 2009

Published 1 July 2009

Online at stacks.iop.org/NF/49/075033

Abstract

Magnetic fusion plasmas feature two major classes of low frequency electromagnetic oscillations: waves in the ion cyclotron range of frequencies (ICRFs) constitute a well established method employed for plasma heating and current drive, whereas waves in the Alfvén range of frequencies naturally occur in the form of modes in close interaction with fast particles. The propagation of these waves is characterized by significant space-dispersion, making it necessary to incorporate non-local effects in the global kinetic full-wave codes which are often employed for their simulation. We present here a variational approach to this problem, which has the advantage of providing a common framework to the wave calculation and to the quasilinear response description. Two important points are discussed: firstly, we show that the irreversible part of the power transferred from the wave to the plasma particles is directly available and does not require an explicit evaluation of the kinetic flux; secondly, it is demonstrated that the symmetry of the obtained plasma functional ensures that these energy transfers are described in a consistent fashion, regardless of the level of approximation employed to evaluate the particle Hamiltonian. Finally, quasi-local, finite Larmor radius expressions are derived in the framework of this formalism and implemented in a new multi-dimensional full-wave code, named EVE, which is employed to analyse two ICRF heating scenarios for ITER.

PACS numbers: 52.35.Hr, 52.50.Qt, 52.55.Fa, 52.65.Ff

(Some figures in this article are in colour only in the electronic version)

1. Introduction

Owing to the robustness of the underlying technologies and to their versatility, waves in the ion cyclotron range of frequencies (ICRFs) are routinely employed in magnetic fusion devices and, as such, constitute one of the key elements for the success of future reactors [1]. Although plasma ion heating through minority fundamental absorption or harmonic damping is currently the most widespread scenario and is therefore favoured in plans for next-step experiments, ICRF waves also offer other possibilities, such as electron heating and/or non-inductive current drive either by direct damping of the fast magnetosonic wave excited by the antenna [2] or by damping of mode converted short wavelength kinetic waves [3], sawtooth stabilization by ion cyclotron current drive [4], and may even be used to generate plasma rotation [5]. Alfvén waves propagate at frequencies below the lowest ion cyclotron frequency. Although schemes involving these waves directly excited by outside antennas for plasma heating have been proposed in the past [6], they occur mostly in the form of various modes, such as toroidal Alfvén eigenmodes (TAEs), intrinsic to fusion plasmas, most notably when the latter feature fast ions [7].

Considerable efforts have been devoted to the modelling of both Alfvén and ICRF waves. Their large vacuum wavelength, added to the fact that most situations in which they occur involve cut-offs and mode conversion regions in the plasma, makes it necessary to describe their propagation and absorption by means of global codes [8]. Various models can be applied to the modelling of Alfvén waves: fluid descriptions [9] can be extended to incorporate kinetic effects [10]. Recently, global gyrokinetic codes have been developed to account for various effects related to Alfvén waves in modern devices [11]. On the other hand, ICRF waves are usually modelled by means of linear kinetic full-wave codes, either retaining all orders in the expansion of the wave-plasma interaction terms in series of $k_{\perp}\rho_i$, where k_{\perp} is the perpendicular wavenumber and ρ_i is the ion Larmor radius, at the price of stringent computational requirements [12], or performing a finite Larmor radius (FLR) expansion in $k_{\perp}\rho_i$ [13]. Although the applications presented in this paper pertain to ICRF waves, the inclusion of plasma space-dispersion in these codes makes them generally suited to describe both linear Alfvén and ICRF waves [8, 14].

This paper is organized as follows: in section 2, the Hamiltonian-based variational approach to the wave

calculation problem is extensively described and the general plasma functional is given in action-angle variables. The issue of energy transfers is also addressed in some detail. This comprehensive description of the dielectric response is, however, rather cumbersome to implement and requires challenging numerical resources. It is therefore of interest to analyse the approximations under which the more familiar quasi-local expressions can be deduced from the full description. The pertinent hypotheses and the situations where they break down are detailed in section 3. A practical expression of the plasma functional is obtained in terms of adiabatic invariants and an expansion of the particle Hamiltonian is performed to yield a tractable second-order FLR version of this functional. The obtained expressions are implemented in a new multi-dimensional full-wave code, named EVE, which is presented in section 4. As an illustration of some of the features of EVE, the simulation of two ICRF heating scenarios envisioned for ITER, i.e. pure second harmonic tritium and helium-3 minority heating, are analysed. Conclusions and prospects are discussed in section 5.

2. Variational formulation of the wave problem

Full-wave descriptions consist of calculating the wave field by a direct solution of the Maxwell's equations. Following [15] and considering a field oscillating at prescribed frequency ω , the current conservation is written in the form

$$\mathbf{j}_{\text{ant}} + \mathbf{j}_{\text{part}} = \frac{1}{\mu_0} \nabla \times \nabla \times \mathbf{A} + i\omega\epsilon_0(i\omega\mathbf{A} - \nabla\varphi) \equiv \mathbf{j}_{\text{maxw}}, \quad (1)$$

where \mathbf{j}_{ant} is the antenna current density, \mathbf{j}_{part} is the current density carried by the plasma particles. (\mathbf{A}, φ) is the wave four-potential. The charge conservation yields

$$\rho_{\text{ant}} + \rho_{\text{part}} = \epsilon_0 \nabla \cdot (i\omega\mathbf{A} - \nabla\varphi) \equiv \rho_{\text{maxw}}. \quad (2)$$

Three gauge-invariant functionals, respectively \mathcal{L}_{ant} , $\mathcal{L}_{\text{part}}$ and $\mathcal{L}_{\text{maxw}}$, are constructed by writing

$$\mathcal{L} \equiv \int d^3\mathbf{r} \{ \mathbf{j}(\mathbf{A}, \varphi) \cdot \mathbf{A}^* - \rho(\mathbf{A}, \varphi)\varphi^* \}, \quad (3)$$

and substituting \mathbf{j} (respectively ρ) with \mathbf{j}_{ant} , \mathbf{j}_{part} and $-\mathbf{j}_{\text{maxw}}$ (respectively ρ_{ant} , ρ_{part} and $-\rho_{\text{maxw}}$). The integrals are performed over the whole (assumed perfectly conducting) vacuum chamber volume. In the linear wave problem considered here, both $\mathcal{L}_{\text{part}}$ and $\mathcal{L}_{\text{maxw}}$ are bi-linear in (\mathbf{A}, φ) and $(\mathbf{A}^*, \varphi^*)$. \mathcal{L}_{ant} is linear in $(\mathbf{A}^*, \varphi^*)$ since \mathbf{j}_{ant} and ρ_{ant} are assumed to be completely determined by the antenna parameters. The variational statement corresponding to the conservation conditions (1) and (2) states that the quantity

$$\mathcal{L}_{\text{part}}(\mathbf{A}, \varphi, \mathbf{A}^*, \varphi^*) + \mathcal{L}_{\text{maxw}}(\mathbf{A}, \varphi, \mathbf{A}^*, \varphi^*) + \mathcal{L}_{\text{ant}}(\mathbf{A}^*, \varphi^*) \quad (4)$$

must be extremal for all variations of \mathbf{A}^* and φ^* , when \mathbf{A} and φ are kept constant. As discussed in [15, 16], this form is directly suited for implementation in a numerical code. The wave electromagnetic field is then obtained by writing

$$\mathbf{E} = i\omega\mathbf{A} - \nabla\varphi, \quad \mathbf{B} = \nabla \times \mathbf{A}. \quad (5)$$

The plasma functional can be decomposed as

$$\mathcal{L}_{\text{part}} \equiv \sum_s \mathcal{L}_{\text{part},s} = \sum_s \int d^3\mathbf{r} \{ \mathbf{j}_{\text{part},s} \cdot \mathbf{A}^* - \rho_{\text{part},s} \varphi^* \}, \quad (6)$$

where the sum is carried over all plasma species. The next step consists of introducing the Hamiltonian of particles with charge q_s and mass m_s in interaction with the total electromagnetic field:

$$H_s = \frac{(\mathbf{p} - q_s\mathbf{A}_0 - q_s\mathbf{A})^2}{2m_s} + q_s\varphi_0 + q_s\varphi, \quad (7)$$

where $(\mathbf{A}_0, \varphi_0)$ is the equilibrium electromagnetic potential. This Hamiltonian is linearized to first order in the wave field amplitude by writing $H_s \approx H_{s,0} + \delta H_s$, where

$$\delta H_s = q_s(\varphi - \mathbf{v}_{s,0} \cdot \mathbf{A}), \quad (8)$$

with $\mathbf{v}_{s,0}$ the unperturbed velocity. The distribution function is written as the sum of an equilibrium distribution function and a harmonic perturbation, $f_s = f_{s,0} + \delta f_s$, so that to first order, the current density perturbation caused by the wave may be written as

$$\mathbf{j}_{\text{part},s} = q_s \int d^3\mathbf{p} \{ \delta \mathbf{v}_s f_{s,0} + \mathbf{v}_{s,0} \delta f_s \}, \quad (9)$$

with the velocity perturbation induced by the wave field

$$\delta \mathbf{v}_s = \frac{\partial H_s}{\partial \mathbf{p}} = -\frac{q_s}{m_s} \mathbf{A}. \quad (10)$$

This yields for the plasma functional

$$\mathcal{L}_{\text{part},s} = -\epsilon_0 \int d^3\mathbf{r} \omega_{ps}^2 |\mathbf{A}|^2 - \int d^3\mathbf{r} d^3\mathbf{p} \delta f_s \delta H_s^*, \quad (11)$$

with $\omega_{ps}^2 \equiv n_s q_s^2 / m_s / \epsilon_0$. n_s is the unperturbed density.

The link between the distribution function and the Hamiltonian is obtained from the Vlasov equation for each species

$$\frac{\partial f_s}{\partial t} + [f_s, H_s] = 0. \quad (12)$$

At this point, it is convenient to introduce the system of conjugate action-angle coordinates, $(J_k, \Phi_k)_{k=1,\dots,3}$, which is associated with the following equations of motion in the unperturbed system

$$\frac{dJ_k}{dt} = -\frac{\partial H_{s,0}}{\partial \Phi_k} = 0, \quad (13)$$

and

$$\frac{d\Phi_k}{dt} \equiv \Omega_k = \frac{\partial H_{s,0}}{\partial J_k}, \quad (14)$$

where $H_{s,0}$ is the unperturbed Hamiltonian. $\Omega_k = \Omega_k(\mathbf{J})$ corresponds to the k th natural frequency of the system. By definition, the unperturbed Hamiltonian depends only on the action variables, so that it is possible to write

$$H_s = H_{s,0}(\mathbf{J}) + \delta H_s(\mathbf{J}, \Phi) \quad (15)$$

and also

$$f_s = f_{s,0}(\mathbf{J}) + \delta f_s(\mathbf{J}, \Phi), \quad (16)$$

δH_s and δf_s are expressed as Fourier series over the generalized angles, i.e.

$$\delta H_s \equiv \sum_N \delta h_N e^{iN_k \Phi_k}, \quad \delta f_s \equiv \sum_N \delta f_N e^{iN_k \Phi_k}, \quad (17)$$

where $N \equiv (N_1, N_2, N_3)$ is a triplet of integers. The linearization of equation (12) is straightforward and yields the linear response of the particles to the wave field as

$$\delta f_N = -\delta h_N \frac{N_i}{\omega - N_k \Omega_k} \frac{\partial f_{s,0}}{\partial J_i}. \quad (18)$$

The transformation from position–momentum to action–angle coordinates is canonical, which implies $d^3\mathbf{r} d^3\mathbf{p} = d^3\mathbf{J} d^3\Phi$. The plasma functional can thus be rewritten as

$$\begin{aligned} \mathcal{L}_{\text{part},s} = & -\epsilon_0 \int d^3\mathbf{r} \omega_{ps}^2 |A|^2 \\ & + (2\pi)^3 \sum_N \int d^3\mathbf{J} \frac{N_i}{\omega - N_k \Omega_k} \frac{\partial f_{s,0}}{\partial J_i} |\delta h_N|^2, \end{aligned} \quad (19)$$

where the integral over the generalized angles has been performed, resulting in the cancellation of all terms containing $\delta h_N \delta h_{N'}^*$ with $N \neq N'$. As discussed in some detail in appendix A, both global and local power balance relations are direct consequences of the variational form of Maxwell's equations. In particular, it is worth mentioning that the issue of distinguishing the power actually dissipated from the reversible energy carried by the particles (kinetic flux) is naturally addressed in the framework of this theory.

Usually, it is more practical to manipulate distribution functions given in terms of the three adiabatic invariants (E, Λ, P_ϕ) , rather than in action variables [17]. As shown in appendix B, the resulting functional may then be cast in the form

$$\begin{aligned} \mathcal{L}_{\text{part},s} = & \mathcal{L}_{\text{part},s}^{(\text{res})} \\ & + (2\pi)^3 \sum_N \int d^3\mathbf{J} \frac{\omega}{\omega - N_k \Omega_k} \mathcal{D} f_{s,0} |\delta h_{N_1, N_2, N_3}|^2, \end{aligned} \quad (20)$$

where $\mathcal{L}_{\text{part},s}^{(\text{res})}$ is a real quantity, yielding a purely reactive term. The second term on the right-hand side of the expression, on the other hand, shows that the condition for an energy exchange to take place between the wave and the particles is two-fold. It requires that (i) the global resonance condition $\omega - N \cdot \Omega = 0$ be verified, (ii) δh_N be not zero. It is worth noting that the sign of $\mathcal{D} f_{s,0}$ completely determines whether the energy transfer occurs from the wave to the particles or *vice versa*. In particular, if the distribution is Maxwellian, i.e. $\mathcal{D} f_{s,0} < 0$, it is readily shown that $\Im(\mathcal{L}_{\text{part},s}^{(\text{res})}) > 0$, so that \mathcal{P}_{abs} is strictly positive (see equation (A.18)), as it should be [18, 19].

In order to obtain a practical expression for $\mathcal{L}_{\text{part}}$, the elementary contributions δh_N have to be evaluated. This is done by inverse Fourier transform of δH_s ,

$$\delta h_{N_1, N_2, N_3} = \frac{1}{(2\pi)^3} \int d\Phi_1 d\Phi_2 d\Phi_3 \delta H_s e^{-N \cdot \Phi}, \quad (21)$$

with

$$\delta H_s \equiv \delta H_s(\mathbf{r}, \mathbf{p}) = \delta H_s(\mathbf{J}, \Phi). \quad (22)$$

To track the particle guiding-centre location on a given orbit, the adiabatic invariants must be supplemented by the

poloidal and toroidal angles at the guiding-centre, θ and ϕ . Finally, the particle gyro-motion is described by adding the gyro-phase ϕ_c . The Hamiltonian perturbation can thus be written as

$$\delta H_s(\mathbf{r}, \mathbf{v}) = \delta H_s(E, \Lambda, P_\phi, \theta, \phi; \phi_c). \quad (23)$$

Given the nature of the problem under consideration, it is natural to reformulate the latter as a Fourier series over the gyro-angle:

$$\delta H_s(E, \Lambda, P_\phi, \theta, \phi; \phi_c) \equiv \sum_{p=-\infty}^{\infty} \delta H_{ps} e^{ip\phi_c}. \quad (24)$$

Since δH_{ps} only depends on quantities evaluated at the guiding-centre, a Fourier expansion can be performed over the toroidal and poloidal angles to obtain

$$\delta H_s(E, \Lambda, P_\phi, \theta, \phi; \phi_c) \equiv \sum_{pmn} \delta H_{pmn}(E, \Lambda, \psi) e^{i(p\phi_c + m\theta + n\phi)}, \quad (25)$$

yielding

$$\begin{aligned} \delta h_{N_1, N_2, N_3} &= \frac{1}{(2\pi)^3} \sum_{pmn} \int d^3\Phi \delta H_{pmn} e^{i[(p\phi_c - N_1\Phi_1) + (n\phi - N_3\Phi_3) + m\theta - N_2\Phi_2]}. \end{aligned} \quad (26)$$

The gyro-phase is linked to the first generalized angle by a relation of the type

$$\phi_c = \Phi_1 + \Theta(E, \Lambda, P_\phi, \theta, \phi), \quad (27)$$

which, since θ and ϕ are the angles tracking the guiding-centre, makes the integral over Φ_1 trivial, yielding

$$\begin{aligned} \delta h_{N_1, N_2, N_3} &= \frac{1}{(2\pi)^2} \\ & \times \sum_{pmn} \int d\Phi_2 d\Phi_3 \delta H_{pmn} e^{i[p\Theta(\theta, \phi) + (n\phi - N_3\Phi_3) + m\theta - N_2\Phi_2]} \delta_{N_1, p}. \end{aligned} \quad (28)$$

The difficulty in this expression comes from the fact that θ and ϕ are functions of the generalized angles Φ_2 and Φ_3 . However, owing to the quasi-periodicities of the particles motion in a confining fusion device, it can be shown that [20]

$$\begin{cases} \theta = \varepsilon \Phi_2 + \hat{\theta}(E, \Lambda, P_\phi, \Phi_2), \\ \phi = \Phi_3 + q \hat{\theta}(E, \Lambda, P_\phi, \Phi_2) + \hat{\phi}(E, \Lambda, P_\phi, \Phi_2), \end{cases} \quad (29)$$

where $\varepsilon = 0$ (respectively 1) for trapped (respectively passing) particles. q is the safety factor. $\hat{\theta}$ and $\hat{\phi}$ are both periodic functions of Φ_2 . The integration over Φ_3 can thus be performed in equation (28) to give

$$\begin{aligned} \delta h_{N_1, N_2, N_3} &= \frac{1}{\tau_b} \sum_{pmn} \int_0^{\tau_b} dt \delta H_{pmn} e^{i[p\Theta + nq\hat{\theta} + n\hat{\phi} + m\theta - N_2\Phi_2]} \delta_{p, N_1} \delta_{N, N_3}, \end{aligned} \quad (30)$$

with $\tau_b = \tau_b(E, \Lambda, P_\phi)$ the bounce period of the considered particles and where $d\Phi_2 = \Omega_2 dt$ has been used. Substituting $p\Theta \equiv p(\phi_c - \Omega_1 t)$ and $nq\hat{\theta} + n\hat{\phi} \equiv n(\phi - \Omega_3 t)$ yields

$$\begin{aligned} \delta h_{N_1, N_2, N_3} &= \frac{1}{\tau_b} \sum_{pmn} \int_0^{\tau_b} dt \delta H_{pmn} e^{i[p\phi_c(t) + m\theta(t) + n\phi(t) - N_1\Omega_1 t]} \delta_{p, N_1} \delta_{n, N_3}. \end{aligned} \quad (31)$$

The above expression is an orbit integral clearly exhibiting the resonant selection process at play between the particles and the partial waves characterized by all possible couples of poloidal and toroidal numbers (m, n) .

3. Quasi-local plasma functional

At this point, the plasma–wave interaction described by equation (19) has a purely global character, as no assumption has been made on the particle trajectories. This is to be contrasted with the usual derivation of the dielectric tensor where the trajectories are approximated prior to the response calculation in order to evaluate the integrals over unperturbed orbits. A direct numerical calculation of the individual contributions described by equation (31) is, however, very challenging from a numerical viewpoint. Furthermore, it is instructive to derive the quasi-local expressions from the global ones, since this allows direct comparisons with the familiar dielectric tensor, and also to identify the approximations needed to recover them. For cyclotron harmonics, the orbit integral lends itself to a steepest descent method evaluation. The same method can be applied to the Cerenkov resonance ($p = 0$) provided the phase varies rapidly over the orbit, i.e. for sufficiently large toroidal numbers and parallel velocities [19]. This results in the expression

$$|\delta h_{p, N_2, n}|^2 \approx \frac{2\pi}{\tau_b^2} \sum_{m_1, m_2} \sum_{t_1, t_2} \frac{\delta H_{pm_1 n}(t_1) \delta H_{pm_2 n}^*(t_2)}{\sqrt{\dot{\gamma}_{m_1}(t_1) \dot{\gamma}_{m_2}(t_2)}} e^{i\{f_{m_1}(t_1) + f_{m_2}^*(t_2)\}}. \quad (32)$$

with the wave–particle phase mismatch

$$f_m(t) \equiv i[\gamma_m(t) - (p\Omega_1 + N_2\Omega_2 + n\Omega_3)t], \quad (33)$$

where

$$\dot{\gamma}_m(t) \equiv p\Omega_{cs}(t) + m\dot{\theta}(t) + n\dot{\phi}(t). \quad (34)$$

t_1 (respectively t_2), is the time corresponding to the wave–particle interaction with the partial wave characterized by poloidal mode m_1 (respectively m_2), i.e.

$$\dot{\gamma}_{m_1}(t_1) = \dot{\gamma}_{m_2}(t_2) = N_i\Omega_i, \quad (35)$$

In equation (32), the sum is performed on all partial ICRF resonances, determined by the above relation. Following [19], the saddle point corresponding to the resonance between the particle and the wave with poloidal mode $m_0 \equiv (m_1 + m_2)/2$ is introduced. The time the particle crosses this particular resonance is denoted t_0 and is given by

$$\dot{\gamma}_{m_0}(t_0) = N_i\Omega_i. \quad (36)$$

Far from third order saddle points and Taylor-expanding γ_{m_1} and γ_{m_2} to first order in time about $t = t_0$ permits to rewrite equation (32) as

$$|\delta h_{p, N_2, n}|^2 \approx \frac{2\pi}{\tau_b^2} \sum_{m_1, m_2} \sum_{t_0} \frac{\delta H_{pm_1 n}(t_1) \delta H_{pm_2 n}^*(t_2)}{|\dot{\gamma}_{m_0}(t_0)|} e^{i\Phi_{12}(t_0)}, \quad (37)$$

with

$$\Phi_{12}(t_0) \equiv (m_1 - m_2)\theta(t_0) + \left(\frac{m_1 - m_2}{2}\right)^3 \frac{\dot{\theta}^2(t_0)\ddot{\theta}(t_0)}{\dot{\gamma}_{m_1}(t_0)\dot{\gamma}_{m_2}(t_0)}. \quad (38)$$

The interaction times for partial wave characterized by poloidal numbers m_1 and m_2 are respectively given by

$$t_1 = t_0 - \frac{m_1 - m_2}{2} \frac{\dot{\theta}(t_0)}{\dot{\gamma}_{m_1}(t_0)}, \quad (39)$$

and

$$t_2 = t_0 + \frac{m_1 - m_2}{2} \frac{\dot{\theta}(t_0)}{\dot{\gamma}_{m_2}(t_0)}. \quad (40)$$

Using equation (37) in the resonant plasma functional (equations (20) and (B.13)) yields

$$\begin{aligned} \mathcal{L}_{\text{part}, s}^{(\text{res})} &= (2\pi)^3 \sum_{p, n} \int d^3\mathbf{J} \sum_{m_1, m_2} \frac{1}{\tau_b} \sum_{N_2} \sum_{t_0} \frac{2\pi}{\tau_b} \frac{1}{|\dot{\gamma}_{m_0}(t_0)|} \\ &\dots \frac{\omega}{\omega - N_i\Omega_i} \mathcal{D}f_{s,0} \delta H_{pm_1 n}(t_1) \delta H_{pm_2 n}^*(t_2) e^{i\Phi_{12}(t_0)}, \end{aligned} \quad (41)$$

From equation (36), the time elapsed between the crossing of the resonance corresponding to N_2 to the resonance corresponding to $N_2 + 1$ is given by

$$\Delta t = \frac{\Omega_2}{|\dot{\gamma}_{m_0}(t_0)|} = \frac{2\pi}{\tau_b} \frac{1}{|\dot{\gamma}_{m_0}(t_0)|}, \quad (42)$$

which means that except in the neighbourhood of third order saddle points, the sum over N_2 and t_0 can be transformed into a time integral. $N_2\Omega_2$ must then be replaced by $\dot{\gamma}_{m_0} - p\Omega_1 - n\Omega_3$. The quasi-local hypothesis consists of simplifying the unperturbed particle motion at each individual resonant point [21]. To lowest order, one can assume that this motion is uniform. The resonant plasma functional then reduces to

$$\begin{aligned} \mathcal{L}_{\text{part}, s}^{(\text{res})} &= (2\pi)^3 \sum_{p, n} \int d^3\mathbf{J} \frac{1}{\tau_b} \int_0^{\tau_b} dt \\ &\dots \sum_{m_1, m_2} \frac{\omega}{\omega - \dot{\gamma}_{m_0}(t)} \mathcal{D}f_{s,0} \delta H_{pm_1 n}(t) \delta H_{pm_2 n}^*(t) e^{i(m_1 - m_2)\theta(t)}. \end{aligned} \quad (43)$$

The previous expression has a Lagrangian character, since particles are followed along their unperturbed orbits. It is independent of Φ_1 and Φ_3 . Furthermore, since $d\Phi_2 = \Omega_2 dt = 2\pi dt/\tau_b$, we can perform the transform to Eulerian coordinates

$$(2\pi)^2 \int d^3\mathbf{J} \frac{2\pi}{\tau_b} \int_0^{\tau_b} dt = \int d^3\mathbf{J} d^3\Phi = \int d^3\mathbf{r} d^3\mathbf{p}. \quad (44)$$

Noting that the uniform approximation implies

$$m_0\dot{\theta}(t) + n\dot{\phi}(t) \approx (m_0\nabla_{\parallel}\theta + n\nabla_{\parallel}\phi)v_{\parallel}, \quad (45)$$

the parallel refractive index corresponding to the average poloidal mode m_0 , $k_{\parallel} \equiv m_0 \nabla_{\parallel} \theta + n \nabla_{\parallel} \phi$ is introduced to obtain the quasi-local expression

$$\mathcal{L}_{\text{part},s}^{(\text{res})} = \sum_{p,m_1,m_2,n} \int d^3r d^3p \frac{\omega}{\omega - p\Omega_{cs} - k_{\parallel} v_{\parallel}} \times \mathcal{D} f_{s,0} e^{i(m_1 - m_2)\theta} \delta H_{pm_1n} \delta H_{pm_2n}^* \quad (46)$$

Note that k_{\parallel} involves both poloidal numbers m_1 and m_2 in a symmetric fashion.

At this point, it is necessary to express the Hamiltonian contributions δH_{pmn} as functions of the electromagnetic potential. This is done by performing a Taylor expansion of the particle Hamiltonian around the guiding-centre location:

$$\delta H_s(\mathbf{r}) = \delta H_s(\mathbf{r}_{gc} + \mathbf{r}_c) = \sum_{l=0}^{\infty} \frac{(\mathbf{r}_c \cdot \nabla)^l}{l!} \delta H_s(\mathbf{r})|_{r_{gc}} \quad (47)$$

The particle unperturbed motion is described in the local magnetic basis with fixed directions ($\mathbf{e}_{\perp 1}$, $\mathbf{e}_{\perp 2}$, \mathbf{e}_{\parallel}) proposed by Jaeger *et al* [22]. Its main advantage over the more traditional local magnetic frame ($\mathbf{e}_{\alpha} \equiv \nabla s / |\nabla s|$, $\mathbf{e}_{\beta} \equiv \mathbf{e}_{\parallel} \times \mathbf{e}_{\alpha}$, $\mathbf{e}_{\parallel} \equiv \mathbf{B}_0 / B_0$) lies in the fact that it is well behaved in the vicinity of the magnetic axis.

The drift approximation, characterized by the ordering parameter $\varepsilon_d \sim |\nabla \rho_c| \ll 1$ with ρ the ion Larmor radius, is employed. In this framework, the particle position is written as $\mathbf{r} \equiv \mathbf{r}_{gc} + \mathbf{r}_c$ with \mathbf{r}_{gc} the guiding-centre location and \mathbf{r}_c the Larmor radius vector, given by

$$\mathbf{r}_c = -i \frac{\rho_c}{\sqrt{2}} (e^{i\phi_c} \mathbf{e}_{-} - e^{-i\phi_c} \mathbf{e}_{+}) \quad (48)$$

with $\rho_c = v_{\perp} / \Omega_{cs}$ and $\dot{\phi}_c = \Omega_{cs} + O(\varepsilon_d)$. In this work, the unperturbed particle motion is described to lowest order in ε_d . Accordingly, the correction to the gyro-angle caused by the slow spatial variation of the basis vectors along the field line [23] is neglected. The complex polarization vectors are defined as

$$\mathbf{e}_{\pm} \equiv \frac{\mathbf{e}_{\perp 1} \mp i \mathbf{e}_{\perp 2}}{\sqrt{2}} \quad (49)$$

The particle velocity is given by $\mathbf{v} \approx v_{\parallel} \mathbf{e}_{\parallel} + \mathbf{v}_{\perp} + O(\varepsilon_d)$ with

$$\mathbf{v}_{\perp} = \frac{v_{\perp}}{\sqrt{2}} (e^{i\phi_c} \mathbf{e}_{-} + e^{-i\phi_c} \mathbf{e}_{+}) \quad (50)$$

Note that to lowest order in ε_d , the variables (v_{\parallel} , v_{\perp} , ϕ) correspond to the cylindrical coordinates of the particle velocity [19]. Introducing $\nabla_{\pm} \equiv \nabla \cdot \mathbf{e}_{\mp}$, the binomial theorem is employed to perform the following expansion

$$(\mathbf{r}_c \cdot \nabla)^l = \left(\frac{\rho_c}{\sqrt{2}} \right)^l \sum_{k=0}^l \binom{l}{k} e^{i(2k-l)\phi_c} \nabla_{+}^k \nabla_{-}^{l-k} \quad (51)$$

which after reordering the sums to express the obtained expression for δH_s in terms of the cyclotron phase harmonics yields the compact formula

$$\delta H_s(\mathbf{r}) = \sum_{p=-\infty}^{\infty} e^{ip(\phi_c - \pi/2)} \sum_{k=0}^{\infty} \left(\frac{\rho_c}{\sqrt{2}} \right)^{2k+|p|} \frac{\nabla_{+}^{k_+} \nabla_{-}^{k_-}}{k_{+}! k_{-}!} \delta H_s(\mathbf{r})|_{r_{gc}} \quad (52)$$

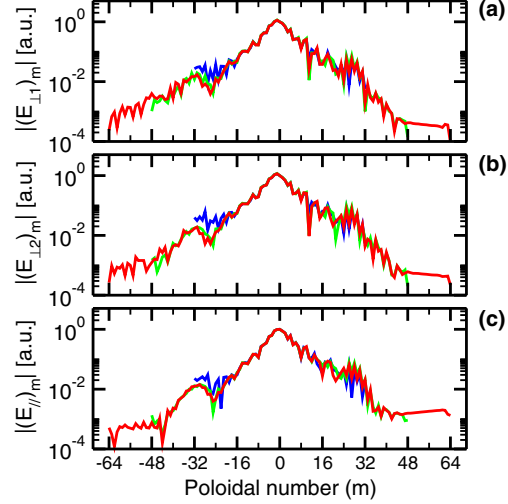


Figure 1. Normalized coefficients of the poloidal decomposition at normalized radius $\rho = 0.3$ of (a) $E_{\perp 1}$; (b) $E_{\perp 2}$; (c) E_{\parallel} . Shown are the results obtained when $-32 \leq m \leq 32$ ($N_m = 65$), $-48 \leq m \leq 48$ ($N_m = 97$) and $-64 \leq m \leq 64$ ($N_m = 129$). The considered toroidal number is $n = 66$.

with

$$\begin{cases} k_{+} = k + p, & k_{-} = k & \text{if } p > 0, \\ k_{+} = k, & k_{-} = k - p & \text{otherwise.} \end{cases} \quad (53)$$

The Hamiltonian at the particle guiding-centre can be rewritten as

$$\delta H_s(\mathbf{r}_{gc}) \equiv \delta H_0 + \delta H_{+1} e^{i\phi_c} + \delta H_{-1} e^{-i\phi_c} \quad (54)$$

with

$$\begin{cases} \delta H_0 & \equiv q_s (\varphi - v_{\parallel} A_{\parallel}), \\ \delta H_{+1} & \equiv -q_s v_{\perp} A_{+} / \sqrt{2}, \\ \delta H_{-1} & \equiv -q_s v_{\perp} A_{-} / \sqrt{2}, \end{cases} \quad (55)$$

where $A_{\pm} \equiv \mathbf{A} \cdot \mathbf{e}_{\mp}$. This yields

$$\delta H_s(\mathbf{r}) = \sum_{p=-\infty}^{\infty} e^{ip(\phi_c - \pi/2)} \times \sum_{L=-1}^1 e^{iL\pi/2} \sum_{\kappa=0}^{\infty} \left(\frac{\rho_c}{\sqrt{2}} \right)^{2\kappa+|p-L|} \frac{\nabla_{+}^{k_+} \nabla_{-}^{k_-}}{k_{+}! k_{-}!} \delta H_L \quad (56)$$

with

$$k_{+} = \kappa + \max(0, p - L), \quad k_{-} = \kappa + \max(0, -p + L), \quad (57)$$

yielding for the contribution to the ICRF resonance harmonic p :

$$\delta H_{ps}(\mathbf{r}) = \sum_{L=-1}^1 e^{i(L-p)\pi/2} \sum_{\kappa=0}^{\infty} \left(\frac{\rho_c}{\sqrt{2}} \right)^{2\kappa+|p-L|} \frac{\nabla_{+}^{k_+} \nabla_{-}^{k_-}}{k_{+}! k_{-}!} \delta H_L \quad (58)$$

It should be noted that in all cases, $k_{+} + k_{-} = 2\kappa + |p - L|$, which is the exponent of ρ_c in equation (56), thus

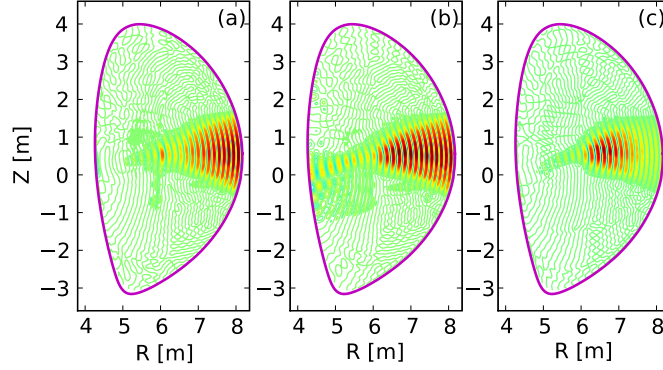


Figure 2. Contours of the real part of the reconstructed (a) left-handed; (b) right-handed; (c) parallel electric field corresponding to the spectra shown in figure 1. Contours are equally spaced and range from (a) -4.2 to 4.0 kV m^{-1} ; (b) -16.8 to 16.0 kV m^{-1} ; and (c) -0.038 to 0.038 kV m^{-1} .

directly providing the small parameter to be considered in FLR expansions. Another important observation is that the symmetry of the plasma functional (equation (46)) is ensured regardless of the order of the Larmor radius expansion without the requirement that any odd-order terms be included [24].

4. The EVE code

The EVE code is a full-wave solver based on the variational formulation described previously. It is based on the quasi-local plasma functional (equation (46)), in which a first order expanded version of the Hamiltonian (equation (58)) has been implemented. The quadratic dependence of the functional on the interaction Hamiltonian makes of EVE a second-order FLR code. The system of coordinates is (s, θ, ϕ) , with s the radial coordinate, related to the poloidal flux by the relation $\nabla\psi \equiv f(s)\nabla s$, and varying between 0 (centre) and 1 (edge) in the plasma volume. θ and ϕ are the poloidal and toroidal angles. The confining magnetic field is written as $\mathbf{B}_0 = \nabla\phi \times \nabla\psi + F(s)\nabla\phi$ with F the toroidal flux function. A spectral treatment is applied in the poloidal and toroidal directions. The components of the potential vector are solved in the local magnetic frame $(\mathbf{e}_\alpha, \mathbf{e}_\beta, \mathbf{e}_\parallel)$, with $\mathbf{e}_\parallel \equiv \mathbf{B}_0/B_0$, $\mathbf{e}_\alpha \equiv \nabla s/|\nabla s|$ and $\mathbf{e}_\beta = \mathbf{e}_\parallel \times \mathbf{e}_\alpha$. Any component u_k of the state vector $\mathbf{u} \equiv (sA_\alpha, sA_\beta, A_\parallel, \varphi/c)$ is decomposed as

$$u_k(s, \theta, \phi) = \sum_{jmn} \alpha_k^{jmn} e^{im\theta} e^{in\phi} h_k(s - s_j). \quad (59)$$

h_k consists of a set of radial finite elements, which are chosen as a mix of quadratic and cubic Hermite polynomials in order to prevent potential spectral pollution effects [25]. s_j is the j th spatial grid point and the α_k^{jmn} are the unknowns of the problem. Furthermore, assuming the equilibrium is toroidally axisymmetric, the complex conjugate to u_k is decomposed as

$$u_k^*(s, \theta, \phi) = \sum_{\bar{j}\bar{m}\bar{n}} \alpha_k^{\bar{j}\bar{m}\bar{n}} e^{-i\bar{m}\theta} e^{-i\bar{n}\phi} h_{\bar{k}}(s - s_{\bar{j}}). \quad (60)$$

In the chosen representation, the parallel wavenumber appearing in the resonant denominator of equation (46) can be

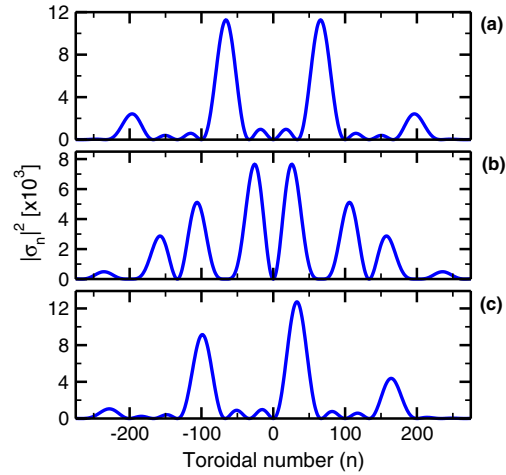


Figure 3. Toroidal antenna spectrum for phasing (a) $[0, \pi, 0, \pi]$; (b) $[0, 0, \pi, \pi]$; (c) $[0, \pi/2, \pi, 3\pi/2]$.

written as

$$k_\parallel = n \frac{F}{R^2 B_0} + \frac{m_1 + m_2}{2} \frac{f}{J B_0}, \quad (61)$$

which accounts for geometrical upshift effects. J is the Jacobian of the (s, θ, ϕ) system. Note that m_1 and m_2 represent the poloidal numbers of the two partial resonant waves, and must not be confused with the poloidal numbers corresponding to the solution expansion. There is no conceptual obstacle to the construction of a numerical code based on these expressions without any requirement to treat the poloidal direction spectrally. The evaluation of the quasi-local functional (equation (46)) is, however, numerically costly, because of the dependence of k_\parallel on both m_1 and m_2 , which imposes to perform Fourier transforms for all possible values of m_1 and m_2 . A significant simplification occurs by using the

ansatz

$$k_{\parallel} \approx n \frac{F}{R^2 B_0} + \frac{m + \bar{m}}{2} \frac{f}{J B_0}. \quad (62)$$

This assumption is equivalent to neglecting the supplemental parallel space dispersion caused by the fact that $\delta H_{pm,n}$ (respectively $\delta H_{\bar{p}\bar{m},n}$) is actually a convolution of the poloidal harmonics of the solution vector, m (respectively \bar{m}). Although comprehensive tests of the validity of this approximation are still needed, practical simulations performed using expressions (61) and (62) have been found to yield indistinguishable results. On the other hand, as expected, the use of equation (62) results in a large reduction in the calculation time. The plasma is assumed to be surrounded by a vacuum region delimited by a perfect conductor, on which the condition $A_{\beta} = A_{\parallel} = 0$ is imposed. The unicity of the solution on the magnetic axis is automatically verified by considering the variables $u_1 \equiv s A_{\alpha}$ and $u_2 \equiv s A_{\beta}$, and imposing $u_1(s = 0) = u_2(s = 0) = 0$. The actual values of $A_{\alpha}(s = 0)$ and $A_{\beta}(s = 0)$ are subsequently obtained by extrapolation. Finally the Fourier coefficients corresponding to variables A_{\parallel} and φ on the vacuum vessel are set to zero for all values of $m \neq 0$. The three functionals (see equation (3)) are constructed and the extremalization of expression (4) yields the (α_k^{jmn}) coefficients. The stiffness matrix construction, inversion and the evaluation of the various energy quantities have been parallelized and EVE may be executed on various parallel architectures, with a speedup essentially determined by the solver performing the stiffness matrix inversion (here, SCALAPACK), owing to the limited necessary inter-processor communications involved in all other operations.

The antenna functional is given by

$$\mathcal{L}_{\text{ant}} \equiv \int ds d\theta d\phi J \{ \mathbf{j}_{\text{ant}} \cdot \mathbf{A}^* - \rho_{\text{ant}} \varphi^* \}. \quad (63)$$

The current conservation in the antenna structure for a current oscillating at frequency ω imposes $i\omega\rho_{\text{ant}} = \nabla \cdot \mathbf{j}_{\text{ant}}$. The following general form is assumed for \mathbf{j}_{ant}

$$J \mathbf{j}_{\text{ant}} = I_0 \sigma_{\theta}(\theta) \sigma_{\phi}(\phi) \delta(s - s_{\text{ant}}) \mathbf{e}_{\theta}, \quad (64)$$

where $\sigma_{\theta}(\theta)$ (respectively $\sigma_{\phi}(\phi)$) determines the poloidal (respectively toroidal) shape of the antenna current on magnetic surface $s = s_{\text{ant}}$.

Equivalently, since the toroidal modes are treated one by one, we may write

$$\{ J \mathbf{j}_{\text{ant}} \}_n \equiv I_0 \sigma_n \sigma_{\theta}(\theta) \delta(s - s_{\text{ant}}) \mathbf{e}_{\theta}, \quad (65)$$

where σ_n is the n th toroidal harmonic of $\sigma_{\phi}(\phi)$.

For ICRF applications, the antenna is assumed to comprise a set of N_s straps with the current flowing in the poloidal direction. Denoting Δl the algebraic poloidal length between the antenna short and a given point on the antenna strap, the following profile is assumed:

$$\begin{cases} \sigma_{\theta}(\theta) = \sigma_{\theta}(\theta_s) \cos(\beta \Delta l) & \text{for } |\Delta l| < L_{\text{ant}}/2, \\ \sigma_{\theta}(\theta) = 0 & \text{otherwise.} \end{cases} \quad (66)$$

In the previous expression, θ_s corresponds to the poloidal angle at the short and L_{ant} is the length of the antenna strap. β is the LC-constant of the matching circuit [13]. Each strap

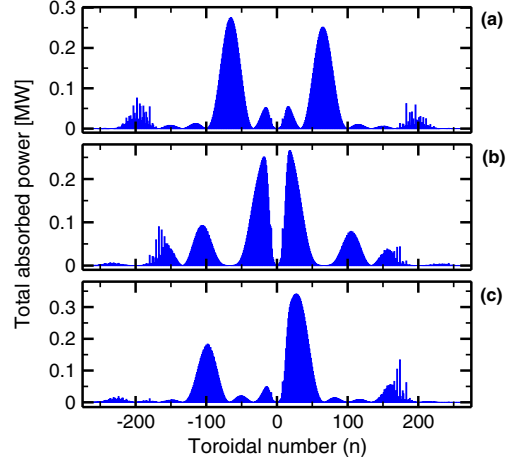


Figure 4. Absorbed power per toroidal number for the phasings corresponding to figure 3 in the presence of ^3He ions. The total absorbed power is 20 MW.

is centred around toroidal angle ϕ_i ($i = 1, \dots, N_s$), with an angular width $\Delta\phi_i = \Delta w_i / R_{\text{ant}}$ where Δw_i is the strap width and R_{ant} is the antenna major radius in the equatorial plane. We set

$$\sigma_{\phi}(\phi) = \sqrt{\frac{2\pi}{N_s}} \sum_{i=1}^{N_s} \frac{1}{(\Delta\phi_i)^{1/2}} \Pi\left(\frac{\phi - \phi_i}{\Delta\phi_i}\right) \exp(i\varphi_i), \quad (67)$$

where φ_i is the relative phase (in radians) of the i th strap and $\Pi()$ is the rectangle function. This yields for toroidal mode n ,

$$\sigma_n = \sum_{i=1}^{N_s} \sqrt{\frac{\Delta\phi_i}{2\pi N_s}} \text{sinc}\left(\frac{n\Delta\phi_i}{2}\right) e^{i(\varphi_i - n\phi_i)}, \quad (68)$$

consistent with Parseval's identity

$$\sum_{n=-\infty}^{\infty} |\sigma_n|^2 = \frac{1}{2\pi} \int_0^{2\pi} d\phi |\sigma_{\phi}(\phi)|^2. \quad (69)$$

For illustrative purpose, the EVE code is employed to simulate ICRF heating in the ITER elmy H-mode plasma scenario 2 [26]. The plasma parameters are provided by the ASTRA code [27]. They can be summarized as follows: major radius $R_0 = 6.21$ m, minor radius $a_0 = 1.96$ m, central density $n_e(0) = 10.2 \times 10^{19} \text{ m}^{-3}$, central electron temperature $T_e(0) = 24.8$ keV, central ion temperature $T_i(0) = 21.2$ keV, where 'i' designates the plasma thermal ions: tritium (T), deuterium (D), helium-3 (^3He), thermalized helium-4 (^4He) and beryllium (Be). Also considered are fusion alphas (α), modelled by an isotropic equivalent Maxwellian with $T_{\alpha}(0) = 1.2$ MeV. Two possible scenarios are compared: helium-3 minority ion heating [28] with concentrations $\eta_D = 32\%$, $\eta_T = 42\%$, $\eta_{\text{He}} = 4\%$, $\eta_{\alpha} = 1\%$, $\eta_{\text{Be}} = 2\%$, and second harmonic tritium heating with $\eta_D = 32\%$, $\eta_T = 50\%$, $\eta_{\text{He}} = 4\%$, $\eta_{\alpha} = 1\%$, $\eta_{\text{Be}} = 2\%$. The magnetic field at the geometric centre is $B_0(R = R_0) = 5.3$ T and the wave frequency is $f = 53$ MHz.

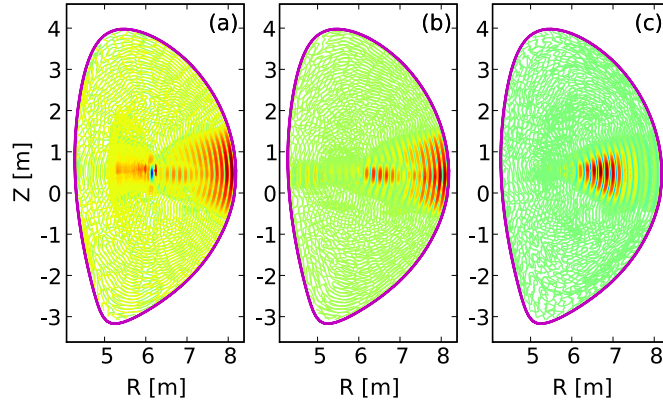


Figure 5. Real part of the (a) left-handed; (b) right-handed; (c) parallel electric field for $[0, \pi, 0, \pi]$ phasing in the presence of ^3He ions for 20 MW absorbed power. Contours are equally spaced and range from (a) -87 to 51 kV m^{-1} ; (b) -230 to 190 kV m^{-1} and (c) -0.255 to 0.255 kV m^{-1} .

These cases have been run with 250 radial points in the plasma region. Because of the toroidicity, poloidal modes are coupled by the equilibrium, which entails a consumption scaling as N_m^2 in memory (with N_m the total number of poloidal modes employed in the calculation) and scaling as N_m^3 in CPU time. Prior to simulating large physical problems, it is therefore of interest to perform a convergence analysis and estimate the minimum required number of poloidal modes. In figure 1 is shown the normalized Fourier decomposition of the three components of the electric field ($E_{\perp 1}$, $E_{\perp 2}$, E_{\parallel}) versus poloidal number for $N_m = 65$ ($-32 \leq m \leq 32$), $N_m = 97$ ($-48 \leq m \leq 48$) and $N_m = 129$ ($-64 \leq m \leq 64$) in the helium-3 minority heating case. The toroidal number is $n = 66$.

It appears that with 65 poloidal modes, the obtained coefficients at the limits of the calculation domain have decreased by two decades with respect to the $m = 0$ value. This decrease reaches four decades with 129 poloidal modes but clearly, the decomposition corresponds to a solution which is essentially equivalent to the result obtained with 97 modes. The latter value has therefore been chosen as a trade-off between accuracy and computational cost. Compatible with this value of N_m , 196 angular points have been considered in the poloidal direction. The three cases actually display minor visual differences in the reconstructed electric field and negligible differences in terms of power deposition profiles. Figure 2 shows the real part of the left-handed ($E_+ \equiv E_{\perp 1} + iE_{\perp 2}$), right-handed ($E_- \equiv E_{\perp 1} - iE_{\perp 2}$) and parallel component of the reconstructed electric field obtained with $N_m = 129$.

Unlike ray-tracing codes, full-wave codes compute global solutions corresponding to superpositions of eigenstates of the considered inhomogeneous plasma. However, because of the high damping rate of hot plasmas in devices such as ITER, the results are qualitatively well understood in WKB terms. Here, for instance, a fast magnetosonic wave excited by the low field side antenna and propagating towards the high field side is clearly observed. This wave experiences damping by the plasma species near the magnetic axis, which results in a large decrease in the electric field amplitude. A small

fraction of the wave is also converted into an ion Bernstein wave, which appears with a small wavelength on the high field side of the mode conversion layer (barely visible in figure 2). In this scenario, however, the rate of conversion is too small to have a significant impact on the power split between the plasma species. Nevertheless, its presence requires sufficient radial and poloidal resolution to reach satisfactory global convergence. Like similar full-wave codes, EVE features an algorithm to artificially damp the IBW wave in the event that the condition $|k_{\perp} \rho_i| \ll 1$ is not verified, and possibly relax these numerical requirements [13, 30], but it was not employed in the present simulations.

The ITER ICRF antenna consists of 24 straps, grouped in 8 poloidal triplets connected in pairs [31]. By introducing phase shifts between these pairs, various antenna phasings are possible. In this work, we consider three different phasings: $[0, \pi, 0, \pi]$, $[0, 0, \pi, \pi]$ and $[0, \pi/2, \pi, 3\pi/2]$. The corresponding spectral density for each case, $|\sigma_n|^2$, is shown in figure 3. To perform simulations accounting for the toroidal structure of the antenna, it is necessary to consider all relevant modes in the toroidal decomposition. In this work, 551 modes are included in the calculation, i.e. $-275 \leq n \leq 275$. For comparison, it is also instructive to isolate the dominant modes in the toroidal spectra, i.e., $n = 66$ for $[0, \pi, 0, \pi]$ phasing, $n = 26$ for $[0, 0, \pi, \pi]$ phasing and $n = 33$ for $[0, \pi/2, \pi, 3\pi/2]$ phasing. A total power of $P_{\text{RF}} = 20 \text{ MW}$ is coupled to the plasma, at frequency $f = 53 \text{ MHz}$.

Figure 4 shows the power absorbed for every toroidal number in the ^3He minority heating case. Owing to the large damping rate characterizing this scenario, the spectral dispersion with respect to n remains moderate and the profiles of absorbed power exhibit a dependence over n qualitatively similar to the spectral density corresponding to each phasing (figure 3). Figure 5 shows the electric field reconstruction for the $[0, \pi, 0, \pi]$ phasing at toroidal angle $\phi = 0$ (in front of the antenna). Although the IBW is more noticeable than in figure 2, its impact on the power split is negligible. The difference in magnitude in the electric field between figures 2 and 5 is the result of the wave focusing in front of the antenna, which is only described when the solution is summed over

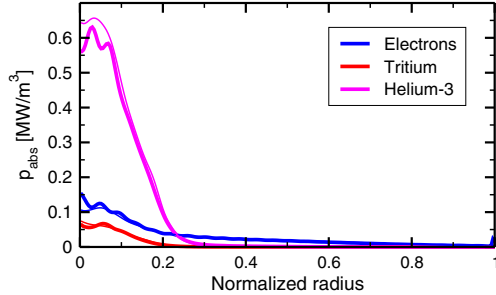


Figure 6. Absorbed power density for $[0, \pi, 0, \pi]$ phasing for 20 MW total absorbed power. Shown as a thin line is the power profile obtained when only the dominant toroidal number (here, $n = 66$) is considered.

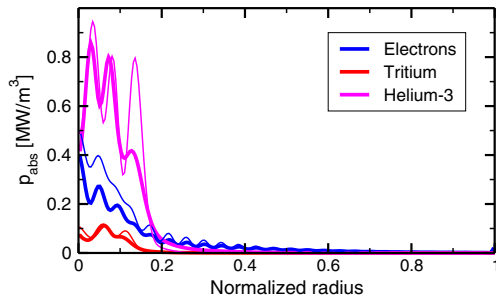


Figure 7. Absorbed power density for $[0, 0, \pi, \pi]$ phasing for 20 MW total absorbed power. Shown as a thin line is the power profile obtained when only the dominant toroidal number (here, $n = 26$) is considered.

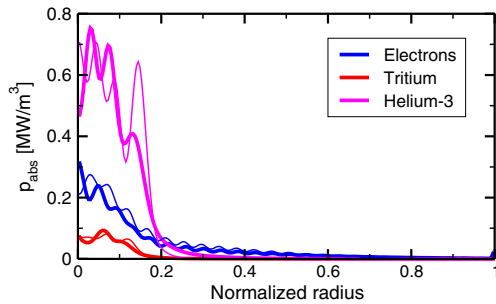


Figure 8. Absorbed power density for $[0, \pi/2, \pi, 3\pi/2]$ phasing for 20 MW total absorbed power. Shown as a thin line is the power profile obtained when only the dominant toroidal number (here, $n = 33$) is considered.

toroidal modes [32]. In figure 6 are shown the corresponding profiles of absorbed power. For the sake of clarity, only the most representative species are shown. The composite power absorption, reconstructed using all toroidal modes, is compared with the power deposition profile obtained when only the dominant peak in the toroidal spectrum ($n = 66$) is considered. In this case, the latter provides an accurate representation of the overall power damping. The same

Table 1. Repartition of the wave power between the plasma species in the ^3He minority heating case for $[0, \pi, 0, \pi]$ (column 1); $[0, 0, \pi, \pi]$ (column 2) and $[0, \pi/2, \pi, 3\pi/2]$ phasing (column 3). Between parentheses is indicated the percentage of power absorbed when only the dominant peak in the toroidal spectrum is considered.

	$[0, \pi, 0, \pi]$	$[0, 0, \pi, \pi]$	$[0, \pi/2, \pi, 3\pi/2]$
Electrons	48.5 (47.7)	43.7 (44.2)	44.4 (47.2)
Deuterium	0.4 (0.3)	0.5 (0.1)	0.4 (0.1)
Tritium	3.8 (3.9)	4.6 (4.9)	4.2 (4.4)
Helium-3	42.5 (44.8)	47.0 (50.1)	46.5 (47.6)
Helium-4	0.1 (0.1)	0.1 (0.0)	0.1 (0.0)
Alphas	4.7 (3.1)	4.2 (0.7)	4.4 (0.7)
Beryllium	0.1 (0.1)	0.0 (0.0)	0.0 (0.0)

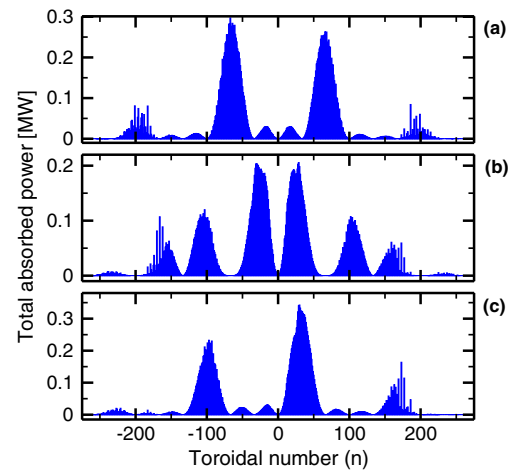


Figure 9. Absorbed power per toroidal number for the phasings corresponding to figure 3 in the absence of ^3He ions. The total absorbed power is 20 MW.

comparison has been performed for the two other phasings, namely $[0, 0, \pi, \pi]$ (figure 7) and $[0, \pi/2, \pi, 3\pi/2]$ (figure 8) and corresponding dominant numbers, respectively $n = 26$ and $n = 33$. The agreement remains satisfactory although the consequences of the differences observed in the profiles in, e.g., an integrated simulation remain to be assessed. Table 1 summarizes the power fraction absorbed by each plasma species. Regardless of the phasing, the ^3He ions absorb a large fraction of the power at the fundamental resonance, which is expected to result in good ion heating [28, 29]. About 5% is absorbed by the tritium ions, at the second harmonic of the cyclotron resonance. With these parameters, a significant part of the power is absorbed by the electrons, through Landau damping and transit time magnetic pumping, essentially because at 53 MHz, the fundamental ^3He and second harmonic resonant layers of the tritium ions are located slightly on the high field side of the magnetic axis, i.e. past the region of good absorption of radiofrequency wave power by the electrons as the wave propagates towards the high field side.

The same simulations have been performed in the absence of ^3He ions. In this case, tritium second harmonic heating is the favoured mechanism. Figure 9 shows the power absorbed

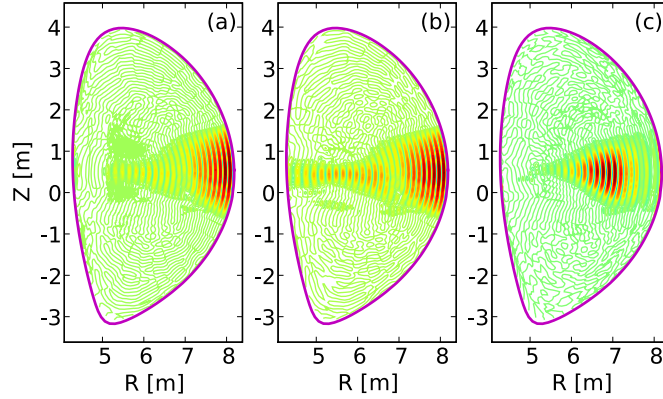


Figure 10. Real part of the (a) left-handed; (b) right-handed; (c) parallel electric field for $[0, \pi, 0, \pi]$ phasing in the absence of ^3He ions for 20 MW absorbed power. Contours are equally spaced and range from (a) -72 to 60 kV m^{-1} ; (b) -240 to 190 kV m^{-1} ; and (c) -0.240 to 0.230 kV m^{-1} .

versus the toroidal number. Although these spectra exhibit more isolated spikes than in figure 4, which is characteristic of a smaller overall single-pass damping rate than in the ^3He case, the shapes of the obtained spectra are still similar to the spectral density of the toroidal decompositions. In figure 10, the field corresponding to $[0, \pi, 0, \pi]$ phasing is shown. The second harmonic tritium absorption layer is clearly seen to result in a large decrease in the electric field amplitude as the wave propagates towards the high field side. The power deposition profiles on species are shown in figure 11 for phasing $[0, \pi, 0, \pi]$. Unlike in the ^3He case, the alphas absorb a non-negligible fraction of the wave power and electron absorption, which takes place over the whole minor radius, is found to be the dominant damping mechanism. At this frequency, the deuterium ions also absorb a small fraction of the wave power. It is worth noticing that the profiles obtained in a calculation based on a single toroidal number slightly differ from the composite profiles. This is more pronounced for the $[0, 0, \pi, \pi]$ and $[0, \pi/2, \pi, 3\pi/2]$ phasings, shown in figures 12 and 13; although the location of the maximum power absorption is correct, the widths of the obtained profiles are substantially different. The numbers corresponding to the power absorption obtained in the second harmonic tritium case are summarized in table 2 for each phasing. The discrepancy between the composite solutions and the single toroidal number solutions results from the differing levels of alpha absorption. For the sake of clarity, the corresponding profiles are shown in figure 14. For each phasing, they are compared with the result associated with the single toroidal number solution. It is clear that whereas the composite power depositions are qualitatively similar for the three phasings, they differ significantly, both from each other and from the corresponding profiles obtained in single toroidal number calculations. This is caused by the large energy of the alphas, which causes their fundamental cyclotron resonance to be significantly Doppler-shifted. Considering that thermal particles are representative of the population resonant with the wave, the approximate location of power deposition corresponding to a given toroidal number n is

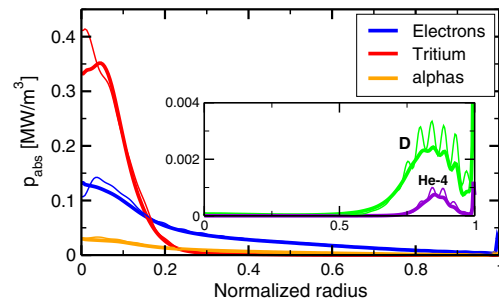


Figure 11. Absorbed power density for $[0, \pi, 0, \pi]$ phasing for 20 MW total absorbed power. Shown as a thin line is the power profile obtained when only the dominant toroidal number (here, $n = 66$) is considered. In the inset is shown the power absorbed by deuterons and thermal helium-4 ions.

obtained by solving

$$\omega = \Omega_{c\alpha} + k_{\parallel} v_{\text{th},\alpha}, \quad (70)$$

with $v_{\text{th},\alpha}$ the thermal velocity of the alpha particles, $\Omega_{c\alpha}$ their cyclotron frequency and $k_{\parallel} \approx N/R$ the parallel wavenumber obtained when the poloidal upshift effects are neglected. The Doppler shift causes the second term on the right-hand side to be large, which results in wide deposition profiles, which are sensitive to the particular value of n . In figure 14, the approximate location of the Doppler-shifted resonance in the equatorial plane is also shown and is representative of the location of power damping in the single toroidal number calculations. On the other hand, when all relevant toroidal numbers are included, this sensitivity is lost and the profiles are similar for the three phasings. These results demonstrate that prior to using ICRF simulations based on simplified toroidal spectra, it is necessary to perform extensive simulations to ascertain the validity of such an approach. It also shows that more realistic alpha distributions should be considered, at least in the second harmonic tritium case: slowing-down distributions are believed to be more representative of the

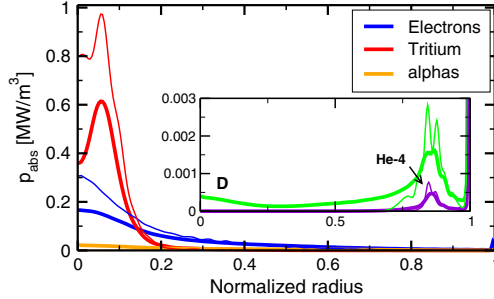


Figure 12. Absorbed power density for $[0, 0, \pi, \pi]$ phasing for 20 MW total absorbed power. Shown as a thin line is the power profile obtained when only the dominant toroidal number (here, $n = 26$) is considered. In the inset is shown the power absorbed by deuterons and thermal helium-4 ions.

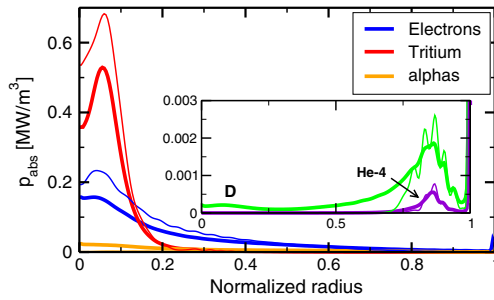


Figure 13. Absorbed power density for $[0, \pi/2, \pi, 3\pi/4]$ phasing for 20 MW total absorbed power. Shown as a thin line is the power profile obtained when only the dominant toroidal number (here, $n = 33$) is considered. In the inset is shown the power absorbed by deuterons and thermal helium-4 ions.

Table 2. Repartition of the wave power between the plasma species in the second harmonic tritium heating case for $[0, \pi, 0, \pi]$ (column 1); $[0, 0, \pi, \pi]$ (column 2) and $[0, \pi/2, \pi, 3\pi/2]$ phasing (column 3). Between parentheses is indicated the percentage of power absorbed when only the dominant peak in the toroidal spectrum is considered.

	$[0, \pi, 0, \pi]$	$[0, 0, \pi, \pi]$	$[0, \pi/2, \pi, 3\pi/2]$
Electrons	61.3 (61.8)	55.9 (53.7)	58.3 (60.1)
Deuterium	5.2 (6.1)	5.6 (6.4)	5.1 (5.1)
Tritium	18.5 (19.1)	25.5 (35.0)	23.1 (28.7)
Helium-3	—	—	—
Helium-4	0.9 (1.0)	1.2 (1.4)	1.0 (1.1)
Alphas	11.9 (10.1)	11.1 (2.8)	11.4 (3.1)
Beryllium	2.3 (2.0)	0.7 (0.7)	1.1 (1.9)

actual population than Maxwellians and can yield significantly different results [38] but more comprehensive simulations, relevant to future reactors, also require the inclusion of orbit effects.

5. Conclusions

The variational approach to the wave problem, initially proposed in [15] and discussed in this paper has several

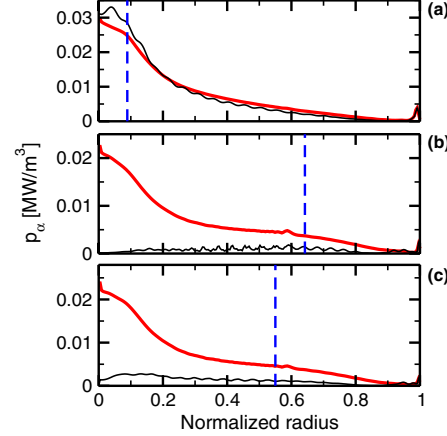


Figure 14. Power deposited on the alpha particles in the second harmonic tritium heating case for (a) $[0, \pi, 0, \pi]$; (b) $[0, 0, \pi, \pi]$ and (c) $[0, \pi/2, \pi, 3\pi/2]$ phasing. In each case, the deposition profile obtained when only the dominant toroidal number is considered appears as a thin curve. The vertical dashed line denotes the approximate location (in the equatorial plane) of the Doppler-shifted fundamental cyclotron resonance for thermal particles. In the three cases, this resonance is located on the high field side.

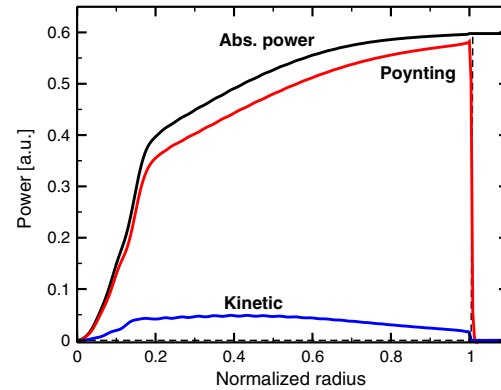


Figure 15. Power balance corresponding to the ^3He case in ITER, for $n = 66$. Shown are the Poynting flux, the (cumulative) absorbed power, and the kinetic flux deduced from the energy balance. The cumulative power coupled by the antenna is also shown as a dashed line and matches the absorbed power on the vacuum vessel.

advantages over alternative descriptions. Firstly, it provides a coherent framework to the wave calculation and to the quasilinear response description as shown, e.g., in [16]. Secondly, it results in symmetric expressions which ensure that the energy transfers are correctly described. Lastly, by providing very general expressions, it is flexible enough to allow various levels of approximations, which should be determined by the physical problem at hand, and also by the computational power available. This last point is illustrated by the development EVE code whose first version, presented in this paper, is based on a quasi-local second-order FLR derivation

of the plasma functional. The resulting tool is available to simulate commonly employed scenarios of ICRF heating in magnetic fusion plasmas, i.e. fundamental minority heating, second harmonic heating, fast wave electron heating and mode conversion electron heating, up to the second harmonic of the cyclotron resonance. Although in some situations, the simulations performed with this code are already numerically demanding, there is no obstacle to the implementation of more comprehensive expressions in the future. For instance, the inclusion of finite orbit width effects is conceptually straightforward: it requires an implementation of the plasma functional embedding the distribution functions of the various plasma species expressed in terms of adiabatic invariants [33, 34]. These distributions are typically provided by a Fokker–Planck code, ideally based on the same formalism. It is planned that such self-consistent simulations will be the subject of forthcoming publications.

Acknowledgments

Continuous and friendly support by L.-G. Eriksson is warmly acknowledged. This effort has also benefited from enlightening discussions with D.N. Smithe, P.U. Lamalle, E. Lerche and D. Van Eester. This work, supported by the European Communities under the contract of Association between EURATOM and CEA, was carried out within the framework of the European Fusion Development Agreement. The views and opinions expressed herein do not necessarily reflect those of the European Commission.

Appendix A. Power balance

It is important to mention that energy conservation relations are direct consequences of the variational formulation [15]. The time-averaged work exerted by the wave on the particles in the volume inside magnetic surface ψ is given by

$$\dot{W}_{\text{part}}(\psi) = \frac{1}{2} \Re \left\{ \int_{\psi' \leq \psi} d^3r \mathbf{E}^* \cdot \mathbf{j}_{\text{part}} \right\} \quad (\text{A.1})$$

It is readily shown that

$$\dot{W}_{\text{part}}(\psi) = \frac{\omega}{2} \Im \{ \mathcal{L}_{\text{part}}(\psi) \} - \frac{1}{2} \Re \left\{ \int_{\psi} d^2S \cdot \mathbf{j}_{\text{part}} \varphi^* \right\}, \quad (\text{A.2})$$

On the other hand, the work provided by the radiofrequency generator to maintain the oscillating field in the system is given by

$$\dot{W}_{\text{ant}}(\psi) = \frac{\omega}{2} \Im \{ \mathcal{L}_{\text{ant}}(\psi) \} - \frac{1}{2} \Re \left\{ \int_{\psi} d^2S \cdot \mathbf{j}_{\text{ant}} \varphi^* \right\}, \quad (\text{A.3})$$

Straightforward algebra allows to cast the Maxwellian functional in the form

$$-i \frac{\omega}{2} \mathcal{L}_{\text{maxw}}(\psi) = -i\omega W_{\text{field}}(\psi) \quad (\text{A.4})$$

$$+ \frac{1}{2\mu_0} \int_{\psi} d^2S \cdot (\mathbf{E}^* \times \mathbf{B}) - \frac{1}{2} \int_{\psi} d^2S \cdot \mathbf{j}_{\text{maxw}} \varphi^*, \quad (\text{A.5})$$

with

$$W_{\text{field}}(\psi) \equiv \int_{\psi' < \psi} d^3r \left(\frac{\epsilon_0 |\mathbf{E}|^2}{2} - \frac{|\mathbf{B}|^2}{2\mu_0} \right), \quad (\text{A.6})$$

which is a purely real quantity. Introducing the Poynting flux

$$\mathcal{S}_{\text{Poynting}}(\psi) \equiv \frac{1}{2\mu_0} \Re \left\{ \int_{\psi} d^2S \cdot (\mathbf{E}^* \times \mathbf{B}) \right\}, \quad (\text{A.7})$$

the combination of equations (A.2), (A.3) and (A.5) yields the local conservation relation

$$\dot{W}_{\text{part}}(\psi) + \mathcal{S}_{\text{Poynting}}(\psi) = -\dot{W}_{\text{ant}}(\psi), \quad (\text{A.8})$$

A well-known feature of \dot{W}_{part} is that it comprises both a reversible and an irreversible part, whose separation is delicate [35–37]. More specifically, denoting \mathcal{P}_{abs} the power transferred from the wave to the plasma species, we have the relation

$$\dot{W}_{\text{part}}(\psi) = \mathcal{P}_{\text{abs}}(\psi) + \mathcal{S}_{\text{kin}}(\psi), \quad (\text{A.9})$$

with \mathcal{S}_{kin} the kinetic flux. The Poynting theorem is thus obtained in the form

$$\mathcal{P}_{\text{abs}}(\psi) + \mathcal{S}_{\text{kin}}(\psi) + \mathcal{S}_{\text{Poynting}}(\psi) = -\dot{W}_{\text{ant}}(\psi). \quad (\text{A.10})$$

To deduce \mathcal{P}_{abs} from this relation requires the evaluation of the kinetic flux. In the present approach, however, this step is unnecessary since the dissipated power is directly available from the particle functional $\Im(\mathcal{L}_{\text{part}})$. To demonstrate this point, it is necessary to evaluate the secular variation of the kinetic energy of the particles in interaction with the wave in the framework of the quasilinear theory. This is done by letting $f_{s,0}$ vary on a slow timescale compared with the inverse of the wave frequency. Keeping second-order terms in equation (12) and averaging over the three generalized angles to eliminate fast variations in f_s , we deduce the Fokker–Planck equation in the form

$$\frac{\partial f_{s,0}}{\partial t} = \hat{C} + \frac{\partial}{\partial J_i} D_{ij}^{(QL)} \frac{\partial f_{s,0}}{\partial J_i}, \quad (\text{A.11})$$

with \hat{C} the collision operator. In the framework of the Hamiltonian theory, the wave quasilinear diffusion operator is given by [17]

$$D_{ij}^{(QL)} = \pi \sum_N N_i N_j |\delta h_N|^2 \delta(\omega - N_k \Omega_k). \quad (\text{A.12})$$

The total kinetic energy characterizing the particles of species s is given by

$$\varepsilon = \frac{m_s}{2} \int d^3r d^3p v^2 f_{s,0}(\mathbf{r}, \mathbf{p}, t), \quad (\text{A.13})$$

so that the energy increase caused by the power transferred from the wave to the particles through non-collisional damping may be written as

$$\mathcal{P}_{\text{abs}} = \frac{\partial \varepsilon}{\partial t} = \frac{m_s}{2} \int d^3r d^3p v^2 \frac{\partial}{\partial J_j} D_{ij}^{(QL)} \frac{\partial f_{s,0}}{\partial J_i}. \quad (\text{A.14})$$

Using $d^3r d^3p = (2\pi)^3 d^3J$ in the integral and integrating by parts yields

$$\mathcal{P}_{\text{abs}} = -\pi \frac{m_s}{2} (2\pi)^3 \int d^3J \left(N_j \frac{\partial v^2}{\partial J_j} \right) N_i \frac{\partial f_{s,0}}{\partial J_i} \times \delta(\omega - N_k \Omega_k) |\delta h_N|^2. \quad (\text{A.15})$$

The quantity in parentheses may be rewritten as

$$N_j \frac{\partial v^2}{\partial J_j} = \frac{2}{m_s} N_j \frac{\partial E}{\partial J_j} = \frac{2}{m_s} N_j \Omega_j, \quad (\text{A.16})$$

so that, using the global resonance condition imposed by the delta function

$$\mathcal{P}_{\text{abs}} = -\omega\pi(2\pi)^3 \int d^3 J N_i \frac{\partial f_{s,0}}{\partial J_i} \delta(\omega - N_k \Omega_k) |\delta h_N|^2, \quad (\text{A.17})$$

which is strictly identical to the imaginary part of the plasma functional (19), thereby demonstrating

$$\mathcal{P}_{\text{abs}} = \frac{\omega}{2} \Im(\mathcal{L}_{\text{part}}). \quad (\text{A.18})$$

We also deduce from equation (A.2) that the kinetic flux is given by

$$\mathcal{S}_{\text{kin}}(\psi) = -\frac{1}{2} \Re \left\{ \int_{\psi} d^2 \mathbf{S} \cdot \mathbf{j}_{\text{part}} \psi^* \right\}. \quad (\text{A.19})$$

Figure 15 shows the power balance corresponding to the ^3He case in ITER discussed in section 4. After the field is reconstructed, the power coupled by the antenna is given by equation (A.3), the Poynting flux is available from equation (A.7), and the power absorbed on species, $\mathcal{P}_{\text{abs},s}$, is directly deduced from the plasma functional (equation (A.18)). The kinetic flux is then deduced from the energy balance, equation (A.10).

It is often convenient to separate the power absorbed by the various plasma species. Using the decomposition of equation (6), we may write

$$\mathcal{P}_{\text{abs}}(\psi) = \sum_s \mathcal{P}_{\text{abs},s}(\psi), \quad (\text{A.20})$$

with

$$\mathcal{P}_{\text{abs},s}(\psi) = \frac{\omega}{2} \Im(\mathcal{L}_{\text{part},s}(\psi)), \quad (\text{A.21})$$

which is directly available from the wave calculation and corresponds to the power absorbed inside magnetic surface ψ . An important quantity for experiment modelling is the power density absorbed by species s on magnetic surface ρ . It is obtained by writing

$$p_s(\psi) = \frac{1}{\mathcal{V}(\rho)} \left. \frac{d\Im(\mathcal{L}_{\text{part},s})}{d\rho} \right|_{\psi}, \quad (\text{A.22})$$

with the volume element defined as

$$\mathcal{V}(\rho) = 2\pi \oint d\theta J(\rho, \theta). \quad (\text{A.23})$$

Appendix B. Plasma functional and adiabatic invariants

Although action variables are mathematically convenient to describe the periodic unperturbed motion, it is more practical to characterize this motion in terms of adiabatic invariants. In this work, we consider the set of invariants of the unperturbed motion $\mathbf{I} \equiv (E, \Lambda, P_\phi)$ with $E \equiv m_s v^2/2$ the particle energy,

$\Lambda \equiv \mu B_0(0)/E$ with $\mu \equiv m_s v_\perp^2/2/B_0$ the magnetic moment and $B_0(0)$ the magnetic field on axis. P_ϕ is the canonical toroidal momentum given by

$$P_\phi \equiv m_s \frac{F}{B_0} v_\parallel + q_s \psi, \quad (\text{B.1})$$

with F the toroidal flux and ψ the poloidal flux. It should be noted that P_ϕ is the only invariant which depends explicitly on the radial position through the poloidal flux ψ .

The first and third action variables are directly linked to the invariants by the relations $J_1 = m_s \mu/q_s$ and $J_3 = P_\phi$. We have

$$\frac{\partial f_{s,0}}{\partial J_i} = \frac{\partial f_{s,0}}{\partial I_k} \frac{\partial I_k}{\partial J_i}, \quad (\text{B.2})$$

where $\partial f_{s,0}/\partial I_k$ is assumed to be a known quantity. From equation (14):

$$\frac{\partial E}{\partial J_k} = \frac{\partial H_{s,0}}{\partial J_k} = \Omega_k. \quad (\text{B.3})$$

It is readily shown that

$$\frac{\partial \Lambda}{\partial J_k} = \frac{1}{E} [\Omega_{cs}(0) \delta_{k,1} - \Lambda \Omega_k]. \quad (\text{B.4})$$

Also

$$\frac{\partial P_\phi}{\partial J_k} = \delta_{k,3}, \quad (\text{B.5})$$

so that

$$N_k \frac{\partial f_{s,0}}{\partial J_k} = N_k \Omega_k \left(\frac{\partial f_{s,0}}{\partial E} - \frac{\Lambda}{E} \frac{\partial f_{s,0}}{\partial \Lambda} \right) + \frac{N_1 \Omega_{cs}(0)}{E} \frac{\partial f_{s,0}}{\partial \Lambda} + N_3 \frac{\partial f_{s,0}}{\partial P_\phi}. \quad (\text{B.6})$$

Using the previous expression in equation (19), the particle functional may be decomposed as

$$\mathcal{L}_{\text{part},s} \equiv \mathcal{L}_{\text{part},s}^{(\text{res})} + \mathcal{L}_{\text{part},s}^{(\text{res})}, \quad (\text{B.7})$$

with the non-resonant particle functional defined as

$$\mathcal{L}_{\text{part},s}^{(\text{res})} = -\epsilon_0 \int d^3 r \omega_{ps}^2 |\mathbf{A}|^2 - (2\pi)^3 \times \sum_N \int d^3 J \left(\frac{\partial f_{s,0}}{\partial E} - \frac{\Lambda}{E} \frac{\partial f_{s,0}}{\partial \Lambda} \right) |\delta h_N|^2, \quad (\text{B.8})$$

Since the equilibrium distribution function is independent of the generalized angles, it is possible to use the Parseval identity for the Hamiltonian:

$$\sum_N |\delta h_N|^2 = \frac{1}{(2\pi)^3} \int d^3 \Phi |\delta H_s|^2. \quad (\text{B.9})$$

In accordance with equation (50), the particle unperturbed velocity is given by $\mathbf{v}_{s,0} \equiv v_\perp [\cos(\phi_c) \mathbf{e}_{\perp 1} - \sin(\phi_c) \mathbf{e}_{\perp 2}] + v_\parallel \mathbf{e}_\parallel$ with ϕ_c the gyro-angle. Using $d^3 \mathbf{p} = d\phi_c d\rho_\parallel d\rho_\perp$, the integration over ϕ_c may be performed, allowing to recast equation (B.8) in the form

$$\mathcal{L}_{\text{part},s}^{(\text{res})} = -q_s^2 \int d^3 r d^3 \mathbf{p} \frac{\partial f_{s,0}}{\partial E_\parallel} \left\{ |\varphi|^2 + \frac{1}{m_s} (E_\perp - 2E_\parallel) |\mathbf{A}_\perp|^2 \right\}, \quad (\text{B.10})$$

with the parallel and perpendicular energy given by

$$E_{\parallel} = E - B_0\mu = E \left(1 - \Lambda \frac{B_0}{B_0(0)} \right), \quad (\text{B.11})$$

and

$$E_{\perp} = B_0\mu = E\Lambda \frac{B_0}{B_0(0)}. \quad (\text{B.12})$$

It is readily seen that equation (B.10) is a real quantity. The contribution of the non-resonant functional is thus purely reactive.

The resonant functional appearing in equation (B.7) is given by

$$\mathcal{L}_{\text{part},s}^{(\text{res})} = (2\pi)^3 \sum_N \int d^3J \frac{\omega}{\omega - N \cdot \Omega} \mathcal{D}f_{s,0} |\delta h_{N_1, N_2, N_3}|^2, \quad (\text{B.13})$$

having introduced the differential operator \mathcal{D} acting on the unperturbed distribution function

$$\mathcal{D}f_{s,0} \equiv \left(\frac{\partial f_{s,0}}{\partial E} - \frac{\Lambda}{E} \frac{\partial f_{s,0}}{\partial \Lambda} \right) + p \frac{\Omega_{cs}(0)}{\omega} \frac{1}{E} \frac{\partial f_{s,0}}{\partial \Lambda} + \frac{n}{\omega} \frac{\partial f_{s,0}}{\partial P_{\phi}}. \quad (\text{B.14})$$

If the distribution function is independent of the toroidal momentum, the previous expression may be recast in the convenient form

$$\mathcal{D}f_{s,0} = \left(1 - \frac{p\Omega_{cs}}{\omega} \right) \frac{\partial f_{s,0}}{\partial E_{\parallel}} + \frac{p\Omega_{cs}}{\omega} \frac{\partial f_{s,0}}{\partial E_{\perp}}. \quad (\text{B.15})$$

Of particular interest is the case of an anisotropic Maxwellian characterized by perpendicular (respectively parallel) temperature $T_{\perp,s}$ (respectively $T_{\parallel,s}$), given by

$$f_{s,0}(\mathbf{r}, \mathbf{p}) = \frac{n_s}{(2\pi m_s)^{3/2} T_{\perp,s} T_{\parallel,s}^{1/2}} e^{-E_{\perp}/T_{\perp,s}} e^{-E_{\parallel}/T_{\parallel,s}}. \quad (\text{B.16})$$

In this case, it is readily shown that the non-resonant functional can be written as

$$\begin{aligned} \mathcal{L}_{\text{part},s}^{(\text{res})} &= \epsilon_0 \int d^3\mathbf{r} \frac{m_s c^2}{T_{\parallel,s}} \left(\frac{\omega_{ps}}{c} \right)^2 |\varphi|^2 \\ &+ \epsilon_0 \int d^3\mathbf{r} \omega_{ps}^2 \left(\frac{T_{\perp,s}}{T_{\parallel,s}} - 1 \right) |A_{\perp}|^2, \end{aligned} \quad (\text{B.17})$$

which reduces to the expression of Gambier and Samain [15] if $T_{\parallel,s} = T_{\perp,s}$. From equation (B.15), we also have the relation

$$\mathcal{D}f_{s,0} = -\frac{f_{s,0}}{T_{\parallel,s}} \mathcal{A}_{ps}, \quad (\text{B.18})$$

with

$$\mathcal{A}_{ps} \equiv 1 - \frac{p\Omega_{cs}}{\omega} \left(1 - \frac{T_{\parallel,s}}{T_{\perp,s}} \right). \quad (\text{B.19})$$

References

- [1] Start D.F.H. and Jacquinot J. 1998 *Phys. Rev. Lett.* **80** 4681
- [2] Hellsten T. *et al* 2005 *Nucl. Fusion* **45** 706
- [3] Mantsinen M.J. *et al* 2004 *Nucl. Fusion* **44** 33
- [4] Eriksson L.G. *et al* 2006 *Nucl. Fusion* **46** S951
- [5] Eriksson L.-G., Hoang G.T. and Bergeaud V. 2001 *Nucl. Fusion* **41** 91
- [6] Vaclavik J. and Appert K. 1991 *Nucl. Fusion* **31** 1945
- [7] Wong K.-L. 1999 *Plasma Phys. Control. Fusion* **41** R1
- [8] Jaun A. *et al* 1995 *Comput. Phys. Commun.* **92** 153
- [9] Borba D. and Kerner W. 1999 *J. Comput. Phys.* **153** 101
- [10] Borba D. *et al* 2002 *Nucl. Fusion* **42** 1029
- [11] Lauber Ph., Günter S. and Pinches S.D. 2005 *Phys. Plasmas* **12** 122501
- [12] Jaeger E.F. *et al* 2006 *Phys. Plasmas* **13** 056101
- [13] Brambilla M. 1999 *Plasma Phys. Control. Fusion* **41** 1
- [14] Popovich P., Cooper W.A. and Villard L. 2004 *Fusion Sci. Technol.* **46** 342
- [15] Gambier D.J. and Samain A. 1985 *Nucl. Fusion* **25** 283
- [16] Bécoulet A., Gambier D.J. and Samain A. 1991 *Phys. Fluids B* **3** 137
- [17] Eriksson L.-G. and Helander P. 1994 *Phys. Plasmas* **1** 308
- [18] Smithe D.N. 1989 *Plasma Phys. Control. Fusion* **31** 1105
- [19] Lamalle P.U. 1997 *Plasma Phys. Control. Fusion* **39** 1409
- [20] Kaufman A. 1972 *Phys. Fluids* **15** 1063
- [21] Smithe D., Colestock P., Kammash T. and Kashuba R. 1988 *Phys. Rev. Lett.* **60** 801
- [22] Jaeger E.F., Berry L.A., D'Azevedo E., Batchelor D.B. and Carter M.D. 2001 *Phys. Plasmas* **8** 1573
- [23] Littlejohn R.G. 1981 *Phys. Fluids* **24** 1730
- [24] Swanson D.G. 1985 *Phys. Fluids* **28** 2645
- [25] Huysmans G.T.A. and Goedbloed J.P. 1993 *Phys. Fluids B* **5** 1545
- [26] 2007 Progress in the ITER Physics Basis *Nucl. Fusion* **47** S1
- [27] Polevoi A. 2002 *J. Plasma Fusion Res. Ser.* **5** 82
- [28] Bergeaud V., Eriksson L.-G. and Start D.F.H. 2000 *Nucl. Fusion* **40** 35
- [29] Van Eester D., Louche F. and Koch R. 2002 *Nucl. Fusion* **42** 310
- [30] Dumont R.J. 2007 *Proc. 17th Topical Conf. on Applications of Radio Frequency Power in Plasmas (Clearwater, FL, 2007)* ed P.M. Ryan and D.A. Rasmussen (New York: American Institute of Physics) p 459
- [31] Lamalle P.U. *et al* 2007 *Final Report on Contract EFDA/05-1334, Laboratory Report* no 129 Laboratory for Plasma Physics (Brussels, Belgium: Royal Military Academy)
- [32] Jaeger E.F. *et al* 2008 *Phys. Plasmas* **15** 072513
- [33] Hellsten T. *et al* 2004 *Nucl. Fusion* **44** 892
- [34] Johnson T., Hellsten T. and Eriksson L.-G. 2006 *Nucl. Fusion* **46** S433
- [35] McVey B.D., Sund R.S. and Scharer J.E. 1985 *Phys. Rev. Lett.* **55** 507
- [36] Brambilla M. and Krücken T. 1988 *Plasma Phys. Control. Fusion* **30** 1083
- [37] Myra J.R., Berry L.A., D'Ippolito D.A. and Jaeger E.F. 2004 *Phys. Plasmas* **11** 1786
- [38] Dumont R.J., Phillips C.K. and Smithe D.N. 2005 *Phys. Plasmas* **12** 042508

Heating and current drive by ion cyclotron waves in the activated phase of ITER

R.J. Dumont and D. Zarzoso

CEA, IRFM, F-13108 Saint-Paul-lez-Durance, France

Received 5 September 2012, accepted for publication 14 November 2012

Published 10 December 2012

Online at stacks.iop.org/NF/53/013002

Abstract

Waves in the ion cyclotron range of frequency (ICRF) are expected to play a central role in the heating of ITER plasmas during deuterium (D)–tritium (T) operation. These waves can also be used to drive current by direct electron damping of the fast wave, provided an appropriate antenna phasing is used. The corresponding current profile is peaked near the magnetic axis, and can have a beneficial effect on the discharge stability and performance. In this paper, two scenarios applicable during the activated phase of ITER operation are compared: second harmonic tritium heating and minority helium-3 heating, which differ in the addition of a small fraction of ^3He ions (2%) in the DT mixture for the latter. The resulting change of the dominant ICRF heating scheme causes the discharge properties to differ appreciably. In this paper, a full-wave code is coupled to a Fokker–Planck solver and a current drive module to investigate in detail the effect of ICRF waves on the discharge. The impact of phasing on the scenario in terms of plasma heating and current drive efficiency is studied by simulating ICRF heating with various antenna toroidal spectra. It is found that despite a lower current drive efficiency, the addition of ^3He in the discharge increases the single-pass absorption rate, the ion heating fraction, and makes the scenario essentially immune to details in the toroidal phasing and fast ion properties.

(Some figures may appear in colour only in the online journal)

1. Introduction

Waves in the ion cyclotron range of frequency (ICRF) are expected to play an important role in the operation of ITER. In its activated phase, i.e. when the plasma will be comprised of a mix of deuterium (D) and tritium (T), it is foreseen to use them mostly for plasma heating [1, 2]. Furthermore, the operation of tokamaks relies upon the drive and sustainment of a significant fraction of the toroidal current by non-inductive methods [3]. Whereas electron cyclotron or lower hybrid waves are the primary candidates for radiofrequency (RF) current drive in ITER, several schemes involving RF waves in the ICRF have also been proposed and most of them have been evaluated in past and ongoing fusion experiments. Among these methods, fast wave (FW) current drive is obtained by exciting the fast magnetosonic wave with a toroidally asymmetric antenna spectrum [4]. Owing to the absence of stringent accessibility limitations for the FW, and to the availability of reliable RF generators in the ICRF, this method is attractive for next-step fusion reactors, including during H-mode operation [5–7]. On the other hand, FW current drive (FWCD) is known to be experimentally challenging due to low absorptivity of the FW electron damping mechanisms and/or to parasitic damping of the wave by ions, even at rather high harmonics of the cyclotron

resonance [8]. In ITER, the situation is different compared with most past experiments [9], as no ‘pure’ FWCD scheme is readily available. The simultaneous presence of multiple species and the magnetic configuration make it impossible to exclude all low-order harmonics cyclotron layers from the plasma in the foreseen frequency range for the ICRF system. Therefore, the idea is to take advantage of the high electron temperature in ITER plasmas, and exploit the ICRF waves whose primary goal is to heat the plasma in order to drive centrally peaked current. In this respect, the FW driven current may be considered as an added value of the ICRF system, as it does not require any supplemental system compared with the ITER baseline design [4]. In the typical ICRF scenarios envisioned for ITER, the driven current profile is peaked on axis, and only the amount of driven current can be controlled to some extent within the limits given by the maximum available power, the flexibility of the RF system in terms of toroidal phasing and the FWCD efficiency. Although the latter is limited as a result of the preferential interaction of the FW with thermal electrons, it has been recognized that even a limited amount of central current may be beneficial in terms of plasma stability and performance [10, 11].

In this paper, several aspects pertaining to the use of ICRF waves in the activated phase of ITER are addressed [12]. Two

ICRF scenarios are compared: (i) second harmonic tritium heating (DT) and (ii) helium-3 minority heating DT(^3He). Their practical implementations differ in that a small fraction of ^3He ions (2%) have been added to the plasma in the latter case. This, however, is known to profoundly affect the ICRF scenario by improving the wave damping and also possibly the nuclear reaction rate, as was demonstrated in JET [13]. In each case, the performance of FWCD is analysed in terms of current drive efficiency. Ideally, the choice of a given antenna toroidal phasing for the purpose of current drive should not affect the power split between the plasma species or the wave coupling properties in a significant way. The minimal set of ingredients required to address the points discussed previously is comprised of the following.

- A multi-dimensional full-wave code able to compute the electromagnetic field excited by the antenna in the whole plasma volume. The Hamiltonian full-wave code EVE [14] is employed. Given the axisymmetric nature of the problem at hand, every toroidal mode is handled independently.
- A post-processor to recombine the solutions corresponding to individual toroidal numbers, appropriately weighted, and estimate the power split between species and the FW driven current. The latter is estimated by means of the heuristic Ehst–Karney formula which has been shown to give reliable results [15, 16].
- A Fokker–Planck (FP) solver to evaluate the fast ion population features resulting from the RF plasma heating. For this purpose, EVE has been supplemented with a FP module named AQL, which takes into account the anisotropic nature of the distribution function. This module is described in the appendix.
- A one-dimensional full-wave code using radiative boundary conditions to estimate the per-pass damping rate in each case. Although it is insufficient to extensively qualify a given ICRF scenario, this quantity is indicative of its overall reliability. In fact, low absorption scenarios are known to be prone to such adverse effects as parasitic damping and sheath development. In this work, we will use the METS [17, 18] code.

This paper is organized as follows: in section 2, the main features of the numerical tools employed for this work are described. In section 3, the physical parameters and characteristics of the two scenarios, DT and DT(^3He), are presented. The issue of FWCD is discussed in the same section. Conclusions are drawn in section 4.

2. Simulation tools and numerical setup

The plasma parameters used in these simulations are based on those employed in a recent benchmark of full-wave codes presented in [19] and pertain to the activated phase of ITER. The magnetic and kinetic equilibrium background plasma profiles, provided by the PTRANSP code, are shown in figure 1. The central magnetic field is $B_0(R_0 = 6.2 \text{ m}) = 5.45 \text{ T}$. Eight ion species are taken into account: thermal deuterium, tritium, argon, beryllium, alphas, thermal ^4He , ^3He and deuterium beam. The location of the main low-order unshifted ion cyclotron layers for these species is shown in figure 2. The

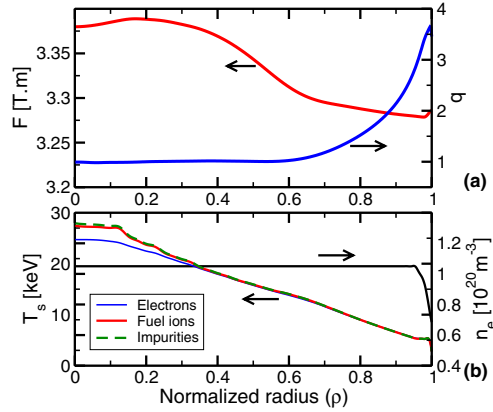


Figure 1. Target profiles employed in the simulations presented in this paper. (a) Toroidal flux function (left y-axis), safety factor (right y-axis); (b) thermal temperature of electrons, fuel ions (deuterium, tritium and helium-3) before heating, and impurities (left y-axis); electron density profile (right y-axis).

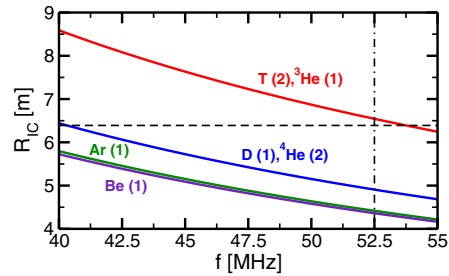


Figure 2. Main low-order ion cyclotron layers in the planned frequency range of ITER ICRF generators. The cyclotron harmonics is shown in parentheses. The vertical dashed line denotes the working frequency considered in this paper.

plasma equilibrium is provided by the EFT code, and is extended by a vacuum region up to a perfectly conducting wall, which is assumed to coincide with a virtual flux surface. Preliminary calculations have shown that the precise location of the vacuum vessel had a negligible influence on the final result in the context of these simulations, which are all characterized by a large per-pass damping rate. The ICRF antenna is located on the low-field side, at midplane position $R_{\text{ant}} = 8.38 \text{ m}$. The resulting geometric setup is shown in figure 3, in which the main cyclotron resonance layers are shown for the considered working frequency $f = 52.5 \text{ MHz}$. Superthermal species, namely alphas, D beam and the heated ion, are modelled using equivalent Maxwellians with $T_{\parallel} \neq T_{\perp}$. However, it must be noted that for consistency reasons, the temperature of the heated species is computed by the AQL module, in contrast to the latter reference, in which it was also provided by PTRANSP. Since AQL accounts for the contribution of every toroidal mode to the RF-induced quasilinear diffusion, this implies that the fast ion distribution also accounts for phasing effects. In this paper, we will also use the nominal value of the ITER system for the total ICRF power,

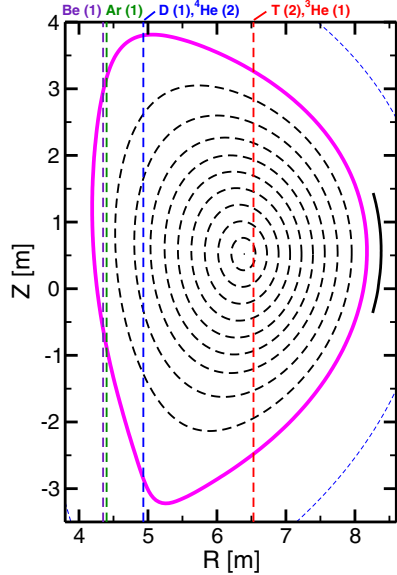


Figure 3. Geometric setup of calculation: plasma boundary and antenna shape ($R_{\text{ant},0} = 8.38$). Also shown are 10 flux surfaces, equidistant in $\sqrt{\psi_r}$. The outermost one coincides with the plasma boundary. For simplicity, the unshifted main cyclotron layers obtained for $f = 52.5$ MHz are shown as vertical lines.

namely $P_{\text{RF}} = 20$ MW as well as $P_{\text{RF}} = 10$ MW. Although AQL accounts for this difference in the superthermal ion tail development and since both scenarios appear to be fairly robust with respect to the background parameters, it is assumed that the background profiles remain identical when $P_{\text{RF}} = 20$ MW or $P_{\text{RF}} = 10$ MW. In order to make comparisons between the DT and DT(^3He) scenarios straightforward, the profiles for the DT case are the same as those provided by PTRANSP for the DT(^3He) case. The only difference is that the helium-3 concentration is set to zero in the latter case, and compensated by a slight increase in the deuterium density. Evidently, the heated species is also different, as well as the main absorption mechanism: tritium heating at the second harmonic of the IC resonance in the DT case, fundamental (minority) helium-3 heating in the DT(^3He) case.

An important aspect in this kind of study is the necessary resolution required to describe the heating scenario. It was established that 460 radial points in the plasma, 512 poloidal angles and retaining poloidal modes between -64 and $+64$ were sufficient to accurately describe the electromagnetic field in the whole plasma volume. Note that in these scenarios, converted waves are nearly absent, which makes the wave code convergence easier. The ITER ICRF antenna consists of 24 straps, grouped into 8 poloidal triplets connected in pairs [20]. By introducing phase shifts between these pairs, various antenna phasings are possible. In EVE and to describe the ITER antenna, the antenna current is written as

$$j_{\text{ant}} = \frac{I_0}{J} \sigma_\theta(\theta) \sigma_\phi(\phi) \delta(\psi - \psi_{\text{ant}}) e_\theta, \quad (1)$$

with $\sigma_\theta(\theta)$ (respectively $\sigma_\phi(\phi)$) a function describing the geometrical shape of the current sheet located on the radial surface denoted by ψ_{ant} in the poloidal (respectively toroidal) direction. I_0 is the total current in the antenna feeder and J is the Jacobian of the (ψ, θ, ϕ) system of coordinates, with ψ the poloidal flux, θ the poloidal angle and ϕ the toroidal angle. It is readily deduced for the n th toroidal harmonics

$$\{J j_{\text{ant}}\}_n = I_0 \sigma_\theta(\theta) \sigma_n \delta(\psi - \psi_{\text{ant}}) e_\theta. \quad (2)$$

Setting the constant $I_0 \sigma_n$ to unity, the wave calculation can be performed for every individual toroidal number. The corresponding normalized power coupled by the antenna for a given toroidal mode n , which is a direct output of the code, is given by

$$\dot{W}_{\text{ant},n} \equiv \frac{1}{2} \Re \left(\int d\psi d\theta \{J j_{\text{ant},n}\}_n \cdot E_n^* \right), \quad (3)$$

where E_n is the n Fourier harmonics of the wave electric field. Physically, the RF power coupled by the antenna is thus given by

$$\dot{W}_{\text{ant}} \equiv \sum_n \dot{W}_{\text{ant},n} = I_0^2 R_c, \quad (4)$$

with the coupling resistance defined as

$$R_c \equiv \sum_n |\sigma_n|^2 \dot{W}_{\text{ant},n}. \quad (5)$$

In the framework of this antenna model, I_0 is essentially unknown. On the other hand, it is assumed that the total coupled power, P_{RF} , is a known quantity. Therefore, it is useful to introduce the normalization constant

$$w_p \equiv \sqrt{\frac{P_{\text{RF}}}{R_c}}. \quad (6)$$

For toroidal number n , the power absorbed by the plasma species is linked to the plasma functional $\mathcal{L}_{\text{part}}$ by the relation [14]

$$\bar{P}_{\text{abs},n} = \frac{\omega}{2} \Im \{ \mathcal{L}_{\text{part},n}(\psi) \} = -\dot{W}_{\text{ant}}, \quad (7)$$

and corresponds to another direct output of the code. Since the wave calculation has been performed assuming $I_0 \sigma_n = 1$, this quantity is normalized. In order to obtain the power actually coupled to the plasma, equations (4) and (6) show that

$$P_{\text{abs}} = w_p^2 \sum_n |\sigma_n|^2 \bar{P}_{\text{abs},n}. \quad (8)$$

Considering the features of the ITER antenna, σ_n is given by

$$\sigma_n = \sum_{i=1}^4 \sqrt{\frac{\Delta\phi_i}{8\pi}} \text{sinc}\left(\frac{n\Delta\phi_i}{2}\right) e^{i(\varphi_i - n\phi_i)}. \quad (9)$$

ϕ_i is the toroidal angle corresponding to the centre of the i th strap, $\Delta\phi_i \equiv \Delta z / R_{\text{ant}}$ with $\Delta z = 0.17$ m its width in the toroidal direction and φ_i corresponds to the applied toroidal phase shift. Figure 4 shows vacuum spectra obtained for various inter-strap phasings assuming the plasma responds

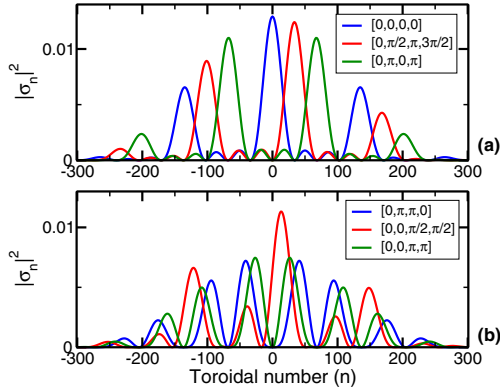


Figure 4. Antenna toroidal spectrum (uniform loading) for various inter-strap phasings. (a) Monopole and dipole-type phasings; (b) super-dipole type phasings.

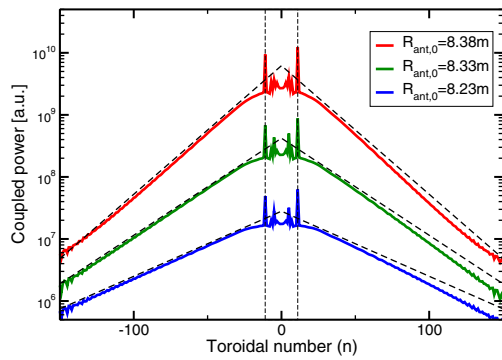


Figure 5. Power absorbed versus toroidal number when a flat antenna spectrum is considered for $R_{\text{ant},0} = 8.38$ m, $R_{\text{ant},0} = 8.33$ m or $R_{\text{ant},0} = 8.28$ m. In each case, the corresponding fit is shown as a dashed line. The two vertical lines denote the toroidal numbers for which the propagation of the main coaxial modes is expected in the considered geometry.

uniformly to each toroidal number n , with the antenna located at $R_{\text{ant}} = 8.18$ m. In reality, however, the plasma response depends on n . This is shown in figure 5, where the power coupled to the plasma assuming $\sigma_n = 1$ for every toroidal number is shown versus n . Depending on the plasma–antenna distance ΔR and the antenna location R_{ant} in the midplane, the coupled power is found to approximately decrease as

$$\dot{W}_{\text{ant},n} \propto \exp(-2|n|\Delta R/R_{\text{ant}}). \quad (10)$$

The combination of the antenna vacuum spectrum and of the attenuation described by equation (10) allows one to define appropriate boundaries to the considered toroidal spectrum. The simulations presented in this paper have been performed retaining toroidal modes between -150 and $+150$, which is adequate for an antenna assumed to be located at midplane major radius $R_{\text{ant}} = 8.38$ m, namely $\Delta R \approx 0.2$ m.

In ICRF regimes with significant part of the wave power directly absorbed by fundamental or harmonic cyclotron

damping, superthermal ion tails are generally observed [1, 21, 22]. In particular, it is necessary to retain fast ion effects in the self-consistent calculation of power deposition profiles in the case of second harmonic heating [21]. Furthermore, in the context of FWCD calculations [8], it is necessary to simulate the temperature of heated ions: the development of an ion tail usually results in a modification of the damping by the considered ion species, and a subsequent change in the power fraction absorbed by electrons since direct FW electron damping is sub-dominant compared with ion cyclotron damping. In this work, we adopt a minimal model to describe these effects: the AQL module complements EVE, simulating the time-dependent development of the superthermal tail of the interacting ion species, retaining anisotropy effects by developing the distribution function on a basis of Legendre polynomials [23]. This coupled wave/FP simulation is performed in an iterative fashion: the electromagnetic wave is computed first assuming that all species are thermal (except for D beam and alphas), including the heated species. The quasilinear diffusion coefficient is then constructed and the resulting distribution function for the heated ion is evaluated, accounting for the antenna toroidal phasing and the absorbed RF power. This distribution function results from the competition between the RF wave and the collisions. Since EVE assumes that all input distribution functions are Maxwellians, an equivalent temperature is deduced and the wave calculation is performed with the updated plasma features. The loop is performed until the distribution function does not evolve which, practically, is found to occur within about five iterations. The AQL module is briefly described in the appendix.

3. ICRH scenarios for ITER

With the numerical tools presented previously, we can compare two scenarios which can be used during the activated phase of ITER, i.e. DT and DT(³He). As an illustration, figure 6 shows a comparison of the contours of the right-handed electric field magnitude in the DT case and in the DT(³He) case, assuming a total absorbed power of 20 MW and a $[0, \pi/2, \pi, 3\pi/2]$ phasing. It is immediately clear that the addition of 2% of ³He in the DT mixture results in improved per-pass damping. This figure shows the result obtained when quasilinear effects are included. It is worth pointing out that the field pattern is not dramatically affected by the fact that fast ions are accounted for. Comparisons with the field obtained when all species are thermal show that in the DT case, the wave amplitude is reduced on the high-field side of the cyclotron layer, indicating an enhancement of the power damping caused by the tritium tail. In the DT(³He) case, however, the field is essentially unchanged.

The power deposition profiles corresponding to the cases shown in figure 6 are shown in figure 7. Whereas the power is roughly evenly split between electron and tritium ions in the DT scenario, a large fraction of the power is damped by minority ions in the DT(³He) scenario (54.9%), the remaining being absorbed by electrons (30.0%) and tritium ions (14.1%). In both cases, the alpha damping is found to be very weak: 1.1% in the DT scenario, 0.3% in DT(³He). An issue which was encountered in these simulations is the impurity absorption.

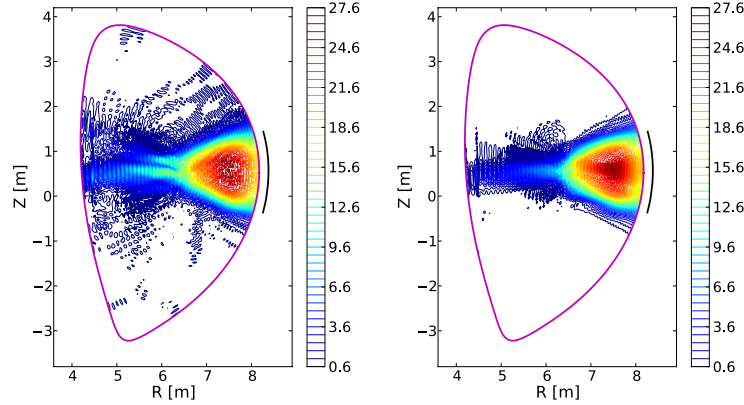


Figure 6. Iso-contours of $|E_-|$ in the DT (left) and DT(^3He) scenarios (right). The values are given in kV m^{-1} for 20 MW absorbed power and the antenna is in $[0, \pi/2, \pi, 3\pi/2]$ phasing.

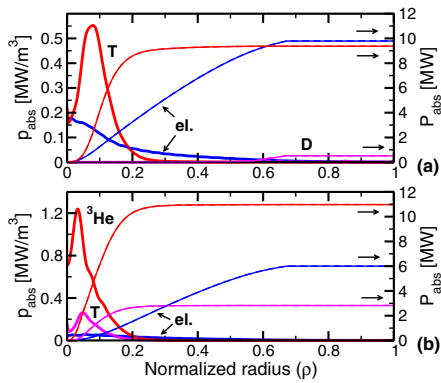


Figure 7. Power absorbed by species for $[0, \pi/2, \pi, 3\pi/2]$ phasing in the (a) DT scenario, (b) DT(^3He) scenario when the heated ions are assumed to be thermal. Reduced spectrum (solid lines) and full spectrum (dashed lines, barely visible). The right y-axis corresponds to the cumulative power. Only species absorbing more than 2% of the total absorbed power (20 MW) are shown.

When the profiles given by PTRANSP are used, EVE predicts a significant absorption by impurities (mostly argon) in the DT scenario, as already discussed in [19]. This absorption occurs at the argon fundamental cyclotron layer on the high-field side of the plasma. This result is found to be robust from a numerical point of view: when the resolution is doubled in both the radial and poloidal directions, this parasitic damping remains unchanged. On the other hand, it was found that doubling the argon density results in a large reduction of the corresponding absorption, which is compatible with damping by minority argon at its fundamental resonance. Owing to the uncertainties on the exact density profiles for the impurity species, it was chosen to use the profiles provided by PTRANSP, but to disregard damping by species occurring at normalized radius $\rho > 0.8$ in the final power balance. Clearly, however, this crucial point with respect to the ICRF operation in ITER deserves further investigation, as well as extensive comparisons with other

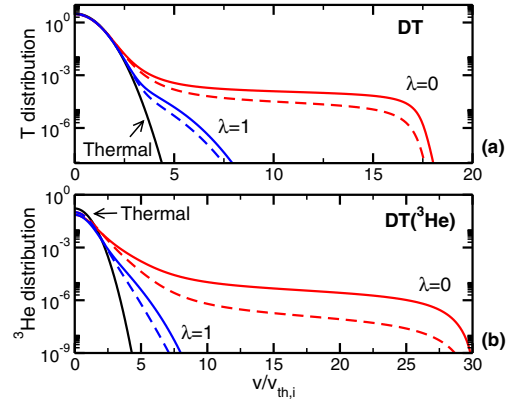


Figure 8. Comparison of the heated ion distribution function during EVE/AQL iterations for $[0, \pi/2, \pi, 3\pi/2]$ antenna phasing in the (a) DT scenario, (b) DT(^3He) scenario at radial location $\rho = 0.1$. The initial and final distributions appear as solid lines (respectively dashed lines) for 20 MW (respectively 10 MW) absorbed power. Each distribution is shown versus normalized thermal velocity for $\lambda = 0$ and $\lambda = 1$.

multi-dimensional wave codes. In figure 7, the result obtained when only one in five toroidal mode numbers are retained in the toroidal spectrum is also compared with the profiles obtained when all toroidal numbers are kept. The results are in very good agreement, which allows one to divide the total computation time by a factor of 5. It should be noted that scenarios with lower per-pass damping rate (e.g. in the non-activated phase) may require more comprehensive toroidal spectra.

The AQL module has been used to evaluate the influence of quasilinear effects linked to superthermal ions. Figure 8 shows the corresponding distribution functions obtained in both scenarios in the parallel ($\lambda = 0$) and perpendicular ($\lambda = 1$) directions versus velocity normalized to the initial heated ion velocity, when 10 or 20 MW of ICRF power are absorbed by the plasma species. Since ion cyclotron damping

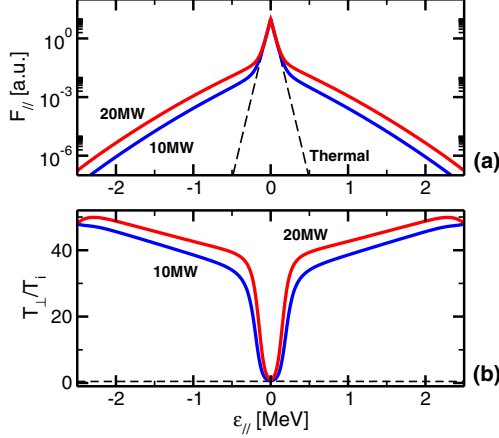


Figure 9. (a) Parallel distribution function; (b) normalized perpendicular temperature in the DT scenario for $[0, \pi/2, \pi, 3\pi/2]$ phasing for a total absorbed power 10 or 20 MW at radial location $\rho = 0.1$. The dashed lines denote the thermal distributions.

almost completely results in a quasilinear diffusion in the perpendicular velocity direction [24], AQL always predicts $T_{\perp} \gg T_{||}$. In the framework of this model, the only mechanism responsible for an increase in $T_{||}$ is pitch-angle scattering, predominantly caused by collisions with background ions. Practically, it is found that after five iterations between EVE and AQL, the calculation is converged and the distribution function does not evolve any further. In order to better visualize the distribution functions and denoting $u \equiv v/v_{th,i}$ with $v_{th,i} \equiv \sqrt{2T_i/m_i}$ the thermal velocity of the heated ion before the application of ICRF power, we define the integrated parallel distribution $F_{||}$ and perpendicular temperature T_{\perp} as

$$F_{||}(u_{||}, \rho) \equiv 2\pi \int_0^{\infty} du_{\perp} u_{\perp} f_i(u_{||}, u_{\perp}, \rho), \quad (11)$$

and

$$T_{\perp}(u_{||}, \rho) \equiv 2\pi T_i(\rho) \int_0^{\infty} du_{\perp} u_{\perp} \left(\frac{u_{\perp}^2}{2} \right) \frac{f_i(u_{||}, u_{\perp}, \rho)}{F_{||}(u_{||}, \rho)}. \quad (12)$$

Figures 9 and 10 show $F_{||}$ and T_{\perp}/T_i versus the parallel energy $\epsilon_{||}$ for both scenarios when $P_{RF} = 10$ MW and $P_{RF} = 20$ MW are coupled to the plasma in the $[0, \pi/2, \pi, 3\pi/2]$ phasing. It can be observed that the converged distributions depart significantly from the initial Maxwellians, which illustrates the importance of quasilinear effects in these calculations. It is worthwhile noting that both scenarios differ in that the helium-3 tail pulled by the RF power in the DT(3 He) scenario extends to higher energies than the tritium tail, owing to the fact that the latter is a fundamental minority scheme, whereas the former is based on second harmonic heating and an associated large number of resonant ions.

Another important aspect in these studies is the influence of the total RF power. These superthermal ion tails generally result in significant modifications of the cyclotron damping and thus the power split between species and associated deposition profiles [18]. In figure 11 the deposition profiles obtained

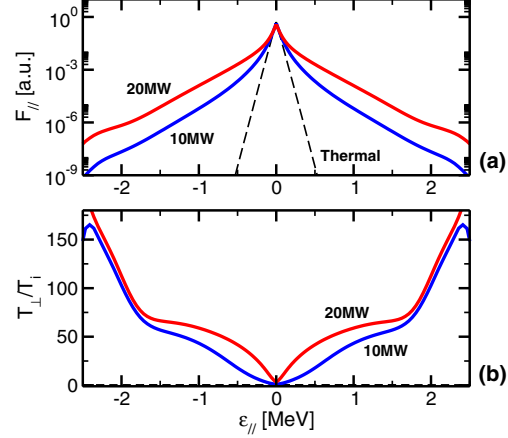


Figure 10. (a) Parallel distribution function; (b) normalized perpendicular temperature in the DT(3 He) scenario for $[0, \pi/2, \pi, 3\pi/2]$ phasing for a total absorbed power 10 or 20 MW at radial location $\rho = 0.1$. The dashed lines denote the thermal distributions.

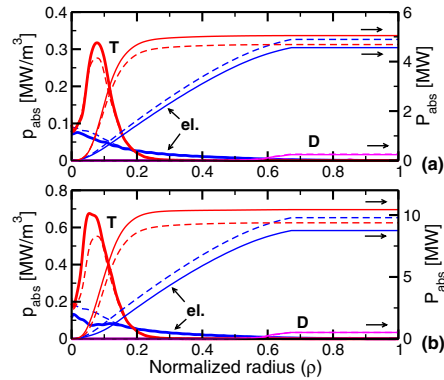


Figure 11. Power deposition profiles (left y-axis) and cumulative power (right y-axis) for $[0, \pi/2, \pi, 3\pi/2]$ phasing in the DT scenario for a total absorbed power of (a) 10 MW; (b) 20 MW. The dashed lines show the power obtained when the tritium tail is not taken into account, whereas the solid lines show the result accounting for quasilinear effects on the heated ions. Only species absorbing more than 1% of the total absorbed power are shown.

in the DT scenario for $P_{RF} = 10$ MW and $P_{RF} = 20$ MW are shown. Compared with the situation with thermal T ions, quasilinear effects tend to enhance the tritium damping, which in turn reduces electron damping, essentially as a result of the large Doppler shift of the tritium resonance caused by increasing $T_{||}$. In the considered scenario, the central location of the ion cyclotron resonance tends to limit the quasilinear effects on the overall power split. When $P_{RF} = 10$ MW, the direct FW electron damping is reduced by ~ 0.3 MW, whereas this reduction amounts to 1 MW in the 20 MW case. In figure 12 the deposition profiles obtained in the DT(3 He) scenario for $P_{RF} = 10$ MW and $P_{RF} = 20$ MW after the

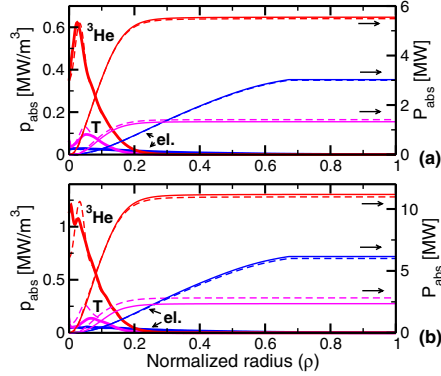


Figure 12. Power deposition profiles (left y-axis) and cumulative power (right y-axis) for $[0, \pi/2, \pi, 3\pi/2]$ phasing in the DT(^3He) scenario for a total absorbed power of (a) 10 MW; (b) 20 MW. The dashed lines show the power obtained when the helium-3 tail is not taken into account, whereas the solid lines show the result accounting for quasilinear effects on the heated ions. Only species absorbing more than 1% of the total absorbed power are shown.

Table 1. Partition (in per cent) of the wave power between the plasma species in the DT and DT(^3He) scenarios for a $[0, \pi/2, \pi, 3\pi/2]$ phasing with $P_{\text{RF}} = 10$ MW and $P_{\text{RF}} = 20$ MW. The two last lines show the power redistributed to electrons (1) in percentage of power damped by the heated ions, (2) in percentage of the total RF power, accounting for collisional and direct electron heating by the wave.

	DT (10 MW)	DT (20 MW)	DT(^3He) (10 MW)	DT(^3He) (20 MW)
Electrons	45.6	43.8	30.3	30.8
Tritium	50.5	52.2	13.3	11.8
$^3\text{Helium}$	—	—	55.5	55.9
Min \rightarrow el. (1)	34.7	45.2	16.9	38.6
Power to el. (2)	63.1	67.4	39.7	52.4

EVE/AQL iterations are shown. These calculations yield a total electron damping slightly increasing at larger P_{RF} compared with the thermal case. However, this effect is too small to be really of significance and falls within the range of uncertainty of the considered model and parameters. This scenario is thus found to be only marginally sensitive to quasilinear effects, which results from the fact that fundamental minority heating is less sensitive to the details of the distribution function than second harmonic damping [21]. In table 1, the obtained results in terms of power split are summarized. Also appearing in this table is the collisional redistribution of the power damped by fast ions to electrons computed with AQL. In the DT scenario results, about 2/3 of the total RF power heats electrons (through direct wave damping + collisions), whereas the DT(^3He) scenario yields at least about 50% ion damping even for a total RF power of 20 MW.

A side effect of the use of ICRF waves for plasma heating is the possibility of driving non-inductive current by direct electron damping of the FW, provided the antenna spectrum can be made toroidally asymmetric by adapting the inter-strap phasing. Superthermal tails may affect the driven current profile, essentially through the modification of the power split

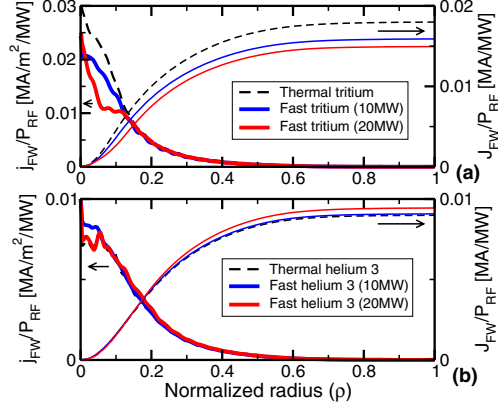


Figure 13. Driven current profile (left y-axis) and cumulative current (right y-axis) per absorbed MW for $[0, \pi/2, \pi, 3\pi/2]$ phasing when the fast ion effects are neglected (dashed) or incorporated for a total absorbed power of 10 or 20 MW (solid) in the (a) DT scenario; (b) DT(^3He) scenario.

between species. Figure 13 shows the profile of driven current when the $[0, \pi/2, \pi, 3\pi/2]$ phasing is used. In order to compare the results obtained for $P_{\text{RF}} = 10$ MW and $P_{\text{RF}} = 20$ MW, the driven current is normalized to P_{RF} . DT and DT(^3He) scenarios differ in the influence of quasilinear effects: whereas the tritium tail results in stronger ion absorption and thus lowers the amount of driven current level with increasing power in the former, the FWCD efficiency is only moderately changed by quasilinear effects in the latter, as a result of the characteristics of minority damping. In fact, we observe a slight increase in the FWCD efficiency at larger P_{RF} but this difference is quite small.

By reverting the phasing in the antenna straps, e.g. using $[0, -\pi/2, -\pi, -3\pi/2]$ instead of $[0, \pi/2, \pi, 3\pi/2]$, it is possible to drive counter-current with FWs, which may be desirable in terms of plasma scenario. However, the presence of a poloidal field induces an asymmetry between opposite phasings and makes it uncertain that the amount of driven current is the same as in the co-current direction, especially if the power split between plasma species is modified. In figure 14, the two phasings are compared in the case of the DT scenario. Although a minor difference appears in the power deposition and driven current profiles, the cumulative quantities show that ~ 300 kA of FWCD can be driven in either co- or counter-current by reverting the antenna phasing, without significantly affecting the power split, and thus the bulk heating properties of the considered scenario. The same conclusion holds for the DT(^3He) scenario although the latter is characterized by a lower FWCD efficiency, which allows one to drive a maximum ~ 200 kA with 20 MW of ICRF power, as shown in figure 15. We also note that the current profile is significantly more peaked in the DT scenario than in the DT(^3He) scenario, as a result of the lower per-pass damping, which has the consequence of improving the wave penetration and thus the direct electron damping near the plasma centre.

Alternatively to $[0, \pi/2, \pi, 3\pi/2]$, other phasings can be used to drive current. For instance, it is possible to pair poloidal

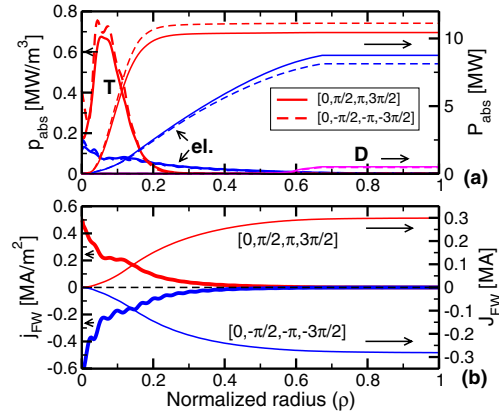


Figure 14. (a) Power absorbed by species for $[0, \pi/2, \pi, 3\pi/2]$ phasing (solid) and $[0, -\pi/2, -\pi, -3\pi/2]$ phasing (dashed) in the DT scenario. (b) Corresponding driven current for both phasings. Only species absorbing more than 1% of the total absorbed power (20 MW) are shown.

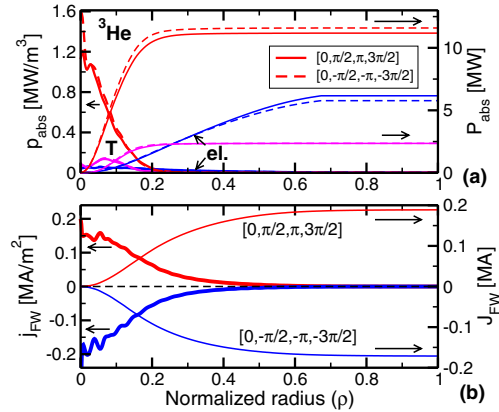


Figure 15. (a) Power absorbed by species for $[0, \pi/2, \pi, 3\pi/2]$ phasing (solid) and $[0, -\pi/2, -\pi, -3\pi/2]$ phasing (dashed) in the DT(^3He) scenario. (b) Total driven current for each phasing. Only species absorbing more than 1% of the total absorbed power (20 MW) are shown.

straps and use a $[0, 0, \pi/2, \pi/2]$ toroidal phasing, as done for instance in JET [2], a configuration sometimes referred to as ‘super-dipole’. In figure 16, we compare phasings $[0, 0, \pi/2, \pi/2]$ and $[0, 0, -\pi/2, -\pi/2]$ in the DT scenario. Compared with the $[0, \pi/2, \pi, 3\pi/2]$ phasing, super-dipole phasings are characterized by a lower averaged value of k_{\parallel} . The contribution of the poloidal field is thus markedly more important. We observe that a reversal of the antenna phasing does not yield the same current magnitude, as a result of the variation of electron damping (higher $\omega/k_{\parallel}v_{\text{th},e}$ tends to favour ion damping) and sensitivity of the current drive efficiency (higher $\omega/k_{\parallel}v_{\text{th},e}$ results in better FWCD). The driven current in the DT scenario is found to reach -400 kA in the counter-direction, but only half this magnitude in the co-current direction upon reverting the toroidal phasing.

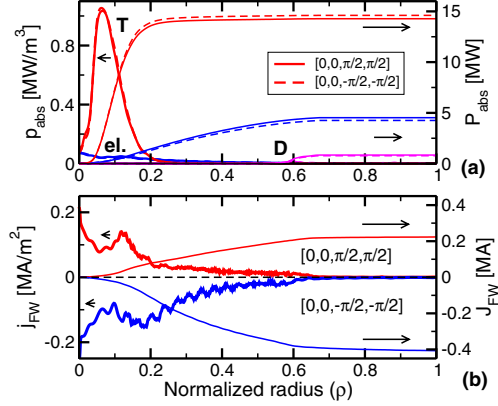


Figure 16. (a) Power absorbed by species for $[0, 0, \pi/2, \pi/2]$ phasing (solid) and $[0, 0, -\pi/2, -\pi/2]$ phasing (dashed) in the DT scenario. (b) Corresponding driven current for both phasings. Only species absorbing more than 1% of the total absorbed power (20 MW) are shown.

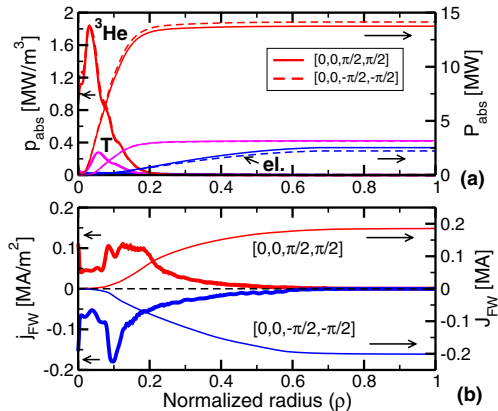


Figure 17. (a) Power absorbed by species for $[0, 0, \pi/2, \pi/2]$ phasing (solid) and $[0, 0, -\pi/2, -\pi/2]$ phasing (dashed) in the DT(^3He) scenario. (b) Total driven current for each phasing. Only species absorbing more than 1% of the total absorbed power (20 MW) are shown.

The same calculation has been performed for the DT(^3He) scenario. As shown in figure 17, in this case, reverting the toroidal phasing results in an essentially exact opposite driven current. It should be pointed out that the operation at low values of k_{\parallel} is experimentally challenging. Furthermore, the per-pass damping rate is comparatively lower than for dipole-like phasings, resulting in ‘choppier’ current profiles, reminiscent of deposition profiles obtained in low absorption ICRF scenarios.

In order to quantify the flexibility of the ITER ICRF system in terms of FWCD, it is interesting to perform a systematic study of various inter-strap phasings. In line with the procedure employed so far, for each toroidal phasing, EVE should be iterated with AQL until a steady-state distribution function is obtained, which is hardly practical

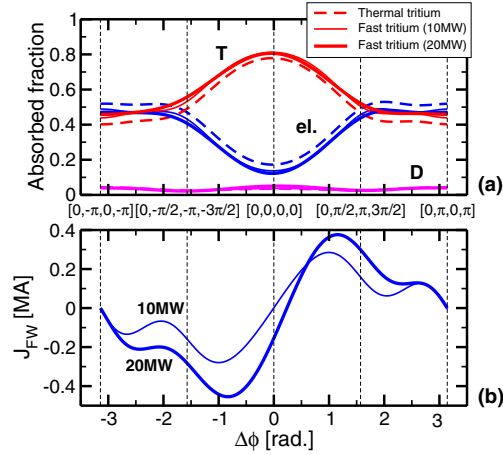


Figure 18. (a) Power fraction absorbed by species; (b) total driven current driven by FWs for antenna phasings in the ‘dipole’ configuration, for the DT scenario. The dashed curves show the result obtained when fuel ions are assumed to be thermal (top), whereas the solid curves show the result obtained when the superthermal tail is considered for a total absorbed power of 10 MW (thin line) or 20 MW (thick line). Only species absorbing more than 1% are shown.

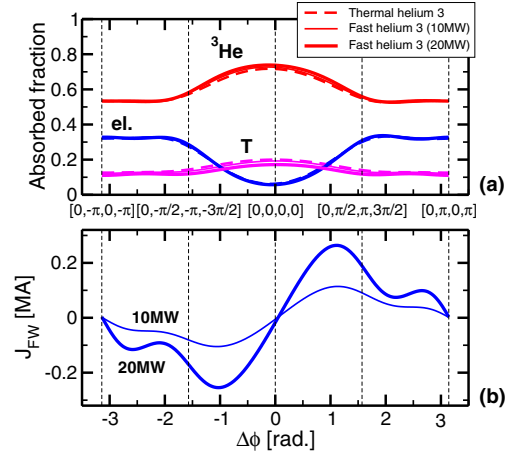


Figure 19. (a) Power fraction absorbed by species; (b) total driven current driven by FWs for antenna phasings in the ‘dipole’ configuration, for the DT(^3He) scenario. The dashed curves show the result obtained when fuel ions are assumed to be thermal (top), whereas the solid curves show the result obtained when the superthermal tail is considered for a total absorbed power of 10 MW (thin line) or 20 MW (thick line). Only species absorbing more than 1% are shown.

in terms of computational requirements. Furthermore, even though quasilinear effects have been found to be important, the final features of the heated species appear to be only weakly dependent on the toroidal phasing. Consequently, we have considered the individual solutions computed by EVE for $[0, \pi/2, \pi, 3\pi/2]$ phasing and recombined them for various dipole-like phasings, i.e. phasings of the type $[0, \Delta\phi/2, \Delta\phi, 3\Delta\phi/2]$ with $\Delta\phi$ varied between $-\pi$ and π . The result is shown in figure 18 for the DT scenario, and in figure 19 for the DT(^3He) scenario. In both cases, the calculation has been performed for $P_{\text{RF}} = 10$ MW and $P_{\text{RF}} = 20$ MW.

In both the DT and DT(^3He) cases, we observe that the $[0, \pm\pi/2, \pm\pi, \pm 3\pi/2]$ phasing is not quite optimal in terms of current drive efficiency. Phasings characterized by lower values of $\langle k_{\parallel} \rangle$ where $\langle \cdot \rangle$ denotes averaging over toroidal numbers allow one to drive more current, even though electron damping decreases. Another interesting effect is that in the DT scenario, even though the curve $J_{\text{FW}}(\Delta\phi)$ is approximately symmetrical in the case $P_{\text{RF}} = 10$ MW, it is not the case when the RF power is 20 MW since quasilinear effects distort the plasma response to individual toroidal numbers. Overall, we find that it is possible to expect up to 200 kA with 10 MW, and up to 400 kA with 20 MW in the DT case. However, a trade-off needs to be found between plasma heating (and ion tail generation) and current drive, since the power split is modified by the phasing in a rather significant way. In this respect, the DT(^3He) scenario is more robust, as shown in figure 19, since ^3He damping always dominates. However, we note that the magnitude of the driven current is approximately half the magnitude obtained in the DT scenario. This conclusion, in terms of FWCD efficiency, is summarized in figure 20 in which the raw efficiency, $J_{\text{FW}}/P_{\text{RF}}$, and the normalized efficiency

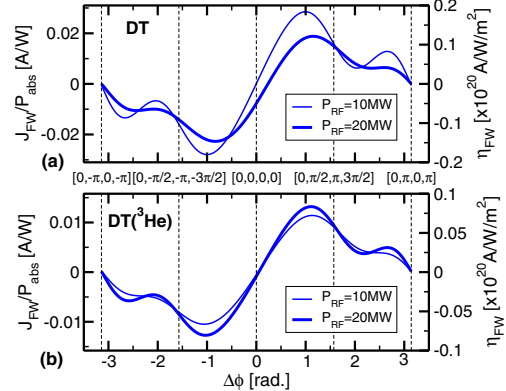


Figure 20. FWCD efficiency in (a) the DT scenario; (b) the DT(^3He) scenario, for phasings in the ‘dipole’ configuration. The right y-axis shows the corresponding normalized efficiency. Thin (respectively thick) curves correspond to the efficiency obtained with 10 MW (respectively 20 MW) absorbed power. The vertical dashed lines denote usual phasings.

$\eta_{\text{FW}} \equiv J_{\text{FW}}/P_{\text{RF}} \times R_0 \bar{n}_{e,20}$ versus toroidal phasing ($\bar{n}_{e,20}$ is the line-averaged electron density in units of 10^{20} m^{-3}) are shown. FWCD efficiencies of the order ~ 0.015 – 0.025 A W^{-1} are obtained in the DT scenario, corresponding to $\eta_{\text{FW}} \sim 0.1$ – $0.2 \text{ A W}^{-1} \text{ m}^{-3}$. In the DT(^3He) case, the sensitivity to the total absorbed power is weak, but the efficiency is also lower: $\sim 0.01 \text{ A W}^{-1}$, corresponding to $\eta_{\text{FW}} \sim 0.05 \text{ A W}^{-1} \text{ m}^{-3}$.

All of the simulations presented so far assume that the ICRF power is entirely coupled and absorbed by the plasma, accounting for multi-pass damping, but disregarding important

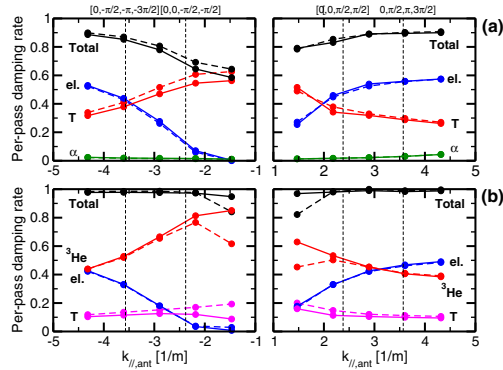


Figure 21. Single-pass damping rate predicted by METS when fuel ions are assumed to be thermal (dashed) or heated by ICRF waves (solid) versus k_{\parallel} at the antenna, when the toroidal spectrum is assumed to be single-valued. The two vertical dashed lines show peak values corresponding to the $[0, \pm\pi/2, \pm\pi, \pm3\pi/2]$ and $[0, 0, \pm\pi/2, \pm\pi/2]$ phasings. (a) DT scenario; (b) DT(^3He) scenario.

effects such as RF sheaths and parasitic edge losses. Although this problem is very difficult to address extensively [2, 25], it has been shown that the per-pass damping rate can be considered as a first indication of the overall quality of a given ICRF scenario [26]. For this study, the METS code [17, 18] has been modified to use the same input distribution functions as EVE, allowing one to estimate the power split between species and the per-pass damping rate. METS has been run for various values of the parallel wavenumber at the antenna ($k_{\parallel,\text{ant}}$), assuming the heated ions are thermal or accounting for quasilinear effects on the fuel temperature. The results are shown in figure 21. It should be noted that the code convergence was sometimes difficult to obtain at very low values of k_{\parallel} .

It clearly appears that the DT(^3He) scenario is characterized by a higher per-pass damping rate than the DT scenario, especially when quasilinear effects are accounted for. We note also that the plasma response is not symmetrical with respect to k_{\parallel} owing to the presence of the poloidal field. In agreement with EVE/AQL, the effects of superthermal tail, although necessary to describe the scenario accurately, have a rather limited impact, except for $|k_{\parallel,\text{ant}}| \lesssim 2 \text{ m}^{-1}$. In this figure the average values of $k_{\parallel,\text{ant}}$ characterizing the dipole and super-dipole phasings discussed above ($\langle k_{\parallel,\text{ant}} \rangle = \pm 3.6 \text{ m}^{-1}$ for dipole phasing, $\langle k_{\parallel,\text{ant}} \rangle = \pm 2.4 \text{ m}^{-1}$ for super-dipole phasing) also appear. The latter is characterized by a lower electron damping, and a lower per-pass efficiency, especially in the DT scenario.

4. Conclusions

In this paper, a detailed comparison of two ICRF scenarios applicable to the activated phase of ITER has been made using the EVE full-wave code, associated with the AQL module to describe the fast ion tail development in a simplified fashion. The corresponding plasmas only differ in that the deuterium–tritium mixture is supplemented with a small

fraction of helium-3 in the latter. However, from a ICRF point of view, they exhibit significant quantitative differences: firstly, the different dominant damping mechanism results in differences in the fast ion tail development and associated collisional relaxation. In particular, the DT scenario is characterized by dominant electron heating (by combined direct wave absorption and collisional heating), whereas the DT(^3He) scenario results in at least half of the RF power on background ions. Even though quasilinear effects have been found to be significant, both scenarios exhibit a rather limited sensitivity to details of the heated distribution function, especially the DT(^3He) case. FWCD performance has been evaluated for various phasings and it is found that the ICRF system envisioned for ITER allows one to drive non-negligible central current with only minor impact on the heating properties of the RF waves. The DT case is characterized by the highest maximum FWCD efficiency ($\eta_{\text{FW}} \sim 0.1\text{--}0.2 \text{ A W}^{-1} \text{ m}^{-3}$), whereas we obtain $\eta_{\text{FW}} \sim 0.05 \text{ A W}^{-1} \text{ m}^{-3}$ in the DT(^3He) case. On the other hand, calculations performed with the METS code have shown that the DT(^3He) case is characterized by a larger single-pass damping rate, associated with a relative insensitivity to both the toroidal phasing and quasilinear effects. It is thus expected that the latter will be more robust from an operational standpoint.

Acknowledgments

This work, supported by the European Communities under the contract of Association between EURATOM and CEA, was carried out within the framework of the European Fusion Development Agreement. The views and opinions expressed herein do not necessarily reflect those of the European Commission. The presented simulations have been performed using HPC resources from GENCI-CCRT (Grant 2012-t2012056088) and HPC-FF.

Appendix. The AQL module

The AQL is a quasilinear module which complements the code EVE. It is aimed at estimating the quasilinear response of the heated ions to the ICRF power, accounting for collisions with the background plasma. Although EVE can be coupled to much more comprehensive FP codes, AQL is a fast module which provides an interface between the wave calculation on the one hand, and the description of the heated ion distribution function and its subsequent relaxation on thermal particles on the other hand.

The orbit-averaged FP equation for the heated ion is written as

$$\frac{\partial f_i}{\partial t} = \langle \mathcal{C}(f_i) \rangle + \langle \mathcal{D}_w(f_i) \rangle, \quad (\text{A.1})$$

where \mathcal{C} is the collision operator and \mathcal{D}_w is the wave quasilinear operator.

On every magnetic surface ψ , it is assumed that the interaction takes place at poloidal angles θ_{res} , determined by the maximum of the 2D power deposition profile $p_i(\psi, \theta)$ computed by EVE, when θ is varied between 0 and π (above midplane) and when θ is varied between π and 2π (below

midplane). For a given interaction angle $\theta = \theta_{\text{res}}$, we thus obtain a local FP equation with the collision term

$$\mathcal{C}(f_i) = \frac{1}{v^2} \left[\frac{\partial}{\partial v} v^2 \left(D_{vv} \frac{\partial f_i}{\partial v} \right) - \frac{\partial}{\partial v} v^2 F_v f_i \right] + \frac{1}{v^2} \left[\frac{\partial}{\partial \lambda} D_{\lambda\lambda} \frac{\partial f_i}{\partial \lambda} \right]. \quad (\text{A.2})$$

$\lambda \equiv v_{\parallel}/v$ where v_{\parallel} is the parallel velocity at $\theta = \theta_{\text{res}}$.

$$D_{vv} \equiv \sum_{\beta} \frac{\Gamma^{i/\beta}}{2v} \Psi(u_{\beta}), \quad (\text{A.3})$$

$$F_v \equiv - \sum_{\beta} \frac{\Gamma^{i/\beta}}{v^2} \frac{m_i}{m_{\beta}} \Psi(u_{\beta}), \quad (\text{A.4})$$

$$D_{\lambda\lambda} \equiv \sum_{\beta} \frac{\Gamma^{i/\beta}}{2v} (1 - \lambda^2) \Theta(u_{\beta}). \quad (\text{A.5})$$

In these expressions, the sum is to be taken over background species and u_{β} is the velocity normalized to the thermal velocity of species β . The expressions for $\Gamma^{i/\beta}$, Ψ and Θ can be found, e.g., in [23].

The main contribution to the wave quasilinear operator is

$$\mathcal{D}_w(f_i) = \frac{1}{v_{\perp}} \frac{\partial}{\partial v_{\perp}} v_{\perp} D_{v_{\perp}v_{\perp}}^{(QL)} \frac{\partial f_i}{\partial v_{\perp}}, \quad (\text{A.6})$$

with

$$D_{v_{\perp}v_{\perp}}^{(QL)} = D_0 \sum_{\theta_{\text{res}}} |E_+ J_{p-1}(k_{\perp} v_{\perp} / \Omega_{ci}) + E_- J_{p+1}(k_{\perp} v_{\perp} / \Omega_{ci})|^2. \quad (\text{A.7})$$

where $E_+(\psi, \theta)$ (respectively $E_-(\psi, \theta)$) corresponds to the left-handed (respectively right-handed) electric field, which is directly provided by EVE. J_n is the n th order Bessel function of the first kind. p is the harmonic number of the cyclotron resonance, i.e. $p = 1$ for minority heating and $p = 2$ for harmonic damping. In the previous expression, the local value of $\Omega_{ci} \equiv \Omega_{ci}(\psi, \theta_{\text{res}})$ is used. k_{\perp} is the perpendicular wavenumber magnitude, which is deduced from the finite Larmor radius (FLR) FW dispersion relation evaluated using the local plasma parameters, and approximating the parallel wavenumber as $k_{\parallel} \approx n/R(\psi, \theta_{\text{res}})$. D_0 is a parameter which is adjusted so as to equate the quasilinear power absorption profile, given by

$$P_{\text{QL}} \equiv \frac{m_i}{2} \int d^3v v^2 \mathcal{D}_w(f_i), \quad (\text{A.8})$$

and the power profile directly computed by EVE [14] at all times, until convergence on D_0 is achieved. Afterwards the solution is introduced in EVE. This implies an iterative process where EVE and AQL are run successively until the distribution function does not evolve anymore. In practice, for the cases presented in this paper, this occurs in five iterations or less. To solve equation (A.1), the distribution function is projected onto an orthogonal polynomial basis as follows:

$$f_i(v, \lambda, t) = \sum_{m=0}^L f_{i,m}(v, t) P_m(\lambda), \quad (\text{A.9})$$

where m is the degree of the polynomials. This decomposition allows one to decouple the variables v and λ and is, in principle, exact as long as the number of polynomials $L \rightarrow \infty$. Nevertheless, the practical resolution of the FP equation requires a finite number of polynomials and choosing an arbitrary $L < \infty$. In this paper $L = 20$. This choice makes the numerical resolution easier since the initial 2D problem in the velocity space is reduced to a 1D problem. The collision and diffusion operators become

$$\mathcal{C}(f_i) = \frac{1}{v^2} \frac{\partial}{\partial v} v^2 \left(D_{vv} \frac{\partial f_{i,m}}{\partial v} P_m - F_v f_{i,m} P_m \right) + \frac{1}{v^2} \frac{\partial}{\partial \lambda} D_{\lambda\lambda} f_{i,m} \frac{dP_m}{d\lambda} \quad (\text{A.10})$$

$$\mathcal{D}_w(f_i) = \frac{1 - \lambda^2}{v^2} \frac{\partial}{\partial v} \left[v D_{v_{\perp}v_{\perp}}^{(QL)} \left(v \frac{\partial f_{i,m}}{\partial v} P_m - \lambda f_{i,m} \frac{dP_m}{d\lambda} \right) \right] - \frac{1}{v^2} \frac{\partial}{\partial \lambda} \left[\lambda (1 - \lambda^2) D_{v_{\perp}v_{\perp}}^{(QL)} \left(v \frac{\partial f_{i,m}}{\partial v} P_m - \lambda f_{i,m} \frac{dP_m}{d\lambda} \right) \right]. \quad (\text{A.11})$$

We can then multiply these two operators by P_n for $n = 0, \dots, L$, integrate between $\lambda = -1$ and $\lambda = 1$ and separate the derivatives following their order, so that we can write the following set of partial differential equations:

$$\left\{ \begin{aligned} \frac{\partial f_{i,m}}{\partial t} &= \alpha_{m,n}^{(2)}(v) \frac{\partial^2 f_{i,m}}{\partial v^2} + \alpha_{m,n}^{(1)}(v) \frac{\partial f_{i,m}}{\partial v} \\ &+ \alpha_{m,n}^{(0)}(v) f_{i,m} \end{aligned} \right\}_{n=0, \dots, L}, \quad (\text{A.12})$$

where the α coefficients are defined as

$$\alpha_{m,n}^{(2)}(v) = D_{vv} \|P_m\|^2 \delta_{mn} + D_{00,m,n}(v) \quad (\text{A.13})$$

$$\alpha_{m,n}^{(1)}(v) = \left(\frac{1}{v^2} \frac{d}{dv} (v^2 D_{vv}) - F_v \right) \|P_n\|^2 \delta_{mn} + \frac{1}{v^2} \frac{d}{dv} \times (v^2 D_{00,m,n}(v)) - \frac{1}{v} (D_{10,m,n}(v) - D_{01,m,n}(v)) \quad (\text{A.14})$$

$$\alpha_{m,n}^{(0)}(v) = \frac{1}{v^2} \left[\left\langle P_n, \frac{\partial}{\partial \lambda} \left(D_{\lambda\lambda} \frac{dP_m}{d\lambda} \right) \right\rangle_{\lambda} - \frac{d}{dv} \left(v^2 F_v \|P_n\|^2 \delta_{mn} + v D_{10,m,n}(v) \right) - D_{11,m,n}(v) \right], \quad (\text{A.15})$$

where $\langle a, b \rangle_{\lambda} \equiv \int_{-1}^1 d\lambda (ab)$ and the following integrated diffusion coefficients are defined:

$$D_{00,m,n}(v) = \int_{-1}^1 d\lambda (1 - \lambda^2) D_{v_{\perp}v_{\perp}}^{(QL)} P_m P_n \quad (\text{A.16})$$

$$D_{10,m,n}(v) = \int_{-1}^1 d\lambda \lambda (1 - \lambda^2) D_{v_{\perp}v_{\perp}}^{(QL)} \frac{dP_m}{d\lambda} P_n \quad (\text{A.17})$$

$$D_{01,m,n}(v) = \int_{-1}^1 d\lambda \lambda (1 - \lambda^2) D_{v_{\perp}v_{\perp}}^{(QL)} P_m \frac{dP_n}{d\lambda} \quad (\text{A.18})$$

$$D_{11,m,n}(v) = \int_{-1}^1 d\lambda \lambda^2 (1 - \lambda^2) D_{v_{\perp}v_{\perp}}^{(QL)} \frac{dP_m}{d\lambda} \frac{dP_n}{d\lambda}. \quad (\text{A.19})$$

References

- [1] Start D.F.H. *et al* 1998 *Phys. Rev. Lett.* **80** 4681
- [2] Lerche E. *et al* and JET EFDA Contributors 2011 *Plasma Phys. Control. Fusion* **53** 124019
- [3] Fisch N.J. 1987 *Rev. Mod. Phys.* **59** 175
- [4] Wort D.J.H. 1971 *Plasma Phys.* **31** 258
- [5] Chiu S.C., Chan V.S., Harvey R.W. and Porkolab M. 1989 *Nucl. Fusion* **29** 2175
- [6] Petty C.C. *et al* 1995 *Nucl. Fusion* **35** 773
- [7] Petty C.C. *et al* 1999 *Nucl. Fusion* **39** 1421
- [8] Hellsten T. *et al* and JET-EFDA Contributors 2005 *Nucl. Fusion* **45** 706
- [9] Becoulet A. 1996 *Plasma Phys. Control. Fusion* **38** A1
- [10] Schneider M., Eriksson L.-G., Basiuk V. and Imbeaux F. 2005 *Plasma Phys. Control. Fusion* **47** 2087
- [11] Garcia J., Giruzzi G., Artaud J.-F., Basiuk V., Decker J., Imbeaux F., Peysson Y. and Schneider M. 2008 *Phys. Rev. Lett.* **100** 255004
- [12] Jaeger E.F. *et al* 2008 *Phys. Plasmas* **15** 072513
- [13] Bergeaud V., Eriksson L.-G. and Start D.F.H. 2000 *Nucl. Fusion* **40** 35
- [14] Dumont R.J. 2009 *Nucl. Fusion* **49** 075033
- [15] Ehst D.A. and Karney C.F.F. 1991 *Nucl. Fusion* **31** 1933
- [16] Bilato R., Brambilla M., Pavlenko I. and Meo F. 2002 *Nucl. Fusion* **42** 1085
- [17] Smithe D.N., Phillips C.K., Hosea J.C., Majeski R.P. and Wilson J.R. 1997 *Proc. 12th Topical Conf. on Radio Frequency Power in Plasmas (Savannah, GA, 1997)* ed P.M. Ryan and T. Intrator (New York: American Institute of Physics) p 367 (doi:10.1063/1.53349)
- [18] Dumont R.J., Phillips C.K. and Smithe D.N. 2005 *Phys. Plasmas* **12** 042508
- [19] Budny R.V. *et al* and members of the ITPA-IOS 2012 *Nucl. Fusion* **52** 023023
- [20] Lamalle P.U., Messiaen A., Dumortier P., Durodié F., Evrard M., Louche F. and Vervier M. 2007 *Final Report on Contract EFDA/05-1334*, Laboratory Report no 129, Laboratory for Plasma Physics, Royal Military Academy, Brussels, Belgium
- [21] Mantsinen M.J. *et al* and contributors to the EFDA-JET Workprogramme 2002 *Plasma Phys. Control. Fusion* **44** 1521
- [22] Mayoral M.-L. *et al* and JET EFDA contributors 2006 *Nucl. Fusion* **46** S550
- [23] Brambilla M. and Bilato R. 2009 *Nucl. Fusion* **49** 085004
- [24] Bécoulet A., Gambier D.J. and Samain A. 1991 *Phys. Fluids B* **3** 137
- [25] Myra J.R., D'Ippolito D.A., Russell D.A., Berry L.A., Jaeger E.F. and Carter M.D. 2006 *Nucl. Fusion* **46** S455
- [26] Lerche E., Bobkov V., Jacquet P., Mayoral M.-L., Messiaen A., Monakhov I., Ongena J., Telesca G., Van Eester D., Weynants R.R. and JET-EFDA contributors 2009 *Proc. 18th Topical Conf. on Radio Frequency Power in Plasmas (Gent, Belgium, 2009); AIP Conf. Proc.* **1187** 93

Interplay between fast ions and turbulence in magnetic fusion plasmas

R J Dumont¹, D Zarzoso^{1,2}, Y Sarazin¹, X Garbet¹, A Strugarek^{1,3},
J Abiteboul^{1,2}, T Cartier-Michaud¹, G Dif-Pradalier¹, Ph Ghendrih¹,
J-B Girardo¹, V Grandgirard¹, G Latu¹, C Passeron¹ and O Thomine¹

¹ CEA, IRFM, F-13108 Saint-Paul-lez-Durance, France

² Max-Planck-Institut für Plasmaphysik, EURATOM Association, Garching, Germany

³ DSM/IRFU, CEA/Saclay, Gif-sur-Yvette, France

Received 4 July 2013, in final form 10 September 2013

Published 28 November 2013

Online at stacks.iop.org/PFCF/55/124012

Abstract

Evidence for the impact of energetic particles (EPs) on turbulence is given in this paper. Firstly, the excitation of electrostatic instabilities in linear gyrokinetic simulations performed with the global GYSELA code by introducing distribution functions typical of fast ions in tokamak plasmas is presented. The obtained mode is unambiguously characterized as an EGAM, i.e. a geodesic acoustic mode (GAM) excited by EPs. The influence of EGAMs on turbulence and associated transport is then analyzed by implementing a source adapted to the inclusion of fast particle populations in non-linear simulations. This source successfully excites EGAMs in the presence of turbulence, which leads to a drastic reduction of the turbulent transport. However, this reduction is only transient; it is followed by an increase of the turbulent activity, characterized by a complex interaction between the EGAMs and the turbulence. In the subsequent steady-state regime, turbulent transport appears to be modulated at the EGAM frequency.

(Some figures may appear in colour only in the online journal)

1. Introduction

Resulting either from the nuclear fusion reactions occurring in the plasma or from external sources, such as ion cyclotron resonance frequency (ICRF) heating and neutral beam injection (NBI) systems, energetic ions are prevalent in modern and future fusion devices. In these experiments, plasma turbulence has also been identified as a major determinant of the energy confinement time and hence of the discharge performance as a whole. In-depth investigation of the potential interactions between the turbulence and energetic particles (EPs) is therefore essential toward reliable performance predictions in next-step fusion reactors.

The direct impact of turbulence on EPs has been found to be limited [1]. The influence of EPs on turbulence, on the other hand, has received relatively little attention so far. The possibility of controlling, to some extent, the creation and features of the fast ion populations opens the possibility of a potential action on an intrinsically self-regulated system involving turbulence, mean flows, zonal flows [2] and also higher frequency phenomena, such as geodesic acoustic modes

(GAMs) [3]. Although the latter have an efficiency presumably smaller than stationary or low frequency flow shear generation mechanisms [4], they have been shown to play a central role in the L–H transition, which is believed to involve the same actors in the plasma edge [5].

The reason why GAMs are only observed in the plasma edge, however, is because they are subject to strong Landau damping and therefore cannot impact core turbulence in a stationary fashion. The possibility of overcoming this limitation by exciting similar modes with fast particles therefore represents an appealing prospect. In this case, the mode is usually referred to as an EGAM; it has been predicted theoretically [6, 7] and has unambiguously been observed in experiments [8, 9]. Recently, detailed numerical studies of the EGAMs properties [10] and their influence on turbulence [11] have been conducted in the framework of gyrokinetic simulations. Another advantage of EGAMs is that unlike GAMs, which are non-linearly generated by the turbulence itself, the EP sources can be tuned to some extent, opening the possibility of turbulence control in the plasma core.

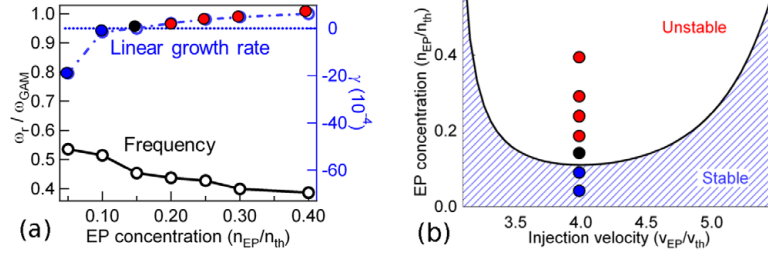


Figure 1. (a) Normalized frequency (left y-axis) and linear damping rate (right y-axis) of the ϕ_{10} oscillation versus fast ion concentration. (b) Dependence of the linear threshold versus injection velocity and fast particle concentration. The points corresponding to $v_0 = 4$ and shown in (a) are reported.

2. EGAMs in gyrokinetic simulations

In this paper, we present flux-driven simulations performed with the GYSELA code [12, 13]. The standard gyrokinetic equation for the full- f ion gyro-centre distribution function F can be written as

$$\frac{\partial F}{\partial t} + \mathbf{v} \cdot \nabla F + \dot{v}_{\parallel} \frac{\partial F}{\partial v_{\parallel}} = \mathcal{C}(F) + S_{\text{th}} + S_{\text{EP}}, \quad (1)$$

where $\mathcal{C}(F)$ represents the collision operator, whose features are extensively discussed in [13]. S_{th} is the thermal source and S_{EP} is the source aimed at introducing fast EPs in the simulations. The electrostatic limit is considered and electrons are assumed adiabatic. The magnetic topology consists of concentric toroidal magnetic flux surfaces with circular poloidal cross-sections. In this work, the time is normalized with respect to $\omega_c^{-1} \equiv m_i/eB_0$ with e the elementary charge, m_i the ion mass and B_0 the confining magnetic field on the axis. Temperatures (respectively, velocities) are normalized to the bulk temperature T_i (respectively, bulk thermal velocity v_{th}).

In order to check the possibility of observing EP instabilities in gyrokinetic simulations and also characterize them as extensively as possible, linear calculations without turbulence have been performed. This has been done by setting $\mathcal{C}(F) + S_{\text{th}} + S_{\text{EP}} = 0$ in equation (1) and assuming flat equilibrium profiles to make sure that the ITG turbulence is not excited. In this case, the initial equilibrium distribution function is written as $F(t=0) \equiv F_{\text{eq}}(1 + \varepsilon(r) \sin(\theta))$ with θ the poloidal angle and $\varepsilon(r)$ the amplitude of the initial perturbation. F_{eq} is made of the sum of a thermal and a fast particle contribution, i.e. $F_{\text{eq}} \equiv F_{\text{eq},i} + F_{\text{eq},h}$ with $F_{\text{eq},i}$ a Maxwellian characterized by the equilibrium density n_i and the temperature T_i . $F_{\text{eq},h}$ is a bump-on-tail distribution, which is written as

$$F_{\text{eq},h} \equiv F_{\text{M},h} \exp\left(-\frac{v_{\parallel}^2}{2T_h}\right) \cosh\left(\frac{v_0 v_{\parallel}}{T_h}\right), \quad (2)$$

where $F_{\text{M},h}$ is a Maxwellian characterized by the density n_h and the temperature T_h . v_{\parallel} is the parallel velocity and v_0 is representative of the excited parallel velocity. Locally, this distribution function may exhibit a positive slope with respect to energy, i.e. $\partial F/\partial E > 0$, which is a necessary condition for the mode excitation.

It has been predicted that EGAMs are unstable only when the fast ion density exceeds a given threshold [6, 10]. A scan in the energetic ion density has therefore been conducted with GYSELA by varying the fast ion concentration (n_h) in the model distribution function (equation (2)). The other parameters are $T_h = 1$ and $v_0 = 4$. From the calculation result, $\Im(\phi_{10})$, the steady-state oscillation of the $(m, n) = (1, 0)$ component of the electrostatic potential ϕ representative of the EGAM, is Fourier analyzed in time. This yields the mode frequency ω . The linear growth rate, γ , is deduced from the time evolution. The scan results are shown in figure 1(a).

In the presence of EPs, an oscillation in ϕ_{10} is systematically observed at $\omega \sim 0.5\omega_{\text{GAM}}$, including below the linear threshold. It is worthwhile mentioning that a peak at $\omega = \omega_{\text{EGAM}}$ is also apparent on other Fourier components as a result of mode coupling in toroidal geometry, but it is systematically most pronounced on $\Im(\phi_{10})$, viz. the up-down asymmetric part of ϕ , as expected for an EGAM. The frequency (respectively, growth rate) decreases (respectively, increases) with the fast ion concentration. These results are consistent with theoretical predictions [6] regarding EGAMs. In order to further characterize the observed oscillation, the obtained results are compared to a theoretical model derived in [10]. In this reference, the stability diagrams of EGAMs for two model distribution functions and various parameters are established. In figure 1, the stability diagram corresponding to the distribution function given by equation (2) with $T_h = 1$ is shown. The simulation points appearing in figure 1(a) with $v_0 = 4$, are reported in this diagram and show that the threshold observed in the numerical simulations is in good agreement with the theoretical prediction. These results point to the successful excitation of EGAMs by fast ions in GYSELA.

3. Turbulent simulations in the presence of EPs

To analyze the interaction between fast ions and turbulence mediated by EGAMs, it is necessary to excite the mode in the ambient turbulence. Since GYSELA simulations are flux-driven and account for collisions, the procedure discussed previously for linear simulations cannot be applied. Indeed, any initial distribution function will rapidly thermalize and the EGAMs drive ($\partial F/\partial E > 0$) will vanish as soon as the system relaxes toward equilibrium. A source aimed at creating fast particles

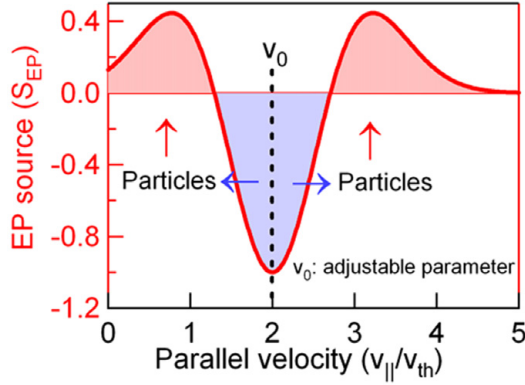


Figure 2. Schematic representation of the source of an EP versus parallel velocity for $\bar{v}_0 = 2$ and $\bar{T}_{\perp,s} = 0.5$.

has therefore been implemented in GYSELA. This bears some resemblance to actual experiments in which ICRF sources or neutral beam injectors are used to heat the plasma by injecting energy. It is worthwhile mentioning that these sources also inject other fluid moments as well, such as momentum or vorticity into the discharge. In the framework of this study, however, it is desirable to separate the various effects; the source is therefore designed so as to inject only energy in the parallel direction. This is done by using the following form [15] for S_{EP} (see equation (1))

$$S_{EP} = S_0(r, t) \{ \mathcal{S}_{\parallel}(\bar{v}_{\parallel} + \bar{v}_0) + \mathcal{S}_{\parallel}(\bar{v}_{\parallel} - \bar{v}_0) \} e^{-\bar{\mu}B}. \quad (3)$$

In the previous expression, $\bar{v}_{\parallel} \equiv v_{\parallel}/\sqrt{2T_{\perp,s}}$ is the parallel injection velocity and $\bar{v}_{\parallel} \equiv v_{\parallel}/\sqrt{2T_{\parallel,s}}$. Both are normalized with respect to parallel temperature $T_{\parallel,s}$, characterizing the source. $\bar{\mu}$ is the magnetic moment, normalized to the transverse temperature of the source $T_{\perp,s}$, which is set to 1 in these simulations. The symmetry of this form with respect to v_{\parallel} ensures that the constraint of zero momentum injection is fulfilled. In figure 2(a), a schematic representation of the source effect is shown versus the parallel energy for $\bar{v}_0 = 2$ and $\bar{T}_{\perp,s} = 0.5$. The source has the effect of pumping particles around \bar{v}_0 , either increasing or decreasing their parallel velocity to maintain a constant density.

A difficulty arising when assessing the effect of EGAMs on turbulence is to clearly isolate this effect when comparing simulations with or without the modes. A possibility would be to simply set S_{EP} to zero in a reference simulation and to a finite value in a simulation with EGAMs, but the obtained results would differ in the total injected power. Consequently, the ITG turbulence would have differing characteristics regardless of EGAMs; so a quantitative assessment of the effect of the mode would be quite complicated. The procedure employed in this study is thus to compare two simulations with the fast particle source switched on, but with $\bar{v}_0 = 0$, $\bar{T}_{\perp,s} = 1$ on the one hand and $\bar{v}_0 = 2$, $\bar{T}_{\perp,s} = 0.5$ on the other hand. These conditions ensure that the total injected power is rigorously the same in both cases. However, in the first one, the source

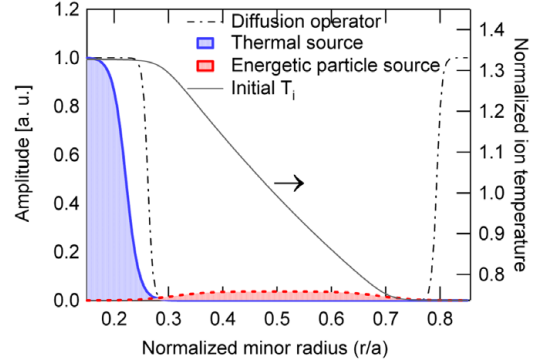


Figure 3. Radial profiles of the thermal source (shaded blue area), the EP source (shaded red area), the ion temperature (solid black line) and the diffusive regions in the boundary of the simulation box.

does not induce a positive slope in the distribution function. As expected, no EGAMs are observed in the simulation. Although the EP source is used in both situations, the first case ($\bar{v}_0 = 0$) will hereinafter be referred to as ‘without EPs’, whereas the second case ($\bar{v}_0 = 2$) will be deemed ‘with EPs’.

Two such simulations are compared, using the same thermal source with an injected power of 4 MW. The collisionality is $\nu_* = 0.02$ (banana regime) and the safety factor q profile is parabolic with a relatively low magnetic shear ($0 < s < 0.4$), such that $q \approx 2.7$ at the mid-radius. The normalized Larmor radius is $\rho_* = 1/150$. The initial density and temperature profiles are characterized by $R/L_n = 2.2$ and $R/L_T = 6.5$ respectively, with R the major radius and L_n and L_T the gradient lengths. Since there is no particle transport, L_n remains constant. Both simulations are strictly identical in the time window $t < t_{\text{init}}$, during which only the thermal source is used. At $t = t_{\text{init}}$, turbulence has reached a statistical steady state; the fast particle source is switched on, leading to an additional input power of 2 MW. The radial profiles of the thermal and EP sources are represented in figure 3. Whereas the thermal source is peaked and localized only in the inner radial region, the EP source spreads over an extended region to minimize its direct impact on the temperature profile. The initial temperature profile and the diffusive boundary regions are plotted in the same figure; in which artificial diffusion and increased collisionality are introduced in order to damp turbulence and regularize the distribution function in the vicinity of the radial simulation boundaries [13].

Firstly, the ability of the EP source at inverting the distribution function and potentially excite EGAMs, is checked by plotting $\partial F/\partial v_{\parallel}$ at the resonant velocity $v_{\parallel,\text{res}} = qR\omega_{\text{GAM}}$ in figure 4.

We observe that after the EP source switch-on, the distribution function is reversed in the outer region $\rho \gtrsim 0.5$. In order to determine whether EGAMs are excited, we compare the frequency spectrum of $\Im(\phi_{1,0})$ in both situations. The result is shown in figure 5. In the presence of fast particles, a clear peak is observed at $\omega \approx 0.4\omega_{\text{GAM}}$, corresponding

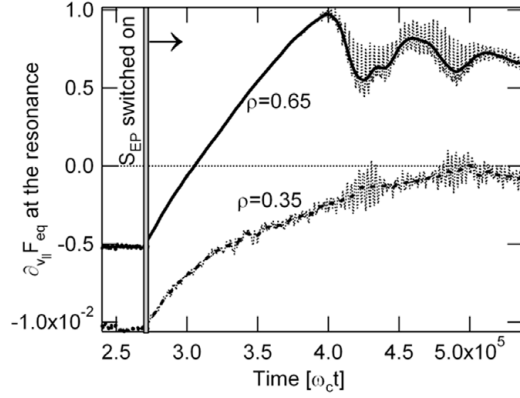


Figure 4. Time evolution of the derivative of the distribution function at the EGAM resonant velocity.

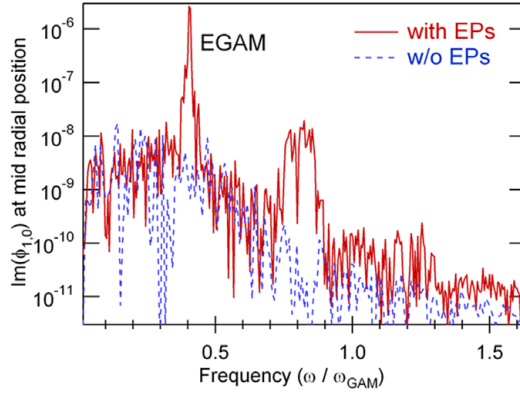


Figure 5. Amplitude of $\Im(\phi_{10})$ in the presence (red line) and in the absence of fast particles (blue, dotted line) (see [11]).

to the EGAM frequency ω_{EGAM} already observed in linear simulations. A secondary lower peak is observed around the harmonic frequency $\omega = 2\omega_{EGAM}$, which we attribute to the resulting non-linear wave–wave interaction. Another observation is that the EGAM frequency is clearly embedded in the turbulent spectrum. This has the consequence that the interaction between EGAMs and turbulence is potentially strong, but also precludes the use of simple models based on scale separation assumptions to investigate it in detail. Interestingly, we note in figure 4 that the distribution function slope remains negative at inner radii ($\rho = 0.35$ in the figure) but EGAMs are nevertheless observed at these positions, despite the fact that they are linearly stable. This underlines the need for a global code, with no separation between equilibrium and fluctuating quantities, to study these phenomena. Regular GAMs are also systematically observed in the initial phase of the simulations but they are damped, as discussed in [14]; therefore, they are not likely to play any significant role in regulating the turbulence in the plasma core.

A relevant quantity to characterize the turbulent transport is the thermal diffusivity $\chi_{E \times B}$, which is governed by

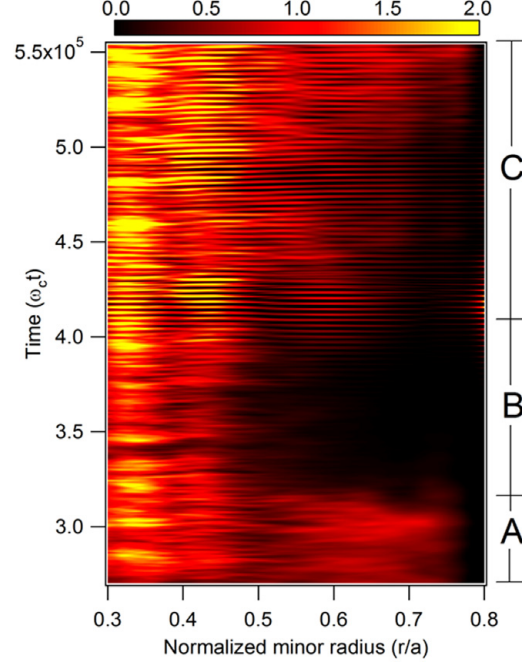


Figure 6. 2D representation of the $E \times B$ heat diffusivity versus normalized radius and time [11], showing the three phases discussed in the article.

fluctuations of the radial component of the $E \times B$ drift velocity v_{Er}

$$\chi_{E \times B} \approx -\frac{Q_{E \times B}}{n_i \nabla_r T}, \quad (4)$$

where $Q_{E \times B} = \langle v_{Er} p \rangle$ is the radial heat flux associated with v_{Er} and p is the pressure. These quantities are directly available from the simulations.

In figure 6, $\chi_{E \times B}$ is shown versus the time and minor radius. Three phases, denoted A, B and C, are visible: (A) the EP source is applied to an established steady-state turbulent regime, (B) a transport barrier develops and (C) EGAMs and the turbulence coexist and interact with each other in a non-trivial fashion.

In order to gain more insight into the turbulent transport in these simulations, figure 7 shows the evolution of $|\delta\phi|^2$ and $\chi_{E \times B}$ versus time, averaged over region $0.5 < \rho < 0.8$. In order to separate the effect of EGAMs and turbulence, the contribution of axisymmetric modes ($n = 0$) and non-axisymmetric modes ($n \neq 0$) are shown separately.

Figure 7 shows that EGAMs only appear near the end of phase B. In phase C, they are observed to coexist with non-axisymmetric contributions to the electrostatic potential with similar magnitudes. After the EP source has been switched on, the turbulent diffusivity is found to drop substantially, as a consequence of a large reduction of the ITG activity. This is attributed to the depletion of the resonant particles driving the ITG instability, directly caused by the source when

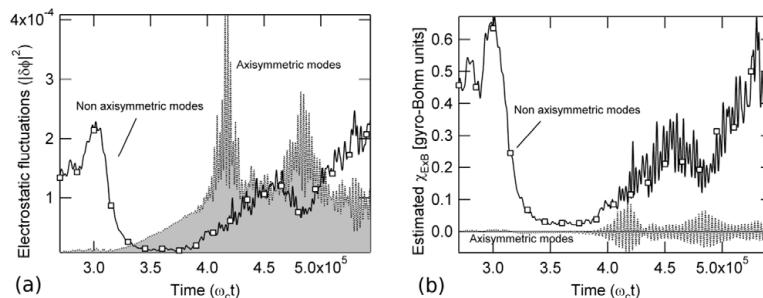


Figure 7. Contribution of $n = 0$ and $n \neq 0$ modes to the time evolution of (a) the electrostatic potential fluctuations and (b) the turbulent diffusivity in the presence of EPs.

$\bar{v}_0 = 2$. Whether this effect is coincidental and results from this particular choice of simulation parameters or is the signature of a more general mechanism related to external heating of fusion plasmas, remains to be firmly established. We also note that other mechanisms, such as a direct effect of the source anisotropy, cannot be excluded [16]. In any case, this drastic reduction of the turbulent transport is only transient; $\chi_{E \times B}$ increases to reach a level comparable to the turbulent diffusivity prior to the application of the EP source. We note, however, that the contribution of $n = 0$ modes to the heat diffusivity remains negligible during the whole simulation, indicating that the transport increase is not directly caused by the EGAMs.

Interestingly, in phase C, a spectral analysis shows that the turbulent diffusivity itself is modulated at the EGAM frequency, suggesting that the net increase of diffusivity and the excitation of EGAMs are correlated. In this phase, E_r , the radial electric field exhibits large oscillations at $\omega = \omega_{EGAM}$. The resulting electric shear does not suppress turbulence. Instead, $\chi_{E \times B}$ itself exhibits oscillations at the EGAM frequency and its time-averaged value increases only when EGAMs are excited. This reveals a strong interaction between the EPs and the turbulence, via the excitation of EGAMs.

The complex interaction between the turbulence and EGAMs is further illustrated in figure 8, where the evolution of the oscillating part of R/L_T , defined as $R/L_T - \langle R/L_T \rangle_t$ with $\langle \cdot \rangle_t$ the time average, is plotted for two different time windows. This figure corresponds to the appearance of EGAMs at the end of phase B (bottom panel) and to the phase where turbulence and EGAMs coexist, during phase C (top panel). When a transport barrier is observed, the inner region exhibits an avalanche-like behavior, with fronts propagating outward and vanishing at $\rho \approx 0.5$. In the same figure, EGAMs manifest themselves as static oscillations in the outer region, characterized by horizontal traces. In phase C, we see that there is not a single propagation velocity, i.e. both outward propagating fronts and static oscillations coexist and the outer radial region is also characterized by an avalanche-like behavior. As a result, energy appears to flow from the plasma core to outer regions along radially elongated structures. Mechanisms underlying this phenomenon are still being studied. One possibility is that the EGAM transfers energy to turbulent modes via a decay parametric process. In

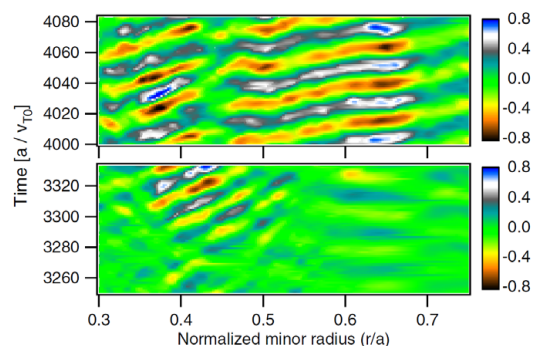


Figure 8. A comparison of the oscillating part of R/L_T in a simulation with fast particles [11] at the end of phase B (bottom) and during phase C (top).

that process, the EGAM is the pump wave, whereas two ITG modes, with identical toroidal and poloidal wave numbers but frequencies shifted by the EGAM frequency, are the daughter waves. The reverse process, i.e. the parametric excitation of a GAM by a pump drift wave via a second drift wave, has been investigated by Zonca and Chen [17]. This may lead to a locking of the avalanches and the electrostatic oscillations [18].

4. Summary

A clear impact of energetic particles (EPs) on turbulence has been observed in gyrokinetic simulations performed with the global GYSELA. By introducing distribution functions typical of fast ions in the absence of turbulence, a mode unambiguously characterized as an EGAM has been observed for parameters consistent with theoretical predictions. The influence of EGAMs on turbulence and associated transport has subsequently been studied using an *ad hoc* source introducing fast particles in non-linear simulations. This source leads to a drastic reduction of the turbulent transport. However, this reduction is only transient; it is followed by an increase of the turbulent activity, characterized by an apparent locking between the EGAMs and avalanches. More generally, this study shows that a radial electric shear oscillating at a

frequency $\omega \sim \omega_{\text{ITG}}$ is unlikely to be an efficient way to suppress turbulence. Nevertheless, future simulations will explore a wider range of source conditions in order to further approach experimentally relevant conditions corresponding to either NBI or ICRF heating in a reactor.

Acknowledgments

This work was granted access to the HPC resources of CINES under the allocation 2012052224 made by GENCI (Grand Equipement National de Calcul Intensif). This work was supported by EURATOM and carried out within the framework of the European Fusion Development Agreement. The views and opinions expressed herein do not necessarily reflect those of the European Commission.

© Euratom 2013.

References

- [1] Zhang W, Lin Z and Chen L 2008 *Phys. Rev. Lett.* **101** 095001
- [2] Diamond P H, Itoh S-I, Itoh K and Hahm T-S 2005 *Plasma Phys. Control. Fusion* **47** R35
- [3] Winsor N, Johnson J L and Dawson J M 1968 *Phys. Fluids* **11** 2448
- [4] Hahm T S 1994 *Phys. Plasmas* **1** 2940
- [5] Conway G D, Angioni C, Ryter F, Sauter P and Vicente J 2011 *Phys. Rev. Lett.* **106** 065001
- [6] Fu G Y 2008 *Phys. Rev. Lett.* **101** 185002
- [7] Qiu Z, Zonca F and Chen L 2010 *Plasma Phys. Control. Fusion* **52** 095003
- [8] Boswell C J, Berk H L, Borba C N, Johnson T, Pinches S D and Sharapov S E 2006 *Phys. Lett. A* **358** 154
- [9] Nazikian R *et al* 2008 *Phys. Rev. Lett.* **101** 185001
- [10] Zarzoso D, Garbet X, Sarazin Y, Dumont R and Grandgirard V 2012 *Phys. Plasmas* **19** 022102
- [11] Zarzoso D *et al* 2013 *Phys. Rev. Lett.* **110** 125002
- [12] Grandgirard V, Sarazin Y, Garbet X, Dif-Pradalier G, Ghendrih Ph, Crouseilles N, Latu G, Sonnendrücker E, Besse N and Bertrand P 2008 *Commun. Nonlinear Sci. Numer. Simul.* **13** 81
- [13] Sarazin Y, Grandgirard V, Abiteboul J, Allfrey S, Garbet X, Ghendrih Ph, Latu G, Strugarek A and Dif-Pradalier G 2010 *Nucl. Fusion* **50** 054004
- [14] Dif-Pradalier G, Grandgirard V, Sarazin Y, Garbet X, Ghendrih P and Angelino P 2008 *Phys. Plasmas* **15** 042315
- [15] Sarazin Y *et al* 2011 *Nucl. Fusion* **51** 103023
- [16] Kim J Y, Horton W, Choi D I, Migliuolo S and Coppi B 1992 *Phys. Fluids B* **4** 152
- [17] Zonca F and Chen L 2008 *Europhys. Lett.* **83** 35001
- [18] Zonca F 2013 private communication

Multi-megawatt, gigajoule plasma operation in Tore Supra

R J Dumont¹, M Goniche¹, A Ekedahl^{1,2}, B Saoutic¹, J-F Artaud¹, V Basiuk¹, C Bourdelle¹, Y Corre¹, J Decker¹, D Elbèze¹, G Giruzzi¹, G-T Hoang¹, F Imbeaux¹, E Joffrin¹, X Litaudon¹, Ph Lotte¹, P Maget¹, D Mazon¹, E Nilsson^{1,2} and The Tore Supra Team¹

¹ CEA, IRFM, F-13108 Saint-Paul-lez-Durance, France

² Applied Physics, Chalmers University of Technology, S-41296 Göteborg, Sweden

Received 28 March 2014, revised 14 May 2014

Accepted for publication 20 May 2014

Published 13 June 2014

Abstract

Integrating several important technological elements required for long pulse operation in magnetic fusion devices, the Tore Supra tokamak routinely addresses the physics and technology issues related to this endeavor and, as a result, contributes essential information on critical issues for ITER. During the last experimental campaign, components of the radiofrequency system including an ITER relevant launcher (passive active multijunction (PAM)) and continuous wave/3.7 GHz klystrons, have been extensively qualified, and then used to develop steady state scenarios in which the lower hybrid (LH), ion cyclotron (IC) and electron cyclotron (EC) systems have been combined in fully stationary shots (duration ~ 150 s, injected power up to ~ 8 MW, injected/extracted energy up to ~ 1 GJ). Injection of LH power in the 5.0–6.0 MW range has extended the domain of accessible plasma parameters to higher densities and non-inductive currents. These discharges exhibit steady electron internal transport barriers (ITBs). We report here on various issues relevant to the steady state operation of future devices, ranging from operational aspects and limitations related to the achievement of long pulses in a fully actively cooled fusion device (e.g. overheating due to fast particle losses), to more fundamental plasma physics topics. The latter include a beneficial influence of IC resonance heating on the magnetohydrodynamic (MHD) stability in these discharges, which has been studied in detail. Another interesting observation is the appearance of oscillations of the central temperature with typical periods of the order of one to several seconds, caused by a nonlinear interplay between LH deposition, MHD activity and bootstrap current in the presence of an ITB.

Keywords: Tore Supra, tokamak, steady-state, gigajoule, lower hybrid, MHD

(Some figures may appear in colour only in the online journal)

1. Long pulse operation in Tore Supra

Achieving long-duration discharges in ongoing magnetic fusion devices is an essential step towards a future fusion reactor. At this point, owing to economic considerations, there is still some uncertainty as to whether a commercial fusion reactor will be operated in a continuous or a pulsed regime [1]. However, regardless of the final choice for a fusion power plant, the discharge duration will be of at least several hours, that is to say, well in excess of the timescale of all physics processes at play in the plasma and its interaction

with the machine structure. Tore Supra, a large tokamak ($R \sim 2.4$ m, $a \sim 0.72$ m, $B_T \lesssim 4.3$ T) equipped with superconducting toroidal field magnets and actively cooled plasma facing components (PFCs), is well adapted to the investigation of the physics and technology issues related to the long pulse operation of future magnetic fusion reactors. Therefore, in past years, among various other topics, numerous experiments have focused on these aspects [2].

Of prime importance to the operation of ongoing fusion experiments, which all require external power to sustain the plasma, is the availability of reliable auxiliary heating

and current drive (H&CD) systems. Tore Supra features radiofrequency (RF) capabilities which have been designed for long pulse and/or continuous wave (CW) operation. Since its first plasma in 1988, the machine has been upgraded on a regular basis to improve its capabilities in terms of steady state operation. Most notably, in 2002, CIEL, a major upgrade of the PFCs and associated infrared (IR) surveillance system, has been completed [3]. As a result, very long pulses (up to more than 6 min) were performed in 2003. In these discharges, called gigajoule (GJ) shots, more than 1 GJ of energy was successfully injected into the plasma, and extracted by the actively cooled PFCs [4]. These shots were inherently steady-state, since the real-time feedback system was imposing a zero inductive flux consumption, which was made possible by the lower hybrid (LH) system. Up to 3 MW of LH power was used as the dominant noninductive current source. These plasmas had typical line-averaged densities $\bar{n}_1 \sim 1.8 \times 10^{19} \text{ m}^{-3}$, plasma currents $I_p \sim 0.5 \text{ MA}$, and exhibited stationary magnetohydrodynamic (MHD) activity related to the presence of a double tearing mode [2] appearing at the surface $q = 3/2$.

More recently, the CIMES project has included an upgrade of the LHCD (LH current drive) system [5]. As a result, Tore Supra is now equipped with two LH antennas based on different designs: a fully active multijunction (FAM) and a passive-active multijunction (PAM) coupler [6]. Coupling of LH power up to 6 MW with this upgraded system has allowed operation at $\bar{n}_1 \sim 3.0 \times 10^{19} \text{ m}^{-3}$, $I_p \sim 700 \text{ kA}$ (poloidal beta $\beta_p \sim 0.6$, normalized toroidal beta $\beta_N \sim 0.7$) with high non-inductive fraction ($f_{ni} \sim 80\%$) either with LH power only, or combining the three available RF systems: LH, ion cyclotron (IC) and electron cyclotron (EC). The steady progress in the long discharge operation of Tore Supra is illustrated in figure 1, which shows that long-duration discharges are now performed at higher levels of RF power compared to in the past.

During the 2010/2011 experimental campaign, the possibilities offered by the expanded operational domain have been exploited to develop advanced scenarios at vanishing loop voltage. This development has proceeded in two directions:

- Operation at higher I_p . However, it is established that the level of LH-driven electron ripple losses increases with I_p [8]. This has turned out to be a stringent limitation, especially in the development of LH-only GJ-class discharges with the electron ripple protection system installed in Tore Supra at the time of these experiments.
- Operation at higher density (closer to the Greenwald limit). Physically, this results in increased electron-ion coupling and therefore allows Tore Supra to operate with T_i closer to T_e despite a dominant electron heating source. From an operational standpoint, this also has the advantage of making the coupling of LH and ICRF (IC range of frequency) waves easier.

One of the goals of the experiments described in the present article is the identification of operation points with V_{loop} as small as possible in order to achieve GJ-class discharges with plasma parameters compatible with the upgraded RF system. In CW, the three antennas comprising the Tore

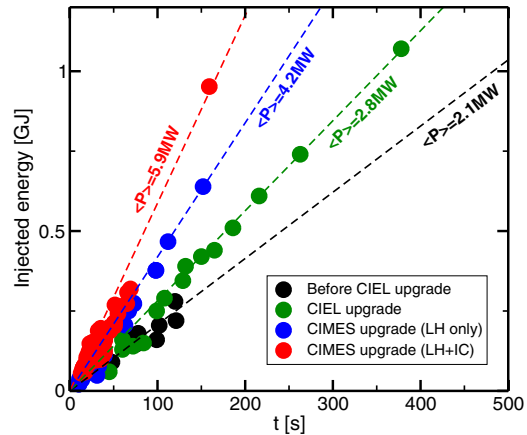


Figure 1. Injected/extracted energy versus discharge duration during steady-state operation in Tore Supra at various periods: before the CIEL upgrade (black symbols), after the CIEL upgrade (green symbols), after the CIMES upgrade using LH power only (blue symbols), after the CIMES upgrade using combined LH and IC waves (red symbols). The dashed lines show linear fits for each group of points, and are characterized by the indicated average total power.

Supra ICRF system have the capability of coupling 1 MW each, which translates into a theoretically achievable power of combined 7 MW LHCD and 3 MW ICRH (IC resonance heating) during 180 s. However, owing to technical issues encountered with the ICRF system (independent of steady-state operation), the experiments have been performed using a total ICRF power of 3 MW at the beginning of the campaign, and 1 MW at the end. Among the most representative discharges performed during the last experimental campaign in the framework of this endeavor are two particular shots, each characterized by a duration exceeding ten times the estimated current diffusion time:

- Discharge #46569: 0.65 GJ injected/extracted energy obtained by coupling 4.5 MW LH power to the plasma during 150 s. The main parameters are $B_T = 3.8 \text{ T}$, $I_p = 0.7 \text{ MA}$, $\bar{n}_1 = 2.6 \times 10^{19} \text{ m}^{-3}$, $\beta_p \sim 0.47$, $\beta_N \sim 0.50$ and $V_{loop} \sim 0.05 \text{ V}$.
- Discharge #47979: 0.95 GJ injected/extracted energy obtained by coupling 6.3 MW combined IC (1 MW) and LH (5.3 MW) power to the plasma during 160 s. The main parameters are $B_T = 3.8 \text{ T}$, $I_p = 0.7 \text{ MA}$, $\bar{n}_1 = 3.0 \times 10^{19} \text{ m}^{-3}$, $\beta_p \sim 0.56$, $\beta_N \sim 0.63$ and $V_{loop} \sim 0.05 \text{ V}$.

The corresponding time traces are shown in figures 2(a) and (b).

The updated domain of operation in terms of density/current in Tore Supra is shown in figure 3. In principle, for a given magnetic field and a given density, it is possible to operate at plasma currents between the Greenwald limit on the one hand, and the stability limit determined by edge safety factor $q_a \approx 3$ on the other hand. However, another constraint is set by the ripple losses protection system. It was established in past experimental campaigns that in the presence of LH power, the level of electron ripple losses scales as $P_R \propto P_{LH} I_p^{0.7} / n_1^{1.2}$

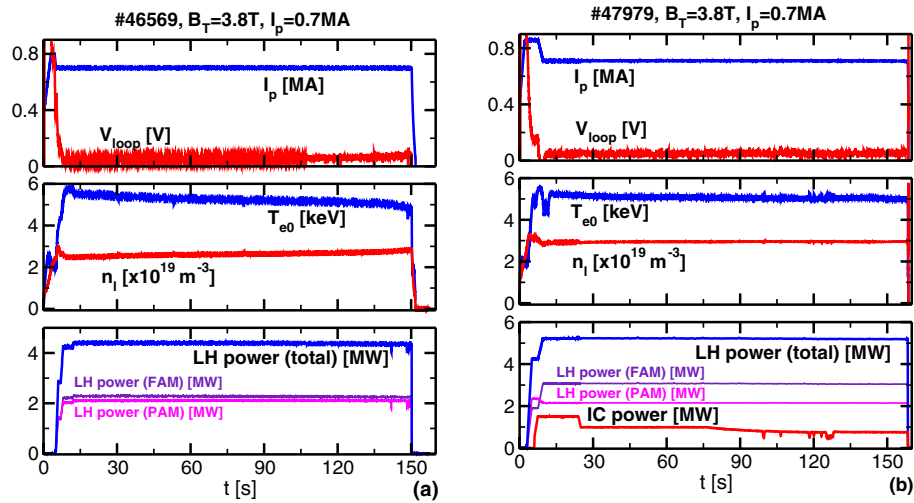


Figure 2. Time traces for shots #46569 with LH power only (a), and #47979 with combined LH and IC power (b). From top to bottom: plasma current and loop voltage; central electron temperature and line-averaged density; LH power coupled with the FAM and PAM antennas.

with P_R the lost power and n_l the line-integrated density. In other words, for a given level of LH power, it is only possible to operate at densities above a certain value, and/or at currents below a certain value. The ripple limits are shown in figure 3 for 3 MW and 5.5 MW LH power, and can be seen to be quite stringent in terms of safe operation at high levels of LH power. Note that this protection system is currently being upgraded in order to prepare for future campaigns. In this figure is highlighted shot #32299, one of the zero loop voltage gigajoule shots performed in 2003 (see also figure 2 in [9]), as well as the two discharges described above.

In the course of the experimental campaign, it clearly appeared that operating with combined LH and IC power was beneficial, notably in terms of MHD stability and also because operation at higher density was possible, thus relaxing the constraint related to electron ripple losses. Compared to the GJ discharges performed in 2003, LH+IC shots are stable with respect to double tearing modes, and the temperature profiles are typical of discharges featuring electron internal transport barriers (ITBs), which are generally maintained throughout the whole plasma duration. These ITBs appear most clearly in shots where the three RF heating systems have been used simultaneously. As an illustration, figure 4 shows the temperature profile in shot #47968, measured prior to and during the application of 700 kW of EC power, in addition to 5.2 MW of LH power and 1 MW of IC power. In this shot, two gyrotrons have been employed; one couples RF power in the plasma through an optical mirror set to inject EC power at toroidal 25° in the direction of the plasma current, and a second one injecting the same level of power with the same toroidal angle in the opposite direction with respect to the plasma current [10]. Ray-tracing calculations indicate that this results in a fairly central power deposition profile (shown in figure 4), with no driven EC current to lowest order. It should be mentioned that for technological reasons, during this

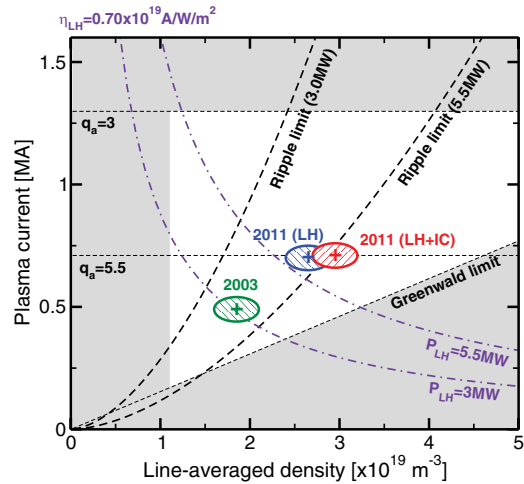


Figure 3. Overview of the Tore Supra (\bar{n}_l, I_p) domain of operation. The shaded area corresponds to inaccessible regions due to stability limits. The ripple limits for 3 and 5.5 MW of LH power appear as dashed lines. The dotted-dashed curves show the theoretical zero-loop voltage points of operation accessible for a normalized LH efficiency $\eta_{LH} = 0.70 \times 10^{20} \text{ AW}^{-1} \text{ m}^{-2}$ with 3 and 5.5 MW of LH power. Shot #32299 is a zero loop voltage gigajoule discharge performed in 2003, and appears as a green cross. Shots #46569 and #47979 have been performed during the last experimental campaign and are shown as blue and red symbols, respectively. Each is surrounded by an ellipse illustrating the corresponding domain of operation.

campaign, the 118 GHz gyrotrons were limited to 5 s power injection. The compatibility of EC waves with these scenarios was thus checked, but their use for actual plasma control is planned for upcoming campaigns.

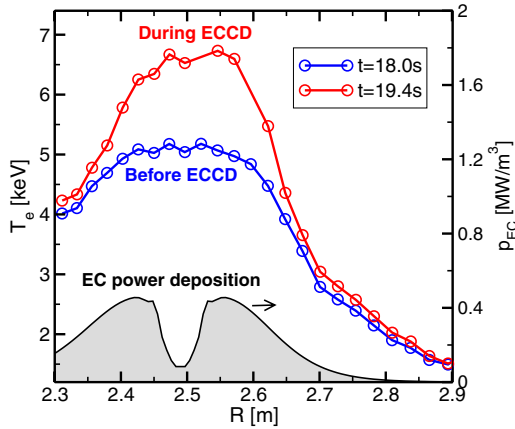


Figure 4. Electron temperature profile in shot #47968 before and during the application of 700 kW of EC power (left y-axis). Also shown is the computed EC power deposition mapped in the equatorial plane (right y-axis).

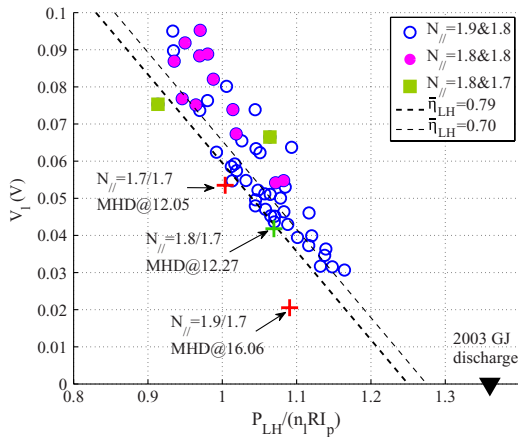


Figure 5. Loop voltage versus normalized LH power for various respective combinations of the FAM and PAM launchers. The two dashed lines show the apparent (thick) and corrected (thin) normalized LH efficiency $\bar{\eta}_{LH} \equiv \eta_{LH} / (10^{19} \text{ AW}^{-1} \text{ m}^{-2})$. Also shown are the zero loop voltage GJ shots performed in 2003 (black triangle).

The slow decrease of the ICRF power in shot #47979 (see figure 2(b)) is an automatic response to an apparent overheating event on the FAM LH coupler detected by the IR surveillance chain. The automated safety system has attributed this event to lost fast ions impacting the front face of the antenna, which triggered a lowering of the ICRF power and a premature shot termination related to the appearance of MHD activity in the discharge (see section 2). It turns out that the observed hot spot actually corresponds to a Langmuir probe flush-mounted on the LH antenna, and should have had no consequence on the scenario since the temperature was within acceptable limits for this particular, non-actively

cooled, object. This underlines the difficulty of designing adequate surveillance and real-time control systems based on IR thermography measurement suited to long pulse operation in the presence of fast particle losses, RF sheaths, etc. These phenomena result in the heating of both actively cooled PFCs and non-actively cooled objects [11, 12]. It is worthwhile pointing out that discharge durations exceeding the current diffusion time are necessary in order to properly assess the possibility of extending a given scenario to stationary operation. Other phenomena (fast particle losses, hot spots, impurities...) can manifest themselves even after several resistive times. In this respect, the operation of steady-state devices such as Tore Supra is crucial in order to prepare for the International Thermonuclear Experimental Reactor (ITER).

The remainder of this article is organized as follows: in section 2, the issue of MHD-safe operation using ICRF waves at high levels of LH power is presented. Global confinement properties of these discharges are discussed in section 3. Finally, a new type of slow oscillation appearing in these plasmas is analyzed in section 4. Conclusions and prospects are drawn in section 5.

2. MHD stability at high levels of LH power

Given the finite amount of magnetic flux available in the poloidal field system, it is necessary to operate at low values of the loop voltage to achieve long-duration discharges. This is accomplished in Tore Supra by using LHCD. Figure 5 shows the loop voltage measured during the steady-state phase versus normalized LH power $P_{LH} / (\bar{n}_1 R I_p)$ in combined LH+IC discharges (R is the plasma major radius). In this figure, the dashed lines show the apparent LH efficiency (defined as $\eta_{LH} \equiv \bar{n}_1 R I_{LH} / P_{LH}$ with I_{LH} the driven current), $\eta_{LH} = 0.79 \times 10^{19} \text{ A W}^{-1} \text{ m}^{-2}$, and the actual efficiency $\eta_{LH} \approx 0.70 \times 10^{19} \text{ A W}^{-1} \text{ m}^{-2}$ obtained by subtracting a mean 12% bootstrap current contribution estimated with the CRONOS suite of codes used for the interpretative simulation of these discharges [13]. This figure has been obtained by averaging the measured loop voltage over a 10 s time window ($t = 13\text{--}23$ s), except when the discharge ends in a MHD disruption, in which case the data is averaged in the time interval $t = 12\text{--}13$ s. For reference, the efficiency characterizing the 2003 GJ discharges is also shown [4].

During this campaign, the possibility of modulating the toroidal spectrum and power balance between the FAM and PAM launchers has been tested. Eventually, the choice of the parallel refractive index peak (denoted n_{\parallel}) of the LH spectrum results from a trade-off between η_{LH} (which scales as $\sim 1/n_{\parallel}^2$) and the MHD stability of the resulting plasmas. Indeed, at these levels of LH power, the discharges obtained are sawtooth-free and characterized by significantly reversed safety factor (q) profiles. According to EFT calculations constrained by polarimetry measurements [14], the minimum is typically located at $r_{\min}/a \sim 0.25$ ($R \sim 2.75$ m). Although this indirect method leaves some uncertainty regarding the precise value of q_{\min} , the obtained hollow current profiles are consistent with CRONOS reconstructions and indicate that whereas q_{\min} is above 1.5 in some pulses, it lies between 1.3 and 1.5 in most cases.

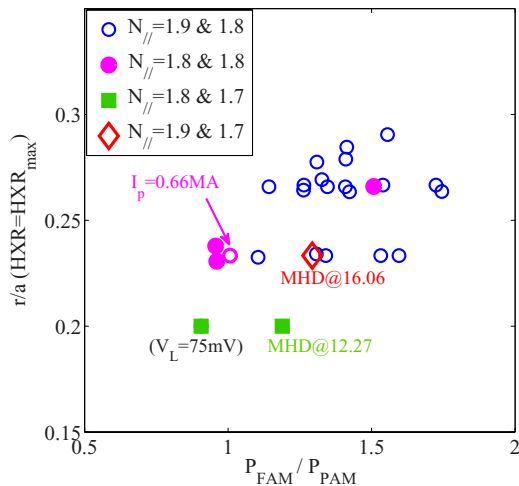


Figure 6. Normalized radius of maximum HXR emission in the 60–80 keV range versus the ratio between the power launched by the FAM and PAM LH launchers for various injected spectra.

A consequence of this reversal is the systematic presence of electron ITBs but for these parameters, this situation is also prone to the triggering of double tearing modes on the surfaces $q = 4/3$ often present in the plasma (see section 4). In this respect, higher values of n_{\parallel} are desirable despite a lower CD efficiency, since they result in broader power deposition profiles and thus a larger spatial separation between the two resonant surfaces. It has been found that stable operation was possible using the combined FAM and PAM antennas with spectra peaked at $n_{\parallel} = 1.9$ and $n_{\parallel} = 1.8$, respectively. It should be noted that the power ratio between both antennas is an important parameter: the PAM coupler spectrum features a secondary peak at relatively moderate $-n_{\parallel}$, which results in a globally more hollow LH current profile than would be driven with FAM antennas only [7]. This is illustrated in figure 6 where the maximum radius of HXR emission in the 60–80 keV range, representative of the location of the maximum LH current, is shown versus the ratio between the power coupled by the FAM and the PAM antennas. At constant total LH power, increasing the power injected by the FAM antenna tends to broaden the current profile. Interestingly, even when the index of the main spectral lobe is set to the same value for both launchers, the power deposition is still sensitive to the ratio $P_{\text{FAM}}/P_{\text{PAM}}$, demonstrating the role of the secondary lobes of the launched spectrum.

During the development of combined LH+IC scenarios, it was routinely observed that the IC power had a stabilizing effect, consistent with past observations in Tore Supra [15]. In several instances, accidental IC power switch-offs have occurred, resulting in the triggering of MHD activity. Figure 7 shows time traces corresponding to shot #47319 in which the IC power is switched off at $t = 25$ s, whereas the LH power is still at its nominal value. A marked increase of the MHD signal picked up by the Mirnov coils is clearly seen approximately 500 ms after the IC termination, immediately followed by a LH

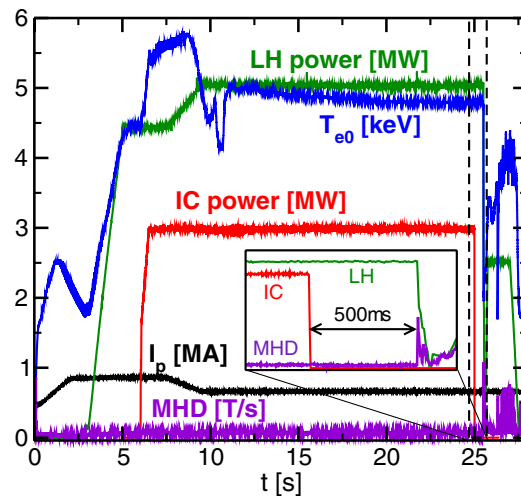


Figure 7. Time traces for shot #47319: LH power, central electron temperature, ICRF power, plasma current and MHD signal. The inset shows a zoom on the period immediately following the ICRF switch-off.

switch-off triggered by the real-time control system in response to the appearance of excessive MHD activity in the discharge. This beneficial effect of the ICRF power can be explained by a direct contribution of the fast ions to the plasma stability [16, 17], and also as a result of the change in equilibrium caused by the ICRF power.

In order to estimate the fast ion pressure in these discharges, the ICRF code EVE/AQL [18] has been used. It combines the full wave solver EVE with the Fokker–Planck module AQL, as detailed in [19]. The fast ion distribution in shot #47319 is firstly modeled at full ICRF power using the kinetic profiles provided by CRONOS prior to the ICRF switch-off at $t = 25$ s. For this purpose, CRONOS is run in interpretative mode and the validity of the simulation is checked by direct comparisons to the measured magnetic flux consumption, internal inductance, diamagnetic energy, neutron rate, electron density and temperature profiles [13]. The power is then set to zero in EVE/AQL, resulting in a decaying fast ion population. In figure 8, the corresponding time traces are shown. In particular, we note that the fueling system is not able to immediately respond to the sharp ICRF switch-off to maintain the required density constant during this event. As a result, a decrease of the density is observed, also impacting on the plasma thermal energy (W_{th}). This effect is taken into account in AQL, although the induced equilibrium changes are not. The agreement between the experimental value of the total energy measured by the diamagnetic loop at full ICRF power $W_{\text{dia}}(t = 25 \text{ s}) \approx 0.38 \text{ MJ}$ is recovered within the error margins inherent to the measurement and ICRF code hypotheses. AQL manages to reproduce the fast ion decay fairly well when the change in the plasma density is taken into account. The computed total energy density profiles at various times after the switch-off are shown in figure 9. According to the modeling result,

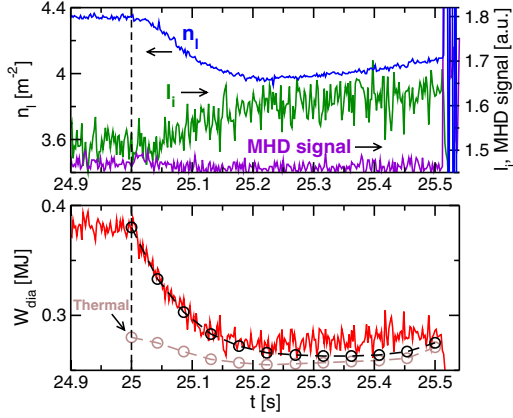


Figure 8. Time traces for shot #47319 after the ICRF switch-off (inset of figure 7), appearing as a dashed line. (Top) line-integrated density (left y-axis), internal inductance and MHD signal (right y-axis); (bottom) measured W_{dia} (solid), EVE/AQL calculation of W_{dia} (dashed, black) and W_{th} (dashed, brown).

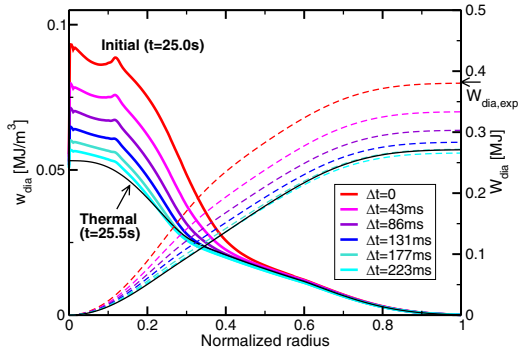


Figure 9. Energy content in shot #47319 after ICRF switch-off computed by AQL. Total energy density (left y-axis), integrated total energy (right y-axis). The thermal level at $t = 25.5$ s is shown as a thin curve. Also shown on the right y-axis is the measured value of W_{dia} at the ICRF switch-off.

the estimated fast ion effective temperature $T_{\text{eff}} \sim 150$ keV drops rapidly and 250 ms after the IC power switch-off, the contribution of the fast ion population is essentially zero (a fit of the energy decrease observed in figure 8 yields a decay time $\tau_{\text{decay}} \approx 85$ ms). In conclusion, both the measurements and simulations indicate that the tail has relaxed well before the MHD onset. Therefore, although a contribution from fast ion energy to the discharge stability can not be excluded, a supplemental stabilization mechanism due to modifications of the equilibrium needs to be invoked. The fact that the latter changes as a result of the ICRF switch-off can be clearly seen on the internal inductance (l_i), which is deduced from real-time magnetic measurements [20] and shown in figure 8.

Linear MHD calculations have been performed using the CASTOR code [21] with resistivity set to $\eta = 10^{-7}$. They predict the potential destabilization of a double-tearing mode on the

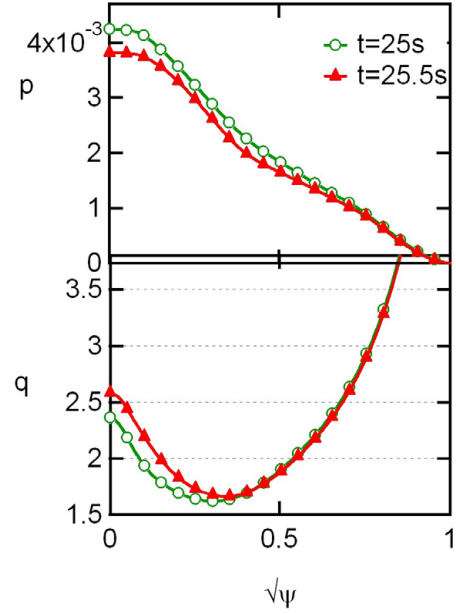


Figure 10. Pressure (top) and safety factor (bottom) profiles computed by CRONOS before and after ICRF switch-off.

$q = 2$ surfaces. This is the combined result of (1) a decrease of the central electron temperature (T_e) after the IC switch-off, which results in enhanced shear reversal, and (2) a decrease of the total pressure. These profiles, shown in figure 10, have been used in CASTOR. The predicted linear growth rate λ , shown in figure 11, increases after the ICRF switch-off as a result of the lower curvature stabilization caused by the pressure decrease [22]. Nonlinear calculations with the XTOR-2F code [23] show the same trend although, in this case, the inclusion of diamagnetic effects results in the simultaneous destabilization of several MHD modes located near the q_{min} surface [24–27].

3. Global confinement and transport

The electron energy content in the discharges performed during the last experimental campaign has been analyzed. The Rebut-Lallia-Watkins (RLW) scaling law is known to fit well Tore Supra measurements in the ohmic phase [28]

$$W_e^{\text{RLW}} \equiv 2.6 \times 10^{-2} n_1^{-3/4} Z_{\text{eff}}^{1/4} B_T^{1/2} I_p^{1/2} (\kappa a^2 R)^{11/12} + 1.2 \times 10^{-2} I_p P_{\text{tot}} Z_{\text{eff}}^{-1/2} (\kappa a^2 R)^{1/2}, \quad (1)$$

with the density in units of 10^{19} m^{-3} , I_p in MA, and P_{tot} the total power in MW. a is the plasma minor radius, κ the plasma elongation, B_T the toroidal field on axis, and Z_{eff} the effective charge. In phases with LH power only, the electron confinement is improved with respect to the RLW scaling, a feature typical of discharges in the LH enhanced performance (LHEP) regime [29]. In LH+IC discharges, it has

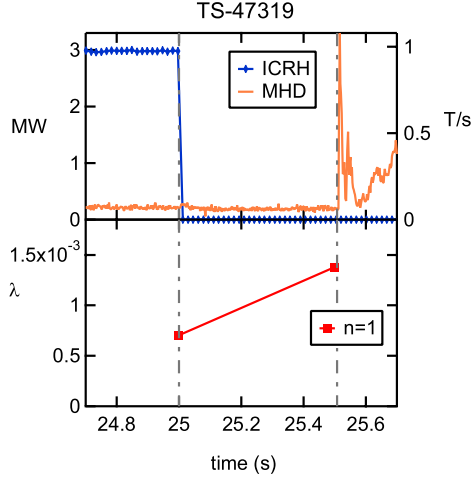


Figure 11. IC power and MHD signal (top); linear growth rate of $n = 1$ resistive modes (bottom), calculated using the CASTOR code with resistivity $\eta = 10^{-7}$.

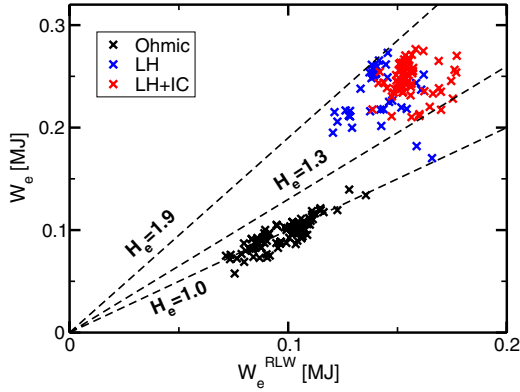


Figure 12. Electron energy content versus Rebut-Lallia-Watkins scaling. The black points denote measurements performed during ohmic phases of the discharges, the blue (respectively red) points show LH only (respectively LH+IC) phases.

been observed that the electron confinement is also improved by a similar factor, which means that at these levels of power, no negative impact of the ICRF waves on electron transport is observed. Figure 12 shows a plot of the electron energy content W_e versus the RLW scaling prediction (equation (1)). Typical improvement of the energy confinement in steady-state phases, determined by $H_e \equiv W_e / W_e^{RLW}$ is in the range 1.3–1.9, and is essentially independent of the presence of ICRH.

Electron ITBs have been systematically observed in the discharges performed during this experimental campaign. These ITBs were routinely sustained during the whole steady-state phase. An example of a CRONOS calculation for shot #47319 already presented in the previous section (see figure 7) is shown in figure 13. The electron temperature profiles, safety

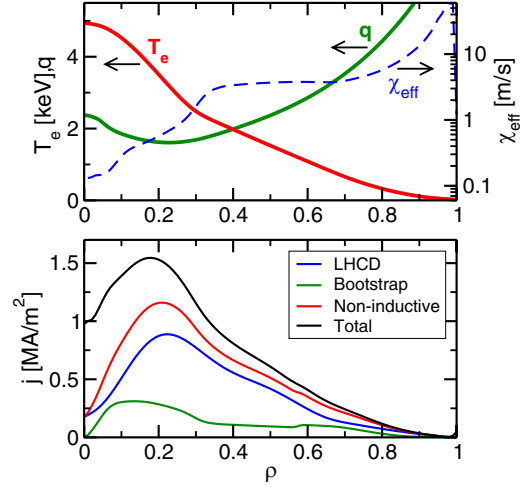


Figure 13. CRONOS interpretative analysis of shot #47319 in time interval 20–25 s. (Top) temperature and safety factor (left y-axis); electron heat diffusivity (right y-axis); (bottom) contributions to the current profile: LH, bootstrap, non-inductive and total.

factor, effective heat diffusivity and various contributions to the current profile are averaged between $t = 20$ s and $t = 25$ s. The electron temperature profile features a steep gradient around the predicted reversal of the safety factor profile $\rho \approx 0.25$. The electron heat diffusivity drops sharply inside $\rho = 0.3$, which is indicative of an ITB. This ITB is believed to be the result of the negative magnetic shear, although a contribution from plasma rotation can not be excluded [30]. As also shown in figure 13, according to the interpretative simulation, in this discharge characterized by $V_{loop} \approx 0.068$ V, the LH current profile is peaked at normalized radius $\rho \approx 0.25$ and accounts for 62% of the total current, whereas the bootstrap current provides 19%.

The total energy content has also been compared to the Tore Supra scaling law, and to the ITERL97-P scaling [28]

$$W_{ITERL97-P} \equiv 0.023 \kappa^{0.64} R^{1.83} \epsilon^{-0.06} I_p^{0.96} B_T^{0.03} \bar{n}_1^{0.4} P^{0.27}, \quad (2)$$

where $\epsilon \equiv R/a$ is the aspect ratio. In this range of parameters, both scaling laws for the total energy exhibit negligible difference. Although it appears at first that the total energy content is significantly improved, this conclusion should be tempered because the measured quantity (W_{dia}) includes the energy contained in fast particles, whereas the Tore Supra and ITERL97-P scaling laws have been established to fit the thermal energy content W_{th} . In these discharges, however, it is difficult to obtain the thermal ion energy directly from the available measurements. In this range of ICRF power (1–3 MW), EVE/AQL calculations for selected discharges predict an approximately linear increase of the fast ion energy content W_f from 10% ($P_{IC} = 1$ MW) to 30% ($P_{IC} = 3$ MW). Using $W_{th} \approx W_{dia} - W_f$ as an estimate of the thermal energy, the results in figure 14 show that the total confinement improvement in the presence of LH+IC power is comparable to that with LH power only. As is consistent with this observation, no clear evidence of ion ITB is seen in these discharges.

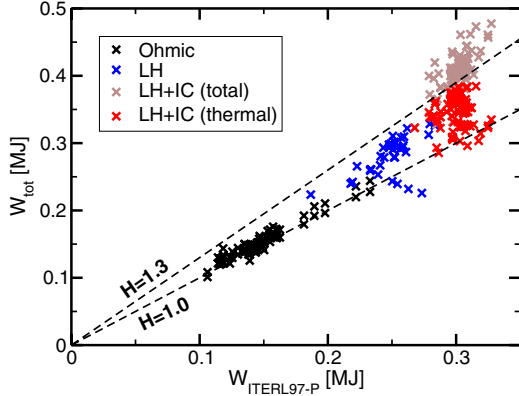


Figure 14. Total energy content versus ITERL97-P scaling law. Ohmic phase (black symbols), LH-only phase (blue symbols), LH+IC phase (brown and red symbols). The latter are obtained by subtracting the superthermal ion content estimated with *EVE/AQL*.

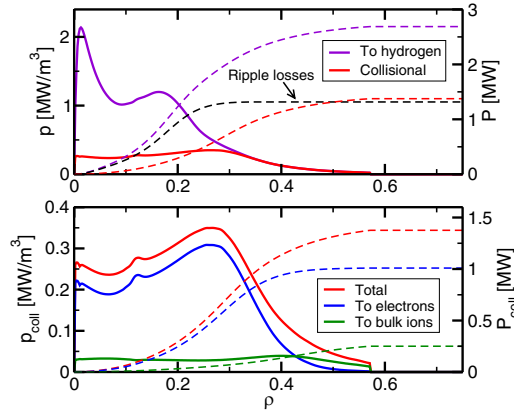


Figure 15. *EVE/AQL* calculation of power density (solid curves, left y-axis) and total power (dashed curves, right y-axis) with 3 MW ICRF power in shot #47319. (Top) power to hydrogen ions, coupled to thermal plasma and ripple-lost; (bottom) power density (left y-axis) and total power (right y-axis) coupled to thermal plasma, to electrons, to bulk ions (bottom).

The *EVE/AQL* simulations of shot #47319 previously discussed have been used to estimate the level of RF power heating the bulk ions through collisional relaxation of the fast proton tail. The obtained profiles at 3 MW of ICRH are shown in figure 15. First, it is observed that the power deposition occurs mainly on the hydrogen minority species (2.7 MW), as expected in a minority heating scheme. Secondly, at these moderate densities, a significant amount of power leaves the plasma due to ripple losses in agreement with established scaling laws for Tore Supra [31]. At 3 MW of total ICRF power, *AQL* predicts that 75% of the power absorbed by protons and transmitted to the thermal species through collisions eventually heats electrons, whereas only 25% go to bulk ions. When considering 1 MW, the power is roughly evenly split

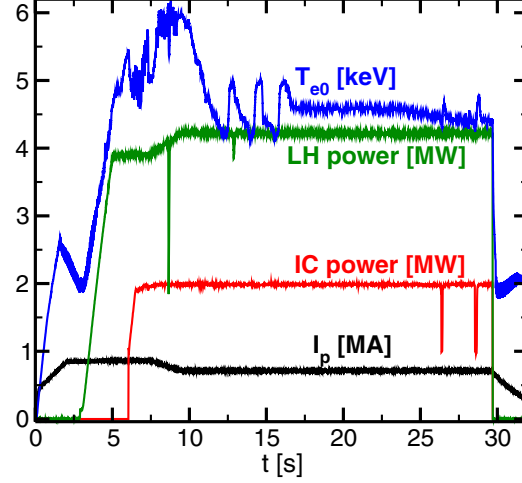


Figure 16. Time traces for shot #48161: central electron temperature; LH power, IC power and total plasma current.

between electrons and ions. In any case, this means that the total power on ions from IC waves is in the range 0.5–1 MW at most. In addition to this, these calculations show that for this magnetic field, the power deposition is slightly shifted towards the high field side, which results in a power deposition occurring in a rather large volume inside $\rho \sim 0.4$. Finally, *CRONOS* calculations indicate that equipartition is negligible for $\rho > 0.1$. As a result, the heating source on thermal ions, either from collisional relaxation by fast ions or from equipartition, is very small inside the ITB ($\rho \sim 0.25$). This is a possible explanation for the absence of any observed ion ITB in these discharges. It is expected that operating at higher densities in future experiments will allow us to better qualify ion transport.

4. Nonlinear oscillations

A recurring observation in the steady-state operation of Tore Supra is the manifestation of nonlinear interplays between the plasma quantities, which generally translates into T_e oscillations with periods extending up to a few seconds. Several oscillation regimes have been identified before in Tore Supra [32]. In the oscillation (O)-regime, an interplay between the LH current and the electron temperature causes almost purely sinusoidal oscillations observed on the central channels of the electron temperature measured by the electron cyclotron emission (ECE) radiometer. In the case of the so-called giant oscillation (GO)-regime, the double/triple tearing modes appearing on the $q = 2$ surfaces are believed to be the underlying mechanism [33]. A new regime was obtained during the last experimental campaign. An example of these new large oscillations, which were observed in several shots, is shown in figure 16. In discharge #48161, the electron temperature exhibits a slow, regular oscillation in the time interval $t = 12$ –17 s. It is not believed to be an occurrence of the O-regime since these oscillations have a different shape,

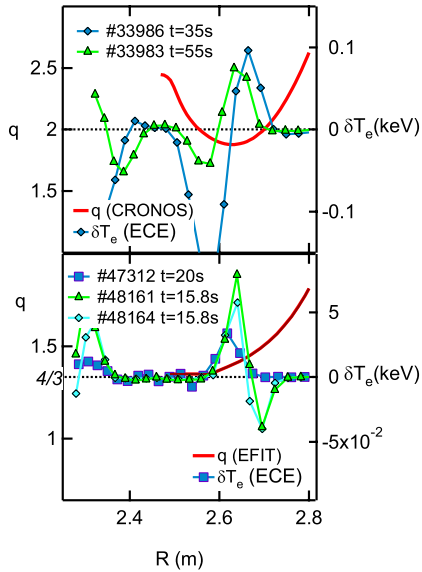


Figure 17. MHD mode structure deduced from ECE measurements of δT_e (right y-axis) in the giant oscillation regime (top) and during the oscillations observed during the last campaign (bottom). Also shown is the safety factor profile reconstructed with CRONOS/EFIT (left y-axis).

and also because the LH current profile itself does not oscillate, as detailed below. The structure of a given MHD mode appearing in Tore Supra discharges can be deduced from correlation ECE measurements, and is characterized by a radial profile of δT_e , the oscillating part of T_e at the mode frequency following the method detailed in [34]. The present oscillation regime is found to differ significantly from the GO regime in that only MHD modes compatible with $q = 4/3$ are present during this shot. The obtained structure in both cases is compared in figure 17, with the safety factor profile reconstructed by CRONOS and EFIT. The common point between the GO and these $q = 4/3$ oscillations reduces to the presence of MHD modes at the pivot of the oscillation cycle, but the latter have a lesser overall impact on the discharge than the former. The time behavior of typical GO in the presence of $q = 2$ modes and the oscillations observed during the last experimental campaign is shown in figure 18. The latter appear to be significantly slower than in the GO regime. Therefore, whereas the MHD modes on $q = 2$ appeared to be a plausible candidate for the triggering of the oscillations in the GO regime, it seems that the MHD activity in these discharges is more an indication of the presence of $q = 4/3$ surfaces in the plasma than a real driving force behind the phenomenon: in particular, no significant changes of the MHD activity are observed during the oscillation cycle, whereas the $q = 2$ MHD mode was alternating between double and triple tearing mode depending on the considered instant during the cycle [33].

In order to gain some insight into the features of the observed oscillations, the CRONOS suite of codes has been used to reconstruct the various contributions to the current profile,

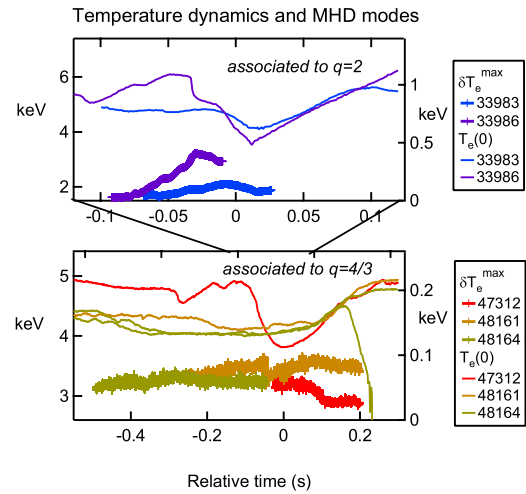


Figure 18. Comparison of central temperature $T_e(0)$ (left y-axis) and maximum of temperature oscillation δT_e^{\max} at the MHD mode frequency (right y-axis) during the oscillations observed in the GO regime (top) and in the last experimental campaign (bottom).

and the resulting transport coefficients. Figure 19 shows the reconstructed contributions to non-inductive current density (j_{ni}), i.e. the bootstrap current (j_{bs}) and the LH-driven current (j_{lh}) at three times during the second oscillation of shot #48161. According to the reconstruction of the HXR emission signal in the 60–80 keV range of energy, the LH current does not evolve during the cycles. This has been checked also for the lower energy ranges in order to ensure that the corresponding power source remains constant over time. In other words, both the LH power and current sources remain unchanged during the oscillation cycles. In the meantime, however, the bootstrap current maximum appears to oscillate between the vicinity of the ITB and the magnetic axis. This displacement results in a shift in the location of the non-inductive current, a shift of the q_{\min} surface location, and a subsequent degradation of the improved confinement. A central negative magnetic shear is believed to be a necessary condition for the plasma to transit into the LHEP regime [29]. Figure 20 shows plots of the central electron temperature T_{e0} , the locations of maximum j_{bs} , j_{lh} and j_{ni} respectively ($\rho_{\max,bs}$, $\rho_{\max,lh}$, $\rho_{\max,ni}$ respectively) as well as $\langle s \rangle$, the magnetic shear averaged between $\rho = 0$ and 0.2. It can be observed that when $\langle s \rangle$ becomes negative, T_{e0} increases rapidly. This entails a shift of $\rho_{\max,bs}$ towards the magnetic axis, and thus an increasing mismatch with $\rho_{\max,lh}$. In these discharges, the local bootstrap current density amounts up to 30% of the total current, which means that a global shift of $\rho_{\max,ni}$ towards the plasma center occurs and $\langle s \rangle$ increases until the improved confinement is lost when $\langle s \rangle \gtrsim 0$. As a consequence T_{e0} decreases and $\rho_{\max,bs}$ shifts outwards, resulting in a gradual realignment of j_{bs} with j_{lh} and a reinforcement of the q -profile reversal triggering a new LHEP transition. Although this mechanism remains to be explored in more detail experimentally, notably to identify the role of the small but finite residual ohmic current in these discharges,

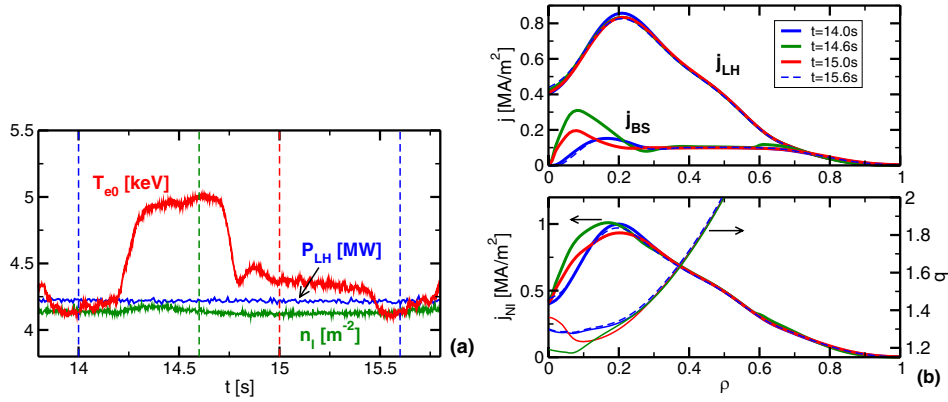


Figure 19. A zoom on the second oscillation shown in figure 16. (a) Central temperature, LH power and line-integrated density; (b) top, LH and bootstrap current profile at various times during the oscillation (denoted by dashed lines in (a)); (b) bottom, total non-inductive current (left y-axis) and corresponding q-profile (right y-axis, thinner curves).

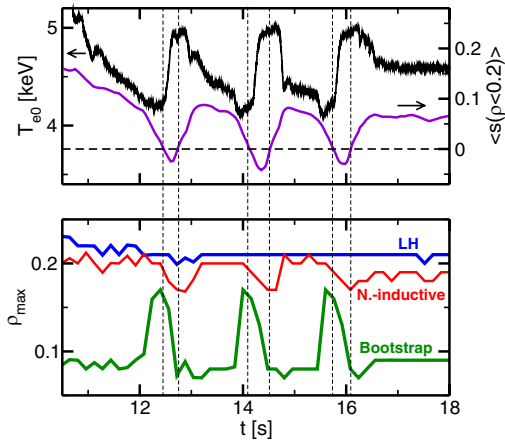


Figure 20. (Top) central electron temperature (left y-axis) and magnetic shear averaged inside $\rho = 0.2$ (right y-axis); (bottom) location (in normalized radius) of maximum LH, bootstrap and non-inductive current.

it is believed to be an occurrence of the misalignment process discussed in Bizarro *et al* [35]. This opens the way to future experiments in Tore Supra in which the bootstrap current plays an important role. In particular, it could be possible to extensively investigate this potential misalignment of the LH and bootstrap currents, possibly using the EC system as an actuator. The prospect of aligning the bootstrap current and the LH driven current profiles would fit the Tore Supra long term objectives: a feedback algorithm to increase P_{LH} as β_p increases would be a method to experimentally simulate discharges at high levels of core bootstrap current in future fusion devices [9].

5. Conclusions

Significant progress has been achieved in the steady-state operation of Tore Supra during the 2010/2011 experimental

campaign. A comprehensive set of shots characterized by injected/extracted energy in the gigajoule range, and a discharge duration well in excess of the timescale characterizing the processes at play (energy, current and momentum diffusion, plasma-wall interaction, hot spots, overheating of actively cooled PFCs. . .) have been performed. In the continuity of past efforts in Tore Supra, these discharges have relied on dominant LH power. However, in this campaign, IC and EC power have also been coupled to the plasma. Interestingly, the presence of significant ICRF power allows the window of stable MHD operation to be extended as a result of changes in the equilibrium and fast ion stabilization. As a consequence, electron ITBs have been routinely observed in LH+IC shots, with global transport properties comparable to the LHEP discharges previously produced, which exhibited improved electron confinement with LH power only. At these densities, compatible with efficient LHCD, the level of RF power actually heating bulk ions inside the ITB is rather low, and no improvement of ion transport could be observed. The level of bootstrap current has been increased with respect to past operation. As a result, a new regime in which oscillations of the bootstrap current between the magnetic axis and the ITB foot has been observed. This oscillation is believed to be caused by a misalignment between the LH current profile and the bootstrap current. Although scenarios employed in future machines are likely to be different by design, for instance in terms of relative importance of the LH power, this misalignment phenomenon is quite generic and could manifest itself in other forms. Super-conducting devices such as Tore Supra and its potential successors have thus a unique capability to investigate a number of key physics and technology processes at play in the steady-state operation of future magnetic fusion devices.

Acknowledgments

This work, supported by the European Communities under the contract of Association between EURATOM and CEA, was carried out within the framework of the European

Fusion Development Agreement, using HPC resources from GENCI (project t2013056088) and from the Mésocentre d'Aix-Marseille Université (project 13b014). The views and opinions expressed herein do not necessarily reflect those of the European Commission.

References

- [1] Pamela J, Bécoulet A, Borba D, Boutard J-L, Horton L and Maisonnier D 2009 *Fusion Eng. Des.* **84** 194
- [2] Saoutic B, Chatelier M and De Michelis C 2009 *Fusion Sci. Technol.* **56** 1079
- [3] Garin P, on behalf of the Tore Supra Team 2001 *Fusion Eng. Des.* **56–7** 117
- [4] Van Houtte D, Martin G, Bécoulet A, Bucalossi J, Giruzzi G, Hoang G T, Loarer Th and Saoutic B on behalf of the Tore Supra Team 2004 *Nucl. Fusion* **44** L11
- [5] Beaumont B *et al* 2001 *Fusion Eng. Des.* **56–7** 667
- [6] Ekedahl A *et al* 2010 *Nucl. Fusion* **50** 112002
- [7] Nilsson E *et al* 2013 *Nucl. Fusion* **53** 083018
- [8] Basiuk V, Peysson Y, Lipa M, Martin G, Chantant M, Guilhem D, Imbeaux F, Mitteau R and Surle F 2001 *Nucl. Fusion* **41** 477
- [9] Litaudon X and The Tore Supra Team 2009 *Fusion Sci. Technol.* **56** 1445
- [10] Lennholm M *et al* 2003 *Nucl. Fusion* **43** 1458
- [11] Corre Y *et al* 2011 *Fusion Eng. Des.* **86** 429
- [12] Ritz G *et al* 2013 *Fusion Eng. Des.* **88** 899
- [13] Artaud J-F *et al* 2010 *Nucl. Fusion* **50** 043001
- [14] Li Y G, Lotte Ph, Zwingmann W, Gil C and Imbeaux F 2011 *Fusion Sci. Technol.* **59** 397
- [15] Imbeaux F *et al* 2011 *Nucl. Fusion* **51** 073033
- [16] White R B, Romanelli F and Bussac M N 1990 *Phys. Fluids B* **2** 745
- [17] Porcelli F 1991 *Plasma Phys. Control. Fusion* **33** 1601
- [18] Dumont R J 2009 *Nucl. Fusion* **49** 075033
- [19] Dumont R J and Zarzoso D 2013 *Nucl. Fusion* **53** 013002
- [20] Saint-Laurent F and Martin G 2001 *Fusion Eng. Des.* **56** 761
- [21] Kerner W, Goedbloed J P, Huysmans G T A, Poedts S and Schwarz E 1998 *J. Comput. Phys.* **142** 271
- [22] Glasser A H, Greene J M and Johnson J L 1975 *Phys. Fluids* **18** 875
- [23] Lütjens H and Luciani J-F 2010 *J. Comput. Phys.* **229** 8130
- [24] Meshcheriakov D, Maget P, Lütjens H, Beyer P and Garbet X 2012 *Phys. Plasmas* **19** 092509
- [25] Maget P, Mellet N, Lütjens H, Meshcheriakov D and Garbet X 2013 *Phys. Plasmas* **20** 112504
- [26] Mellet N, Maget P, Lütjens H, Meshcheriakov D and The Tore Supra Team 2013 *Nucl. Fusion* **53** 043022
- [27] Maget P, Lütjens H, Luciani J-F, Garbet X, Février O and Ségui J-L 2014 *Phys. Plasmas* accepted
- [28] Kaye S M *et al* 1997 *Nucl. Fusion* **37** 1303
- [29] Hoang G T *et al* 1994 *Nucl. Fusion* **34** 75
- [30] Chouli B *et al* 2014 *Plasma Phys. Control. Fusion* submitted
- [31] Basiuk V, Eriksson L-G, Bergeaud V, Chantant M, Martin G, Nguyen F, Reichle R, Vallet J C, Delpech L and Surle F 2004 *Nucl. Fusion* **44** 181
- [32] Imbeaux F *et al* 2006 *Phys. Rev. Lett.* **97** 045004
- [33] Maget P, Imbeaux F, Giruzzi G, Udintsev V, Huysmans G T A, Ségui J-L, Goniche M, Moreau P, Sabot R and Garbet X 2006 *Nucl. Fusion* **46** 797
- [34] Udintsev V S, Goniche M, Ségui J-L, Giruzzi G, Molina D, Turco F, Huysmans G T A, Maget P, Tore Supra Team and Krämer-Flecken A 2006 *Fusion Sci. Technol.* **50** 508
- [35] Bizarro J P S, Litaudon X, Tala T J J and JET EFDA Contributors 2007 *Nucl. Fusion* **47** L41